

**INVESTIGATING THE NATURE OF PASSIVE FILMS ON
AUSTENITIC STAINLESS STEELS**

T. L. SUDESH L. WIJESINGHE

(B.Sc. (Eng.), Moratuwa, Sri Lanka)

**A THESIS SUBMITTED
FOR THE DEGREE OF DOCTOR OF PHILOSOPHY
DEPARTMENT OF MATERIALS SCIENCE
NATIONAL UNIVERSITY OF SINGAPORE**

2005

ACKNOWLEDGEMENTS

I wish to express my heartfelt gratitude to my supervisor, Associate Professor Daniel John Blackwood who was the main inspiration behind my research. I am so grateful to him for all your guidance and encouragement throughout my project, at the same time for his outstanding tolerance and tenderness helped me for a peaceful mindset to overcome the obstacles.

I would like to thank the both academic and non-academic members of the Department of Materials Science, NUS for their support and help. Special thanks go to Agnus and Serene for their generous support. I also wish to thank the workshop staff of the Department of Physics, NUS for their help rendered on sample preparations.

It is a pleasure to remember my research group; Hu Xiaoping, Pan Xiaoran, Lui Minghui and Vijayalakshmi being nice and cool friends. I never can forget all my friends who were around me during last three years; made the time joyful.

My gratitude goes to the National University of Singapore research fund for financing the project.

There are a few people who have always been around me ever since the day I was born who are fully responsible for all my achievements I gain in my life; my parents, two sisters and their families. My parents gave me “everything” to climb the “ladder of life” and my two sisters who are always with me to make my life fruitful. I love you all.

To my parents with love

TABLE OF CONTENTS

ACKNOWLEDGMENT	i
TABLE OF CONTENT	iii
RESEARCH PROBLEM	viii
SUMMARY	ix
LIST OF TABLES AND FIGURES	xi
LIST OF SYMBOLS	xvii
<u>CHAPTER 1</u> <u>INTRODUCTION</u>	01
<u>CHAPTER 2</u> <u>THEORY</u>	04
2.1 Passivation	04
2.1.1 Active-passive behaviour	05
2.1.2 Chemical and electrochemical passivity	08
2.1.3 Stainless steels	08
2.2 Growth of the passive film	10
2.2.1 Rate of film growth	10
2.2.2 Growth laws	12
2.3 Characterisation of the passive film	18
2.3.1 Composition	18
2.3.2 Thickness	19
2.3.3 Amorphous nature	19
2.3.4 Proposed research models for stainless steel passive film characteristics and the role of alloying elements	20

2.4	Breakdown of the passivity: localized corrosion	25
2.4.1	Pitting corrosion and pitting potential	25
2.4.2	Pit initiation and propagation	26
2.5	Electronic properties	31
2.5.1	Semiconductor (Sc)–electrolyte (El) interface	31
2.5.2	Photoelectrochemistry	33
2.5.3	Mott–Schottky (MS) equation and the space charge capacitance	38
2.5.4	Electronic properties of amorphous materials: validity of the application of photocurrent and capacitive concepts developed for crystalline materials to stainless steel passive films	41
2.5.5	Capacity behaviour and Mott Schottky plots for amorphous passive films	46
2.5.6	Photoelectrochemical characterization of stainless steel passive films	51
2.5.7	Proposed research models for stainless steel passive films	58
	References	64
<u>CHAPTER 3</u> <u>EXPERIMENTAL PROCEDURES</u>		75
3.1	Electrochemical experiments	76
3.1.1	Electrochemical cell	76
3.1.2	Sample preparation and working electrode design	76
3.1.2	Cyclic voltammetry	77
3.1.3	Potentiostatic	78

3.1.4	Electrochemical Impedance Spectroscopy (EIS)	80
3.2	Photocurrent spectroscopy	81
3.3	Raman spectroscopy	88
3.3.1	Raman process: a brief theoretical explanation	88
3.3.2	Raman instrumentation and experiment	91
3.4	<i>In situ</i> atomic force microscopy	92
3.5	Photocurrent transients	93
	References	97
 <u>CHAPTER 4</u> <u>RESULTS</u>		98
4.1	Cyclic voltammetry in a borate solution	98
4.1.1	316L and 304L	99
4.1.2	254SMO	102
4.2	Elemental analysis results	109
4.3	Thickness estimations	109
4.4	Pitting corrosion	110
4.4.1	Pitting potential and metastable pitting	110
4.4.2	Pitting potential and metastable pitting	112
4.4.3	Sulphide inclusions	113
4.5	Photocurrent spectroscopy	119
4.5.1	Photocurrent-voltage behaviour	119
4.5.2	Photocurrent spectra and bandgap estimations	120
4.5.3	Investigation of cathodic photocurrent of stainless steel ..	129
4.5.4	Photocurrent transients	131
4.6	Capacitive measurements	138

4.6.1	Capacity-potential measurements	138
4.6.2	Mott-Schottky (MS) plots	142
4.7	<i>In situ</i> Raman spectroscopy	149
4.7.1	Background peaks	149
4.7.2	Raman spectra of 316L in 0.1M borate solution	152
4.7.3	Raman spectra of 316L in 0.28M NaCl	160
4.7.4	Raman spectra of 254SMO in 0.1M borate solution	162
	References	168
 <u>CHAPTER 5</u> <u>DISCUSSION</u>		172
5.1	Amorphous or crystalline	172
5.2	Compositional characterisation	172
5.3	Pitting characteristics	177
5.4	Electronic properties of the passive films	178
5.4.1	Photocurrent–potential behaviour	178
5.4.2	Electronic band structures	179
5.4.3	Frequency dependence of electronic properties	183
	References	186
 <u>CHAPTER 6</u> <u>CONCLUSIONS</u>		187
 <u>CHAPTER 7</u> <u>FUTURE STUDIES</u>		191
Appendix A	Surface states at solid/liquid interfaces	194
Appendix B	Recombination processes	196
Appendix C	Optical transitions	198

Appendix D	Correlation between the bandgap and composition	200
------------	---	-----

RESEARCH PROBLEM

Stainless steels as one of the most widely used alloys are extremely important economically. However, the mechanism by which these stainless steels maintain their passivity is still not fully understood.

The formation and breakdown of the passive film on stainless steels are mainly controlled by ionic and electronic transport processes. Both these processes are in part controlled by the electronic properties of the oxide film. Consequently it is vital to gain a detailed perception of the electronic properties of the passive films. This together with structural and compositional information will eventually lead to a widespread understanding of the mechanisms behind passivity and localised corrosion. As a step towards this goal the nature of the passive films formed on three common austenitic stainless steels AISI 316L, AISI 304 and AISI 254SMO in borate solution were characterised by *in situ* Raman and photocurrent spectroscopies coupled with electrochemical measurements.

SUMMARY

Passivity of stainless steel is achieved due the formation of a protective oxide film, which inhibits harmful corrosion. It is indispensable to study the characteristics of stainless steel passive films in order to understand the mechanisms behind the passivity.

The observation of frequency dependent capacitance behaviour suggested the presence of a density of states localised within the bandgap of the passive films. This demonstrated the amorphous nature of the stainless steel passive films and was further testified by analysing the donor concentrations at various frequencies.

Raman spectroscopy together with bandgap measurements revealed that a Fe-Cr spinel was a major constituent in the passive films on 316L and 304L stainless steels, whilst the possible existence of a Ni-Fe-Cr phase was found in the passive film on 254SMO stainless steel. The existence of Ni in the passive film of 254SMO was also supported by scrutinising the cyclic voltammograms. The Raman results also revealed potential dependent phase transformations throughout the passive and the transpassive regions, which correlated well with changes in the dark current potentiodynamic measurements. Especially the phase change that occurred around 100mV(SCE) on the reverse potential scan; the formation of a Cr(III) phase was found to be responsible for the alternation electronic properties of the passive films below that potential. There was no evidence for the dissolution of Cr(VI) into the solution in the transpassive region.

Photocurrent measurements together with capacitance data revealed n-type and p-type semiconductivities above and below the flat band potential respectively. These results were further supported by photocurrent transients. Bandgap readings suggested that three different applied potential regions existed, in each of which the passive films had separate structures and compositions. Overall the structure of the passive films in the different potential regions is thought to be:

- (a) 800mV (SCE) to around 300mV (SCE): a single n-type oxide phase with a bandgap value of $1.95 \pm 0.5 \text{ eV}$, most likely Fe_2O_3 , was observed on all three stainless steels;
- (b) 200mV (SCE) to -300mV (SCE): two bandgap values existed in all stainless steels in this potential region suggesting the existence a dual layered structure, which consists of an n-type chromium based inner layer (probably an Fe-Cr spinel structure for 316L or 304L and a Ni-Fe-Cr structure for 254SMO) and an n-type iron oxide outer layer (most likely Fe_2O_3);
- (c) -500mV (SCE) to -900mV (SCE): a single p-type oxide phase with a bandgap that varied according to the type of stainless steel; $2.9 \pm 0.5 \text{ eV}$ for 316L, $2.8 \pm 0.5 \text{ eV}$ for 304L and $2.4 \pm 0.5 \text{ eV}$ for 254SMO. This phase was probably an Fe-Cr spinel oxide for 316L or 304L and Ni-Fe-Cr oxide for 254SMO.

Pitting characteristics confirmed the deleterious effect of sulphide inclusions on stainless steel in chloride media. Preferential pit initiation near sulphide inclusions is postulated. *In situ* Raman spectroscopy revealed the existence of Fe-Cr spinel until the onset of pitting. This Fe-Cr spinel appears to be stabilised by Mo, thus it was postulated that this is the mechanism whereby Mo helps prevent pitting corrosion.

LIST OF TABLES AND FIGURES

TABLES

CHAPTER 2 THEORY

2.01	Nominal chemical compositions of stainless steels	09
------	---	----

CHAPTER 4 RESULTS

4.01	Corrosion potentials and open circuit potentials of different stainless steels in a deaerated 0.1M borate solution	98
4.02	Bandgap values in eV of three stainless steels according to Figure 4.16	127
4.03	Bandgap values of different stainless steels for case II	127
4.04	Donor concentrations of 316L, 304L and 254SMO in a 0.1M borate solution (pH=9.2) at different frequencies	146
4.05	Acceptor concentrations of 316L, 304L and 254SMO in a 0.1M borate solution (pH=9.2) at different frequencies	146
4.06	Raman shifts recorded in the literature for ferrous compounds	150
4.07	Raman shifts recorded in the literature for Ni and Mo compounds...	150
4.08	Raman shifts recorded in the literature for Cr compounds	151
4.09	Summary of the Raman spectroscopy results obtained for 316L in a borate solution	159
4.10	Summary of the Raman spectroscopy results obtained for 254SMO in a borate solution	167

CHAPTER 5 DISCUSSION

5.01	Summary of the phases that are believed to form, and their bandgap values and semiconductivities at different potentials for 316L, 304L and 254SMO	185
------	--	-----

APPENDICES

D.01	Band gap values of some oxides, hydroxides and spinel oxides, and electronegativities of relevant metallic cations	200
------	--	-----

FIGURES

CHAPTER 2 THEORY

2.01	Schematic Evans diagram	06
2.02	Schematic active–passive polarization behaviour	06
2.03	Schematic anodic polarization curve of a metal	07
2.04	Schematic potential energy profile for a mobile ion across the film vs. distance	11
2.05	Schematic potential energy profiles for ion migration explaining the limiting cases with respect to (a) Verwey’ theory (b) Cabrera–Mott theory	15
2.06	Schematic potential distribution across an n-type Sc/El interface ...	32
2.07	Energy band diagram of an n-type semiconductor, band bending due to the space charge region	32
2.08	Effect of illumination in depletion layer and electron transfer reactions at the semiconductor–electrolyte interface for (a) n-type and (b) p-type semiconductor	34
2.09	Schematic representation of DOS as a function of the energy for an amorphous semiconductor	43
2.10	Schematic density of states distribution in amorphous semiconductors: (a) CFO model (b) Mott–Davis model	45
2.11	Di Quarto <i>et al.</i> model for an n-type semiconductor: (a) schematic density of states distribution in an amorphous semiconductor having a constant DOS; (b) energetics at an amorphous Sc/El Junction	45
2.12	Equivalent circuit proposed by Di Quarto <i>et al.</i> to fit impedance data for Sc/El junction of an amorphous semiconductor	47
2.13	Schematic representation of capacity–voltage behaviour observed for iron electrodes	49
2.14	Schematic representation of MS plots at different frequencies	51
2.15	Schematic representation of possible photocurrent transients effects that can occur by illuminating a passive film with monochromatic light	56
2.16	Schematic representation of the electronic structure of the passive	

	film formed on 304L stainless steel.....	61
2.17	Schematic presentation of the electronic structure of the passive films formed on Fe-Cr alloys	63

CHAPTER 3 EXPERIMENTAL PROCEDURES

3.01	Schematic of three compartment electrochemical cell	78
3.02	Working electrode design for electrochemical experiments: (a) PTFE tube; (b) glass tube	79
3.03	Schematic representation of the experimental setup for potentiostatic, cyclic sweep and EIS experiments	79
3.04	(a) Representation of the equivalent circuit model for the oxide film (b) The schematic Nyquist plot	81
3.05	Electrochemical glass cell designed for photocurrent spectroscopy ..	84
3.06	Schematic representation of the photocurrent spectroscopy instrumentation	85
3.07	Calibration curve (photosensitivity) of the photodiode	86
3.08	Photocurrent conversion efficiency of the photodiode	87
3.09	Simplified presentation of the Raman mechanism	89
3.10	Energy level diagram for Raman scattering	90
3.11	Electrochemical cell designed for <i>in situ</i> Raman spectroscopy	94
3.12	Raman instrumentation set up	95
3.13	Schematic representation of EC-AFM experimental setup	96
3.14	EC-AFM glass cell	96

CHAPTER 4 RESULTS

4.01	Cyclic voltammogram of 316L in a 0.1M borate solution	103
4.02	Cyclic voltammogram of 254SMO in a 0.1M borate solution	105
4.03	Cyclic voltammograms of 254SMO in a 0.1M borate solution	108
4.04	The incremental thicknesses of stainless steels	110
4.05	Polarization curve for 304L stainless steel in a 0.1 M NaCl	114
4.06	E_{pit} vs. NaCl concentration of different stainless steels	114
4.07	Metastable current transients of 304L stainless steel in a 0.1 M NaCl solution at 100 mV	115

4.08	Number of metastable pits occurred per 1000 seconds per unit area (λ) against the potential	115
4.09	Scanning electron microscope image of a MnS inclusion in 304L high sulphur stainless steel	116
4.10	<i>In situ</i> AFM images of 304L stainless steel	118
4.11	The amplitude of the photocurrent vs. electrode potential of 316L in 0.1M borate solution recorded at a constant wave length ($\lambda=340\text{nm}$) under reverse scan	121
4.12	The photocurrent vs. electrode potential of 316L in 0.1M borate solution recorded at a constant wave length ($\lambda=550\text{nm}$) under reverse scan	122
4.13	Photocurrent spectrum and the relevant $I_{\text{ph}}.h\nu$ vs. $h\nu$ plot (Tauc plot) for bandgap determination (inset) for passive film grown on 316L stainless steel in 0.1 M borate solution	133
4.14	$(I_{\text{ph}}.h\nu)^{0.5}$ vs. $h\nu$ plot for 316L in borate solution at 400mV ...	124
4.15	$(I_{\text{ph}}.h\nu)^{0.5}$ vs. $h\nu$ plot for 316L in borate solution at -100mV ...	126
4.16	Dependence of the bandgap on the electrode potential for 316L, 304L and 254SMO	126
4.17	$(I_{\text{ph}}.h\nu)^{0.5}$ vs. $h\nu$ plot for 316L in borate solution at -100mV ...	128
4.18	$I_{\text{ph}}^{0.4}$ vs. $h\nu$ plot for 316L stainless steel in 0.1M borate solution ..	130
4.19	Set 1: photocurrent transients of 316L stainless steel in 0.1M borate solution measured with monochromatic illumination ($\lambda=325\text{nm}$)	134
4.20	Set 2: photocurrent transients of 316L stainless steel in 0.1M borate solution measured with monochromatic illumination ($\lambda=514\text{nm}$)	135
4.21	Set 2. photocurrent transients of 254SMO stainless steel in 0.1M borate solution measured with monochromatic illumination ($\lambda=514\text{nm}$)	135
4.22	Schematic representation of the effect of mid bandgap states on photocurrent in an n-type semiconductor	137
4.23	Plots of capacitance vs. potential for passive films on 304L, 316L and 254SMO in 0.1M borate solution	140

4.24	Plots of capacitance vs. potential for 316L in 0.1M borate solution at different frequencies	141
4.25	Plot of capacitance vs. log (frequency) of 316L in a 0.1M borate solution at 0mV	142
4.26	Mott-Schottky plots for 304L, 316L and 254SMO in 0.1M borate solution at 500Hz	145
4.27	Mott-Schottky plots for 316L in 0.1M borate solution at different frequencies	146
4.28	The plot of donor density versus ln(frequency) for 304L, 316L and 254SMO in a borate solution	147
4.29	Raman spectrum of sodium borate solution and quartz window	152
4.30	The <i>in situ</i> Raman spectrum of 316L at -900mV in a 0.1M borate	154
4.31	The <i>in situ</i> Raman spectrum of 316L at -600mV in a 0.1M borate	154
4.32	The <i>in situ</i> Raman spectrum of 316L at -500mV in a 0.1M borate	155
4.33	The growth of the 700cm ⁻¹ Raman shift in the potential region from -400mV to 200mV	156
4.34	The <i>in situ</i> Raman spectrum of 316L at 200mV in a 0.1M borate	158
4.35	The <i>in situ</i> Raman spectrum of 316L at 300mV in a 0.1M borate	158
4.36	The <i>in situ</i> Raman spectrum of 316L at 100mV under reverse potential scan in a 0.1M borate solution	159
4.37	The <i>in situ</i> Raman spectra of 316L in 0.028M NaCl; the growth and the displacement of the Raman shift close to 700cm ⁻¹	161
4.38	The <i>in situ</i> Raman spectrum of 254SMO at -600mV in a 0.1M borate	164
4.39	The <i>in situ</i> Raman spectrum of 254SMO at -500mV in a 0.1M borate	164
4.40	The <i>in situ</i> Raman spectrum of 254SMO at -100mV in 0.1M borate	165
4.41	The <i>in situ</i> Raman spectrum of 254SMO at 200mV in a 0.1M borate	165

CHAPTER 5 DISCUSSION

5.01 Schematic representations of electronic band structures of

stainless steel passive films formed in 0.1M borate solution	182
--	-------	-----

APPENDICES

B.01	Photocurrent loss mechanisms	194
C.01	The scheme for optical transition from the valance band to the conduction band	197

LIST OF SYMBOLS

A	constant (film growth models) or constant (light absorption)	E_F^{red}	Fermi level of the redox couple in the solution
A''	constant (in PDM model)		
a	half barrier jump width (ion migration)	El	electrolyte
a	radius of the pit	E_{oc}	open circuit potential
B	constant (in film growth model)	E_p	passivation potential
B''	constant (in PDM model)	E_{pit}	pitting potential
C	capacitance	E_{ω}	energy level that separates mid bandgap states which are responding to signal against those that are not responding in Di Quarto model
CE	counter electrode		
C_H	Helmholtz capacitance		
C_{sc}	space charge capacitance		
C_{ox}	capacitance of the oxide film	e	modulus of the electronic charge or an electron
C_{meas}	experimental measured capacitance	e_{CB}^-	electron in the conduction band
DOS	density of states	F	Faraday's constant
D_p	hole diffusion coefficient	f	frequency
d.l.	Helmholtz double layer	$g(x)$	number of electron-hole pairs generated per second, per unit volume in the Sc
d_{sc}	depth of the space charge layer		
dQ_{sc}	charge in the space charge region	h	planks constant
E	field strength in the film (V/x)	h^+	hole
E_C	energy level of the bottom of the conduction band	h_{VB}^+	hole in the valance band
E_g	energy of the bandgap	$h\nu$	energy of a photon (in eV)
E_g^{opt}	optical bandgap energy	$h\nu_0$	photoelectric threshold at $V_e=0$
E_g^{m}	mobility gap energy	I_{ph}	photocurrent (from an oxide film)
E_V	energy level of the top of the valance band	I_{ph}	photocurrent (from the photo diode)
E_{corr}	corrosion potential	I'_{ph}	photoemission current
E_F	Fermi energy level		

I_{diff}	diffusion current density (photocurrent)	R	gas constant
I_{drift}	drift current density (photocurrent)	RE	reference electrode
i	current density	R_{OX}	oxide resistance
i_a	anodic current density	R_U	uncompensated solution resistance
i_{app}	applied current density	SCE	saturated calomel electrode
i_b	rate of ions moving backwards	Sc	semiconductor
i_c	cathodic current density	Sc/EI	semiconductor-electrolyte interface junction
i_{corr}	corrosion current density	SHE	standard hydrogen electrode
i_f	rate of ions moving forward	T	absolute temperature
i_{crit}	critical current density	t	time
i_{pass}	passive current density	u	function of temperature (parameter in Cabrera-Mott film growth model)
k	rate constant (film growth) or Boltzmanns constant	V	applied overpotential
k'	constant in film growth (Sato's model)	V_e	electrode potential
L_p	hole diffusion length	V_{fb}	flat band potential
L_n	electron diffusion length	V_i	intersection potential of Mott-Schottky plots
M	metal	WE	working electrode
M/EI	metal-electrolyte interface junction	X, x	thickness of the oxide film
M	molecular weight	X_1	characteristic distance in the oxide film growth (Cabrera-Mott model)
N_a	acceptor density	X_C	the location in the Schottky barrier that separates two regions where all electronic states fully respond to the AC signal and where no states respond (Di Quarto model)
N_c	effective density of states at the bottom of the conduction band	X_L	limiting film thickness
$N(E)$	density of states	Z'	real part of the impedance
N_d	donor density	Z''	imaginary part of the impedance
N_v	effective density of states at the top of the valance band		
n	parameter depends on the kind of optical transmission of a Sc		
Q_T	total charge in the passive film		
q	charge passed		

Z_U	impedance representing the uncompensated solution resistance	ϕ_{OX}	photocurrent conversion efficiency (oxide)
z	charge on a migrating ion	ϕ_0	photon flux entering the Sc
α	light absorption coefficient	Ψ_{Sc}	energy corresponding to the band bending of the semiconductor electrolyte interface
α_0	constant (absorption of light)	Ψ_C	energy corresponding to the band bending at X_C
β	constant in film growth (Sato's model)	ω	angular frequency
γ	constant (absorption of light)		
ε	relative permittivity		
ε_0	permittivity of free space		
η	collection efficiency (photocurrent)		
ΔG^*	activation energy		
$\Delta\Phi$	potential drop across the Sc/El interface		
$\Delta\phi_{sc}$	potential across the space charge region		
λ	wavelength (in nm)		
ρ	density of the oxide		
τ	relaxation time for the capture/emission of electrons in/from the electronic states below the Fermi level		
τ_0	constant (related to the relaxation time for the capture/emission of electrons in/from the electronic states below Fermi level)		
ϕ	voltage across a capacitor		
ϕ_e	photocurrent conversion efficiency (photo diode)		

CHAPTER 1 INTRODUCTION

Stainless steels as one the most widely used alloys in the world are gaining more attraction day by day in both commercial and research aspects. Only developed in the first decade of the 20th century stainless steels are irreplaceable in the world today. Emphasize of the importance of stainless steels as corrosion resistance alloys is almost unnecessary. Applications are disseminated to almost all industries; architecture, marine engineering, medical equipments, chemical engineering, food and drink production and distribution, domestic and catering applications, textile applications etc.

Iron alloys which have more than 12% - 13% Cr are classified under the category of stainless steels. Various alloying elements are added to stainless steels, each for a specific reason: chromium addition is quite obvious without which the word “stainless steel” would not exist; nickel is added as an austenitic former (*fcc*) and molybdenum particularly for enhance localised corrosion resistance.

Out of the different classes of stainless steels, austenitic stainless steels claim more than 70% of the production. Due to the flexibility of both their metallurgical and mechanical properties austenitic stainless steels provide a blend of corrosion resistance, durability and ease of manipulation.

The corrosion resistance of stainless steel arises from a "passive" chromium-rich oxide film that forms on the surface. Although extremely thin, less than 5nm, this protective film is strongly adherent and chemically stable. Nevertheless in certain

environments, especially ones containing chloride, this oxide film breakdown and rapid corrosion ensues. Despite the enormous research undertaken over the last nine decades the complete answer to explain the mechanisms behind both passivity and its breakdown are still not understood; theories developed to date will be presented in Chapter 2 of this thesis.

The composition and structure of the passive films are paramount factors to be considered in a study in this field. However, due to their extreme thinness ($< 5\text{nm}$) and the fact that at least to a certain extent their composition and structure depend on the nature of the surrounding environment the study of stainless steel passive films is extremely difficult. Another principal factor thought to control the behaviour of a passive film is its electronic properties. Since the formation and breakdown of the passive film are electrochemical processes, these will undoubtedly be mainly controlled by ionic and electronic transport processes; processes that are in turn controlled by the electronic properties of the film.

Consequently, the research problem is recognised as to obtain a detail perception of the electronic properties together with structural and compositional information to characterise stainless steel passive films. This would be a step towards achieving a comprehensive understanding of the mechanisms behind passivity and localised corrosion.

Organisation of the thesis

Chapter two (Theory) will furnish the theoretical background of the research study. Based on a literature review the chapter will elucidate broadly passivity, film growth, characterisation of films, localised corrosion and electronic properties related to stainless steels. In addition various models that have been proposed by different authors to explain the behaviour of passive films will be presented. The discrepancies between different models will intensify the importance of the research problem.

Chapter three (Experimental) will outline the experimental approach which has been conducted to solve the research problem. Experimental procedures and apparatus will be explained based on five main categories; (1) electrochemical experimentations (cyclic sweep, potentiostatic and electrochemical impedance spectroscopy); (2) photocurrent experiments; (3) photocurrent transient experiments; (4) *in situ* Raman spectroscopy and (5) *in situ* atomic force microscopy (AFM).

Chapter four (Results) will describe the outcome of the experimental strategies. This will summarised the results from each category of experiment and compare these to some of the models postulated by other researchers.

Chapter five (Discussion) will combine the results of all five categories of experiments to present the authors current understanding on the nature of passive films of austenitic stainless steels.

Chapter six (Conclusion) will summarise the findings presented in this thesis.

Chapter seven (Future work) will suggest direction for future work to yield an even more complete understanding of the nature of passive films.

CHAPTER 2 THEORY

2.1 Passivation

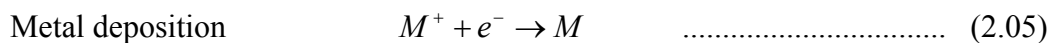
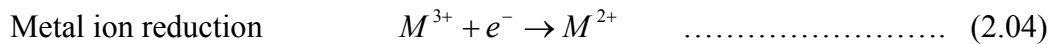
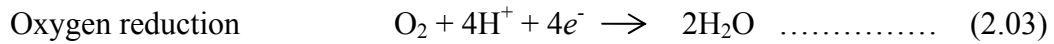
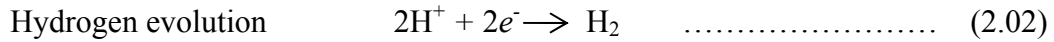
Passivity is the decrease in the corrosion rate of a metal resulting from the formation of a thin and generally non visible protective film formed by the oxidation of the metal. This film curbs the interaction of the potentially active metal with its environment. From an engineering point of view it is remarkable; this extremely thin passive film which may range from 1 to 10nm in thickness is protecting even huge structures.

Kier, in 1790,¹ first observed and reported the passivity of iron. He kept an iron wire dipping in an acid for weeks and remarked a “surface effect” has “altered” the iron and precluded reaction with the acid. The first report that passivity could be achieved by anodic polarization can be attributed to Gmelin, Hisinger and Berzelius of Sweden in 1807, which was repeated in 1836 by Schönbein who also coined the word “passive” for Kier’s observations.²⁻⁴ Ever since these discoveries enormous research has been undertaken in this area, whilst in the 1840’s Michael Faraday’s experimentations on the passivity of iron in dilute and concentrated nitric acid became a benchmark and a standard method for demonstrating the phenomena.^{3,5}

Metallic corrosion occurs due to coupling of two different electrochemical reactions on the metal surface, metal oxidation and reduction of solution species or in other words anodic and cathodic reactions. The anodic reaction in every corrosion reaction is the oxidation of a metal to its ions:⁵



In each case the number of electrons produced equals the valence of the ion. In an aqueous system several cathodic reactions are frequently come across in metallic corrosion:



Evans diagrams,⁶ named in honour of its creator, U. R. Evans, illustrate cathodic and anodic conditions (Figure 2.01). The lines represent the reaction kinetics of two reactions, useful parameters like corrosion potential (E_{corr}) and corrosion rate (i_{corr}) can be determined.³ The polarization curve makes this interpretation more realistic as it is based on experimental measurements. The main difference between an Evans diagram and a polarization curve is that in the former data are displayed as applied current densities whereas the latter displays reaction rates in terms of current densities. Applied current density (i_{app}) is the difference between the total anodic (i_a) and the total cathodic (i_c) current densities (reaction rates) at a given potential:

$$i_{app} = i_a - |i_c| \quad \dots\dots\dots (2.06)$$

2.1.1 Active–passive behaviour

Schematic active passive polarization behaviour is presented in Figure 2.02;⁷ in the absence of strong oxidizing agents in the solution the metal corrodes freely under anodic driving force (i.e. the *Active region*). As the driving force towards oxidation increases the rate of dissolution also increases. When the potential is raised in this *active region* the dissolution rate of the metal increases until a potential E_p is reached,

which is known as the passivation potential. The dissolution rate decreases dramatically above E_p , and remains low with further increases in the potential. This latter state is the state of “*passivity*” and any further increase of the potential has a little effect on the passive current density, i_{pass} .

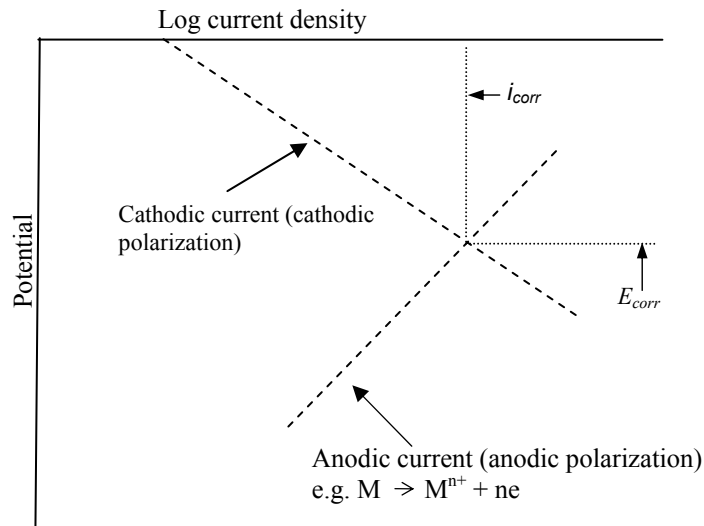


Figure 2.01 Schematic Evans diagram

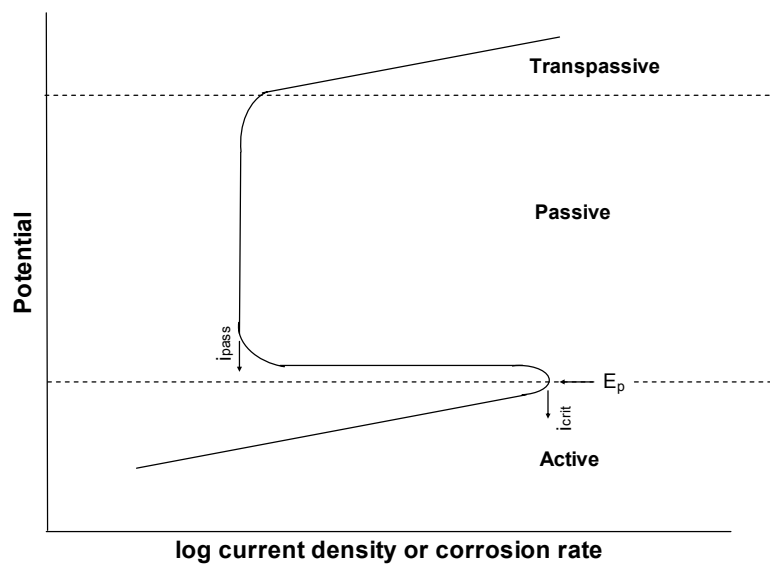


Figure 2.02. Schematic active–passive polarization behaviour.

Raising the potential in the passive state, while increasing the driving force towards oxidation, tends to thicken the surface oxide film.^{7,8} This leads to an increase the barrier (with the environment) towards further oxidation, causing the potential independence of the oxidation rate as long as metal remains passive.

In solutions without aggressive species such as Cl^- , further increase in the potential will eventually lead to an increase in the current density due to a combination of oxygen evolution and/or *transpassive dissolution* of the passive film. For stainless steels and chromium bearing nickel alloys, the transpassive breakdown occurs near the oxygen evolution potential. The schematic anodic polarization curve in Fig 2.03 explains the possible behaviour of the passive region of a metal.

The basic mechanism for passivity of pure metals also applies in a similar manner to alloys, although processes involved in the passivation of alloys are more complicated.

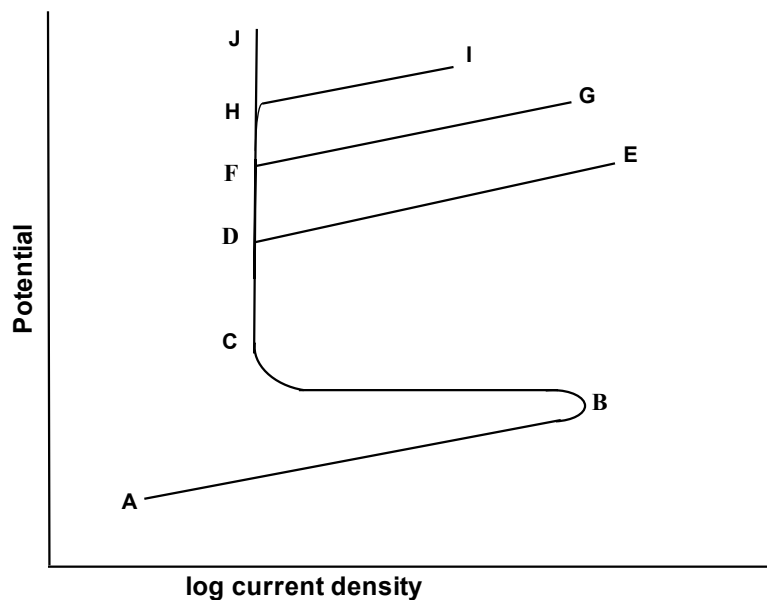


Figure 2.03. Schematic anodic polarization curve of a metal; possible behaviour of the passive region. AB is the active region and BC the active-passive transition. If the solution having aggressive anions such as chloride, passivity may breakdown at D (the pitting potential) and the current rises with further increase in the potential (DE). Transpassive dissolution of the passive film starts at F in the absence of pitting agents; increasing in rate with increasing potential (FG). If the passive film chemically and electrochemically stable, and is conductive to electrons, oxygen evolution commences at H, and increases in rate to I; the metal remains passive. If the film is stable and insulating to electrons, oxide film growth continues with further increase in potential (HJ) and the metal remains passive. (Adapted from the reference 7)

2.1.2 Chemical and electrochemical passivity

The above description of the passivity refers to passivity stimulated by an externally applied potential. This is called electrochemical passivity in contrast to chemical passivity, where it has been achieved in the absence of externally applied power; for example in the presence of a strong oxidising agent. Both are electrochemical in nature and the only difference lies in the fact that under chemical passivity, the transferred electrons must pass through the passivating oxide film while under externally applied anodic stimulation electrons are passed around an external circuit.⁷

2.1.3 Stainless steels

Brearley was the first to introduced stainless steel (SS) in 1912–1915 in the form of cutlery. Though he is widely considered as the “inventor” of stainless steels, a remarkable amount of research had been made on such alloys over the previous decade by Gillet (1902–1906), Portevin (1909–1911) and Giesen (1907–1909), who had worked on the metallurgy and physical properties. On the other hand, Monnartz during 1908–1909 had given a detail consideration to corrosion resistance properties and also the advantage of Mo additions.^{9,10}

The main aspiration of this thesis is a detail study of the passivation process of stainless steel considering the role of each of the major alloying elements. Consequently all the next sections will be based on passive film/s formed on stainless steels. Table 2.1 lists out the austenitic stainless steels that will be investigated in the experimental part of this thesis, along with their compositions. These stainless steels will also be used as examples in the discussion in the following sections.

	Stainless steel (AISI)	Cr	Ni	Mo	Mn	Si	C	P	S	N	Remarks
1	316L	16.0-18.0	10.0-14.0	2.0-3.0	1.0-2.0	0.5-1.0	0.04-0.08	Max 0.045	0.006-0.03		
2	304L	18.0-20.0	8.0-12.0	Max 0.02	1.0-2.0	0.5-1.0	0.04-0.08	Max 0.045	0.03-0.3		
3	304High Sulphur (304HS)	18.0-19.0	10.0 – 11.0	Max 0.02	1.0-1.6	0.5-1.0	0.04-0.08	Max 0.045	0.4-0.8		A research sample with high S content, not commercially available.
4	316LVM	17.0-18.0	13.0-14.0	2.5-3.0	1.0-2.0	0.5-1.0	Max 0.025	Max 0.003	Max 0.003	≤ 0.20	Vacuum melted SS to remove sulphur, mainly used for medical applications.
5	254SMO	19.5- 20.5	17.5-18.5	6.0-6.4	Max 1.00	Max 0.80	Max 0.20	Max 0.03	Max 0.01	≤ 0.20	High Mo SS, developed to use in seawater and other aggressive chloride-bearing media.

Table 2.01. Chemical composition of various stainless steels.

2.2 Growth of the passive film

The first monolayer of the passive film is generally formed before any significant film thickening occurs. This is because of a very strong dependence of the film growth rate on the electric field across the reacting interface. Burstien *et al.*^{11,12} analysed the growth kinetics of Fe and other metals and alloys experimentally and theoretically. This work suggested that a random oxidation of the exposed surface of metal atoms occurred until the first monolayer of oxide was complete. This leads to the formation of an amorphous film with no definable crystal structure. Considerable reduction of the rate of oxidation of the metal occurs after the growth of the first monolayer, although the process does not stop there.

Once the metal is separated from its environment by forming the first monolayer, the oxide film starts thickening. Steady state occurs when the rate of film thickening equals the rate of film dissolution. Metal cations and oxygen anions are transported through the existing oxide film under the electric field. The ion migration mechanism across the film becomes the salient factor here, which has been contemplated by many researchers since the 1930s and will be briefly described in the next section.

2.2.1 Rate of film growth

When the metal carrying its oxide film is at its equilibrium potential, no overpotential exists across the oxide, the rate of ions moving forward (i_f , expressed as current densities) through the oxide equals the rate of ions moving backwards (i_b). Ions then encounter an energy barrier, which they must surmount to move further (Figure 2.04)^{7,13,15} such that:

$$i_f = i_b = zFk \exp\left[-\frac{\Delta G}{RT}\right] \dots\dots\dots (2.07)$$

where k is the rate constant, z is the charge number, F is the Faraday's constant, R is the gas constant and T is the absolute temperature.

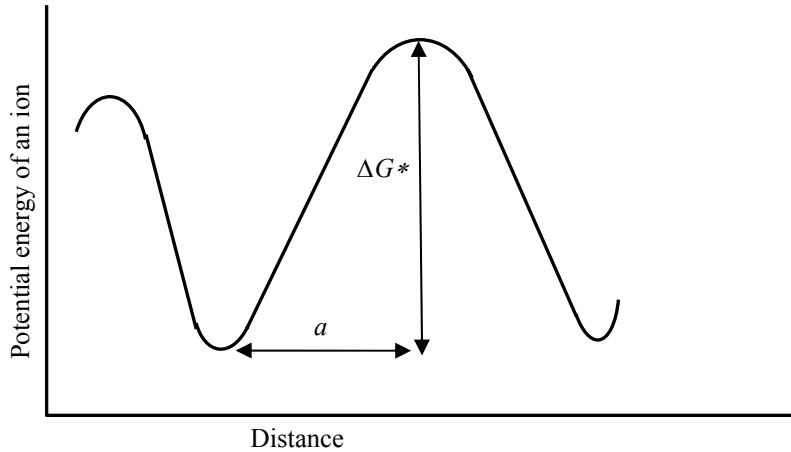


Fig 2.04. Schematic potential energy profile for a mobile ion across the film vs. distance, without an applied field. (a is known as the activation distance for a symmetrical barrier or the “half barrier width” or the “half jump distance”. ΔG^* is the height of the energy barrier which is the activation energy).

On application of an over potential V for film growth, the potential drop across the energy barrier ($2a$) is $2aV/x$, where x is the oxide film thickness, assuming V lies linearly and entirely across the film. The activation energy ΔG in the forward direction is thereby reduced an amount of $aVzF/x$ and that in backward direction increased by $aVzF/x$. Thus the net current density, i , in the forward direction (for film growth) under applied overpotential can be shown to be:^{13,15}

$$i = A \sinh\left[\frac{BV}{x}\right] - A \exp\left[-\frac{BV}{x}\right] \dots\dots\dots (2.08)$$

$$i = 2A \sinh\left[\frac{BV}{x}\right] \dots\dots\dots (2.09)$$

where $A = zFk \exp\left[-\frac{\Delta G^*}{RT}\right] \dots\dots\dots (2.10)$

and
$$B = \frac{azF}{RT} \dots\dots\dots (2.11)$$

are constants for a particular oxide at a constant temperature.

Equation (2.09) has two limiting approximations:

- (a) when the electric field strength $E = V/x$ is large (for high V and/or small film thickness);

$$i = A \exp\left[\frac{BV}{x}\right] \dots\dots\dots (2.12a)$$

which is called as “high field equation” and,

- (b) when the electric field strength is small (i.e. V is small and/or x is large);

$$i = \frac{2ABE}{x} \dots\dots\dots (2.12b)$$

2.2.2 Growth laws

Verwey’s model: The kinetics out lined above were first observed empirically by Güntherschulze and Betz in 1934.¹⁴ They represent the dependence of i on E in the form of $i = A \exp BE$. The fundamental equation was first applied to anodic oxide films by Verwey in 1935.¹⁵ As schematically presented in Figure 2.05(a), he considered the rate controlling energy barrier to be located between two cation sites within the oxide film.

Cabrera and Mott’s model: The metal–oxide interface was taken into account by Cabrera and Mott in 1948-49.¹⁶ In this case the location of the rate controlling energy barrier was considered to be between a metal atom on the metal surface and an adjacent cation site in the film, as schematically presented in Figure

2.05(b). These authors described the thickening as due to ion migration at a rate given by:

$$\frac{dX}{dt} = 2u \sinh\left[\frac{X_1}{X}\right] \dots\dots\dots (2.13)$$

where X is the oxide thickness at time t , X_1 is a characteristic distance depending on the interfacial potential difference and temperature, and u is a function of temperature.

For small film thickness ($X \ll X_1$), Equation (2.13) becomes:

$$\frac{dX}{dt} = u \exp\left[\frac{X_1}{X}\right] \dots\dots\dots (2.14)$$

which is a form of the high field equation (2.12a). Rearrangement and integration of Equation (2.14) considering a limiting case, where X in the exponential term can be replaced by a limiting film thickness, X_L , beyond which the film ceases to grow, Equation (2.14) takes the form of:

$$\frac{-X_1}{X} = \ln\left[\frac{X_1 u t}{X_L^2}\right] \dots\dots\dots (2.15)$$

This is in the inverse logarithmic form for film growth by field assisted ion conduction.

Validity of Cabrera–Mott model: Validity of the inverse logarithmic model of film growth has been debated by many researchers. Young¹⁵ claimed the Cabrera and Mott model could apply in principle for a “thin enough” film though practically as the film can never be less than a unit cell thick, it may never be thin enough. Fromhold¹³ addressed that Cabrera–Mott model neglects concentration gradients and space charges in the growing film, i.e. the electric field is assumed to be uniform in the oxide and inversely proportional to the oxide thickness. He also showed the importance of “coupled currents” since more than one species is involved in the

overall transport mechanism, e.g. metal cations, oxide anions and electrons. Dewald (1955)¹⁷ addressed the transient effects in the ionic conductance of anodic oxide films at high fields and interpreted that the charge of the carriers is electrically compensated by the presence of vacancies. He stated that the Cabrera–Mott picture is incapable of explaining a detailed account of the structure. A logarithmic fit for the steady state film growth had been formulated by Sato *et al.*^{18,19} where the rate of film growth is given by:

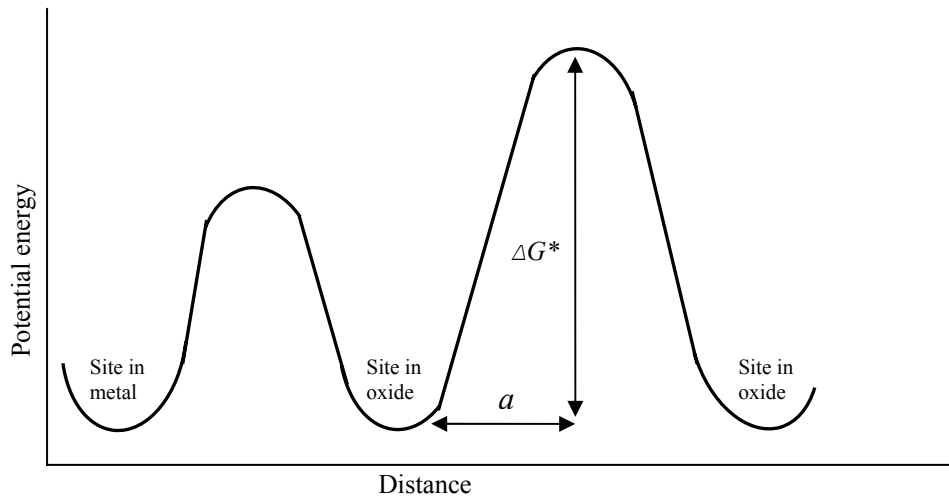
$$i = k' \exp\left[\beta E - \frac{Q_T}{B}\right] \dots\dots\dots (2.16)$$

where Q_T quantity of total charge in the passive film, V the potential, and k' , β and B are constants. The model was proposed based on a “place–exchange” mechanism in which all the metal ions and oxygen ions exchanges in a given row take place simultaneously. Ghez²⁰ stated the limited validity of the Mott–Cabrera concept due to erroneous approximations made such as neglecting the concentration gradients and space charges in the growing oxide.

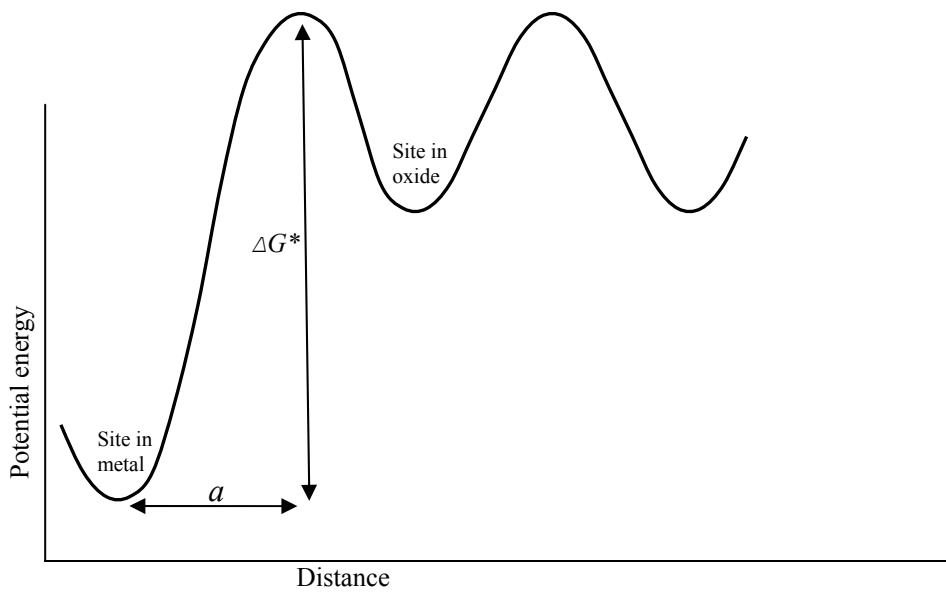
Burstein and Davenport^{21,24} evaluated both, inverse and direct logarithmic¹ forms for film growth and showed for measurements under potentiostatic conditions, these two kinetic forms are very close, and the difference can be further obscured by the change in iR drop as the current changes. They presented the relationship of $\log i$ vs. $(i-t)^{-1/2}$ as:

$$\log i = \log \bar{A} + \frac{(B'E)^{1/2}}{2.3} (i-t)^{-1/2} \dots\dots\dots (2.17)$$

¹ $X = \frac{X_L^2}{X_1} \ln t + const.$



(a) Verwey theory



(b) Cabrera - Mott theory

Fig 2.05. Schematic potential energy profiles for ion migration explaining the limiting cases with respect to (a) Verwey' theory* (b) Cabrera-Mott theory**.

* adapted from the reference 15

**adapted from the reference 16

where i and t have their usual meanings and:

$$\bar{A} = \frac{zF\rho u}{M} \dots\dots\dots (2.18)$$

$$B'E = \frac{zF\rho X_1}{M} \dots\dots\dots (2.19)$$

The film thickness X at time t (through Faraday's law) is:

$$X = \frac{Mq}{zF\rho} \dots\dots\dots (2.20)$$

and M is the molecular weight, z is the oxidation number of the metal ion, ρ the density of the oxide, q is the charge density with X_1 and U being as in Equation (2.14). Davenport *et al.*^{22,23} further extended this approach to investigate the growth of a passive film on stainless steels using galvanostatic measurements.

Point defect model (PDM): The PDM of Macdonald *et al.*²⁵⁻²⁸ draws a distinction between cation and anion mobility; and also the vacancy diffusion mechanism on passivation and breakdown of the oxide film. The model considered the significance of the vacancy concentration gradient on ionic transport and determined these as being significant, except in cases where very high electric field strengths exist in the passive films. In addition to the growth of the passive film, Macdonald *et al.* also extended their model to the distribution of breakdown parameters (i.e. breakdown voltage and induction time); the role of alloying elements on enhancing the passivity breakdown resistance and transpassive dissolution. They concluded an integrated rate law for film growth in the form of:

$$\exp(2KX) - 2KX - 1 = 2KA''(B'' - 1)t \dots\dots\dots (2.21)$$

where X is the film thickness, t is the time, A'' and B'' are constants and K is defined as:

$$K = \frac{FE}{RT} \dots\dots\dots (2.22)$$

where F is the Faraday constant, E is the field strength in the film, R is the gas constant and T is the temperature.

The ability of a “surface charge approach” to describe the film growth considered by Bonjinov *et al.*²⁹⁻³⁰ and presented a kinetic model known as the “surface charge model” for passivation of Bi, Sb and W which was later generalised for most metals.³¹ The influence of ionic surface charges, which are formed both at the metal / barrier film and the barrier film / electrolyte interfaces, on the transport of defects during film growth were considered. For example, a negative surface charge due to accumulation of metal vacancies near the film / solution interface accelerates the oxygen vacancy transport. This surface charge model was able to predict quantitatively the *ac* impedance response of the system metal / surface layer(s) / electrolyte in the passive range. There is a general agreement between the predictions of Bonjinov *et.*’s surface charge model and the Macdonald’s point defect model.²⁵⁻²⁸

2.3 Characterization of the passive film

It is certain that passivity is achieved in stainless steels due to the formation of a thin surface oxide layer. Chromium as the highly passive component as well as the principal alloying element in stainless steel obviously must be enriched in the oxide film. However, the full composition, structure, thickness and the formation mechanism of the passive film are still in question. Due to the extreme thinness (<5nm) and the possibility of elements being combined together in the passive film and the fact that to a certain extent some parameters depend on the surrounding environment its scrutinization becomes very difficult.

2.3.1 Composition

The sceptical nature of most of the analyzing techniques, such as Auger electron spectroscopy (AES), X-ray photo electron spectroscopy (XPS) and secondary ion mass spectroscopy (SIMS) leads to ambiguities on the true nature of the passive film. These *ex situ* techniques, where the sample is being analysed under a vacuum, do not reveal the precise character of the passive film which forms in an aqueous environment. However, these techniques have been extensively used to study the passive film and much useful information has been obtained.

Besides the role of Cr other alloying elements, mainly Ni and Mo play a significant role. The presence and role of Ni and Mo in the passive layer is still controversial. It is well known that Mo inevitably enhances the pitting corrosion resistance[†] but “how” is still a question. Furthermore it is a difficult task to single out the individual role of alloying elements due to a possible “synergetic” behaviour.

[†] Pitting Resistance Equivalent Number (PREN) = %Cr + 3.3(%Mo) + 16(%N); where chromium, molybdenum and nitrogen are in weight percent.

The invention of a number of *in situ* techniques has intensified the potential of examining the characteristics of the film to a better extent of accuracy. For example indirect evidence from *in situ* photocurrent measurements and direct indications by *in situ* Raman spectroscopy together with electrochemical measurements can lead us to a more precise conclusion on film characteristics.

2.3.2 Thickness

The thickness of the passive layer on stainless steels can be estimated considering the charge involved in forming the film (Equation 2.20). It is necessary to assume that there are no charge competing electrochemical reactions (i.e. 100% charge transfer efficiency) and also the composition of the film since the density is involved in the calculations. Film thicknesses determined by ellipsometry has been used successfully for decades but again assumptions on refractive index of both the film and the substrate must be made (it is difficult to get “film free” stainless steel, so it is hard to get its true refractive index).

It is proposed³⁶ that basic solutions give considerably thicker films (around 6 to 7nm) since dissolution is less pronounced than in acidic solutions (around 1 to 2nm), irrespective of the composition of the stainless steel. Arguments like influence of Cr and/or Mo on the film thickness^{32,33} and thickness dependence corrosion resistance properties³³ are still sceptical.

2.3.3 Amorphous nature

The amorphous nature of the passive film on stainless steels as well as many other metals, was recognized a long time ago due to their highly disordered character.⁹ The

random oxidation of the exposed surface metal atoms to form the first monolayer, experimentally shown by Burstein *et al.*,⁷ initiates amorphous characteristics. On the contrary, a handful of research papers proposed its crystalline character or at least a nano crystalline structure.^{34,35} However, both photocurrent and Raman spectroscopical techniques support an amorphous structure. From the experimental observations and considering the nano-scale thickness it is rather precise to conclude it as an “amorphous film confined in a nano-scale”. Thus, despite the absence of long range order, the atoms are more or less the same distance apart as in their crystalline counterpart; this has important implications for explaining the electronic properties of the passive film (see Section 2.5).

2.3.4 Proposed research models for stainless steel passive film characteristics and the role of alloying elements

Remarkable discoveries have been made during the last four decades, by numerous research groups on the composition and the structure of the stainless steel passive films and their influence on corrosion resistance properties.³⁷⁻⁷⁵ However, most of the arguments related to corrosion resistance are diverse.

Single or duplex layered structure and the stoichiometry of Cr and Fe components are the two main considerations that are the source of most of the arguments related to passivation of stainless steels. A potential dependence for the formation of different phases has also been presented due to the different behaviour in the passive and transpassive regions.³⁷ The influence of Ni and Mo is a paramount consideration and also other factors, such as solution pH value and temperature. Some striking

arguments will be briefly described below, whilst ideas related to semiconductive properties will be presented under electronic properties (Section 2.5).

Frankenthal³⁸ hypothesized the formation of two different potential dependent films on Fe–Cr alloys. The primary film contains Cr and oxygen ions and possibly also some constituents of the electrolyte solution. The duplex nature of the film has been proposed based on XPS studies by Castle *et al.*³⁹⁻⁴¹ These authors postulated that the passive film contains an inner Cr rich layer with an outer Fe rich layer. The Cr(III), Fe(II) and Fe(III) cations are incorporated in layers containing both OH⁻ and O²⁻. Uhlig⁴² rationalized the beneficial effect of Cr by its greater affinity for oxygen than Fe and that of Mo by its lower affinity for chloride than Cr. The presence of Mo as a barrier layer in the metal–oxide interface instead of being incorporated in the film had been speculated by Yaniv *et al.*⁴³ These authors further clarified Mo exerts its beneficial effect by improving the quality of the bonding between the chromium oxide layer and metal and also between metallic iron and the chromium oxide matrix.

The absence of both Mo and Ni from the film had been suggested by many researchers in the 1970's and the early 1980's.⁴⁴⁻⁴⁶ Galvele *et al.*⁴⁶ conducted AES studies on stainless steels in NaCl and acidic solutions and suggested that Mo retards the dissolution of the salt layer of CrCl₃ despite its absence in the passive film. It was suggested that the Mo either increase the pitting potential, E_{pit} or changed the rate of pit propagation. Similar arguments were later made by other authors,⁴⁷ on the contrary in 1998 Pettersson and Pound⁴⁸ suggested that Mo suppresses the salt film formation, which was based on impedance measurements.

Sugimoto *et al.*³³ proposed that the thickness of the passive film increases almost linearly with the Mo content. They further suggested the passive films of Mo containing stainless steels are composed of a complex oxyhydroxide containing Cr(III), Fe(III), Ni(II), Mo(VI) and even Cl⁻ if the film is grown in a chloride environment. The presence of a critical amount of Cr was proposed to be essential to impede the transpassive dissolution of Mo. Hashimoto and co-workers⁴⁹⁻⁵¹ insinuated that micro-cracks on the surface act as active sites with high current densities and that the Mo suppress their detrimental behaviour by forming molybdenum oxy-hydroxide or molybdate on these sites.

A two layer structure has been proposed by Olefjord *et al.*³² based on electron spectroscopy for chemical analysis (ESCA) studies, where the inner layer is a mixture of Fe(III) and Cr(III), oxides while the outer layer is a mixture of Mo, Fe and Cr hydroxides. The Mo(IV) and Mo(VI), formed at low and high potentials respectively were proposed to cancel out defects created by Fe(II). The bipolar model of the passivity of stainless steel introduced by Clayton *et al.*⁵² states that MoO₄²⁻ and CrO₄²⁻ incorporation modifies the immediate surrounding lattice from an intrinsically anion selective region to a cation selective one. This enhances the degree of bipolarity in the film, retards OH⁻ and Cl⁻ ingress and also forms a glassy barrier layer of XCr₂O₃.YCrO₃.

Elbiache and co-workers⁵³ brought up a different idea, stating that Mo causes the desorption of sulphur in the active state and this counteracts the detrimental effect of sulphur; which is added intentionally to increase the machinability of the stainless steel. By using AES, XPS and ion sputtering on AISI 304L, Lorang *et al.*⁵⁴ found two

oxide regions, Cr₂O₃ with approximately constant stoichiometry as the inner layer, which was proposed to be responsible for protectiveness, along with different forms of Fe oxides [Fe₃O₄, Fe₂O₃, Fe(OH)₂ and FeOOH] as the outer layer. Schmuki *et al.*⁵⁵ pointed out the importance of considering the chemistry of the environment, in which the film grows.

In situ X-ray absorption near edge spectroscopic studies⁵⁶ at different potentials in the passive and the transpassive regions revealed the existence of a non-reducible Cr(III) oxide/hydroxide phase and also Fe(II)/Fe(III) in the film at different stages in the polarization process. Qvarfort⁵⁷ suggested that Mo repassivates metastable pits by forming an unsaturated Mo(V,VI) oxide while the Cr may be either in this oxide or present as a separate chromium oxide.

Molybdenum influences basically all the principal reactions: dissolution; intermediate formation and repassivation.⁴⁸ Betova *et al.*⁵⁸ proposed that molybdenum retards passivity breakdown by inhibiting the formation of cation vacancy clusters at the metal–film interface and at the same time decreases the rate of iron dissolution, whilst Kaneko and Isaacs⁵⁹ suggested that Mo limits pit initiation events. Betova and co workers⁵⁸ further suggested that Cr and Mo form an inverse spinel–like structure, with Mo present both in the octahedral and the tetrahedral positions, changing the spatial distribution of point defects and thus effecting ion and electron migration processes. A duplex structure of inner Cr(III) / Fe(III) mixture and outer Cr(III) hydroxide had been suggested by Bastidas *et al.*⁶⁰ based on XPS depth profiles and these authors proposed that Mo reduces the number of active sites by forming a uniform passive layer.

A very recent publication⁶¹ suggests the possible formation of a FeCr_2O_4 spinel, which is stable even in acidic solutions. A similar structure has been proposed by researchers based on Raman spectroscopic results,⁶²⁻⁶⁵ this structure consists of a cubic–close packed oxygen lattice with cations at both the octahedral and tetrahedral interstices.⁶² $\text{Fe}_{3-x}\text{Cr}_x\text{O}_4$ ($0 \leq x \leq 2$) and $\text{Fe}_{1-x}\text{Cr}_{2-x}\text{O}_4$ ($0 \leq x \leq 2$) as possible models have been proposed.

The transpassive dissolution of Cr [Cr(III) into Cr(VI)] is also faced with controversies. The oxidation of Cr(III) into Cr(VI) in the form of CrO_4^{2-} ⁵² or $\text{Cr}_2\text{O}_7^{2-}$ ^{66,67} and the transpassive potential range⁶⁸⁻⁷⁰ differ between various authors. Moreover some authors suggest Mo enhances the transpassivity of Cr by a catalytic effect^{58,67,71,72} or by decreasing the transpassive potential.⁷³

The role of Ni in passivity has become more important since the advent of high Ni stainless steels like 254SMO in the last two decades. On the contrary to the aged idea that Ni does not participate in the passivity (Ni is not included in calculation of the PREN number), it has been postulated^{74,75} that high Ni content forms a Cr–Fe–Ni oxide layer that is stable and homogenous thereby enhancing pitting corrosion resistance.

2.4 Breakdown of the passivity: localized corrosion

2.4.1 Pitting corrosion and pitting potential

Localized corrosion is a direct result of the breakdown of the passive film surface at one or more sites. The attack remains confined to a limited number of sites so both active and passive areas exist on the same surface. The most familiar of these localized mechanisms in stainless steels is pitting corrosion, where the attack is confined to small pits. Pitting is often characterised by a pitting potential (E_{pit}) or in other words, a breakdown potential, above which pitting corrosion takes place. In 1966, Leckie and Uhlig⁷⁶ confirmed the existence of a critical breakdown potential for stainless steels. However, the full definition for E_{pit} is being debated due to the existence of *metastable pits* above and below the pitting potential and also due to the fact that simple cyclic polarisation measures the formation potential of only one pit. Most authors suggest that the “pitting potential” is a more precise term than the “breakdown potential”, since “breakdown” of the passive film occurs by metastable pits well before the formation of a stable pit. In this thesis “the lowest potential above which stable pits are observed” is considered to be an adequate definition for E_{pit} . Furthermore, this critical potential depends on the environment and the surface finish, etc.^{4,7}

The pitting resistance equivalent number (i.e. PREN) is another way of categorising stainless steels against the pitting behaviour based on their composition. It is defined as:

$$\text{PREN} = \% \text{Cr} + 3.3(\% \text{Mo}) + 16(\% \text{N}) \quad \dots \dots \dots (2.23)$$

where chromium, molybdenum and nitrogen are in weight percent.

2.4.2 Pit initiation and propagation

The development of an aggressive local solution chemistry to destroy the passivity, physical separation of anodic and cathodic sites and the stability of high rate dissolution are the main physical processes that control pitting,³ although detail characteristics of these phenomena are still controversial. Charge–transfer processes, ohmic effects and mass–transport may be involved in the pit growth, as in any other electrochemical reactions.⁷⁷

Effect of sulphide inclusions: Pit initiation may be caused by various processes according to different authors, some of which contradict each other. It is widely agreed that sulphide inclusions (mainly MnS) inflict the most deleterious effect against pitting corrosion resistance. However, there is no unique concept for the way sulphide inclusions are involved in the process.

Dissolution of sulphide inclusions is the most commonly postulated reason for pit initiation; forming an aggressive local environment due to dissolution products is the main attribute. Dissolution products have been identified as sulphates,^{78,79} thiosulphates,^{80,81} $\text{H}_2\text{S}/\text{HSO}_3^-$,^{82,83} and elemental sulphur^{84,85} by different authors. The formation of a sulphur layer that prevents repassivation has been postulated.^{82,85} Williams and co workers⁸² postulated that the very high local current density of inclusion dissolution enhances electromigration and eventually increases the local concentration of Cl^- and decreases the local pH. On the other hand Baker *et al.*⁸⁶ suggested that repassivation is impeded due to the formation of a MnCl_2 salt film. Ryan *et al.*⁸⁷ has provided micro-analytical evidence using focused ion beam/secondary ion mass spectroscopy (FIB/SIMS) measurements that Cr depletion

occurs around the sulphide inclusion and hence this favours pit initiation. In contrast, Meng and co workers⁸⁸ have argued there is no such evidence for Cr depletion around MnS. The conclusion of these latter authors was based on scanning transmission electron microscopy (STEM) and FIB/SIMS results; even on samples supplied by Ryan's group. Nevertheless Ryan *et al.*⁸⁷ pointed out that Cr depletion occurs only around a small percentage of inclusions.

The idea that pits form at the edge of inclusions has been suggested by many authors^{86,89} as MnS dissolving preferentially at the edges, rather than uniformly, forming a crevice. This feature is due to lower electronic conductivity of sulphide inclusions than that of the metal matrix, which was shown in the 1970's.⁹⁰ The shape, size, composition and distribution of inclusions are also significant. Dowling *et al.*⁹¹ commented that the nature and distribution of inclusions determine the probability of corrosion. Several authors^{78,89,92} have observed that large shallow inclusions fail to initiate pitting, while narrow and deep inclusions are more hazardous. A "critical defect size" for the onset of stable pitting, has been proposed by Williams *et al.*^{82,93,94} and also by some other authors.⁹⁵⁻⁹⁷ Stewart and Williams⁹⁸ further proposed that nucleation frequency and lifetime of micro-pits depend on sulphide inclusions and their sizes and suggested a critical inclusion size of 0.7 μ m.

Effect of Chloride environment: Chloride is recognised as a universal pitting agent, although some other halides and anions (such as SCN) can also cause pitting. The existence of chloride salt islands⁴ are believed to be involved in both initiation and propagation steps. The effect of Cl⁻ concentrations on pitting potential has been extensively studied through the last four decades and many models have been

proposed.^{76,99-102} The roles of chloride is evident in the dependence of both the number of metastable pits and the value of E_{pit} on Cl^- concentration. The relationship and reasons have both been modelled by different authors. Catalyzing sulphur inclusions⁷⁸ and an increase in the number of surface sites available for metastable pits⁹⁹ by chloride ions are two of the ideas recently proposed.

Metastable to stable transition: The next consideration of the pitting process is the transition from metastable to stable pitting. The conditions that govern this transition (or else repassivation of metastable pit occurs by avoiding a stable pit) are broadly discussed in numerous models.^{77,99,103-107,113,114} Precipitation of a metal salt layer within the pit is extensively considered as an important factor for stable pit growth together with dissolution kinetics.¹⁰³⁻¹⁰⁶ Frankel⁷⁷ suggested pits are covered by a porous cover which produces an ohmic barrier, unless pits survive long enough to precipitate the salt film they repassivate as this cover ruptures and the ohmic barrier is lost. Laylock and Newman¹⁰⁴⁻¹⁰⁷ postulated two regimes of pit growth, mixed activation/ohmic control at lower potentials and diffusion control at higher potentials with the salt film present on the metal surface.

Pistorius and Burstein⁹⁹ suggested the importance of rupturing the pit cover; minor rupture leads to growth of the pit whilst a major rupture will cause repassivation. They further explained the condition for a stable pit using the “pit stability product (ia)” which is the product of pit current density (i) and its radius (a , assuming the pits are hemispherical). This work was based on a somewhat similar idea earlier proposed by Galvele.¹⁰⁸ Researchers have also studied the effect of surface roughness on pit growth¹⁰⁹⁻¹¹¹ and found that pitting occurs more readily on a rough surface.

Sato¹¹² explained that film breakdown is controlled not only by the electrochemical reactivity to aggressive ions, but also by the mechanical and the dielectrical properties of the film itself. Burstein and co workers^{113,114} proposed a different perception for pitting mechanism. They implied that the depassivation event that engenders pitting corrosion alone is also mechanical in origin. Chloride ions from the environment pass through the passivating oxide to the metal surface. When sufficient chloride is accumulated in the metal–oxide interface; the higher molar volume of the metal chloride compared to the oxide causes the oxide film to rupture mechanically. This event leads either to propagation of a metastable pit or to repassivation. Burstein *et al.*^{113,114} have also given a more detail outlook for metastable pitting. They explained the pitting process in four consecutive kinetic steps as:

- i. nucleation of the pit by microscopic rupture of the passivating oxide;
- ii. dissolution of the chloride nucleus which gives rise to the embryonic pit (this embryonic pit is not yet truly propagating, and may repassivate once the chloride has diluted far enough);
- iii. metastable pit propagation (whereby the pit propagates with a pit stability product less than 3 mA cm^{-1} and can at any stage be terminated by a rupture of the cover over the pit mouth);
- iv. stable pit propagation (where the pit propagates effectively indefinitely, with or without the perforated cover over the pit mouth, and is fully sustainable by its own kinetics, occurs above the E_{pit}).

This model is supported by the observation that pits appear to occur at discrete sizes, rather than a continuous size distribution, which would be expected for a random process.

A semiconductor electrochemistry based approach for the pitting process has been developed by Quarto *et al.*¹¹⁵ These authors discussed the role of semiconducting properties in determining the pitting behaviour of passive films in solutions containing halides. Considering the energetics of the junctions and kinetic mechanisms of oxygen and chlorine evolution reactions they ruled out the chloride penetration mechanism as a possible explanation for the initiation of pitting. Instead they suggested that local dissolution is favoured by an electronic avalanche mechanism by a multiplication of electronic carriers and that pitting is strictly an electrical breakdown mechanism. A similar explanation was given earlier by Smialowska,¹¹⁶ claiming the nucleation of pits occurs by electrical breakdown probably by the Zener mechanism. However, as yet there is not sufficient evidence to justify this semiconductor argument and no comprehensive studies so far have been reported for stainless steels.

2.5 Electronic properties

The formation and breakdown of the passive film layer are mainly controlled by ionic transport reactions (ITR) and electronic transport reactions (ETR). Both ITR and ETR are controlled by the energetics of the metal/film and film/electrolyte interfaces and the electronic properties of the passive film. Consequently, it is indispensable to incorporate a detailed study on the electronic properties of the film.

With very few exceptions, most of the passive films grown on metals and alloys behave like semiconductors or insulators. There is no exception in stainless steels; the passive film inherits the common semiconductive properties. As most of the classical theories and models introduced to explain the electronic structure of semiconductors are based on crystalline materials, it is important to study the extent of crystallinity in stainless steel passive films and hence to assess the applicability of such theories and models. A brief theoretical introduction on the important semiconductive properties of crystalline materials will be presented first. This will be extended to amorphous passive films in order to assess the validity of the concepts and models due to the departure from single crystal behaviour.

2.5.1 Semiconductor (Sc)–electrolyte (El) interface

When an electrode is in contact with a solution, an electrical double layer is formed at the electrode–electrolyte interface due to segregation of positive and negative charges in a direction normal to the boundary. The two main models are the compact double layer (Helmholtz layer) and the diffuse double layer (Gouy layer), where the Gouy layer can be neglected in a sufficiently concentrated electrolyte.^{118,119} The presence of this double layer has to be accounted for when the charge and potential distribution are considered across the interface. In the case of a metal-electrolyte (M/El) interface,

the majority of any applied potential is dropped across the double layer. In contrast to the semiconductor-electrolyte (Sc/EI) interface, owing to the much lower concentration of mobile electrical carriers (electron and holes for the n-type and p-type semiconductors, respectively), a “space charge” region is formed in the interior of the semiconductor phase and the majority of any applied potential drops across this region. (Figures 2.06 and 2.07).¹¹⁹

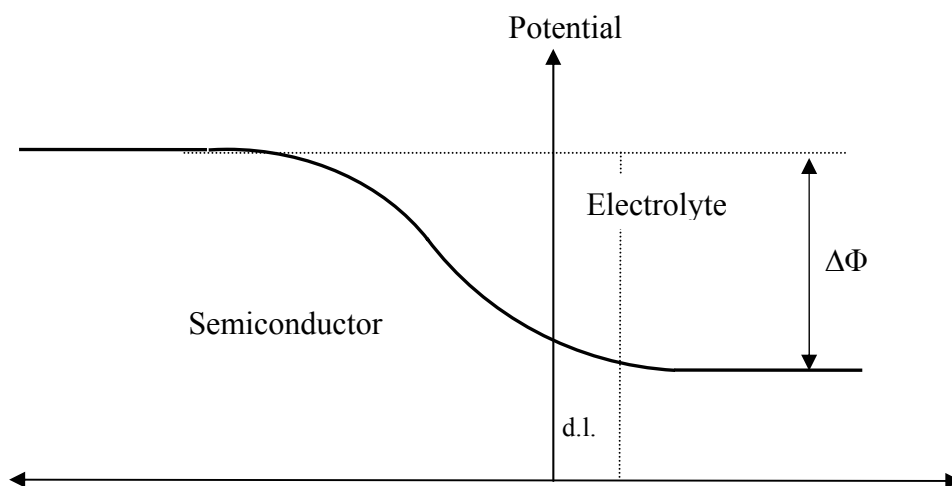


Figure 2.06. Schematic potential distribution across an n-type Sc/EI interface. $\Delta\Phi$ is the total potential drop across the interface. d.l. is the Helmholtz double layer.

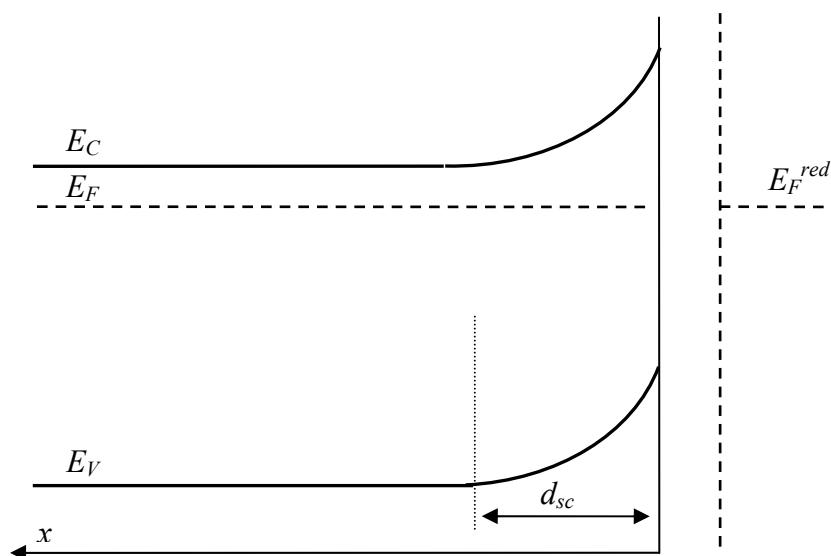


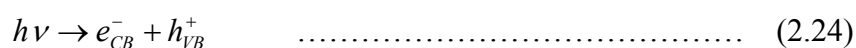
Figure 2.07. Energy band diagram of an n-type semiconductor, band bending due to the space charge region. E_C , E_F and E_V are conduction band, Fermi level and valence band of the semiconductor respectively. E_F^{red} is the Fermi level of the redox couple of the solution. d_{sc} is the depth of the space charge region. Assumption is made that the surface states[‡] are not present at the Sc/EI interface.

[‡] Surface states are electronic energy levels of the solid that are localized at the surface and lie within the bandgap. (check Appendix A)

2.5.2 Photoelectrochemistry

Photoeffects in electrochemical systems, in which an additional current can be stimulated by irradiating a semiconductor with light were first recognized by Becquerel in the early 19th century.¹¹⁷ He used metal electrodes covered with oxide films. Ever since, there have been continuous efforts to utilize the photoeffect in order to study the properties of passive films. Although results and interpretations of experimentations still remain controversial, enormous advancements have been made in this area. It is recognised that even very thin films constitute their own phase with their own characteristic properties. Application of photoelectrochemistry to study the passive film is based on this concept. Consequently, photoelectrochemistry can be used as an *in situ* technique to characterize passive films with respect to their optical and electronic properties.

Theoretical aspects of photoelectrochemistry: If a semiconductor electrode is illuminated by light with a suitable energy, $h\nu$, electrons can be excited from occupied electronic states to unoccupied states. This generates an electron–hole pair which can be separated by an electric field in the space charge region (Depletion region is formed at the Sc/El interface due to the withdrawn majority carriers.):



In the case of an n-type semiconducting film, the hole migrates to the surface, where it reacts with a donor, while the electron migrates to the bulk, so that an anodic photocurrent is passed. In a p-type semiconductor, the process is reversed as the electron moves to the surface to join with an acceptor, while the hole migrates to the

bulk, this gives rise to a cathodic photocurrent. Figure 2.08 schematically explains these two conditions.

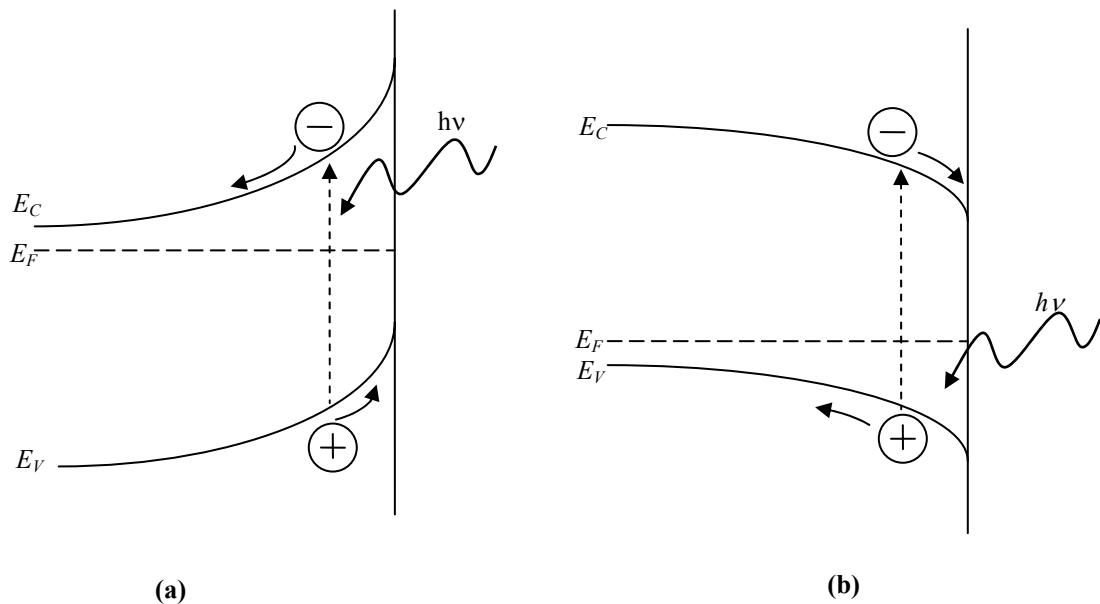


Figure 2.08. Effect of illumination in depletion layer and electron transfer reactions at the semiconductor–electrolyte interface for (a) n-type and (b) p-type semiconductor.

The first attempt to describe the magnitude of the photocurrent was by Gärtner,¹²⁰ considering metal-semiconductor interface as an ideal Schottky barrier with parabolic band bending. According to the model, the total photocurrent (I_{ph}) is a combination of two terms, I_{drift} (drift current density), due to the contribution of carriers generated in the space charge layer by the incoming photons and I_{diff} (diffusion current density), due to the minority carriers generated in the neutral region (in the bulk of the semiconductor) that diffuse into the depletion layer. The model assumed no reflection of the light at the rear interface; all the entering light is absorbed within the semiconductor; and no recombination[§] occurs. According to the model:

$$I_{ph} = I_{diff} + I_{drift} \quad \dots\dots\dots (2.25)$$

Substituting terms for diffusion and drift parts, the Gärtner's equation for an n-type semiconductor becomes:

[§] Appendix B

$$I_{ph} = e\phi_0 \frac{1 - \exp(-\alpha d_{sc})}{1 + \alpha L_p} + ep_0 \frac{D_p}{L_p} \dots\dots\dots (2.26)$$

where e is the absolute value of the electronic charge, ϕ_0 is the photon flux entering the semiconductor, α is the light absorption coefficient, d_{sc} is the space charge length, L_p is the hole diffusion length, p_0 is the boundary condition for hole concentration when $x = \infty$ and the D_p -holes diffusion coefficient.

Equation 2.26 was further simplified for the case of an Sc/EI interface by Butler¹²¹ into the form of:

$$I_{ph} = e\phi_0 \alpha d_{sc}^0 \left(V_e - V_{fb} - \frac{kT}{e} \right)^{\frac{1}{2}} \dots\dots\dots (2.27)$$

where d_{sc}^0 is the space charge width at the semiconductor electrode at 1V of band bending, V_e and V_{fb} are the electrode potential and the flat band potential, respectively, T is the absolute temperature and k is the Boltzmann's constant. This relationship can be used to find out the flat band potential by plotting I_{ph}^2 vs. V_e .

The number of electron-hole pairs generated per second and unit volume at any distance from the semiconductor surface, $g(x)$, is given by the Beer-Lambert law:

$$g(x) = \phi_0 \alpha \exp^{-\alpha x} \dots\dots\dots (2.28)$$

where ϕ_0 is the photon flux entering the semiconductor after correction for the reflection losses at the Sc/EI interface. This describes the amount of light absorbed by the semiconductor.

The relationship between absorption coefficient α and the bandgap E_g of a material in the vicinity of the optical absorption threshold (mobility edge in an amorphous semiconductor or band edge in a crystalline semiconductor)¹²² is:

$$\alpha = A \frac{(h\nu - E_g)^n}{h\nu} \dots\dots\dots (2.29)$$

where the value of n depends on the kind of optical transition** between occupied electronic states and vacant sites of the semiconductor and A is a constant.¹²³

From Equations (2.27) and (2.29) it is possible to derive an expression for the quantum yield:

$$\frac{I_{ph}}{e\phi_0} = \eta h\nu = A(h\nu - E_g)^n (L_i + d_{sc}^0 \sqrt{|V_e - V_{fb}|}) \dots\dots (2.30)$$

where η denotes the collection efficiency, $L_i = L_p$ or L_n (for holes and electrons respectively). Equation 2.30 at a constant potential (when $V_e - V_{fb}$ is a constant), can be used to the optical bandgap of a material by plotting $(\eta h\nu)^n$ vs. $h\nu$.

The accuracy of Gärtner and Butler relationships has been reviewed by many researchers.¹²⁴⁻¹²⁹ Apart from the initial assumption of parabolic energy levels based on the ideal Schottky barrier, the assumption of the absence of any recombination either in the space charge region or at the surface of the semiconductor is not consistent for the case of passive films. The effect of surface states is also a vital consideration. Wilson¹²⁴ pointed out that in addition to bulk recombination, both surface recombination and surface electron transfer processes, must also be considered and these effects could cause higher band bending than otherwise predicted. However, Wilson¹²⁴ neglected space charge recombination and assumed all

** Appendix C

incident photons absorbed in the space charge region give rise to a photocurrent. Reichman *et al.*¹²⁵ considered recombination effects in the space charge region as well as in the neutral region and showed the rate limiting effect of charge transfer across the interface enhances the recombination rate with the effect increasing with the magnitude of the applied field.

Guibaly and Colbow¹²⁷ considered all types of recombination effects and charge transfer kinetics and pointed out the effect of light intensity on the efficiency of charge transfer. They further suggested that the surface transfer velocity of minority carriers is a very important parameter in determining the photocurrent. Fonash *et al.*¹³⁰ postulated that photocurrent is opposed by five bucking current (loss) mechanisms:

- (I) bulk recombination;
- (II) diffusion;
- (III) space charge recombination;
- (IV) interface (surface) recombination and
- (V) direct/indirect electron emission into the oxidised species.

The square root dependence of the photocurrent on the electrode potential predicted by the Butler Equation (Equation 2.27) has also been questioned. Stimming¹¹⁹ pointed out that due to the involvement of localised states, the potential dependence of the photocurrent may be different. Quarto *et al.*¹¹⁸ explained that although the Butler model (equation 2.30) is important when photoelectrochemical data is used to find the optical bandgap, Equation 2.27 is not convincing to obtain the flat band potential.

2.5.3 Mott–Schottky (MS) equation and the space charge capacitance

A material's capacity is a measure of the storage of charge during half of an ac cycle, with the charge returned during the other half of the cycle.¹³¹ The differential capacity is defined by:

$$C = \frac{dQ}{d\phi} \quad \dots\dots\dots (2.31)$$

where dQ is the charge stored when the voltage is altered by $d\phi$. With the depletion layer at the semiconductor surface, the space charge capacitance, C_{sc} is given by:

$$C_{sc} = -\frac{dQ_{sc}}{d\Delta\phi_{sc}} \quad \dots\dots\dots (2.32)$$

where $d\Delta\phi_{sc}$ is the potential difference across the space charge region and dQ_{sc} is the charge in the space charge region (Q_{sc} is not at the surface of the conducting layer, but it is spread throughout the depletion layer).

It can be shown by using Poisson's equation and Gauss' law, that in the limit $\exp(-e\Delta\phi/kT) \ll 1$:¹³²

$$\frac{1}{C_{sc}^2} = \frac{2}{e\epsilon\epsilon_0 N_d} \left(V_e - V_{fb} - \frac{kT}{e} \right) \quad \dots\dots\dots (2.33)$$

where ϵ_0 is the vacuum permittivity and ϵ is the relative permittivity, N_d is the donor density (in n-type semiconductors and the same equation analogous for p-type with a minus sign in the right hand side and acceptor density, N_a instead of N_d) while other notations hold similar definitions as in earlier cases ($\frac{kT}{e}$ is the thermal voltage contribution). Equation (2.33) is the well known "Mott-Schottky" (MS) equation, which for a crystalline semiconductor can be used to derive the flat band potential V_{fb} of the Sc/El junction by extrapolating the plots to $1/C^2 = 0$, while the slope indicates

the density of donors (or acceptors). The sign of the slope indicates the type of conductivity; a positive slope represents n-type, while a negative slope represents p-type.

However, in an electrochemical system, charging of the Helmholtz capacitance C_H cannot always be neglected (Figure 2.06), such that:^{133, 134}

$$\frac{1}{C_{meas}} = \frac{1}{C_{sc}} + \frac{1}{C_H} \dots\dots\dots (2.34)$$

where C_{meas} is the experimentally measured capacity. The relationship between the C_{sc} per unit area and the space charge width, d_{sc} is given by:

$$C_{sc} = \left(\frac{\epsilon \epsilon_0}{d_{sc}} \right) \dots\dots\dots (2.35)$$

Furthermore, Equations 2.33 and 2.35 can be combined to obtain the dependence of d_{sc} on the applied field:

$$d_{sc} = \left(\frac{2\epsilon \epsilon_0}{eN_d} \right)^{1/2} \left(\Delta\phi_{sc} - \frac{kT}{e} \right)^{1/2} \dots\dots\dots (2.36)$$

and $\Delta\phi_{sc} = V_e - V_{fb} \dots\dots\dots (2.37)$

The Fermi level of the Sc, with respect to the electrochemical scale, can be found once V_{fb} is known:¹¹⁸

$$E_F^0(eI) = -eV_{fb} \dots\dots\dots (2.38)$$

where both terms are with respect to the electrochemical scale. This approach can be further extended to locate E_C and E_V :

$$E_C = E_F^0 + kT \ln \left(\frac{N_c}{N_d} \right) \text{ for n-type Sc} \dots\dots\dots (2.39)$$

and
$$E_V = E_F^0 - kT \ln \left(\frac{N_v}{N_a} \right) \text{ for p-type Sc} \dots\dots\dots (2.40)$$

where N_c and N_v are the effective densities of states at the bottom of the conduction band and at the top of the valance band of the semiconductor. The bandgap of the Sc is:

$$E_g = E_C - E_V \dots\dots\dots (2.41)$$

However, the validity of the Mott–Schottky relation has been rigorously argued against, especially for the case of disordered amorphous passive films.^{132,133,135-137} Gomes and Cardon¹³³ discussed possible complications in the capacitance–voltage behaviour in detail: non negligible series resistance; imperfectly blocking barrier due to Faradaic current; influence of Helmholtz layer; contribution of surface states; frequency dependence of dielectric constant; presence of deep lying donors; and non uniform distribution of donors are some of the main causes of potential errors that they pointed out. Dewald¹³² concluded that the surface state capacitance is negligible compared to the space charge capacitance; however he made the conclusion using his experimental results on single crystals.

A frequency dependent capacitance due to strongly disordered behaviour of amorphous films, which has been observed by many researchers,^{118,131} violates the conditions laid out to obtain Equation (2.33). Using Gomes and Cardons¹³³ considerations, Quarto *et al.*¹¹⁸ summarised the main assumptions made to obtain the capacitive characteristics of a semiconductor in this Equation (2.33), which contradict with the known properties of amorphous passive materials:

- a) crystalline Sc electrodes are homogeneously doped in the depletion region;

- b) a fully ionised single donor (or acceptor) exists;
- c) absence of deep donor (or acceptor) levels in the forbidden gap of the Sc;
- d) contribution of surface states and minority carriers on the measured capacitance is negligible;
- e) the absence of electrochemical Faradaic processes at the Sc/El interface.

Despite all these remarks, the classical relationships on photocurrent spectroscopy and capacitive measurements derived for crystalline materials are still widely used with or without some amendments. This discussion will be further extended in the next sections with respect to the passive film on stainless steel.

2.5.4 Electronic properties of amorphous materials: validity of the application of photocurrent and capacitive concepts developed for crystalline materials to stainless steel passive films

Amorphous nature: Most of the classical relationships on photocurrent and capacitive behaviours of semiconductors that have been discussed in the above sections are interpreted for crystalline materials. These concepts allow researchers to obtain information on the solid state properties (i.e., bandgap, concentration of donors or acceptors) and on the energetics (flat band potential) of a crystalline material quite easily. However, the validity of using the same concepts for amorphous films is extremely dubious due to the disparity of the assumptions made. The presence of lattice disorders, the extreme thinness of the passive film, extreme high donor/acceptor concentrations and geminate recombination effects could cause complications in the case of amorphous passive films.¹¹⁵

Density of states and band structure models: The density of states (DOS) denoted by $N(E)$ is defined as the number of occupiable states per unit volume available for an electron of a given spin direction with energies between E and $E+dE$.¹²² In crystalline solids the states can be occupied or empty, and $N(E)f(E)dE$ is the number of occupied states per unit volume, where f is the Fermi distribution. Although the density of states in a non-crystalline material does not differ greatly from the corresponding form in the crystal, in amorphous materials, the finer features may be smeared out, and some localized electronic states appear in the forbidden energy range where electronic charges can be trapped.¹³⁸ Consequently, the lack of long range order and the high concentration of defects due to its amorphous nature, generate a finite DOS within the mobility gap ($E_C - E_V$) in real oxide films defined by the two sharp mobility edges, E_C and E_V in the conduction band and the valance band, respectively.¹²³ As a result, in the models the bandgap for amorphous oxides has to be substituted by a term known as the mobility gap.^{119,139} A schematic representation of DOS distribution in the forbidden gap of an amorphous semiconductor is shown in Figure 2.09.

Different band models had been proposed over last four decades for amorphous semiconductors.^{115,118,122,140,141} Some of the main models are presented schematically in Figures 2.10 and 2.11.

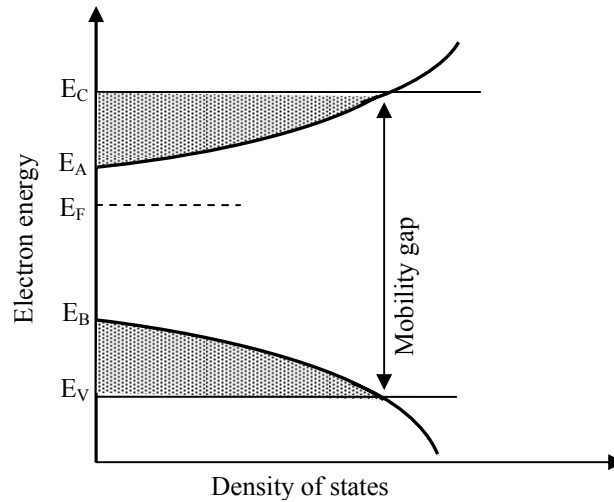


Figure 2.09. Schematic representation of DOS as a function of the energy for an amorphous semiconductor.

Figure 2.10 (a) shows the CFO model, named after its proposers Cohen, Fritzsche and Ovishinsky¹⁴¹. These authors envisaged that tails of localised states are pulled out from E_C and E_V by the disorder and that there is some overlap between these tails; where the overlap occurs when the equal numbers of charged states of each sign are formed.

Mott and Davis¹²² considered an ideal amorphous nature, in which only long range lattice disorders is taken into account [Figure 2.10(b)]. Here short range order was considered to be the same as in a crystalline materials, *i.e.* the distance between nearest neighbours is virtually the same in crystalline and amorphous materials, such that conventional band theory could be applied locally. This model ruled out the possibility of overlapping tails and suggested a linear decay of donor states below the E_C and above the E_V , which differentiate it from an earlier model by Tauc¹⁴⁰ that used a parabolic decay. In the Mott and Davis model, the optical gap is a measure of the smaller energy difference between localized states of the valance band and extended states of the conduction band or vice versa, $(E_C - E_B)$ or $(E_A - E_V)$ whichever is

smaller. This explanation helps to distinguish the optical gap, E_g^{opt} from the mobility gap, $E_g^m (E_C - E_V)$ of amorphous materials.

Quarto and co workers^{115,142} brought up another out look for DOS distribution. They postulated that due to the presence of the large number of electronic states lying within the forbidden mobility gap, most of the electronic charge is located below the Fermi level in localised states quite some distant in energy from the E_C mobility edge, thus separating the extended states region from the localised once. In its simplest form, this model assumed a constant DOS, $N(E) = N$, within the mobility gap as shown in Figure 2.11(a). Quarto at al.^{115,142} further pointed out that filled electronic states within the gap do not instantaneously follow any imposed AC signal, but need a finite response time. These authors also commented on how the differences of electronic state distribution between amorphous passive films and their crystalline counterparts have a significant influence on both capacitive and photoelectrochemical behaviour of Sc/EI junctions.

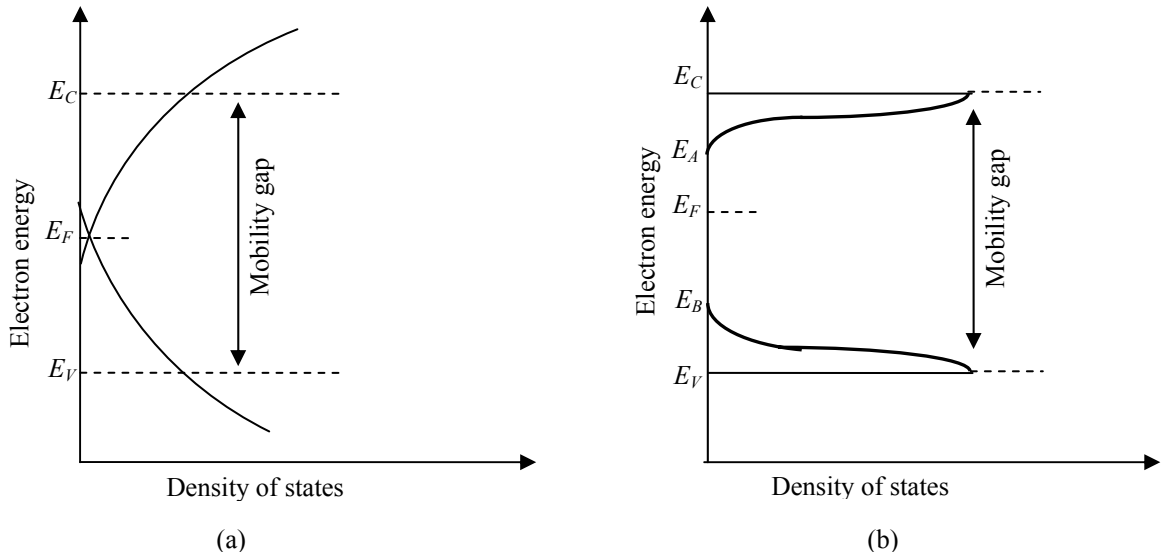


Figure 2.10 Schematic density of states distribution in amorphous semiconductor: (a) CFO model* (b) Mott-Davis model**. Notations are the same as given in the text.
 * adapted from reference 141, **adapted from reference 122.

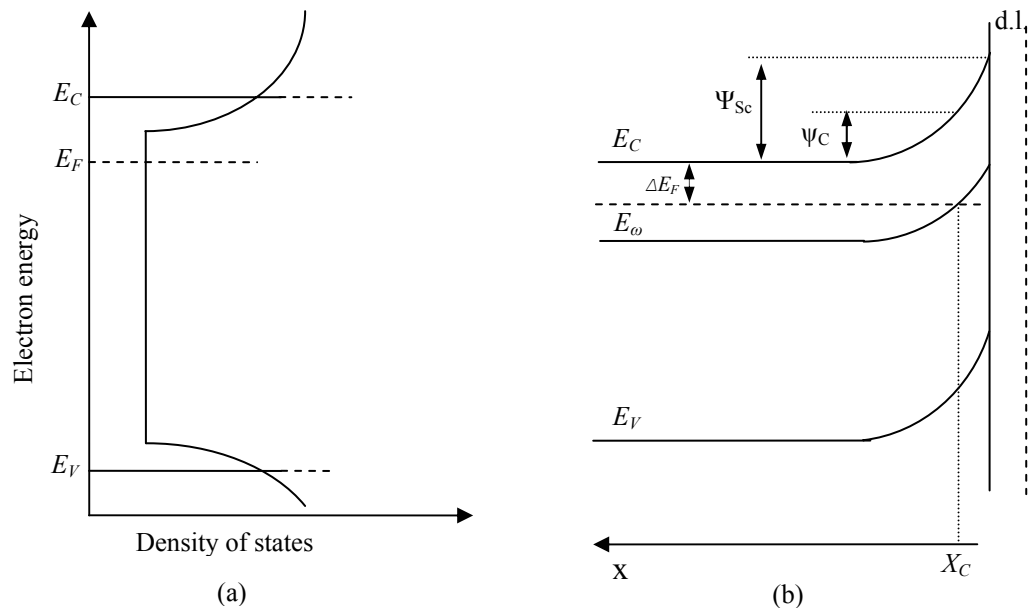


Figure 2.11. Di Quarto *et al.* model for an n-type semiconductor: (a) schematic density of states distribution in an amorphous semiconductor having a constant DOS; (b) energetics at an amorphous Sc/El junction. Ψ_{Sc} and ψ_C are energies corresponding to the band bending at the semiconductor electrolyte interface and at x_C (the location in the Schottky barrier that separates two regions where all electronic states fully respond to the AC signal and where no states respond) respectively. Other notations are the same as given in the text. (adapted from the reference 115)

2.5.5 Capacity behaviour and Mott Schottky plots for amorphous passive films

Frequency dependent capacitance: As mentioned in the previous section, the electronic states located in the gap do not follow any imposed AC field having an angular frequency ω instantaneously, but need a finite response time that depends on their energy.^{115,118}

Relaxation time, τ , for the capture of emission of electrons from the electronic states below E_F can be assumed to follow the relationship:

$$\tau = \tau_0 \exp\left(\frac{E_C - E}{kT}\right) \dots\dots\dots (2.42)$$

where, at constant temperature, τ_0 is a constant characteristic of each material.

According to Equation (2.42), on decreasing the energy of the localised state in the gap τ increases sharply, so that deep states (for which $\omega\tau \gg 1$) do not respond to the AC signal at all. Consequently Quarto *et al.*^{115,118} introduced a “cutoff” energy level, E_ω , separating states responding to the signal from those not responding ($\omega\tau \ll 1$ and $\omega\tau \gg 1$, respectively). Substituting the limiting condition of $\omega\tau = 1$ for $E = E_\omega$ in Equation (2.42):

$$E_C - E_\omega = -kT \ln(\omega\tau_0) \dots\dots\dots (2.43)$$

The intersection of the cutoff level with the Fermi level allows one to locate a corresponding point within the Schottky barrier, X_C , that separates two regions (Fig. 2.11 b); $x > X_C$ where all electronic states fully respond to the AC signal and $x < X_C$, where no states respond. Consequently Quarto and co workers¹⁴² presented an equivalent circuit model for amorphous Sc/El junction for passive films based on the theory of an amorphous Sc Schottky barrier¹⁴³ (Figure 2.12). In contrast to the Sc/El

junction of crystalline materials, this equivalent circuit is represented on the semiconductor electrode side by a frequency dependent resistance, $R(\Delta\Psi_{sc}, \omega)$, in parallel with two capacitors in series, the first of which, $C(\Psi_C, 0)$, is quite insensitive to both frequency and bias, while the second, $C(X_C)$, is both frequency and bias dependent. Consequently Quarto's model questions the validity of the Mott-Schottky equation [Equation (2.33); $\frac{1}{C_{sc}^2} = \frac{2}{e\epsilon\epsilon_0 N_d} \left(V_e - V_{fb} - \frac{kT}{e} \right)$] to either locate the V_{fb} or calculate N_d and the validity of Equations (2.39) and (2.40) to locate E_C and E_V .

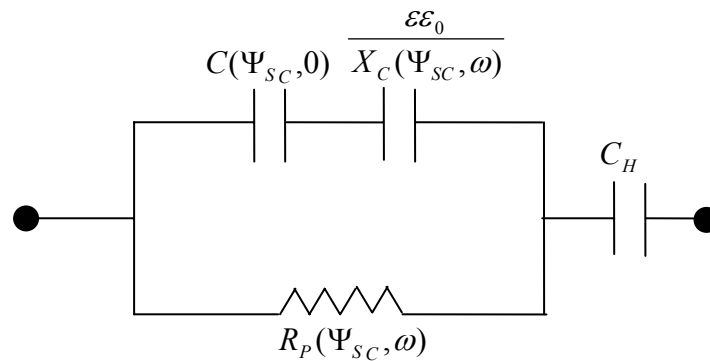


Figure 2.12. Equivalent circuit proposed by Di Quarto *et al.* to fit impedance data for an Sc/El junction of an amorphous semiconductor, related to Figure 2.16, notations as described in the text. (adapted from the reference 115)

Peterson and Parkinson¹⁴⁴ stated that the strong frequency dependence and the large hysteresis in the capacitance behaviour are due to a high density of surface states. Since amorphous semiconductors have a more continuous distribution of surface states between the valance and conduction bands than a crystalline material, a stronger frequency dependence is observed. Several other causes for the non-ideal behaviour of passive films have been suggested, including non-uniform distribution of donors, dielectric relaxation phenomena, which occur throughout the depletion layer, as well as the presence of deep donor levels.¹⁴⁵

Young in the 1950s,¹⁴⁶ observed the frequency dependence capacity behaviour of an amorphous Nb₂O₅ film and rationalised it in terms of resistivity variance in the film. This was based on an exponential conductivity profile within the oxide due to the variable non-stoichiometry. However, he did not consider mid-bandgap conditions in his explanation. Wood and Pearson¹⁴⁷ used the same approach as Young in their interpretation of the frequency dependence of the conductance of Nb, Ta, Al, Zr, Ti and W anodic films. Cahan and Chen¹⁴⁸ proposed a model to describe the behaviour of the passive film on iron, defining a “chemi-conductor” as an insulator, whose stoichiometry can be varied by oxidative and/or reductive valency state changes; consequently modifying the local electronic (and/or ionic) conductivity of the film.

Capacitive-voltage behaviour and Mott-Schottky relationship: Capacitive-voltage measurements have been interpreted with respect to the band structure model by different authors.^{119,134,145,149,150} The capacity-voltage behaviour observed by Stimming and Schultze¹⁵⁰ for iron electrodes is schematically shown in Figure 2.13. Stimming and Schultze¹⁵⁰ explained that the decrease in the capacitance, as the potential is made more positive (region A of Figure 2.13) can be attributed to increased thickness of the depletion layer, such that the space-charge capacitance declines and in the region B of Figure 2.13, the capacitance becomes almost independent of potential as the donors of the oxide layer get exhausted and the oxide behaves as an insulator. Stimming and Schultze¹⁵⁰ further explained the region C (Figure 2.13) is due to a formation of an inversion layer, as a result of increasing hole concentration in the valance band. Hence these authors concluded that the Mott-Schottky relationship is valid only for a limited range, where the space charge

length is smaller than the oxide film thickness. A similar explanation was given by Khan and Schmickler¹³⁴ for the capacity-voltage behaviour of passive films, who envisaged two contributions to the capacity of thin passive films; one from the space charge in the film and one from the surface charge on the underlying metal.

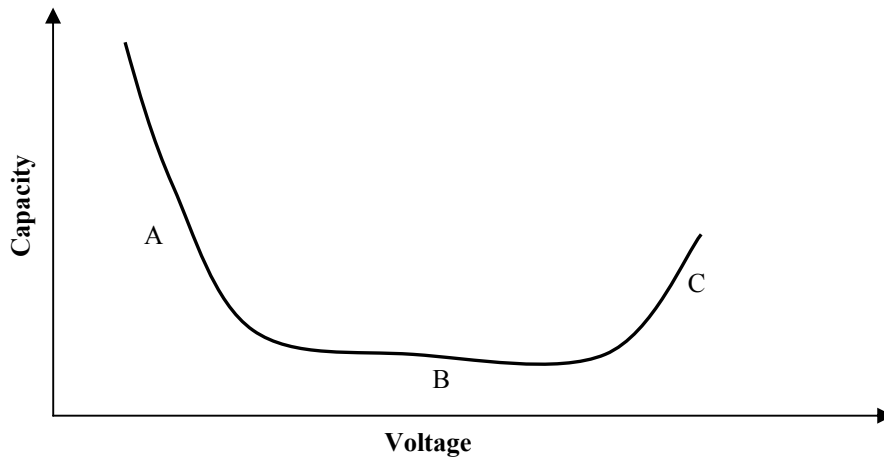


Figure 2.13. Schematic representation of capacity–voltage behaviour observed for iron electrodes in Reference 150.

The validity of Mott Schottky plots to locate the flat band potential for stainless steels is questionable. Some authors accept the validity of MS plots for stainless steels,¹⁵²⁻¹⁵⁷ whilst others argue the inconsistency.^{142,145,150} It was shown by Di Paola¹⁴⁵ that the determination of V_{fb} by extrapolating the MS plots according to Equation (2.33) is accurate, when the space charge capacitance is small compared to the C_H and when the potential drop caused by the applied potential is virtually all across the space charge region within the semiconductor. The effect of C_H does not change the slope, but the intersection potential V_i away from V_{fb} . Consequently, a correction has to be made as:¹³⁴

$$V_i = V_{fb} + \frac{kT}{e} - \frac{\epsilon\epsilon_0 e N_d}{2C_H^2} \dots\dots\dots (2.44)$$

Di Paola¹⁴⁵ also pointed out the importance of the above correction in the case of stainless steels due to high N_d values. When this correction is applied, it is assumed in most cases that C_H is around $20 \mu\text{F} / \text{cm}^2$ and remains constant over the range of measurements, this latter assumption is at best dubious.

Another controversy arises over the estimation of the dielectric constant (ϵ) of the passive film.¹⁵¹ Frequency dependent behaviour of ϵ creates further ambiguities. Gomes *et al.*¹³³ showed that although ϵ is frequency dependent, it is homogenous over the space charge layer, thus the MS plots are linear and allow the determination of the flat band potential. Despite the controversies, some authors^{152,153} have used 12 as the dielectric constant, the value for iron oxide and chromium oxide, while other authors^{145,156} use 15.6, for stainless steel passive films, regardless of the measuring frequency. These estimations of the dielectric constant are based on the experimental parameters measured during the growth of the oxide film, when the space charge extends across the whole thickness of the film, with the film thickness being determined by ellipsometry. However, these were measured at a single frequency.

Two diverse types of MS behaviours are reported for stainless steels.¹⁴⁵ In “A” type behaviour, MS plots are nearly parallel at every frequency [Figure 2.14 (a)] and the intercepts with V_e are shifted towards more cathodic potentials with increasing frequency. This type of behaviour is suited to calculate N_d , but not to locate V_{fb} . All graphs at different frequencies converge to a common point in type “B” behaviour, which is shown schematically in Figure 2.14(b), is adequate to determine only V_{fb} .

However, due to enormous controversies, MS plot could not be the best consistence method to determine V_{fb} . Blackwood and Peter¹⁵⁸ experimented with the potential modulated reflectance spectroscopy and claimed its reliability to determine the flat band potential was better than MS plots. Unfortunately, the experimental arrangement is not as simple as for photocurrent and capacitance measurements.

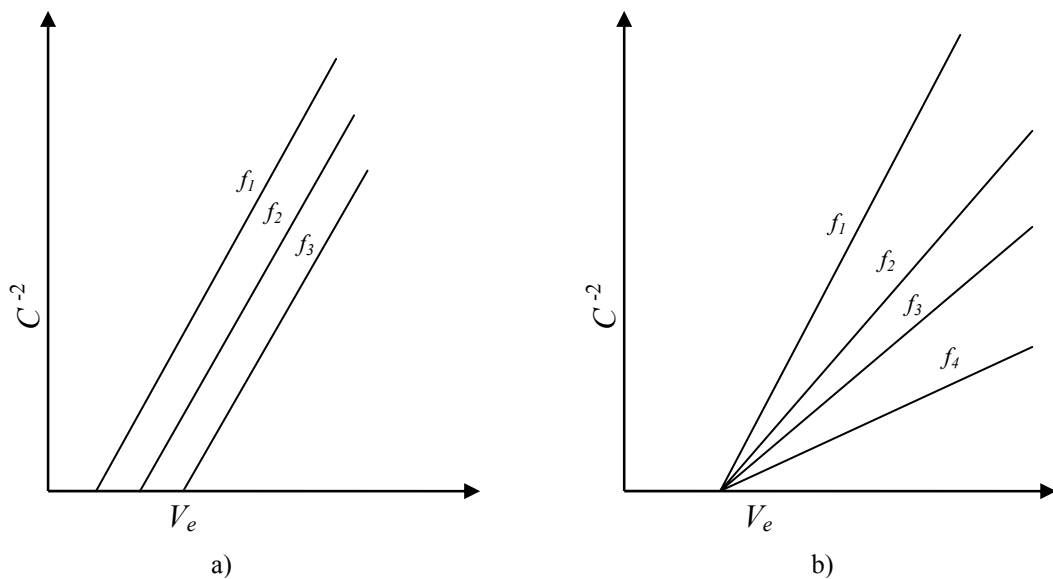


Figure 2.14. Schematic representation of MS plots at different frequencies ($f_1 \dots f_4$) reported in reference 145 for a) “A” type b) “B” type

Finally, possible phase changes may occur both within the passive and transpassive regions, postulations on forming a duplex structure^{153,154,156} and the existence of deep donor levels,^{152,153} have made the understanding the capacitive behaviour even more complicated.

2.5.6 Photoelectrochemical characterization of stainless steel passive films

The amorphous nature of the passive films on stainless steels alters its optical absorption behaviour from crystalline characteristics. The main differences in

photoelectrochemical characteristics of an amorphous passive film competed with its crystalline counterpart are caused mainly by:¹¹⁸

- a) modification of the DOS in amorphous semiconductors due to the presence of different kinds of defects and the optical bandgap may or may not coincide with that of its crystalline counterpart;
- b) rapid bulk recombination effects;
- c) possible interference effects due to multiple reflections at the metal–film and film–electrolyte interfaces;
- d) internal or external photoemission due to possible optical excitation at the inner metal–film interface owing to the small film thickness.

One or more of the above facts may divert the photoelectrochemical behaviour of amorphous passive films away from that expected for crystalline materials. This will be discussed in detail with respect to the stainless steel passive films in the following sub sections.

Bandgap of amorphous semiconductors: Equation (2.29), the relationship between the optical absorption coefficient and the bandgap for optical transition can be re-written in the form:

$$\alpha h\nu = A(h\nu - E_g)^n \dots\dots\dots (2.29 \text{ b})$$

where the value of the n depends on the nature of the optical transition and A is a constant. Tauc¹⁴⁰ concluded that $n = 2$ for amorphous semiconductors under the assumption of parabolic bands. A similar value had been obtained by Mott and Davis¹²² assuming the DOS at the band edges were linear functions of energy. These authors further explained that in the case of amorphous materials, owing to the

relaxation of the k -conservation rule, no intervention of phonons is invoked to conserve momentum and all the energy required is provided by the incident photons.

In contrast to indirect optical transition in crystalline materials (with the same n value), in amorphous materials, photons interact with the solid as a whole and are termed *nondirect* transitions. Substituting the bandgap with the mobility gap, E_g^m where $E_g^m = E_C - E_V$ for amorphous semiconductors, Equation (2.29 b) can be written as:

$$\alpha h\nu = \text{const.}(h\nu - E_g^m)^2 \quad \dots\dots\dots (2.45)$$

Due to the presence of some tailing of states, which is predicted by the models proposed for DOS, E_g^m represents the extrapolated zero in the DOS, rather than the real zero. According to Mott and Davis model (Figure 2.10 b), a similar relationship as Equation (2.45) can be obtained for E_g^{opt} where $E_g^{opt} = E_C - E_B$ or $E_A - E_V$, whichever is the smaller:

$$\alpha h\nu = \text{const.}(h\nu - E_g^{opt})^2 \quad \dots\dots\dots (2.46)$$

Piazza et al. reported¹⁵⁹ the coexistence of both types of transitions for thin anodic films grown on niobium. However, the Mott–Davis relationship for E_g^{opt} , as in Equation (2.46), should only be valid in a narrow range of energies below the mobility gap, usually in order of about 0.3eV (*i.e.* the magnitude of $E_C - E_B$ or $E_A - E_V$).^{118,123} This can be used to discriminate between E_g^{opt} and E_g^m . It has been shown experimentally and theoretically that the assumption of a direct proportionality between corrected photocurrent (I_{ph}) and absorption coefficient (α) in the vicinity of

the absorption edge is valid even for amorphous semiconductors.¹¹⁸ Consequently, Equation (2.46) can be further simplified to suit the photocurrent experiment:

$$(I_{ph} h\nu)^{1/2} = \text{const.}(h\nu - E_g) \dots\dots\dots (2.47)$$

where E_g could be either E_g^m or E_g^{opt} as explained above.

Di Quarto and co workers¹¹⁸ pointed out that the differences in the bandgaps ($\Delta E_g = E_g^m - E_g^{cry}$) obtained between amorphous semiconductors and their crystalline counterparts in a range of 0.1 to 0.35 eV replicate the lattice disorder and differences in short range order between the two phases. A different short range order can lead to the formation of a defective structure, with a high density of localized states within the mobility gap.

Another striking feature that is frequently observed in amorphous materials is an exponentially decreasing absorption tail for photon energies lower than the mobility gap, the so call Urbach tail.^{122,140,160} Such a behaviour is also occasionally found in crystalline materials, although it is rare. The Urbach tail is described by the following exponential relationship between the absorption coefficient and the photon energy:

$$\alpha = \alpha_0 \exp[\gamma(h\nu - E_0)/kT] \dots\dots\dots (2.48)$$

where α_0 and γ are constants. The value of E_0 can be apparently obtained from a plot of $\log \alpha$ vs. $h\nu$ at the point where $\log \alpha$ ceases to be linear with $h\nu$ and coincides with the mobility gap determined according to Equation 2.45.¹⁶¹ An exponential distribution of localized states in the band edge tails has been proposed as the reason for the Urbach tail.¹²²

On the basis of bandgap determinations, photocurrent spectroscopy has been widely used as a tool for obtaining indirect information on the composition and the structure of passive films.^{123,182,154} This correlation between the composition and the bandgap for oxides, hydroxides and mixed oxides is explained in Appendix D.

Effect of recombination in amorphous films: The Gärtner's equation (2.26) represents the upper limit of the photocurrent response, neglecting surface and bulk recombination. As a result, no influence of the photon energy on the shape of the I_{ph} vs. V_e is predicted and a linear dependence of I_{ph}^2 on V_e at a constant wavelength is expected. However, this is often not the case in practice as the photocurrent conversion efficiency is determined not only by generation and collection terms, but also by an electron hole recombination via energy levels in the space charge region and at the surface (ie., surface states).¹⁶² This phenomenon can exist in any material, including single crystals. However, in the case of amorphous films, initial recombination is quite probable due to the presence of localised states between the conduction and valence bands as a repercussion of lattice disorder. The mobility of carriers in these states is much lower than the extended states.¹¹⁸ Hence electron-hole pairs are only separated slowly, making recombination more likely.

Pie and Enck¹⁶³ introduced a model for recombination effects in amorphous materials. According to their model, every absorbed photon creates a pair of thermalized carriers bound by their mutual coulombic attraction. As a result, electron-hole pairs do not cover a distance long enough to prevent recombination. Consequently, a certain fraction of the photogenerated carriers recombine.

The transient behaviour of the photocurrent as a function of time has been investigated^{162,164-166} and employed in the study of surface recombination processes. Figure 2.15 schematically shows three types of possible photocurrent transients. As surface recombination is caused by combining the majority carriers, which are flowing to the surface, with minority carriers, the photocurrent decays with time. When the illumination is turned off, carriers at the surface continue to recombine and the current changes sign; since current measured in an external circuit is now due to the majority carriers flowing to surface states.^{162,164-166}

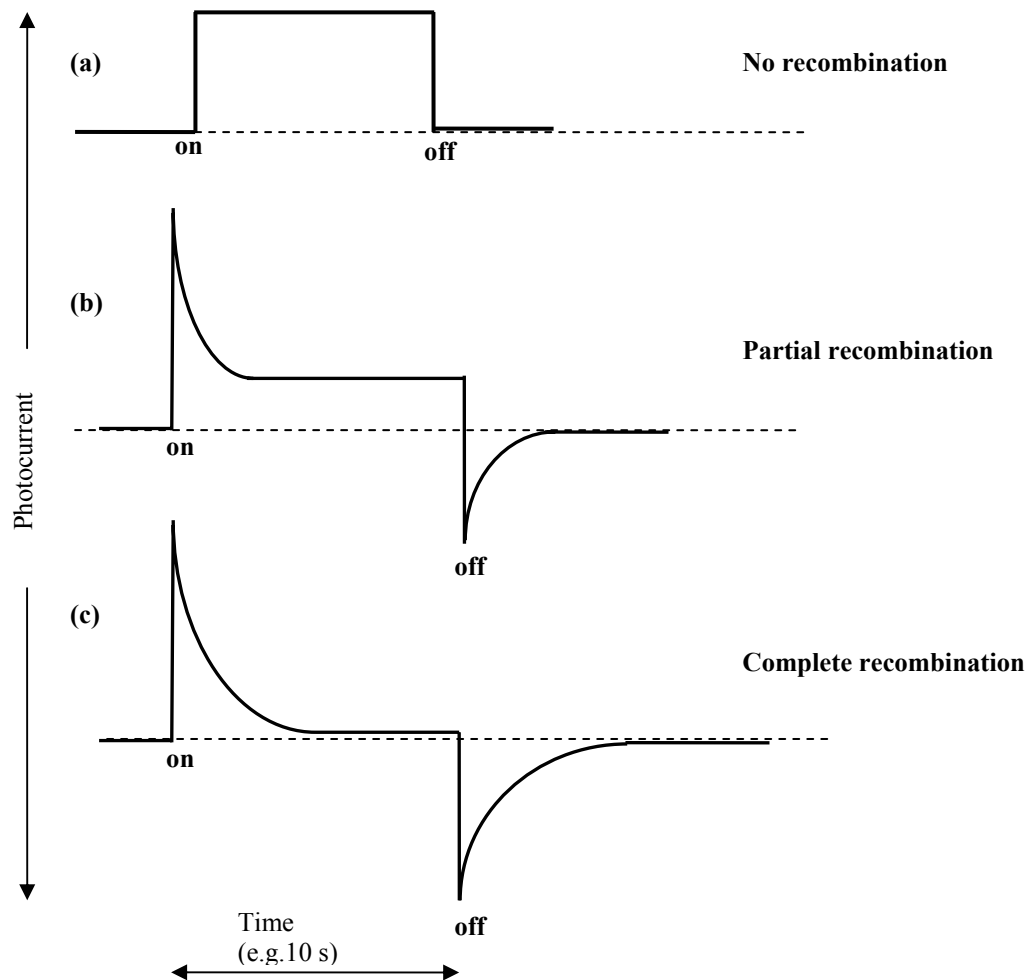


Figure 2.15. Schematic representation of possible photocurrent transients effects that may occur by illuminating a passive film by monochromatic light.

Effect of photoemission at the metal–passive film interface: Photoemission originates from the interaction of photons with the metal at the metal–passive film interface, which results in energy transfer to the metal electrons. If the energy acquired by electrons is sufficiently high, they escape from the metal, giving rise to a photoemission current.¹⁶⁷ This phenomenon is likely in metals covered only by a small film thicknesses due to the possibility of a large fraction of photons irradiating the oxide–solution interface reaching the metal–film interface.

In very thin passive films ($d_{ox} \leq 2\text{nm}$) tunnelling of excited electrons and holes through the passive film directly to the solution is possible; so call external photoemission.¹⁶⁸⁻¹⁷⁰ On the other hand, internal photoemission, the injection of photoexcited electrons (or holes) from the metal to the conduction band (or the valence band), is probable in thicker films ($d_{ox} \geq 5\text{nm}$) as the tunnelling through the film is less probable.

It is necessary to consider the possibility of external photoemission process in the case of stainless steels as the passive films can be $< 2\text{nm}$. Especially if one wishes to determine if any observed cathodic photocurrent is due to external photoemission or represent evidence for the existence of a p-type semiconducting within the passive film. It has been shown¹⁶⁷ that the photoemission current I'_{ph} is given by:

$$I'_{ph} \propto [h\nu - h\nu_0 - eV_e] \dots\dots\dots (2.49)$$

where V_e is the electrode potential, $h\nu_0$ is the photoelectric threshold at $V_e = 0$. In the absence of a diffuse double layer effect or adsorbed molecules, the above mentioned behaviour has been developed into a relationship to analyse the photoemission phenomena:

$$I'_{ph} = A'(h\nu - h\nu_0 - eV_e)^{5/2} \dots\dots\dots (2.50)$$

The above is called the “5/2 power law”; here A' is a constant. According to Equation (2.50) at a constant potential V_e , $h\nu_0$ can be obtained from a plot of $(I'_{ph})^{0.4}$ vs. $h\nu$. If the obtained photocurrent is due to the photoemission process, the threshold energy value should shift by 1eV/V .¹⁷⁰

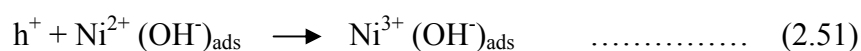
Multiple internal reflections: Multiple internal reflections of unabsorbed light at the metal–passive film–electrolyte junctions may entice interference effects in the photocurrent measured as a function of film thickness¹⁷¹ and this has to be taken into account in photocharacteristics. However, this has only be observed in certain metal passive films, such as Ta, W and Ti, where the film grows thicker on anodising, while the negligibility of this effect for constant film thicknesses was shown by Sukamoto *et al.*¹⁷²

2.5.7 Proposed research models for stainless steel passive films

The above arguments on how the semiconductive properties of amorphous oxide films vary from their crystalline counterparts have been used as the basis for a handful of models to describe passive films on stainless steels.

Di Paola^{74,75} investigated the semiconductive properties of passive films formed on different stainless steels and attributed the variation in the bandgap with potential to the simultaneous presence of iron and chromium oxides within the passive film. The bandgap values for 304L stainless steel obtained at low potentials and high potentials were assigned to the presence of chromium oxide and iron oxide, respectively. A critical potential of about 0.4 V (SCE) in neutral solutions was revealed by the

analysis of the photoelectrochemical measurements. Di Paola⁷⁴ attributed the different photocurrent responses exhibited at potentials lower or higher than 0.4 V (SCE) to a change in the relative ratio between chromium and iron oxide phases. This author further clarified that at low potentials, an enrichment of chromium takes place which is accompanied by a selective dissolution of nickel and iron. The model proposed by Di Paola⁷⁵ also suggested a role for Ni in the semiconductive properties of passive films, based on the analysis of photocurrent transients, it was suggested that surface states may arise by the trapping of holes at the surface in the nickel oxide sites according to the following reaction:



The high pitting corrosion resistance of 254SMO has been explained by Di Paola⁷⁵ with reference to the bandgap concept which shows an almost complete lack of variation in the bandgap value at different potentials suggesting the formation of a homogeneous and stable phase; probably a Cr-Fe-Ni oxide or hydroxide.

Hakiki *et al.*¹⁷³ extended Kennedy and Frees¹⁵⁵ postulation of the existence of two donor levels in polycrystalline Fe₂O₃ to the stainless steel passive film. The capacitive behaviour of the stainless steel passive film was related to a contribution from a shallow donor level very close to the conduction band and a deep donor level around 0.4eV(SCE) below the conduction band. The shallow and deep donor levels were attributed to Fe²⁺ ions located in the tetrahedral and octahedral sites, respectively.¹⁷⁴ Hakiki *et al.*^{173,174} further mentioned that the photoeffects observed for subbandgap photon energies reveal that this deep donor level behaves like a trapping electronic state situated in the space charge zone of the passive film.

The presence of chromium oxide (p-type) and iron oxide (n-type) in the internal and external layers respectively, of passive films such that a p-n heterojunction is established has been proposed by Ferreira *et al.*^{153,154,174,176} This model is shown schematically in Figure 2.16, where the flat band potentials in a borate solution (pH=9.2) for iron oxide and chromium oxide are -0.5 V(SCE) and +0.5 V(SCE) respectively Figure 2.16(a) depicts the situation at potentials below -0.5 V and Figure 2.16 (b) at potentials above 0.5 V In Figure 2.16(a) the film-electrolyte interface is in a situation of accumulation at potentials lower than -0.5 V. In Figure 2.16(b) the same interface is in a situation of depletion at potentials higher than -0.5 V. Space charges are also developed at the metal-film and film-electrolyte interfaces; these are in equilibrium with the space charges created at the heterojunction. The influence of molybdenum on the film capacitance has been proposed as being related to a decrease in the number of donors in the iron oxide layer of the film. Consequently the space charge developed at the oxide/solution interface is modified, this which influences the electrochemical potential of the stainless steel.¹⁵²

Jang *et al.*^{176,177} reported that photocurrent spectra for passive films on Fe-20Cr and Fe-20Cr-10Ni are almost the same in shape as that for the passive film on Fe, except for a lower photocurrent intensity. The photocurrent spectra were resolved into two components which originated from d-d ($E_g=2.87\text{eV}$) and p-d ($E_g=3.67\text{eV}$) electronic transitions in $\gamma\text{-Fe}_2\text{O}_3$,¹⁸⁰ suggesting that the passive films on Fe-20Cr and Fe-20Cr-10Ni are composed of Cr-substituted $\gamma\text{-Fe}_2\text{O}_3$. Jang *et al.*^{176,177} also proposed that Cr^{3+} ions in the passive film act as effective recombination sites of electron-hole pairs in the Cr-substituted $\gamma\text{-Fe}_2\text{O}_3$, thereby reducing the photocurrent intensity significantly. Thus they concluded that the semiconductive properties of Fe-20Cr are

governed by the Fe-oxide in spite of the high Cr concentration. The constancy of the E_g measured for Fe-20Cr at different film formation potentials suggested that E_g for the passive film on this material is not affected by potential dependent properties such as surface states and deep localized states in the bandgap. The model of Jang *et al.*^{176,177} further envisaged that Ni addition does not change the semiconductive properties, at least not up to a certain critical concentration between 10% and 15%. Exceeding the critical level, Fe-20Cr-15Ni alloy is comprised of two spectral components; one for the Cr-substituted γ -Fe₂O₃ and the other for NiO. Jang *et al.*^{176,177} found n-type semiconductivity and a flat band potential around -0.3V(SCE) in a buffer solution (pH=8.5) for all three alloys irrespective of the Ni content.

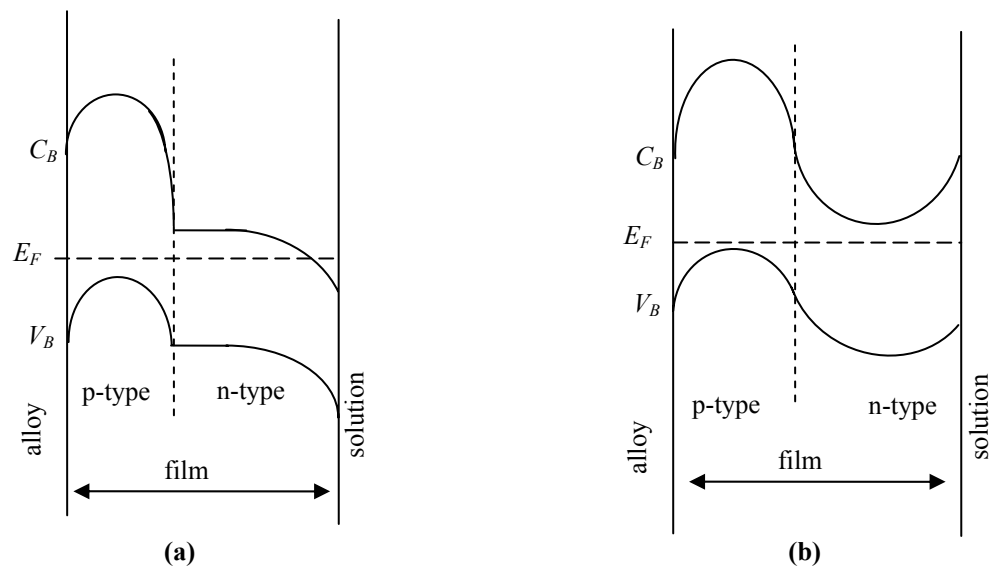


Figure 2.16. Schematic representation of the electronic structure of the passive film formed on 304L stainless steel considering the flat band potentials of the iron and chromium oxides are situated at -0.5V (SCE) and 0.5V (SCE) respectively: (a) potentials below -0.5V and (b) potentials above 0.5V.. (adapted from Reference 154)

Bojinov *et al.*¹⁷⁹ presented a model emphasising the coupling between the ionic defect structure and electronic conduction. According to their model, the passive film is represented as a heavily doped n-type semiconductor-insulator-p-type semiconductor junction. The model assumed that the local electronic conductivity is proportional to the local concentration of ionic defects. At low potentials, the positive defects injected

at the metal/film interface play the role of electron donors, while at high potentials, negative defects injected at the film/solution interface play the role of electron acceptors. There is evidence that higher quantum efficiencies are obtained if the photocurrent spectra are measured after polarising in either the at the transpassive region or the oxygen evolution region. At sufficiently high positive potentials the concentration of ionic defects and corresponding electron holes reach high enough values for the film to transform into a conductor and this enables transpassive dissolution of Cr and oxygen evolution on the film's surface.

Two different models based on combined photocurrent and capacitance measurements have been proposed by Tsuchiya and Fujimoto^{156,157} for Fe-Cr alloys depending on the solution, in which the alloys are passivated; for borate buffer and for sulphuric acid (Figure 2.17).¹⁸⁰ Passive films formed in a borate buffer solution (pH=9.2) are proposed to consist of an outer n-type chromium hydroxide layer with an E_g of 2.4eV and an inner n-type chromium oxide layer with an E_g of 3.4–3.5eV. This proposed model has three interfaces; (I) substrate alloy/inner oxide, (II) inner oxide/outer hydroxide and (III) outer hydroxide/electrolyte [Figure 2.17 (a)]. At interface (II), the two n-type semiconductor layers with different optical bandgap energies are connected as an isotype heterojunction. The model further explained that the space charge region in the oxide layer (II_a) is depleted as a positive photocurrent is always generated and increases as the potential increases, while the space charge region inside the hydroxide layer (II_b) may be under a accumulation; as an n-n junction usually forms with a depleted region on one side of the interface and an accumulation region in the other. The model clarified that the accumulated region should not affect the photocurrent behaviour as typically the width of the accumulated region is very

thin compared to the depleted region and nearly constant regardless of the applied potential. In sulphuric acid, a p-type inner oxide layer with an outer n-type hydroxide layer was proposed to be formed [Figure 2.17(a)].

Tsuchiya and Fujimoto^{156,157} further explained that in a borate buffer solution, both n-type layers are simultaneously polarized at potentials more noble than their flat band potential to generate depleted space charge regions in both. These conditions allow the migration of ionic species and electrons, which results in the continuous growth of the film. On the contrary, in acidic solutions, although the inner oxide layer grows in the initial stage of passivation, it exhibits p-type semiconductivity. This makes field assisted growth difficult, so passive film growth is terminated and passivity is achieved within a very short time period. These authors¹⁵⁶ further signified that additive elements; Mo, Nb, W, Al, Ni, Cu and Co; did not change the bandgap energy of passive films, although they did influence the carrier density. However, these investigations were carried out using sputtered films on ferritic stainless steels and may not be applicable to bulk austenitic stainless steels.

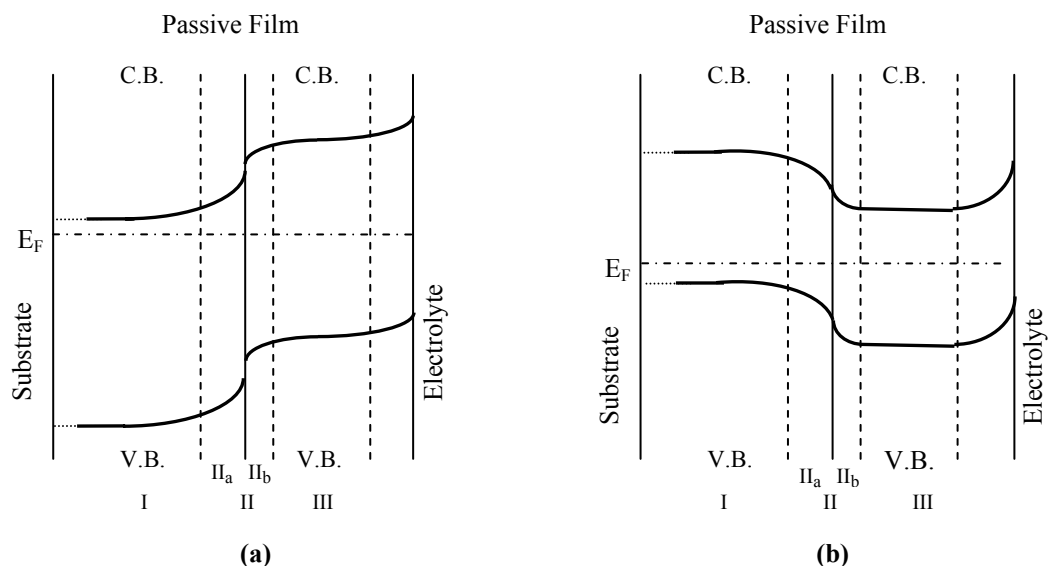


Figure 2.17. Schematic presentation of the electronic structure of passive films formed on Fe-Cr alloys: (a) in a borate buffer (b) in an acidic solution. (adapted from References 157 and 179)

References

- (1) Keir, J., *Phil. Trans.*, **80** (1790) 359.
- (2) Uhlig, H.H., “*Passivity of Metals*”, (eds. Frankenthal, R.P. and Kruger, J.), Electrochemical Society, New Jersey (1978) 1- 28.
- (3) Kelly, R.G., Scully, J.R., Shoesmith, D.E. and Buchheit, R.G., “*Electrochemical Techniques in Corrosion Science and Engineering*”, Marcel Dekker, New York (2003).
- (4) Jones, D.A., “*Principles and Prevention of Corrosion (2nd ed.)*”, Prentice-Hall, New Jersey (1996).
- (5) Fontana, M.G., “*Corrosion Engineering (2nd ed.)*”, McGraw-Hill, Singapore (1986).
- (6) Evans U.R., “*The Corrosion and Oxidation of Metals, Second Supplementary Volume*”, Edward Arnold, London (1976).
- (7) Shreir, L.L., Jarman, R.A. and Burstein, G.T., “*Corrosion, Volume I: Metal/Environmental Reactions*”, Butterworth-Heinemann, Oxford (1994).
- (8) Sato, N., “*Passivity of Metals*”, (eds. Frankenthal, R.P. and Kruger, J.), Electrochemical Society, New Jersey (1978) p 28-58.
- (9) Okamoto, G. and Shibata, T., “*Passivity of Metals*”, (ed. Frankenthal, R.P. and Kruger, J.), Electrochemical Society, New Jersey (1978) p 646-677.
- (10) Schweitzer, P.A., “*Metallic materials: physical, mechanical, and corrosion properties*”, Marcel Dekker, New York (2003).
- (11) Burstein, G.T. and Ashley, G.W., *Corrosion*, **39** (1983) 241.
- (12) Burstein, G.T. and Newman, R.C., *Electrochim. Acta*, **25** (1980) 1009.

- (13) Fromhold, Jr. A.T., “*Theory of Metal Oxidation, Volume 1: Fundamentals*”, North-Holland, New York (1976), “*Theory of Metal Oxidation, Volume 2: Space Charge*”, North-Holland Publishers, New York (1980).
- (14) Günterschulze, A. and Betz, H, *Z. Physik*, **92** (1934) 367.
- (15) Young, L., “*Anodic Oxide Films*”, Academic Press, London (1961).
- (16) Cabrera, N. and Mott, N.F., *Rep. Prog. Phys.*, **12** (1948/1949) 163.
- (17) Dewald, J.F., *J. Phys. Chem. Solids*, **2** (1957) 55.
- (18) Sato, N. and Cohen, M., *J. Electrochem. Soc.*, **111** (1964) 512.
- (19) Sato, N. and Cohen, M., *J. Electrochem. Soc.*, **111** (1964) 519.
- (20) Ghez, R., *J. Chem. Phys.*, **58** (1973) 1838.
- (21) Burstein, G.T. and Davenport, A.J., *J. Electrochem. Soc.*, **136** (1989) 936.
- (22) Davenport, A.J. and Lee, B.K., *201st Electrochemical Society Proceedings*, Philadelphia, USA (2001) abstract 286.
- (23) Davenport, A.J., Sansone, M., Bardwell, J.A., Aldykiewicz, A.J., Taube, M. and Vitus, C.M., *J. Electrochem. Soc.*, **141** (1994) L6.
- (24) Davenport, A.J. and Burstein, G.T., *J. Electrochem. Soc.*, **137** (1990) 1496.
- (25) Macdonald, D.D., *J. Electrochem. Soc.*, **139** (1992) 3434.
- (26) Chao, C.Y., Lin, L.F. and Macdonald, D.D., *J. Electrochem. Soc.*, **128** (1981) 1187.
- (27) Chao, C.Y., Lin, L.F. and Macdonald, D.D., *J. Electrochem. Soc.*, **128** (1981) 1194
- (28) Zhang, L. and Macdonald, D.D., *Electrochim. Acta*, **43** (1998) 679.
- (29) Bojinov, M., Kanazirski, I. and Girginov, A., *Electrochim. Acta*, **41** (1996) 2695.
- (30) Bonjinov, M., *Electrochim. Acta*, **42** (1997) 3489.

- (31) Bonjinov, M., Fabricius, G., Laitinen, T., Saario, T. and Sundholm, G., *Electrochim. Acta*, **44** (1998) 247.
- (32) Olefjord, I. and Jelvestam, U., *J. Electrochem. Soc.*, **132** (1985) 2854.
- (33) Sugimoto, K. and Sadawa, Y., *Corros. Sci.*, **17** (1977) 425.
- (34) Maurice, V., Yang, W.P. and Marcus, P., *J. Electrochem. Soc.*, **145** (1998) 909.
- (35) Toney, M.F., Davenport, A.J., Oblonsky, L.J., Ryan, M.P. and Vitus, M., *Phys. Rev. Lett.*, **79** (1997) 4282.
- (36) Olsson, C.-O.A. and Landolt, D., *Electrochim. Acta*, **48** (2003) 1093.
- (37) Ramasubramanian, N., Preocanin, N. and Davidson, R.D., *J. Electrochem. Soc.*, **132** (1985) 793.
- (38) Frankenthal, R.P., *J. Electrochem. Soc.*, **114** (1967) 542, 580.
- (39) Castle, J.E. and Clayton, C.R., *Corros. Sci.*, **17** (1977) 7.
- (40) Castle, J.E. and Qiu, J.H., *Corros. Sci.*, **29** (1989) 591.
- (41) Castle, J.E. and Qiu, J.H., *Corros. Sci.*, **29** (1989) 605.
- (42) Uhlig, H.H., *Joint Japan–USA Seminar on Passivity and its Breakdown on Iron and Iron Base Alloys*, National Association of Corrosion Engineers, Houston (1976) 19.
- (43) Yaniv, A.E., Lumsden, J.B. and Staehle, R.W., *J. Electrochem. Soc.*, **124** (1977) 490.
- (44) Goetz, R. and Landolt, D., *Electrochim. Acta.*, **29** (1984) 667
- (45) Yaniv, A.E., Lumsden, J.B. and Staehle, R.W., *J. Electrochem. Soc.*, **124** (1977) 490.
- (46) Galvele, J.R., Lumsden, J.B. and Staehle, R.W., *J. Electrochem. Soc.*, **125** (1978) 1204.

- (47) Schneider, A., Kuron, D., Hofmann, S. and Kirshheim, R., *Corros. Sci.*, **31** (1990) 191.
- (48) Jargelius-Pettersson, R. F. A., and Pound, B. G., *J. Electrochem. Soc.*, **145** (1998) 1462
- (49) Hashimoto, K., Asami, K. and Teramoto, K., *Corros. Sci.*, **19** (1979) 3.
- (50) Asami, K. and Hashimoto, K., *Corros. Sci.*, **17** (1977) 713.
- (51) Asami, K., Hashimoto, K. and Shimodaira, S., *Corros. Sci.*, **18** (1978) 151.
- (52) Clayton, C.R. and Lu, Y.C., *J. Electrochem. Soc.*, **133** (1986) 2465.
- (53) Elbiache, A. and Marcus, P., *Corros. Sci.*, **33** (1992) 261.
- (54) Lorang, G., Belo, M.Da.C., Simões, A.M.P. and Ferreira, M.G.S., *J. Electrochem. Soc.*, **141** (1994) 3347.
- (55) Schumuki, P., Virtanen, S., Isaacs, H.S., Ryan, M.P., Davenport, A.J., Böhni, H. and Stenberg, T., *J. Electrochem. Soc.*, **145** (1998) 791.
- (56) Oblonsky, L.J., Ryan, M.P. and Isaacs, H.S., *J. Electrochem. Soc.*, **145** (1998) 1922.
- (57) Qvarfort, R., *Corros. Sci.*, **40** (1998) 215.
- (58) Betova, I., Bojinov, M., Englund, A., Fabricius, G., Laitinen, T., Mäkela, K., Saario, T. and Sundholm, G., *Electrochim. Acta*, **46** (2001) 3627.
- (59) Kaneko, M. and Isaacs, H.S., *Corros. Sci.*, **44** (2002) 1825.
- (60) Bastidas, J.M., Torres, C.L., Cano, E. and Polo, J.L., *Corros. Sci.*, **44** (2002) 625.
- (61) Keller, P. and Strehblow, H.H., *Corros. Sci.*, **46** (2004) 1939.
- (62) McCarty, K.F. and Boehme, D.R., *J. Solid State Chem.*, **79** (1989) 19.
- (63) Thanos, I.C.G., *Electrochim. Acta*, **31** (1986) 1585.
- (64) Zeng, Z., Natesan, K. and Grimsditch, M., *Corrosion*, **60** (2004) 632.

- (65) Boucherit, N., Goff, A.H. and Joiret, S., *Corrosion*, **48** (1992) 569.
- (66) Bonjinov, M., Fabricius, G., Laitinen, Mäkelä, K., Sundhlo, G. and Saario, T., *Electrochim. Acta*, **46** (2001) 1339.
- (67) Bonjinov, M., Fabricius, G., Laitinen, T. and T., Saario, *Electrochim. Acta*, **44** (1998) 4331.
- (68) Hara, N. and Sugimoto, K., *J. Electrochem. Soc.*, **126** (1979) 1328
- (69) Bonjinov, Betova, I., M., Fabricius, G., Laitinen, T., Raicheff, R. and Saario, T., *Corros. Sci.*, **41** (1999) 1557.
- (70) Hamme, D., Ogle, K., Olsson, C.O.A., Weber, S. and Landolt, D., *Corros. Sci.*, **44** (2002) 1443.
- (71) Betova, I., Bojinov, M., Laitinen, T., Mäkelä, K., Pohjanne, P. and Saario, T., *Corros. Sci.*, **44** (2002) 2675.
- (72) Betova, I., Bojinov, M., Laitinen, T., Mäkelä, K., Pohjanne, P. and Saario, T., *Corros. Sci.*, **44** (2002) 2699.
- (73) Kim, J.S., Peelen, W.H.A., Hemmes, K. and Makkus, R.C., *Corros. Sci.*, **44** (2002) 635.
- (74) Di Paola, A., *Corros. Sci.*, **31** (1990) 739.
- (75) Di Paola, A., Di Quarto, F. and Sunseri, C., *Corros. Sci.*, **26** (1986) 935.
- (76) Leckie, H.P. and Uhlig, H.H., *J. Electrochem. Soc.*, **113** (1966) 1245.
- (77) Frankel, G.S., *J. Electrochem. Soc.*, **145** (1998) 2186.
- (78) Webb, E.G. and Alkire, C., *J. Electrochem. Soc.*, **149** (2002) B272.
- (79) Webb, E.G. and Alkire, C., *J. Electrochem. Soc.*, **149** (2002) B280.
- (80) Lott, S.E. and Alkire, R.C., *J. Electrochem. Soc.*, **136** (1989) 973.
- (81) Riley, M., Wells, D.B. and Williams, D.E., *Corros. Sci.*, **32** (1991) 1307.

- (82) Williams, D.E., Mohiuddin., T.F. and Zhu, Y.Y., *J. Electrochem. Soc.*, 145 (1998) 2664.
- (83) Brossia, C.S. and Kelly, R.G., *Corros. Sci.*, **40** (1998) 1851.
- (84) Suter, T., Peter, T. and Böhni, H., *Mater. Sci. For.*, **192-194** (1995) 25.
- (85) Kucernak, A.R.J., Peat, R. and Williams, D.E., *J. Electrochem. Soc.*, **139** (1992) 2337.
- (86) Baker, M.A. and Castle, J.E., *Corros. Sci.*, **34** (1997) 667.
- (87) Ryan, M.P., Williams, D.E., Chater, J., Hutton, B.M. and McPhail, D.S., *Nature*, **415** (2002) 770.
- (88) Meng, Q., Frnakel, G.S., Colijin, H.O. and Goss, S.H., *Corros. Sci.*, **60** (2004) 346.
- (89) Webb, E.G., Suter, T. and Alkire, R.C., *J. Electrochem. Soc.*, **148** (2001) B 186.
- (90) Eklund, G.S., *J. Electrochem. Soc.*, **121** (1974) 467.
- (91) Dowling, N.J.E., Duret – Thual, C., Auclair, G. Audour, J.P. and Combrade, P., *Corros. Sci.*, **51** (1995) 343.
- (92) Suter, T., Webb, E.G., Böhni, H. and Alkire, R.C., *J. Electrochem. Soc.*, **148** (2001) B 174.
- (93) Williams, D.E., Westcott. C. and Fleischmann, M., *J. Electrochem. Soc.*, **132** (1985) 1796.
- (94) Williams, D.E., Westcott. C. and Fleischmann, M., *J. Electrochem. Soc.*, **132** (1985) 1804.
- (95) Suter, T. and Böhni, H., *Electrochim. Acta*, **42** (1995) 3275.
- (96) Ke, R. and Alkire, R., *J. Electrochem. Soc.*, **139** (1992) 1573.
- (97) Ke, R. and Alkire, R., *J. Electrochem. Soc.*, **142** (1995) 4056.

- (98) Stewart, J. and Williams, D.E., *Corros. Sci.*, **33** (1992) 475.
- (99) Pistorius, P.C. and Burstein, G.T., *Corros. Sci.*, **36** (1994) 525.
- (100) Lin, L.F., Chao, C.Y. and Macdonald, D.D., *J. Electrochem. Soc.*, **128** (1981) 1194.
- (101) Wang, J.H., Su, C.C. and Smialowska, Z.S., *Corrosion*, **44** (1988) 732.
- (102) Ernst, P. and Newman, R.C., *Corros. Sci.*, **44** (2002) 943.
- (103) Beck, T.R. and Alkire, R.C., *J. Electrochem. Soc.*, **126** (1979) 1662.
- (104) Laylock, N.J. and Newman, R.C., *Corros. Sci.*, **39** (1997) 1771.
- (105) Ernst, P. and Newman, R.C., *Corros. Sci.*, **44** (2002) 927.
- (106) Newman, R.C., *Corrosion*, **57** (2001) 1030.
- (107) Isaacs, H.S. and Newman, R.C., “*Corrosion Chemistry within Pits, Crevices and Cracks*”, (ed. Turnbull, A.), H.M.S.O, London, (1984) 45–60.
- (108) Galvele, J.R., *J. Electrochem. Soc.*, **123** (1976) 464.
- (109) Burstein, G.T. and Vines, S.P., *J. Electrochem. Soc.*, **148** (2001) B504.
- (110) Zuo, Y., Wang, H. and Xiong, J., *Corros. Sci.*, **44** (2002) 25.
- (111) Park, J.O., Suter, T. and Böhni, H., *Corrosion*, **59** (2003) 59.
- (112) Sato, N., *Electrochim. Acta*, **16** (1971) 1683.
- (113) Burstein, G.T., Saaki, C.L.K., Souto, R.M. and Vines, S.P., *15th International Corrosion, Congress*, Granada, Spain (2002).
- (114) Burstein, G.T., Liu, C., Souto, R.M. and Vines, S.P., *Corros. Eng. Sci. Tech.*, **39** (2004) 25.
- (115) Di Quarto, F. and Santamaria, M., *Corros. Eng. Sci. Tech.*, **39** (2004) 71.
- (116) Smialowska, Z.S., *Corros. Sci.*, **44** (2002) 1143.
- (117) Becquerel, E., *C. R. Hebl. Séances Acad. Sc.*, **9** (1839) 561.

- (118) Di Quarto, F., Piazza, S., Santamaria, M. and Sunseri, C., “*Handbook of Thin Film Materials, Volume 2: Characterization and Spectroscopy of Thin Films*”, (ed. Nalwa, H.S.), Academic Press, San Diego (2002) 373–414.
- (119) Southampton Electrochemistry Group, “*Instrumental Methods in Electrochemistry*”, Ellis Horwood, Chichester (1985).
- (120) Gärtner, W.W., *Phys. Rev.*, **116** (1959) 84.
- (121) Butler, M.A., *J. Appl. Phys.*, **48** (1977) 4292.
- (122) Mott, N.F. and Davis, E.A., “*Electronic Processes in Non-crystalline Materials (2nd ed.)*”, Clarendon Press, Oxford (1979).
- (123) Di Quarto, F., Piazza, S. and Sunseri, C., *Mater. Sci. For.*, **192–194** (1995) 633.
- (124) Wilson, R.H., *J. Appl. Phys.*, **48** (1977) 4292.
- (125) Reichman, J., *Appl. Phys. Lett.*, **36** (1980) 574.
- (126) Albery, W.J. and Bartlett, N., *J. Electrochem. Soc.*, **128** (1981) 1493.
- (127) Guibaly, F.E. and Colbow, K., *J. Appl. Phys.*, **53** (1982) 1737.
- (128) Reiss, H., *J. Electrochem. Soc.*, **125** (1978) 937.
- (129) Laser, D. and Bard, A.J., *J. Electrochem. Soc.*, **123** (1976) 1838.
- (130) Fonash, S., Rose, M., Corby, K. and Jordan, J., “*Photoelectrochemistry: Fundamental Processes and Measurement Techniques*”, Electrochemical Society, New Jersey (1982).
- (131) Morrison, S.R., “*Electrochemistry at Semiconductor and Oxidised Metal Electrodes*”, Plenum Press, New York (1980).
- (132) Dewald, J.F., *J. Phys. Chem. Solids*, **14** (1960) 155.
- (133) Gomes, W.P. and Cardon, F., *Prog. Surf. Sci.*, **12** (1982) 155
- (134) Khan, S.U.M. and Schmickler, W., *J. Electroanal. Chem.*, **108** (1980) 329.

- (135) Gerischer, H. and McIntyre, R., *J. Chem. Phys.*, **83** (1985) 1363.
- (136) Cooper, G., Tunner, J.A. and Nozik, A.J., *J. Electroanal. Chem.*, **129** (1982) 1973.
- (137) Finklea, H.O., *J. Electroanal. Chem.*, **129** (1982) 2003.
- (138) Gerischer, H., *Corros. Sci.*, **31** (1990) 81.
- (139) Schultze, J.W. and Lohrengel, M.M., *Electrochim. Acta*, **45** (2000) 2499.
- (140) Tauc, J., “*Amorphous and Liquid Semiconductors*”, Plenum Publishers, London (1974).
- (141) Cohen, M.H., Fritzsche, H. and Ovshinsky, S.R., *Phys. Rev. Lett.*, **22** (1969) 1065.
- (142) Di. Quarto, F., Piazza, S. and Suneri, C., *Electrochim. Acta*, **35** (1990) 99.
- (143) Cohen, J.D. and Lang, D.V., *Phys. Rev. B*, **25** (1981) 15.
- (144) Peterson, M.W. and Parkinson, B.A., *J. Electrochem. Soc.*, **133** (1986) 2538.
- (145) Di Paola, A., *Electrochim. Acta*, **34** (1989) 203.
- (146) Young, L., *Trans. Far. Soc.*, **51** (1955) 1250.
- (147) Wood, G.C. and Pearson, C., *Nature*, **208** (1965) 547.
- (148) Cahan, B.D. and Chen, C-T., *J. Electrochem. Soc.*, **129** (1982) 921.
- (149) Hakiki, N.E., Boudin, S., Rondot, B. and Belo, M.D.C., *Corros. Sci.*, **37** (1995) 1809.
- (150) Stimming, U. and Schultze, J.W., *Ber. Bunsenges. Phys. Chem.*, **80** (1976) 129.
- (151) Gevers, M. and Du Pre, K., *Trans. Faraday Soc.*, **42** (1946) 47.
- (152) Montemor, M.F., Simões, A.M.P., Ferreira, M.G.S. and Belo, M.D.C., *Corros. Sci.*, **41** (1999) 17.

- (153) Ferreira, M.G.S., Hakiki, N.E., Goodlet, G., Faty, S., Simões, A.M.P. and Belo, M.D.C., *Electrochim. Acta*, **46** (2001) 3767.
- (154) Ferreira, M.G.S., Belo, M.D.C., Hakiki, N.E., Goodlet, G., Montemor, M.F., and Simões, A.M.P., *J. Braz. Chem. Soc.*, **13** (2002) 433.
- (155) Kennedy, J.H. and Frees, Jr. W., *J. Electrochem. Soc.*, **125** (1977) 723.
- (156) Tsuchiya, H. and Fujimoto, S., *13th Asian-Pacific Corrosion Control Conference*, Japan (2003) paper F-01.
- (157) Tsuchiya, H., Fujimoto, S. and Shibata, T., *J. Electrochem. Soc.*, **151** (2004) B39.
- (158) Blackwood, D.J. and Peter, L.M., *Electrochim. Acta*, **35** (1990) 1073.
- (159) Piazza, S., Sunseri, C. and Di Quarto, F., *J. Electroanal. Chem.*, **293** (1990) 69.
- (160) Martienssen, W., *J. Phys. Chem. Solids.*, **2** (1957) 257.
- (161) Santamaria, M., Huerta, D., Piazza, S., Sunseri, C. and Di Quarto, F., *J. Electrochem. Soc.*, **147** (2000) 1366.
- (162) Peter, L.M., *Chem. Rev.*, **90** (1990) 753.
- (163) Pai, D.M. and Enck, R.C., *Phys. Rev. B.*, **11** (1975) 5163.
- (164) Abrates, L.M. and Peter, L.M., *J. Electroanal. Chem.*, **150** (1983) 593.
- (165) Li, J. and Peter, L.M., *J. Electroanal. Chem.*, **193** (1985) 27.
- (166) Li, J. and Peter, L.M., *J. Electroanal. Chem.*, **199** (1986) 1.
- (167) Gurevich, Y.Y., Pleskov, Y.V. and Rotenberg, Z.A., “*Photoelectrochemistry*”, Consultants Bureau, New York (1980).
- (168) Piazza, S., Splendore, A., Di Paola, A., Sunseri, C. and Di Quarto, F., *J. Electrochem. Soc.*, **140** (1993) 3146.
- (169) Sunseri, C., Di Quarto, F. and Piazza, S., *Mater. Sci. Forum*, **185-188** (1995) 435.

- (170) Di Quarto, F., Piazza, S., Sunseri, C., Yang, M. and Cai, S-M., *Electrochim. Acta*, **41** (1996) 2511.
- (171) Di Quarto, F., Piazza, S. and Sunseri, C., *Corros. Sci.*, **31** (1990) 267.
- (172) Sukamoto, J.P.H., Smyrl, W.H., McMillan, C.S. and Kozlowski, M.R., *J. Electrochem. Soc.*, **139** (1992) 1033.
- (173) Hakiki, N.E. and Belo, M.D.C., *J. Electrochem. Soc.*, **143** (1996) 3088.
- (174) Hakiki, N.E., Belo, M.D.C., Simões, A.M.P. and Ferreira, M.G.S., *J. Electrochem. Soc.*, **145** (1998) 3821.
- (175) Simões, A.M.P., Ferreira, M.G.S., Rondot, B. and Belo, M.D.C., *J. Electrochem. Soc.*, **137** (1990) 82.
- (176) Jang, H.J., Cho, E.A. and Kwon, H.S., *13th Asian-Pacific Corrosion Control Conference*, Japan (2003) paper PL-7.
- (177) Cho, E.A., Kwon, H.S. and Macdonald, D.D., *Electrochim. Acta*, **47** (2002) 1661.
- (178) Kim, J.S., Cho, E.A. and Kwon, H.S., *Corros. Sci.*, **43** (2001) 1403.
- (179) Bojinov, M., Fabricius, G., Laitinen, T., Mäkelä, K., Saario, T. and Sundholm., *Electrochim. Acta*, **45** (2000) 2029.
- (180) Tsuchiya, H., Fujimoto, S., Chihara, O. and Shibata, T., *Electrochim. Acta*, **47** (2002) 4357.

CHAPTER 3 EXPERIMENTAL PROCEDURES

All the experiments have been grouped under five categories: (1) electrochemical experimentations (cyclic sweep, potentiostatic and electrochemical impedance spectroscopy); (2) photocurrent experiments; (3) *in situ* Raman spectroscopy; (4) photocurrent transient experiments and (5) *in situ* atomic force microscopy (AFM).

A conventional three electrode system (WE-working electrode, CE-counter electrode and RE-reference electrode) was used for almost all the experiments, although the electrochemical cell design was changed depending on the experimental category. A saturated calomel electrode (SCE); Hg/Hg₂Cl₂/Sat.KCl [+241 mV vs. standard hydrogen electrode (SHE)] system, was used in all cases except for *in situ* AFM studies where Ag/AgCl/0.028M NaCl (+322mV vs. SHE) was used. However, all potential values and figures shown in this thesis have been converted to SCE. A platinum wire or a mesh (2cm x 2 cm) connected to a wire was used as the counter electrode.

The compositions of the different stainless steels are as tabulated in Table 2.1. Commercial AISI 304L and AISI 316L were from *Advent Research Materials*, AISI 316LVM from *Sandvik* and AISI 254 SMO from *Sumitomo Metals*. The AISI 304L high sulphur research sample was produced by the Sheffield University advisory centre. Sample preparation and the design of the working electrode design were different according to the experiment.

Electrolytes were either 0.1M borate solution (pH=9.2, prepared from $\text{Na}_2\text{B}_4\text{O}_7 \cdot 10\text{H}_2\text{O}$) or different concentrations of NaCl solutions. These were prepared in de-ionized water using reagent grade chemicals. Before any experiment was carried out, the electrolyte was deoxygenated with highly purified nitrogen gas for one hour. The pH value was measured before and after each experiment to make sure it remained consistent throughout the experiment. Unless otherwise stated the photocurrent spectroscopy and capacitive measurements were made on the reverse sweep, that is after the passive film had been grown on the forward sweep to the desired potential. This procedure was used in order to minimise the influence of the film thickness changing during the course of the experiment

Each category of experiment is detailed in the next section describing the cell design, sample preparation and experimental setup.

3.1 Electrochemical experiments

3.1.1 Electrochemical cell

The cell design for all electrochemical experiments; cyclic sweep, potentiostatic and electrochemical impedance spectroscopy (EIS) is shown in Figure 3.01. However, on the occasions, where N_2 gas purging was necessary throughout the experiment for deaeration, the cell that was designed for photocurrent experiments was used (see Section 3.2)

3.1.2 Sample preparation and working electrode design

Rod materials (AISI 304L, 316L and 316LVM) having 6mm diameter were cut into the appropriate lengths according to the working electrode design. The plate

materials, AISI 254 SMO and 304L high sulphur, were cut into rectangular shapes having approximately the same cross sectional area of cylindrical samples. One side of each sample was drilled and tapped to screw a threaded connector. This settlement was either embedded in a PTFE tubing sealed with an O-ring placed at the edge (Figure 3.02 a.) or cemented in a glass tube held using non-conducting epoxy [Figure 3.02(b)]. All specimens were ground and polished with 600 and 1200 grit SiC paper. Specimens used for SEM, photocurrent spectroscopy, *in situ* Raman spectroscopy or *in situ* AFM imaging were further polished with alumina polishing powder in 15, 12, 5, 3, 1 and 0.1 micron sizes, successively. Samples were then cleaned thoroughly in deionised water and degreased in pure ethanol. Specimens designed to be inserted in the PTFE tubing were cleaned ultrasonically. Samples used for microscopical examination were cleaned in deionised water between each successive polishing step and finally in deionised water, acetone, methanol and ethanol (ultrasonically), respectively to avoid any contamination.

3.1.3 Cyclic voltammetry

Cyclic voltammetry is used to examine the current characteristics of the sample under a voltage cycle. The growth of the stainless steel films and their pitting behaviour were studied. The start and reverse (or end) potentials, sweep rate and the number of cycles were the main parameters controlled. To study the film growth in the borate solution, the sample was swept between -1.2 V (SCE) and 1.2V (SCE) usually at a rate of 10 mV / min. To examine the pitting behaviour samples were swept forward until a current limit of $100 \mu\text{A} / \text{cm}^2$ was measured, which was taken to represent the formation of a stable pit. An ACM field machine DSP together with its software from ACM instruments was used. This instrument was used for potentiostatic (except for

Raman and photocurrent experiments) and EIS experiments. A schematic representation of the experimental setup used is shown in Figure 3.03.

3.1.4 Potentiostatic

The potentiostatic technique was used to study current–time relationships, while polarising the sample at a constant potential. Metastable pitting current transients were measured accordingly by this technique.

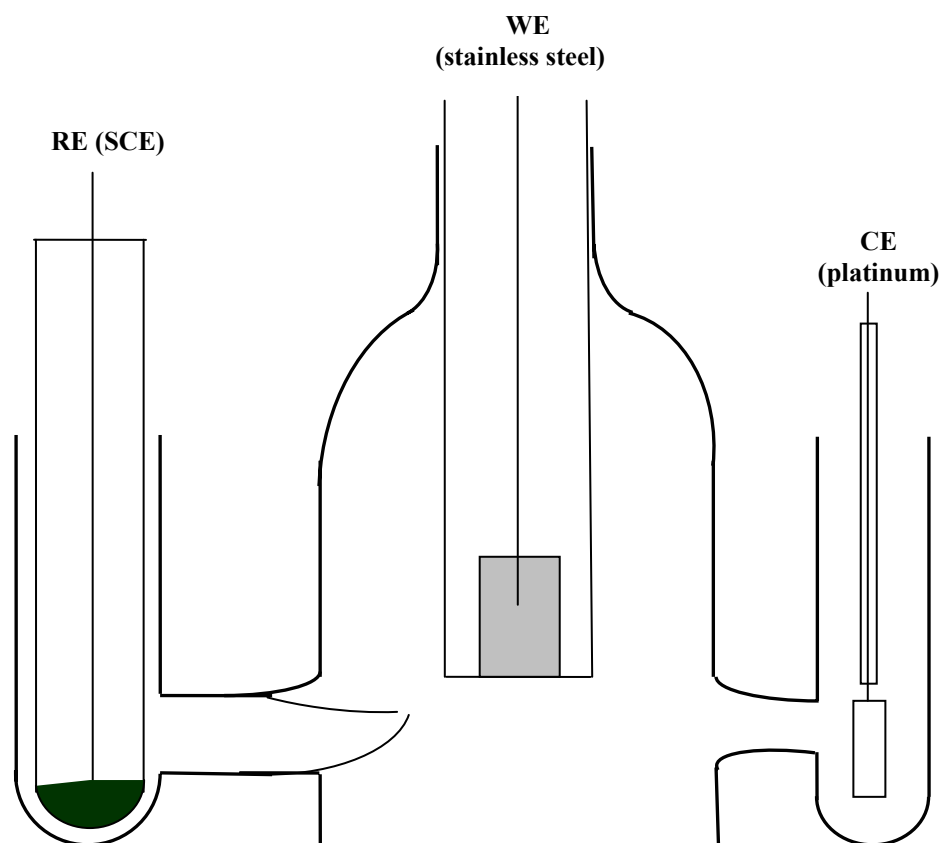


Figure 3.01. Schematic of three component electrochemical cell.

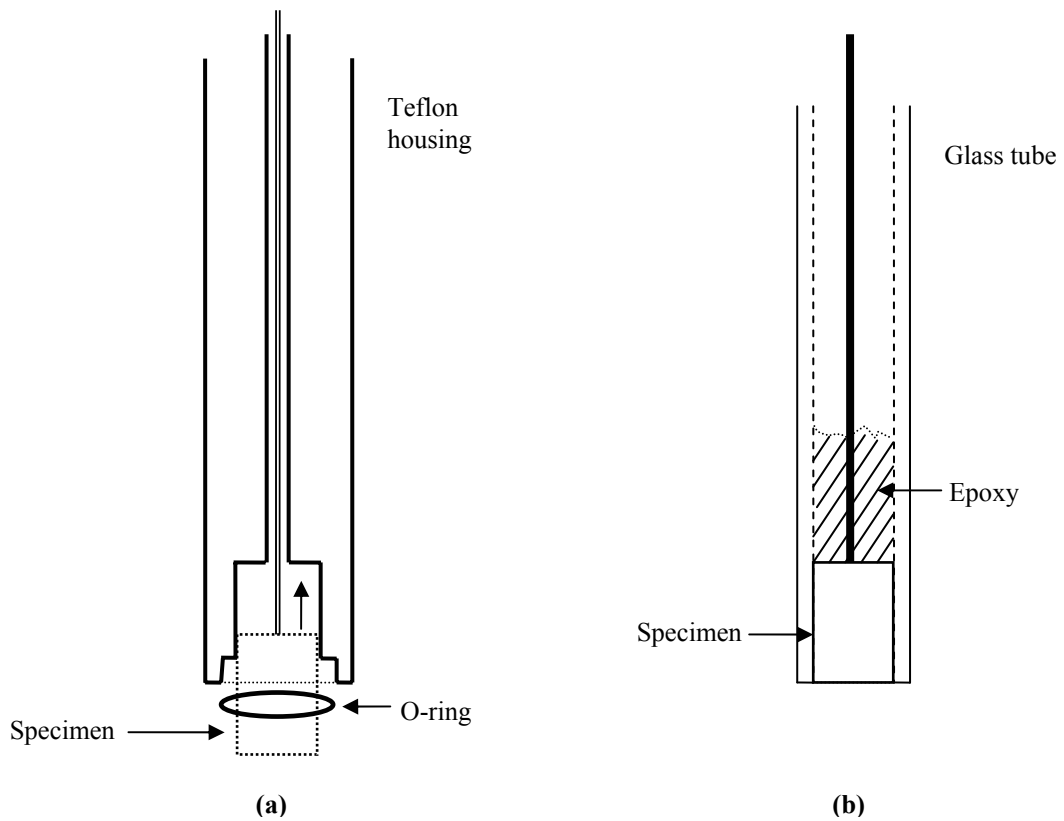


Figure 3.02. Working electrode design for the electrochemical experiments: (a) PTFE tube; (b) glass tube.

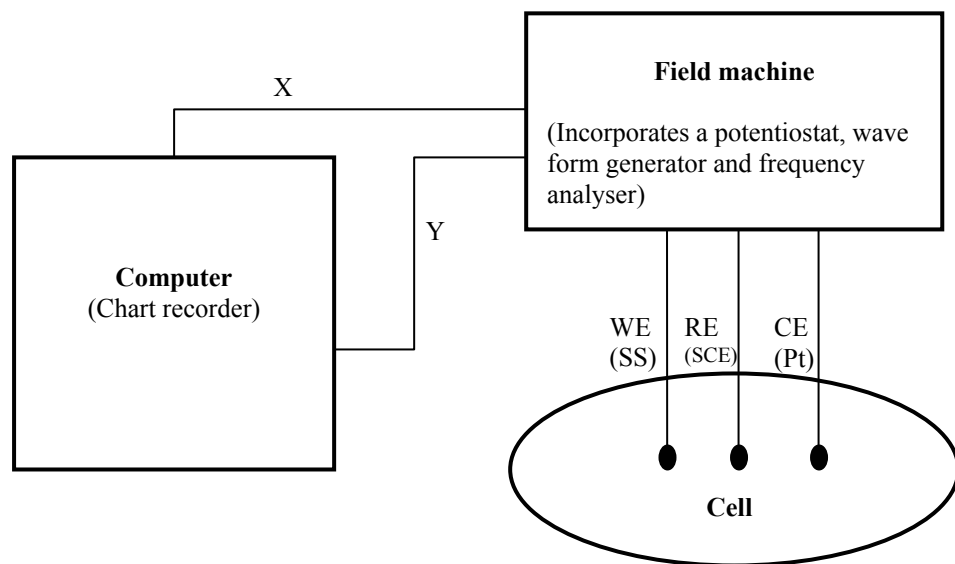


Figure 3.03. Schematic representation of the experimental setup for potentiostatic, cyclic sweep and EIS experiments.

3.1.5 Electrochemical Impedance Spectroscopy (EIS)

The EIS technique was used to obtain capacitive measurements of the passive film. First the film was grown potentiodynamically from -900mV up to 800mV(SCE) at a rate of 10 mV/min. The impedance measurements were then recorded on the reverse sweep at each 100mV successive interval (or 50mV in some cases) between 800mV(SCE) and -900mV(SCE). At each interval potential the sample was held for 10 minutes prior to initiating the impedance measurements. The frequency range used was from 1Hz to 10kHz, unless otherwise stated and the signal was perturbed by an RMS amplitude of ± 10 mV. The impedance data were displayed in the form of Nyquist plot, that is the real against imaginary impedance.

Based on the simple circuit model, which is shown in Figure 3.04(a),^{1,2} the capacitance (C_{OX})–impedance relationship of an oxide film is given by:

$$C_{OX} = \frac{Z''}{[(Z'')^2 + (Z' - Z_U)^2] \omega} \quad \dots\dots\dots (3.01)$$

Here Z'' and Z' are the imaginary and real parts of the impedance, respectively, Z_U is for the uncompensated solution resistance and ω is the angular frequency. It was assumed that the double layer impedances were negligible compared to that of the oxide film. The relevant Nyquist plot is schematically shown in Figure 3.04(b).

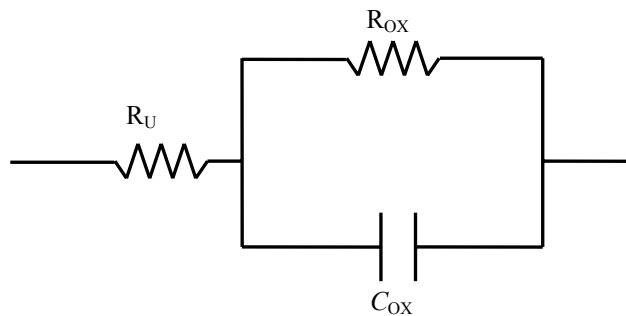


Figure 3.04 (a). Representation of the equivalent circuit model for the oxide film.

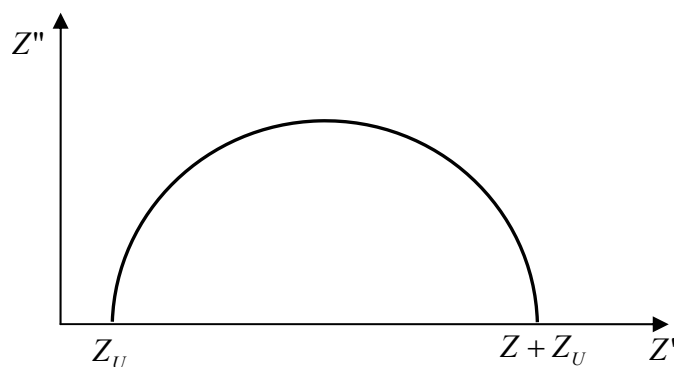


Figure 3.04 (b). The schematic Nyquist plot for the circuit shown in Figure 3.05(a).

3.2 Photocurrent spectroscopy

The photoelectrochemical technique was mainly used to obtain information regarding the electronic properties of the passive film. At the same time, due to the recognition that very thin films constitute their own phase with their specific properties, photoelectrochemistry has proved a valuable *in situ* method for characterising the composition of passive films of metals and alloys. Owing to the risk of changing the

structure and composition of very thin passive films posed by studying with *ex situ* methods, photocurrent spectroscopy and other *in situ* techniques have proven their advantage. However, as with any other technique, photocurrent spectroscopy also has some limitations based on common aspects.³⁻⁵

- Only able to study passive films having semiconducting or insulating properties.
- Requirement of complementary investigation by other techniques on the structure and the chemical composition of the passive film.

Photoelectrochemical measurements were performed by using a 300W xenon lamp and a monochromator. The photocurrents were generated by focusing the light with a fused silica lens through the quartz window of the electrochemical cell [Figures 3.05(a) and (b)] onto the working electrode. The lock-in amplifier technique was used to separate the photocurrent from the passive current by chopping the light at a constant frequency of 29Hz. The measuring procedure was that first the film was grown potentiodynamically at a rate of 10 mV / min from -900mV (SCE) up to 800mV (SCE). Then photocurrent spectra were obtained as the potential was brought back in the negative direction, the potential being held constant during the course of each measurement. The wavelength of the light was changed in steps of 10nm. The instrumentation setup is schematically shown in Figure 3.06. *Oriel Cornerstone ¼ M* monochromator was used with a 1.5mm slit width.

In order to enhance the accuracy, the photocurrent was corrected for the output of the lamp and the efficiency of the monochromator by using a calibrated photodiode (type S1227-1010BQ). Calibration was performed before and after every set of

experiments. A calibration curve for the photodiode (photosensitivity) is shown in Figure 3.07.

The photocurrent conversion efficiency, ϕ_e can be calculated using:²

$$\phi_e = (\textit{photosensitivity}) \times \left(\frac{h\nu}{\lambda} \right) \dots\dots\dots (3.02)$$

Figure 3.09 shows the relevant spectrum. Consequently the photocurrent conversion efficiency of the oxide film, ϕ_{OX} can be found from:

$$\phi_{OX} = \frac{I_{ph}}{I_{PD}} \times \phi_e \dots\dots\dots (3.03)$$

where I_{ph} and I_{PD} are the photocurrents observed from the oxide and the photodiode respectively.

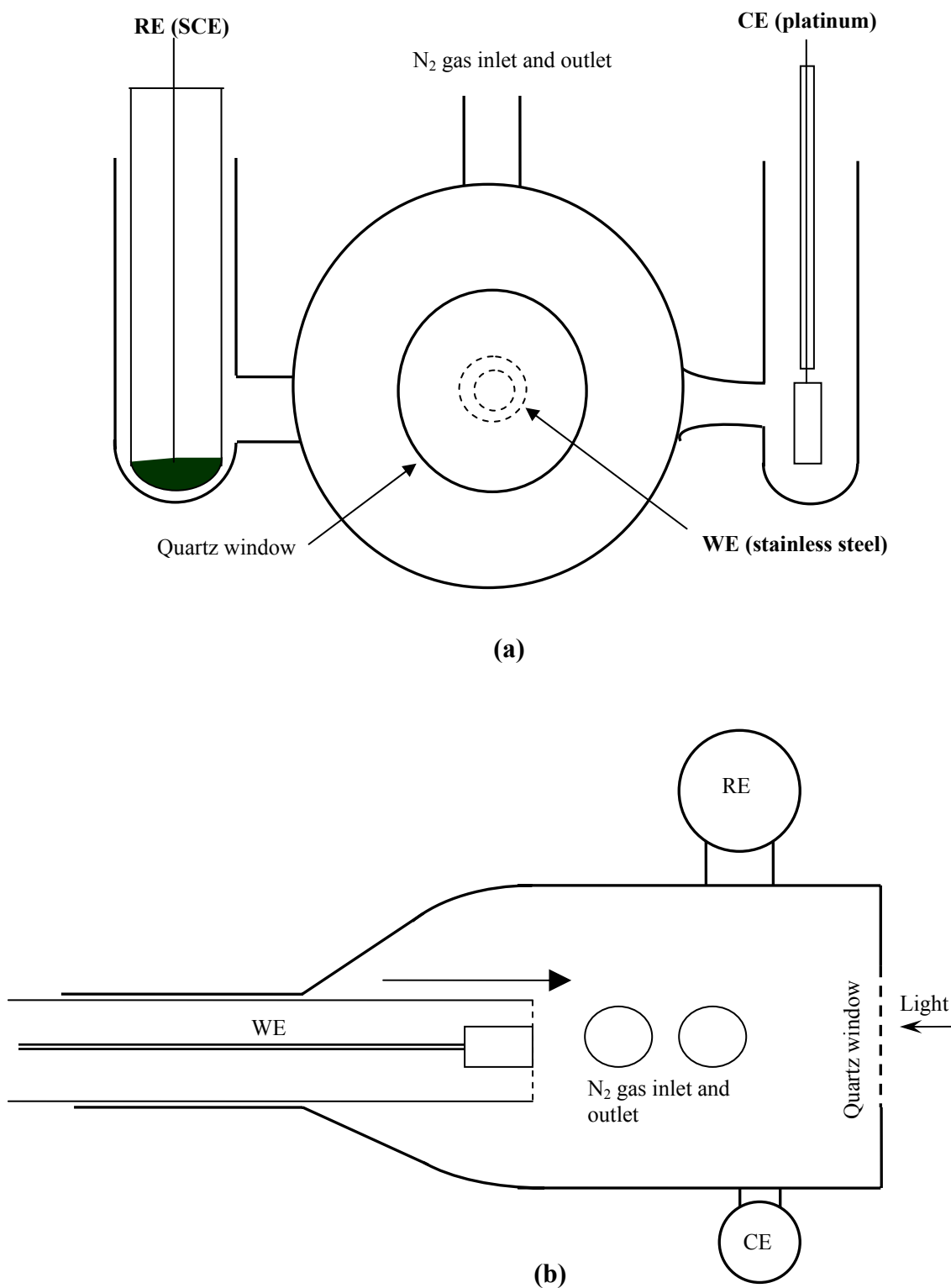


Figure 3.05. Electrochemical glass cell designed for photocurrent spectroscopy: (a) front and (b) top view.

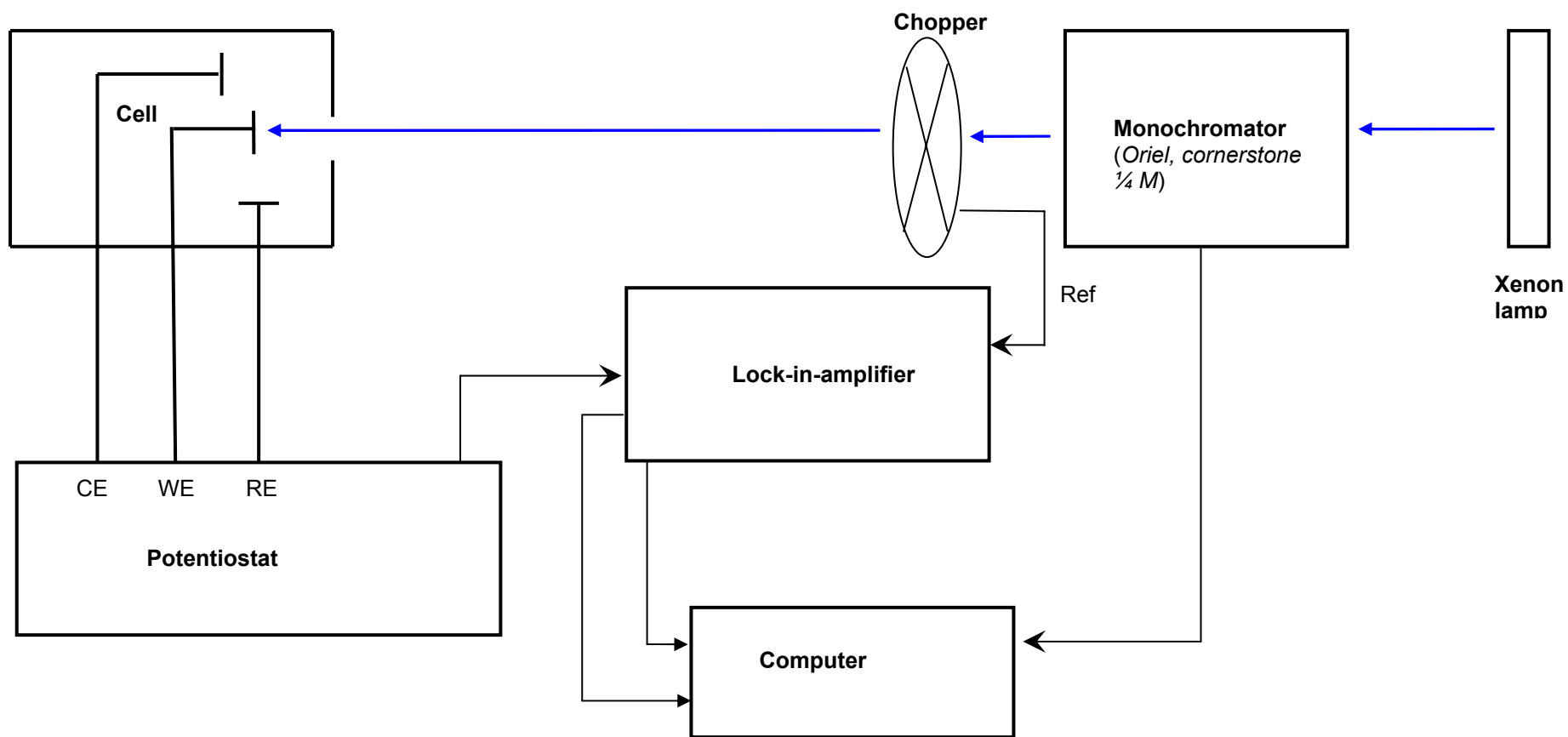


Figure 3.06 Schematic representation of the photocurrent spectroscopy instrumentation.

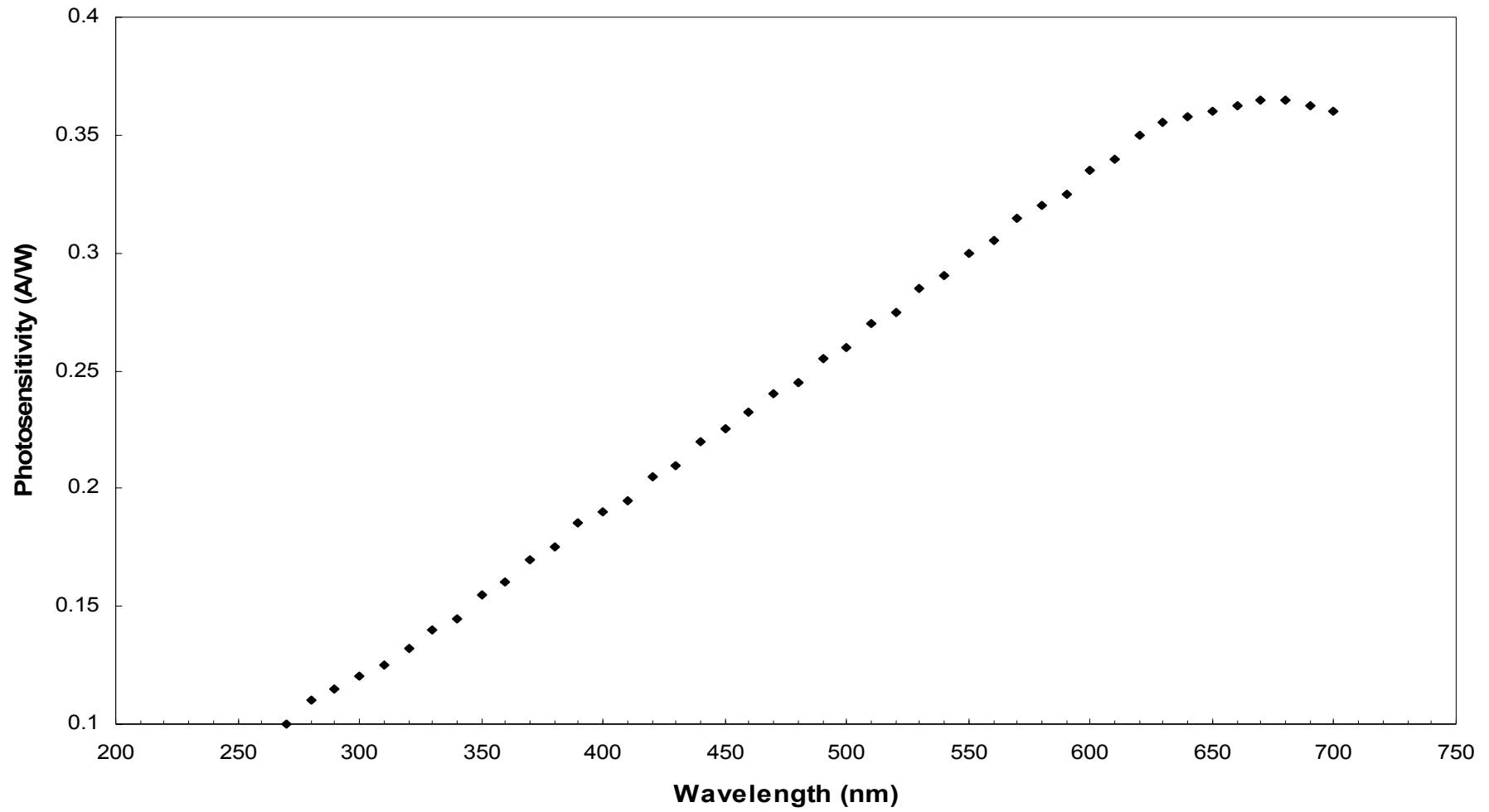


Figure 3.07. Calibration curve (photosensitivity) of the photodiode (type S1227-1010BQ).

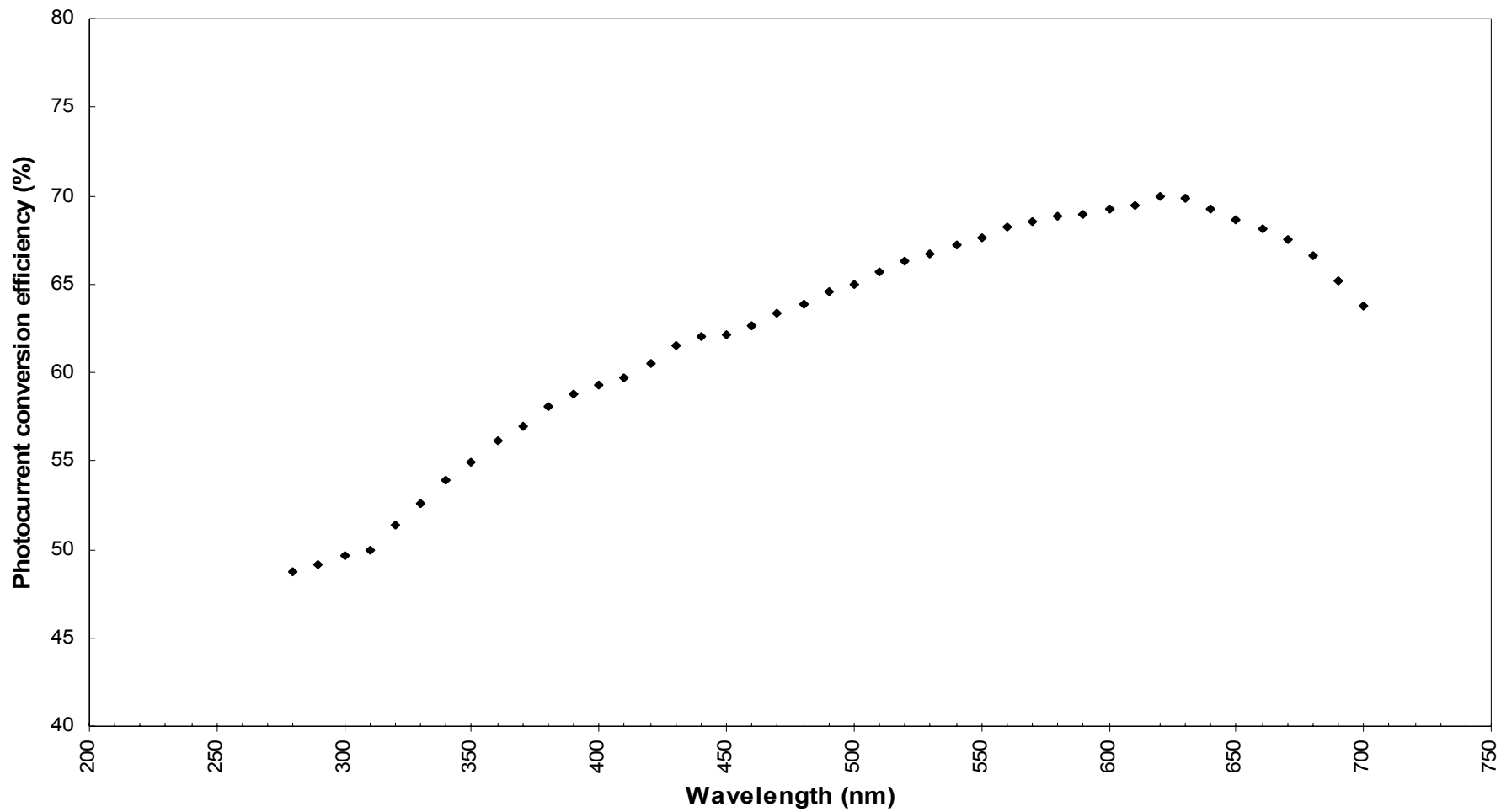


Figure 3.08. Photocurrent conversion efficiency of the photodiode.

3.3 Raman Spectroscopy

3.3.1 Raman process: a brief theoretical explanation

When a sample is irradiated by intense laser beams in the UV–visible region (frequency ν_0) the light is scattered in all directions. (Figure 3.09) The scattered light consists of two types; one, called *Rayleigh scattering* (elastic scatter), is strong and has the same frequency (ν_0) as the incident beam, and the other, called *Raman scattering* (inelastic scatter), is very weak (approximately 1 in 10^7 incident photons) and has frequencies $\nu_0 \pm \nu_m$, where ν_m is the vibrational frequency of the molecule. Raman scattering can occur with a change in vibrational, rotational or electronic energy of a molecule. However, in Raman spectroscopy, only the vibrational Raman is considered and usually observed in the direction perpendicular to the incident beam. In Raman spectroscopy, the vibrational frequency, ν_m as a shift from the incident beam frequency, ν_0 is measured. It is normal to report the Raman shift in terms of wavenumbers ($1/\lambda$) in units of cm^{-1} instead of frequency.

The $\nu_0 - \nu_m$ shift is observed when the molecule is brought up from a lower energy level to an upper energy level by incident photons and the observed response is called *Stokes* lines as schematically shown in Figure 3.10(a). On the other hand, the scattered light with frequency $\nu_0 + \nu_m$ is observed when the molecule is transferred to a lower energy level from the initial upper state and called anti-stokes, which is less probable, since fewer molecules are initially in the excited states than in the ground state. [Figure 3.11(b)]⁶

Vibrational spectra of a molecule can be explained in terms of stretching and bending motions involving various bonds in the molecules. Since the vibrational energy levels

are characteristic of the bond between atoms, these are chemical compound specific and correspond to wavelength shifts.⁷ Measurements of these shifts enable identification of the scattering compounds. Moreover detail analysing of peaks facilitates information regarding stoichiometry, stress and degree of crystallinity.

Raman spectroscopy has become an important tool for the *in situ* characterisation of passive films formed on metals and alloys in any liquid environment. One of the main advantages that makes this possible is the enhancement of the Raman peak by the roughness of the surface during polarisation. However, some drawbacks may limit *in situ* Raman studies for certain systems. Not all substances are Raman active, and also as a considerable amount of material is necessary for its identification some phases formed in the passive film may be undetectable.

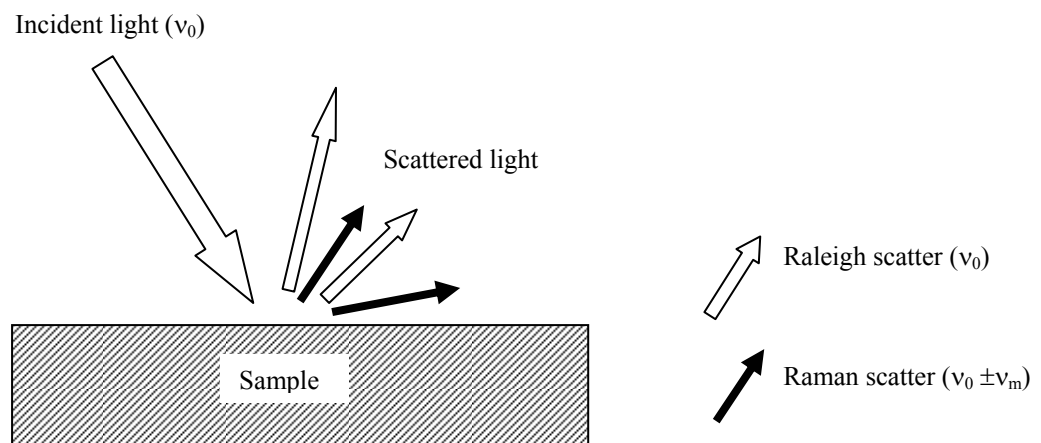


Figure 3.09. Simplified presentation of the Raman phenomenon.

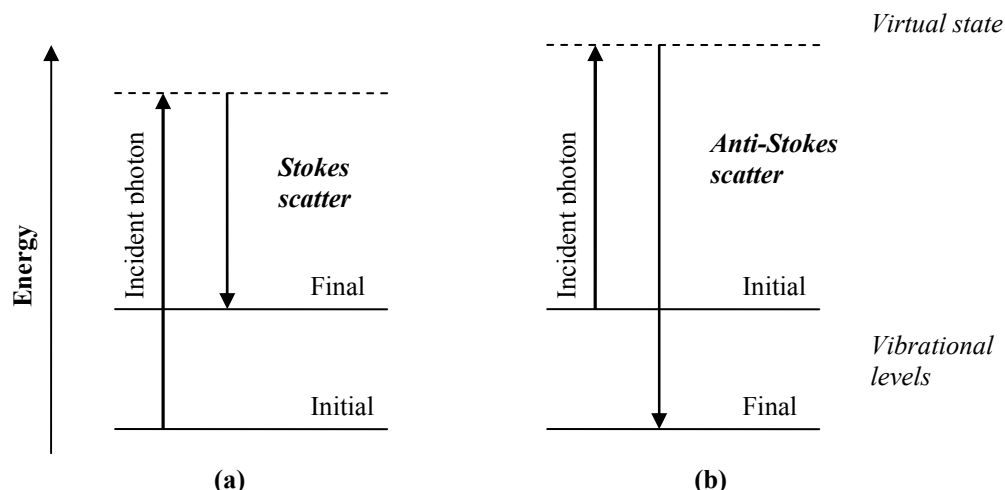


Figure 3.10. Energy level diagram for Raman scattering: (a) Stokes Raman scattering and (b) anti-stokes Raman scattering.

Surface enhance Raman spectroscopy (SERS): Although *in situ* Raman spectroscopy had been recognised as one of the outstanding techniques to study the passive film formed on metals and alloys, weak intensities of peaks restrict the detectability. The discovery of SERS has fascinated researchers giving a remedial action for this particular problem facilitating *in situ* characterisation studies.

SERS was first discovered in the 1970's.^{8,9} The idea of SERS is somewhat relatively simple; deposit a discontinuous silver layer on top of the stainless steel specimen and use the enhancement generated by silver to enhance the Raman scattering originated from the passive film.¹⁰ Although silver is the most commonly used SERS “agent” gold is also used in some cases and occasionally copper; order of enhancement $Ag \gg Au > Cu$. depending on the experimental conditions. Silver is found as the best choice for stainless steels passive film grown in borate solutions and in low concentrated chloride solutions. It is vital to control the cathodic charge density of silver deposition to obtain the adequate size, shape and distribution combination of

silver particles deposited on the surface to achieve the optimum enhancement, but without generating a continuous silver film.¹⁰⁻¹²

The exact mechanism behind the SERS effect is not yet confirmed. However, the two most probable contributions for the enhancement are identified as electromagnetic field enhancement and chemical enhancement. The enhancement to electromagnetic resonances of the SERS-active metal, which enhances local electric fields at the surface, is the source behind the electromagnetic field enhancement, while the effects on the Raman cross section of increasing the molecular polarizability is the reason behind the chemical enhancement.¹⁰ All Raman spectra collected for this thesis made use of the SERS effect.

3.3.2 Raman instrumentation and experiment

The Raman electrochemical glass cell with a quartz window was designed to accommodate the three-electrode system as shown in Figures 3.11 (a) and (b). Sample preparation was the same as discussed earlier in Section 3.1.2. After polishing and cleaning, the silver deposition process required for SERS was performed immediately prior to the Raman experimentation. A Dilor–Jobin HR 800 confocal Raman spectrometer was used. The spectral resolution of the Raman instrument was $\pm 2.5\text{cm}^{-1}$. The Raman experimental arrangement is shown in Figure 3.12. *In situ* Raman procedure was as follows:

- i. the sample was cathodically polarised at -1.0V (SCE) for around 10 minutes in 0.1M borate solution;
- ii. the electrode was next transferred to a 1mM AgNO₃–HNO₃ solution and silver was deposited by passing 50 mC/cm² charge at a potential -0.6V;

- iii. the electrode was lightly washed with deionised water and transferred to the electrochemical cell (Figure 3.13) for *in situ* Raman observation. The sample was placed flat in the cell, covered by an electrolyte layer of a thickness *ca.* 1mm.;
- iv. the sample was cathodically polarised at -1V (SCE) in an effort to remove an air formed film and then potentiostatically polarised in the positive direction in a 0.1M borate solution (or a 0.028M NaCl solution) up to 900mV (SCE) in 100mV intervals;
- v. an argon ion green laser (514.5nm) operating at 40mW was focused on to the sample through a $\times 10$ objective. The Raman spectra were recorded at each 100mV interval.

3.4 *In situ* atomic force microscopy

A multimode scanning probe microscope (SPM) supplied by *Digital Instruments* manifested with an electrochemical atomic force microscope (EC-AFM) and an electrochemical scanning tunnelling microscope (EC-STM) was used to image the surface of stainless steel samples under polarization. EC-AFM measures the surface structure of conducting materials immersed in electrolyte solutions either by sliding the probe's tip across the sample surface (i.e., the contact mode) or by tapping the surface with an oscillating tip (i.e., the tapping mode). EC-STM measures the topography of surface electronic states using a tunnelling current, which is dependent on the separation between the probe tip and a conductive sample surface immersed in electrolyte solutions.

A type 304L stainless steel sample of 14mm diameter and around 3mm thickness was polished down to 0.1 μ m alumina as mentioned in the section 3.1.2. A gold layer was sputtered on the cleaned sample leaving a confined area of 250 μ m \times 250 μ m unsputtered. A specially designed glass cell provided by *Veeco Metrology* to accommodate a three electrode system was used. Schematic figures of the EC-AFM experimental setup and the glass cell are shown in Figures 3.13 and 3.14. The sample was imaged continuously at a constant potential in 0.028M NaCl (1000ppm Cl⁻), after an image had been collected the potential was stepped in the positive direction. Here the Ag/AgCl/0.028M NaCl (+322mV vs. SHE) system was used as the reference electrode.

3.5 Photocurrent transients

Photocurrent transients' studies were carried out by illuminating stainless steel samples under potentiostatic condition with monochromic light. Sample preparation and the electrochemical cell were the same as in Raman experiments (Section 3.3). The sample was polarised cathodically at -1V (SCE) and then swept potentiodynamically at 10 mV / min up to different film formation potentials. Measurements were made as the potential was reversed back in the negative direction. Current transients were recorded with the sample under potentiostatic polarisation by illuminating the sample for 10 or 20 second time intervals. The potential was then stepped back in the negative direction prior to the next illumination. An argon ion green laser or a He-Cd UV laser with wavelengths 514.5nm and 325nm, respectively were used as the illuminating sources. Approximate power densities of the Ar ion and the He-Cd lasers were 1.36 mW / μ m² and 5.77 mW / μ m² respectively.

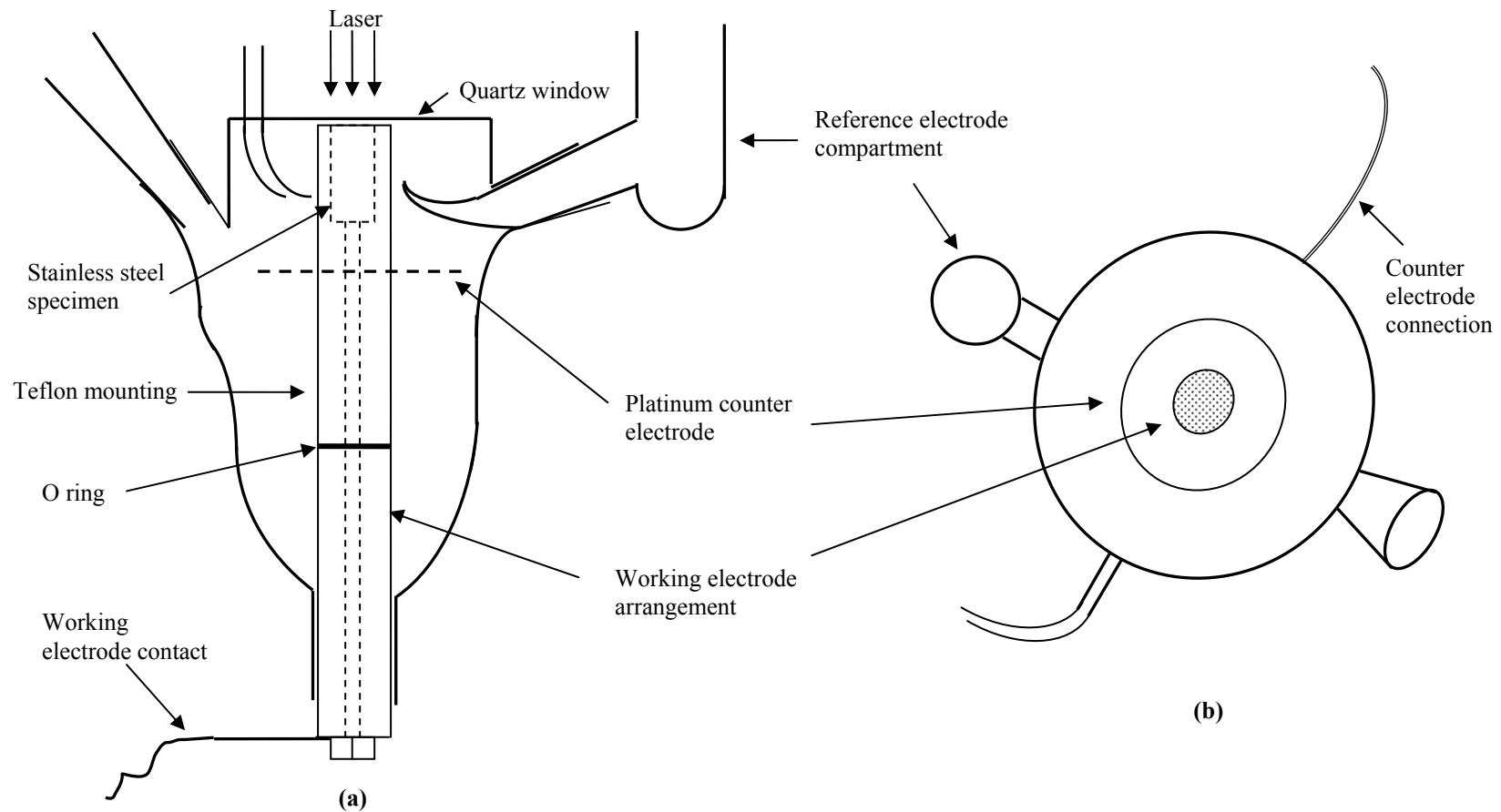


Figure 3.11. Electrochemical cell designed for *in situ* Raman spectroscopy: (a) side view and (b) top view.

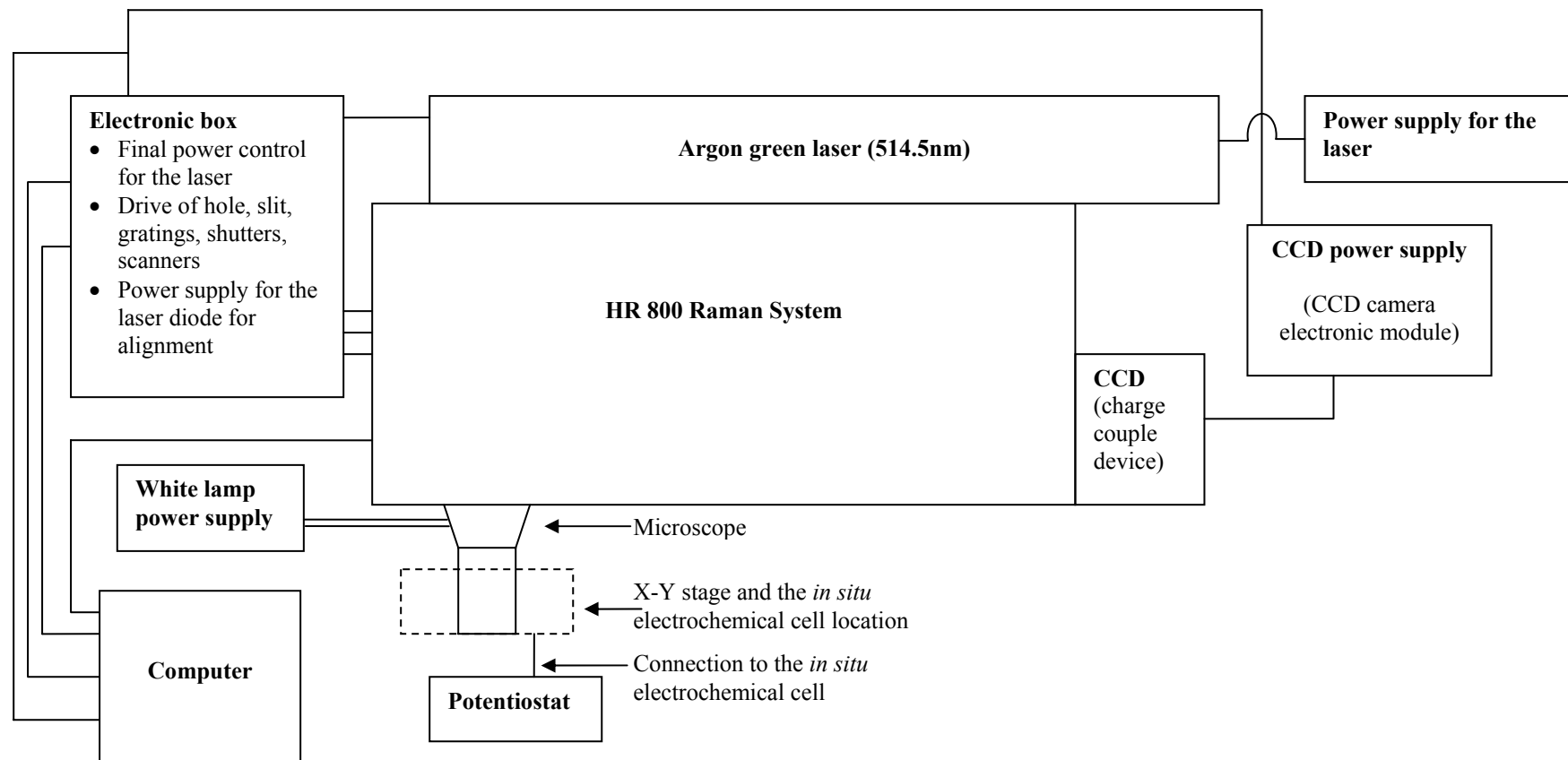


Figure 3.12. Raman instrumentation set up.

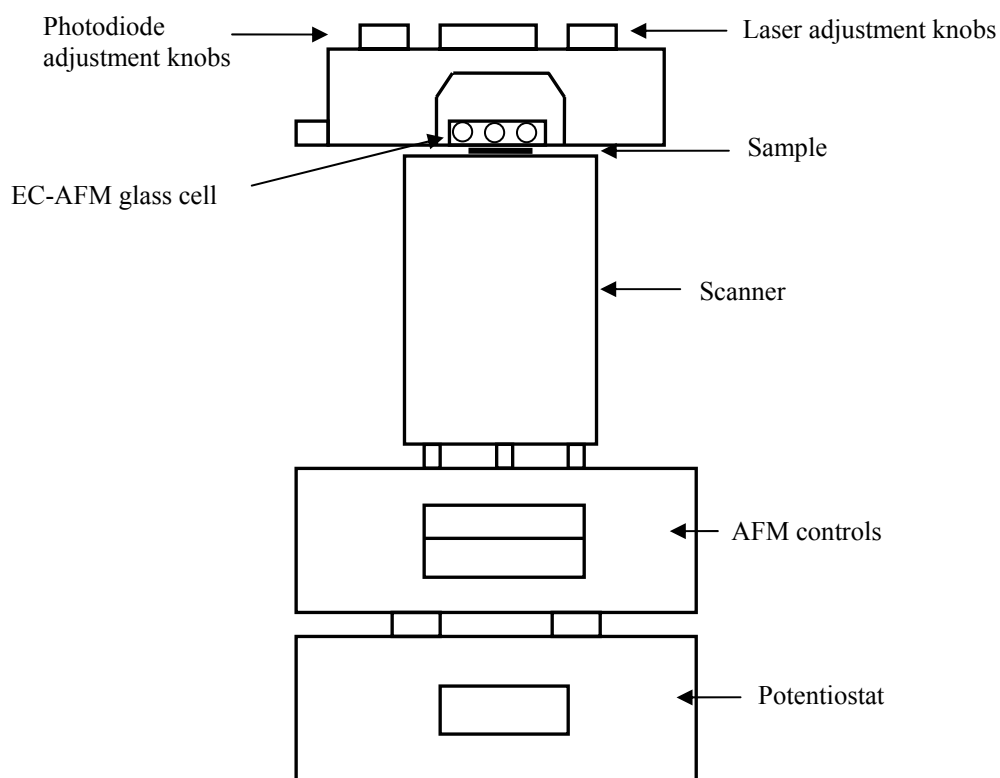


Figure 3.13 Schematic representation of the EC-AFM experimental setup.

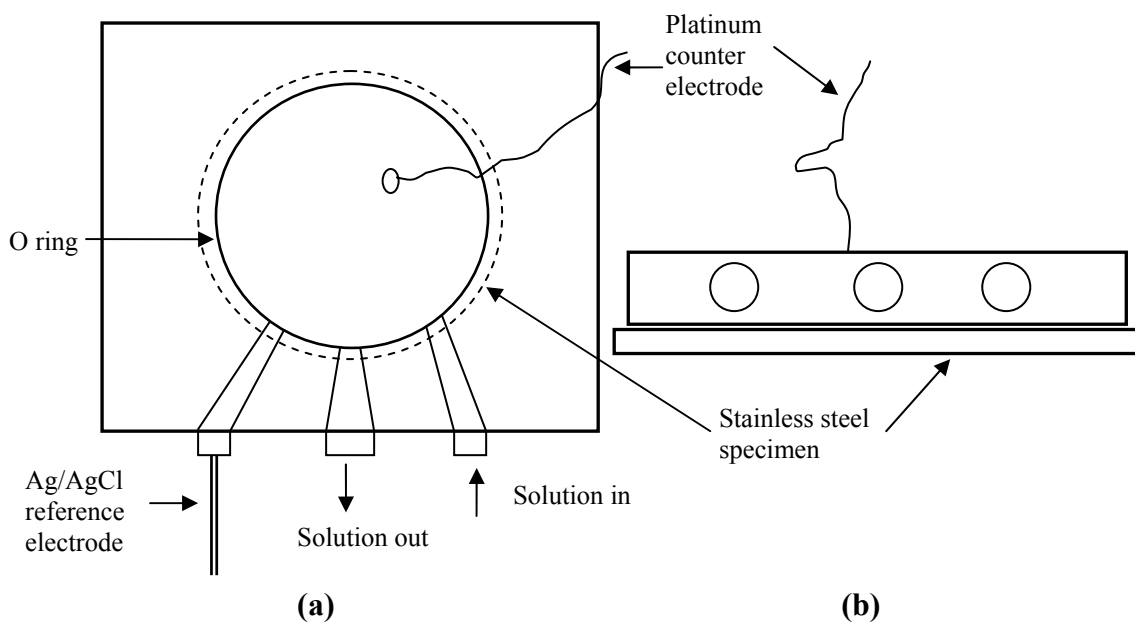


Figure 3.14. EC-AFM glass cell: (a) top view and (b) side view.

References

- (1) Southampton Electrochemistry Group, “*Instrumental Methods in Electrochemistry*”, Ellis Horwood, Chichester (1985).
- (2) Blackwood, D.J., *University of Southampton, Ph.D. Thesis* (1986).
- (3) Di Quarto, F., Piazza, S., Santamaria, M. and Sunseri, C., “*Handbook of Thin Film Materials, Volume 2: Characterization and Spectroscopy of Thin Films*”, (ed. Nalwa, H.S.), Academic Press, San Diego (2002) 373 – 414.
- (4) Stimming, U., *Electrochim. Acta*, **31** (1986) 415.
- (5) Di Quarto, F., Piazza, S. and Sunseri, C., *Mats. Sci. For.*, **192 – 194** (1995) 633.
- (6) Ferraro, J., R. and Nakamoto, K., “*Introductory Raman Spectroscopy*”, Academic Press, San Diego (1994).
- (7) England, W.A., Bennett, M.J., Greenhalgh, D.A., Jenny, S.N. and Knights, C.F., *Corros. Sci.*, **26** (1986) 537.
- (8) Fleischmann, M., Hendra, P.J. and McQuillan, A.J., *Chem. Phys. Let.*, **26** (1974) 163.
- (9) Jeanmaire, D.L. and Dwyne, R.P.V., *J. Electroanal. Chem.*, **84** (1977) 1.
- (10) Giu, J. and Devine, T.M., *J. Electrochem. Soc.*, **138** (1991) 1376.
- (11) Melendres, C.A., Acho, J. and Knight, R.L., *J. Electrochem. Soc.*, **138** (1991) 877.
- (12) Rubim, J.C. and Dünwald, J., *J. Electroanal. Chem.*, **258** (1989) 327.

CHAPTER 4 RESULTS

4.1 Cyclic voltammetry in a borate solution

Cyclic voltammograms obtained for different stainless steels cycled between -1.2V (SCE) and 1.2V (SCE) at a sweep rate of 10 mV / min in a 0.1M borate solution (pH=9.2) revealed both similarities and divergences between the various grades of stainless steels. Table 4.01 shows the measured open circuit potentials (E_{oc}) and corrosion potentials (E_{corr}). The E_{oc} was first measured by leaving the sample in the deoxygenated solution for 10 minutes prior to the standard cyclic voltammetry experiment. The value of E_{corr} was abstracted from the cyclic voltammogram being defined by the point, where the total anodic current density equalled the total cathodic current density. It can be seen that the corrosion potentials are not consistent with the open circuit potentials measured immediately prior to cyclic sweep. This difference may be caused by two main reasons:

- possible surface changes occur at more negative potentials than the open circuit potentials. For example, a spontaneous air-formed oxide film probably existed on the sample prior to the measurement of E_{oc} , which could lower the corrosion rate and drive the potential more positive such an oxide may be reduced at negative potentials;
- due to the current involved in charging the double layer capacitance.

Stainless steel	E_{corr} (in a de-aerated borate solution) (mV/SCE)	E_{oc} (in a de-aerated borate solution) (mV/SCE)
AISI 304L	-850 ± 20	-350 ± 20
AISI 316L	-820 ± 20	-430 ± 20
AISI 316LVM	-760 ± 20	-340 ± 20
AISI 254SMO	-840 ± 20	-450 ± 20

Table 4.01. Corrosion potentials and open circuit potentials of different stainless steels in a deaerated 0.1M borate solution.

The E_{corr} values of the various grades of stainless steels in a deaerated 0.1M borate solution were similar, with the 316LVM being slightly more positive than the other three alloys. This could indicate that the expected lower number of surface inclusions on the vacuum melted sample either enables the cathodic hydrogen evolution reaction to be more efficient or, more likely, slightly reduces the anodic general corrosion rate of the alloy by stabilizing the passive films.

Cyclic voltammetry results obtained for AISI 316L, AISI 304L and AISI 254SMO in a borate solution are presented and discussed next.

4.1.1 316L and 304L

A Cyclic voltammogram for 316L in borate solution is presented in Figure 4.01. Salient characteristics of the curve are noted below.

- The high cathodic current densities at point A in the forward sweep and point N in the reversed sweep are due to hydrogen evolution. However, in the forward scan the hydrogen evolution starts at a slightly more positive potential than in the reverse scan due to surface oxide formed on the sample during the forward scan.
- The anodic peak B (-800mV to -750mV) can be ascribed to formation of the oxide film. This could be attributed to the oxidation of Cr to Cr(III) assuming that the native air-formed film was removed by the initial cathodic polarisation. However, which oxide would form by Cr oxidation is difficult to justify using electrochemical data alone. However, this particular peak has been attributed to the electroformation of a $\text{Fe}(\text{OH})_2$ layer on the passivating Cr(III) containing layer by several authors.^{1,2} Another possibility is to form the Fe_3O_4 inverse spinel as a stable phase that exist around these potentials.^{4,5}

- No clear active-passive transition can be seen in the forward scan. Around -500mV to -275mV (*CD* region) another anodic current feature can be observed; probably the oxidation of Fe(II) to Fe(III). Some authors reported that Fe(OH)₂ oxidises to FeOOH to form a Fe(III) hydrous film on the Cr₂O₃ film^{1,2}, whilst others suggest the formation of Fe₂O₃.^{3,6} Langevoort *et al.*⁵ speculated the formation of an FeCr₂O₄ layer at the interface between iron and chromium oxide using XPS results.
- After the point *D* the voltammogram descends to a plateau (-50mV to 200mV) indicating steady state film growth in the passive region.
- At the point *E* (200mV) the current starts to rise but the rate of increase is arrested at the point *F* (500mV), possibly indicating another oxidation phase change. This may be attributed to transpassivation due to the oxidation of Cr(III) into Cr(VI) in the film. However, there are different views on whether the Cr(VI) phase is soluble or not.^{1-3, 6-8} Urretabizkaya *et al.*² suggested that there are two kinds of Cr(III) species in the passive film; one in the outer layer, which oxidises to soluble Cr(VI) and the other in an inner layer, which oxidises to Cr(VI) that is retained in the passive film. These authors further postulated that with increasing polarization time, Fe-chromite will form, which hinders the oxidation of Cr(III) to soluble Cr(VI). This will be further discussed when the voltammograms of the 254SMO alloy is presented. However, there is no evidence for any oxidation change for the Fe(III) layer in this region.
- At point *G* (850mV to 880mV) oxygen evolution starts in the transpassive region (bubbling was observed).

- In the reverse scan, several cathodic peaks can be observed. The peak *J* at around 30mV to 80mV may be attributed to the reduction of Cr(VI) back to Cr(III) in the passive film.
- The cathodic current wave observed at point *L* (-600mV to -700mV) may be related to the reduction of Fe(III).
- The rapid cathodic increase that starts around *M* is probably due to the onset of hydrogen evolution. At the same time it has been suggested that the electroreduction of Fe(II) to Fe and Cr(III) to Cr could occur at potentials more negative than -800mV.^{1,2} However, due to a high cathodic current dominated by hydrogen evolution makes it ambiguous to distinguish any other possible processes. According to the Pourbaix diagrams of iron and chromium⁴ both Cr(III) and Fe(II) states [Cr(III) as Cr₂O₃ or Cr(OH)₃ and Fe(II) as Fe(OH)₂] are stable over this voltage range in a borate solution (pH=9.2).
- The only effect of leaving dissolved oxygen in the solution was to increase the cathodic current density flowing in the *KM* region; consistence with the reduction of dissolved oxygen. The other characteristic features of the voltammogram were unchanged.

The cyclic voltammogram of 304L stainless steel in a borate solution under the same conditions was similar to that of 316L except for two features:

- (i) slightly lower current densities in 304L throughout the passive region than with the 316L, which can be explained as a slight thickness variation between the two stainless steels;
- (ii) the current densities of 304L in the transpassivation region were only about 50% the value of their 316L counterparts.

However, the major anodic and cathodic features of 304L were consistent with those of 316L indicating similar oxidation phase changes in both stainless steels. Similar anodic and cathodic characteristics were apparent in 316LVM under the same conditions, with current densities that were between those of 316L and 304L.

4.1.2 254SMO

Figure 4.02 shows the cyclic voltammogram of 254SMO super austenitic stainless steel in a borate solution. One of the significant differences in the anodic polarization behaviours between 316L (also 304L) and 254SMO is the current density plateau in the latter over the passive region from -700mV up to 0mV. This implies the formation of a stable oxide phase in 254SMO. However, the anodic current starts to rise again around 0mV, an anodic peak appears around 470mV to 480mV (\dot{F}), and then reaches a stable high current density plateau (\dot{GH}) that lasts until oxygen evolution starts. These features are related to the transpassivation to Cr(VI) and it is evident that the transpassivation of 254SMO starts at a more negative potential than in either 316L or 304L. In 254SMO the charge passed in the transpassive region greatly exceeded that in the passive region (in contrast with the case of 316L where there is no significant difference in the charge passed between the passive and transpassive regions). This excess charge in 254SMO must be due to the oxidation of metallic chromium Cr(0) to Cr(VI). Consequently the anodic peak at around 470mV (\dot{F}) may be due the oxidation of Cr(III) into Cr(VI) whilst the plateau \dot{GH} is due to the oxidation of Cr(0) into Cr(VI). However, elementary analysis conducted by inductively coupled plasma-optical emission spectrometer and the atomic absorption spectrometer for the borate solution after the samples of each stainless steel had been polarised at transpassive potentials did not detect any Cr ions (see Section 4.2).

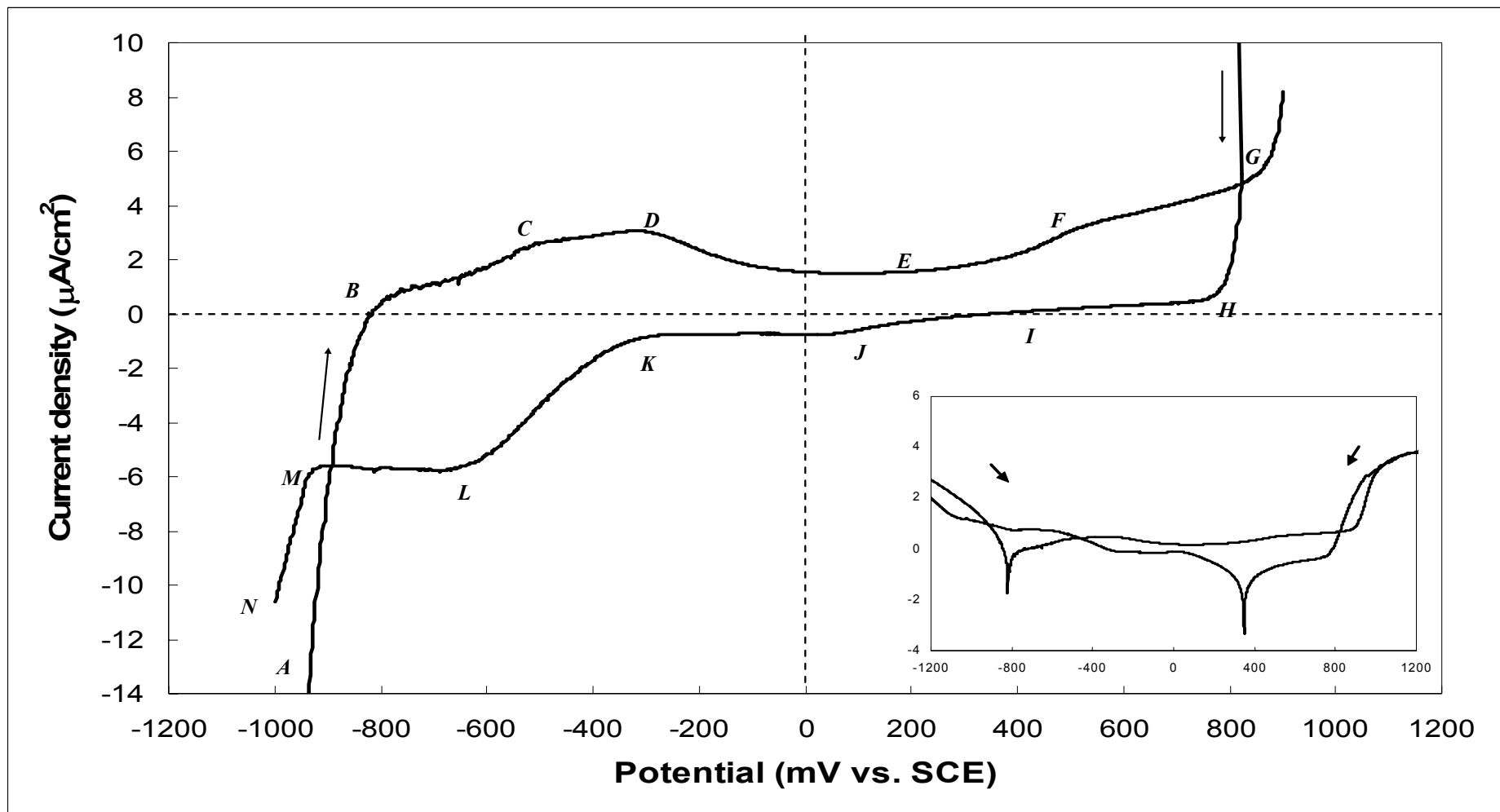


Figure 4.01. Cyclic voltammogram of 316L in a 0.1M borate solution (deaerated). The sample was swept between -1.2 V (SCE) and 1.2 V (SCE) at 10 mV / min. Inset is the same curve with log current density axis.

Three significant cathodic features can be observed in the reverse sweep of 254SMO (Figure 4.02): (i) around 670mV (J'); (ii) around 80mV to 110mV (K'); (iii) around 600mV (L'). Figure 4.03 presents the dependence of these cathodic features on the positive limit used in the forward scan. Prominent features are explained below.

- (i) The reduction around 670mV appears only if the sample is swept above 900mV [Figure 4.02(f)]. This peak may represent the reduction of intermediates produced in the oxygen evolution reaction.⁹ However, this cathodic feature was not seen in voltammograms of 316L and 304L under the same conditions. This feature has been attributed by previous authors to the reduction of nickel from high valence [Ni(III)] to the lower valence state [Ni(II)] in the oxide.³ A similar peak was observed when pure nickel and nichrome alloys (80% Ni / 20% Cr) were investigated under similar experimental conditions (not shown in this thesis).
- (ii) The reduction peak that appears around 80mV to 120mV (K') is directly related to the transpassive region that starts with the existence of the anodic peak at F' . Figure 4.03 clearly shows the different steps; the reduction peak (K') starts to appear only in Figure 4.03(c), where the sample was swept positive of 440mV. And its area (K') increased as the positive limit of the forward scan was increased. It was also found that the charge under the peak K' is slightly less than 50% of that passed in the transpassive region beyond the point G' thought to be due to Cr(0) to Cr(VI). Consequently, this peak K' was attributed to the electroreduction of Cr(VI) into Cr(III) oxide.
- (iii) Around -600mV, another smaller cathodic peak appears, this feature was also seen with 316L stainless steel, where it was attributed to the reduction of Fe(III) probably to Fe(II).

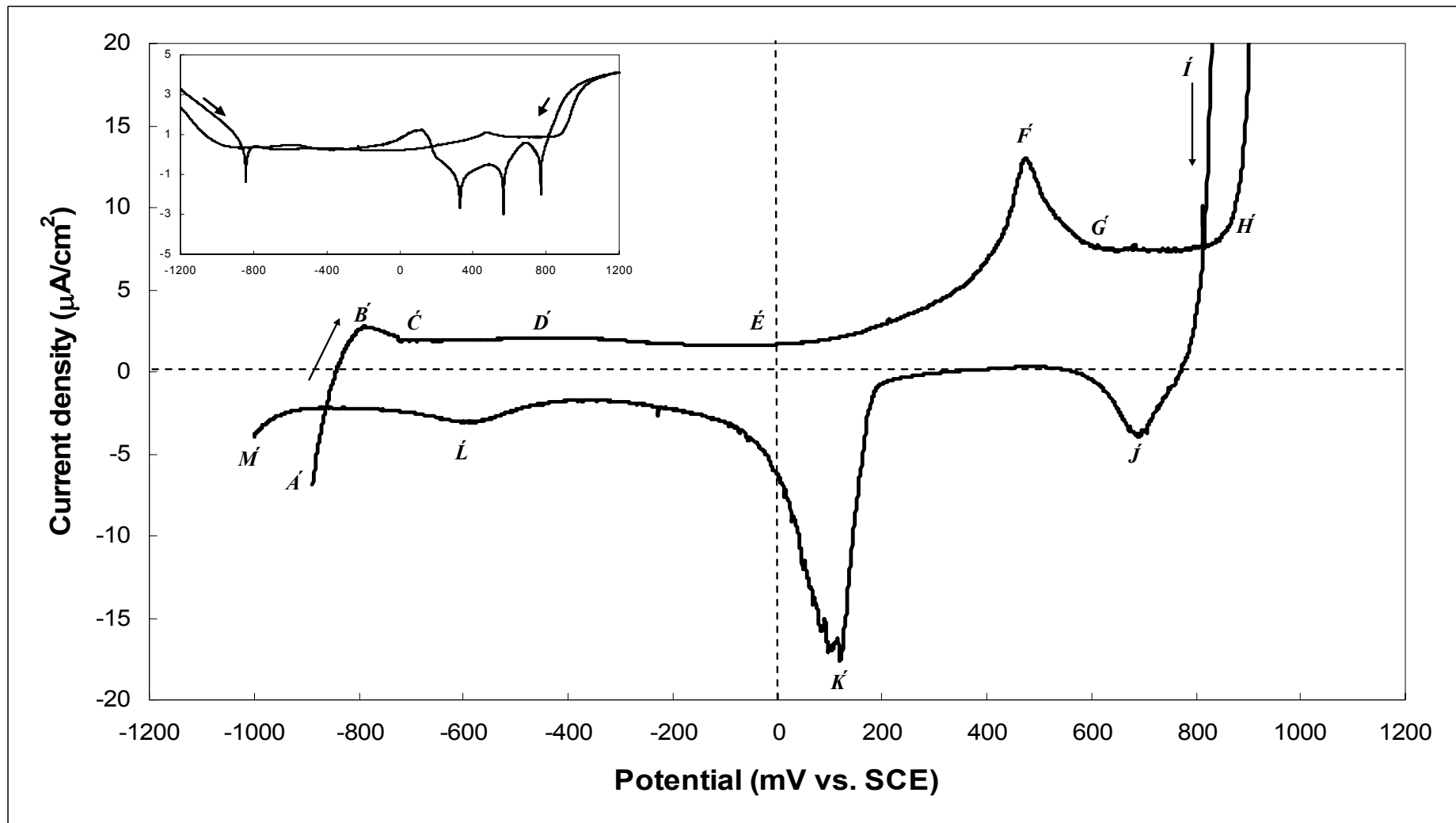
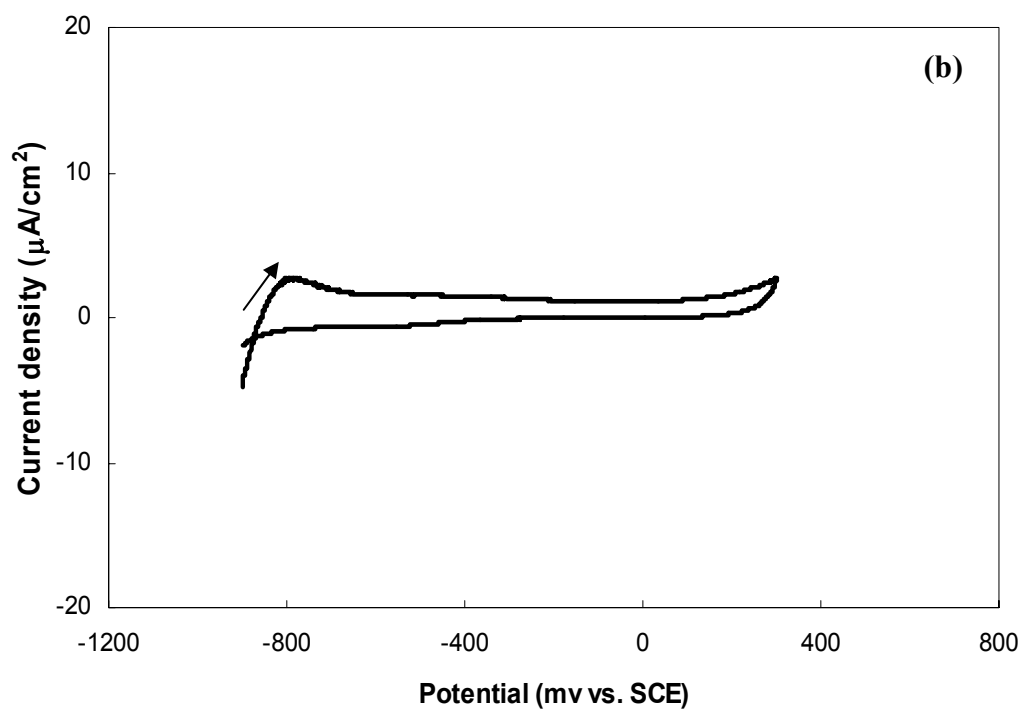
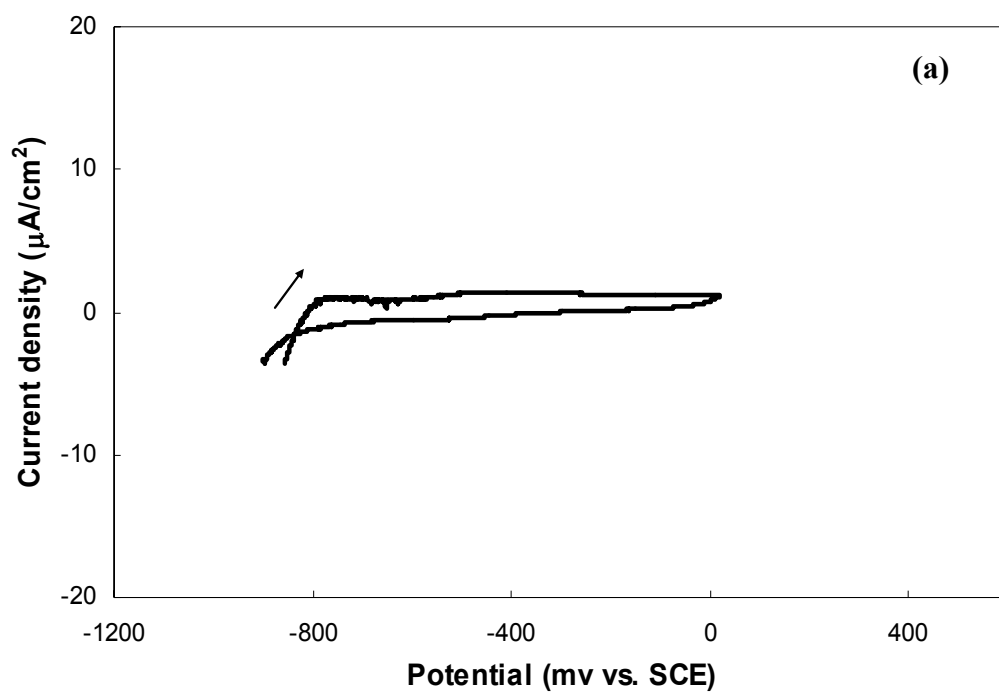
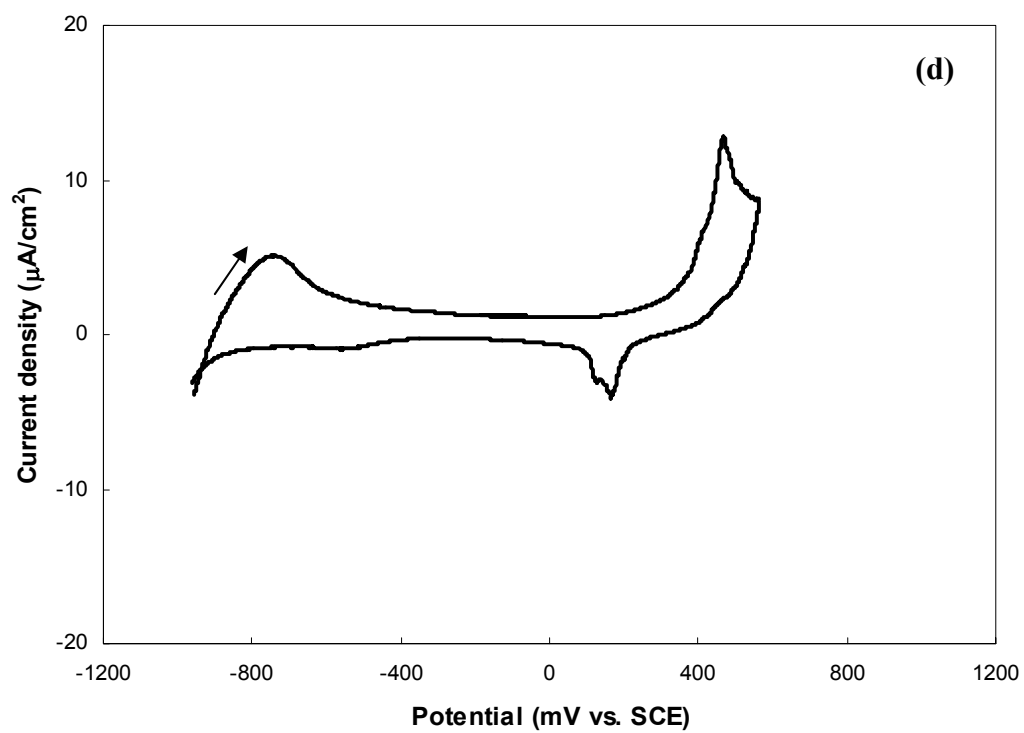
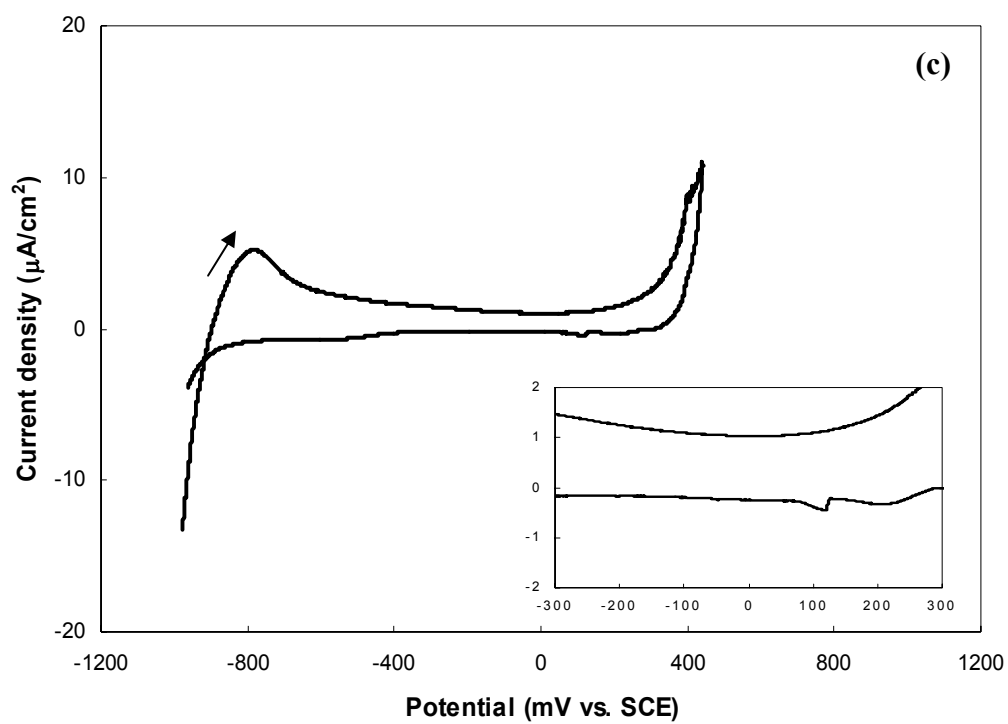


Figure 4.02. Cyclic voltammogram of 254SMO in a 0.1M borate solution (deaerated). The sample was swept between -1.2 V (SCE) and 1.2 V (SCE) at 10 mV / min. Inset is the same curve with log current density axis.





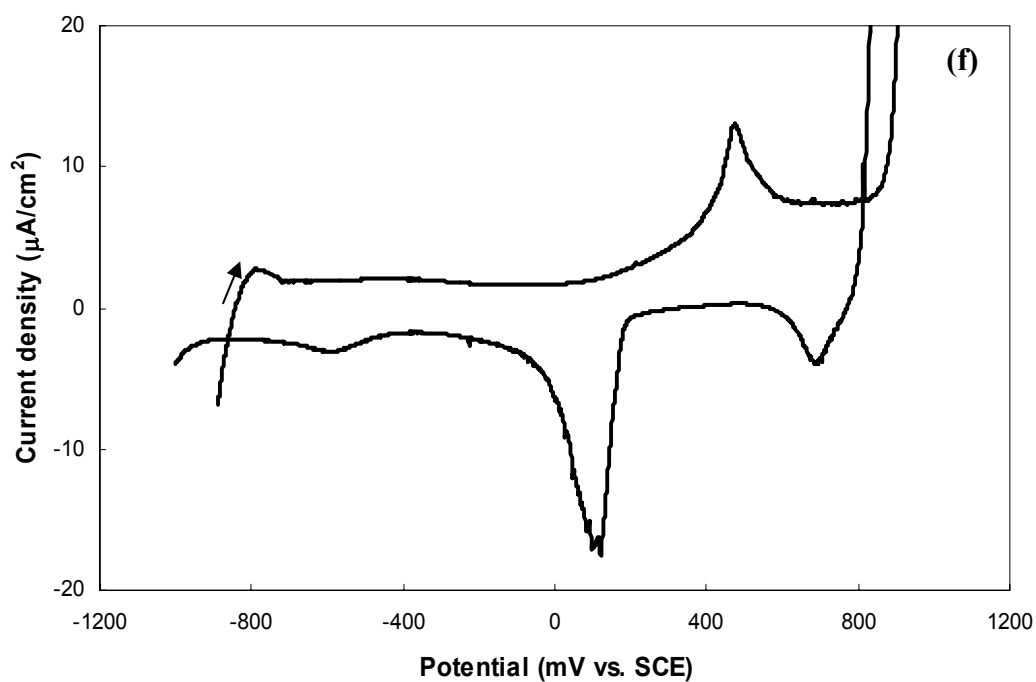
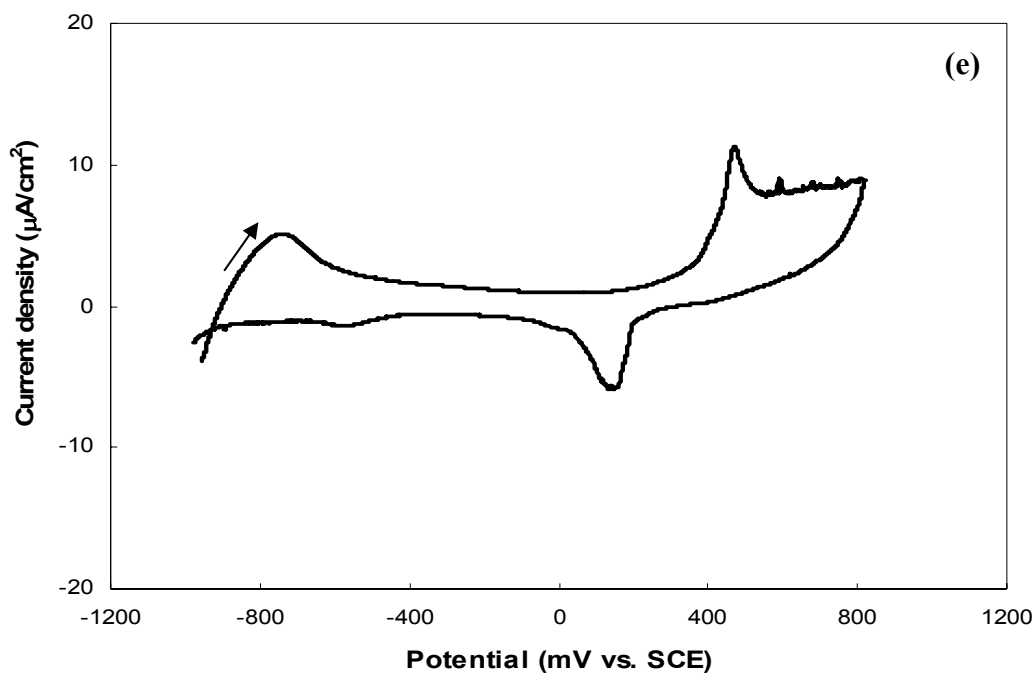


Figure 4.03. Cyclic voltammograms of 254SMO in a 0.1M borate solution. Sample was swept at a rate of 10 mV / min between -1200mV and: (a) 20mV; (b) 300mV; (c) 440mV; (d) 565mV; (e) 900mV; (f) 1200mV. Inset of (c) is the enlargement of the same voltammogram to signify the initiation of the cathodic peak at around 100mV.

4.2 Elemental analysis results

The borate solution was analysed for metallic elements Cr, Fe, Ni and Mo using the inductively coupled plasma-optical emission spectrometer and the atomic absorption spectrophotometer after the samples of each stainless steel had being polarised at their transpassive potentials up to 180 minutes. None of the above mentioned metallic elements could be observed above 10ppb, the lowest detection limit of the instruments. However, the background interference due to the high Na ion concentration made the results ambiguous.

4.3 Thickness estimations

Figure 4.04 shows the incremental thicknesses of 316L, 304L and 254SMO stainless steels calculated considering the total charge involved in passive film formation according to the Equation 2.20. It is assumed 100% charge transfer efficiency and the density of the oxide was taken as 5.2 g / cm^3 for Cr_2O_3 for all three stainless steels. The potential region between -200mV and 500mV was considered as a common sector for all three types of stainless steels where a steady state film growth was apparent, although in the 254SMO stable film growth was reached before -200mV. According to the calculations, the following points were concluded:

- 304L and 316L have similar characteristics; thicknesses increase approximately in a liner manner with anodising ratios 10 nm / V and 10.5 nm / V respectively until the transpassivation starts around 500mV. This is consistent with high field growth theory;
- 254SMO the anodising ratios initially only 5.5 nm / V , but rapidly increases to 17 nm / V above 200mV.

- No direct relationship is evident between the thickness and the stainless steel's composition or pitting corrosion resistance number (PREN)^{††}.

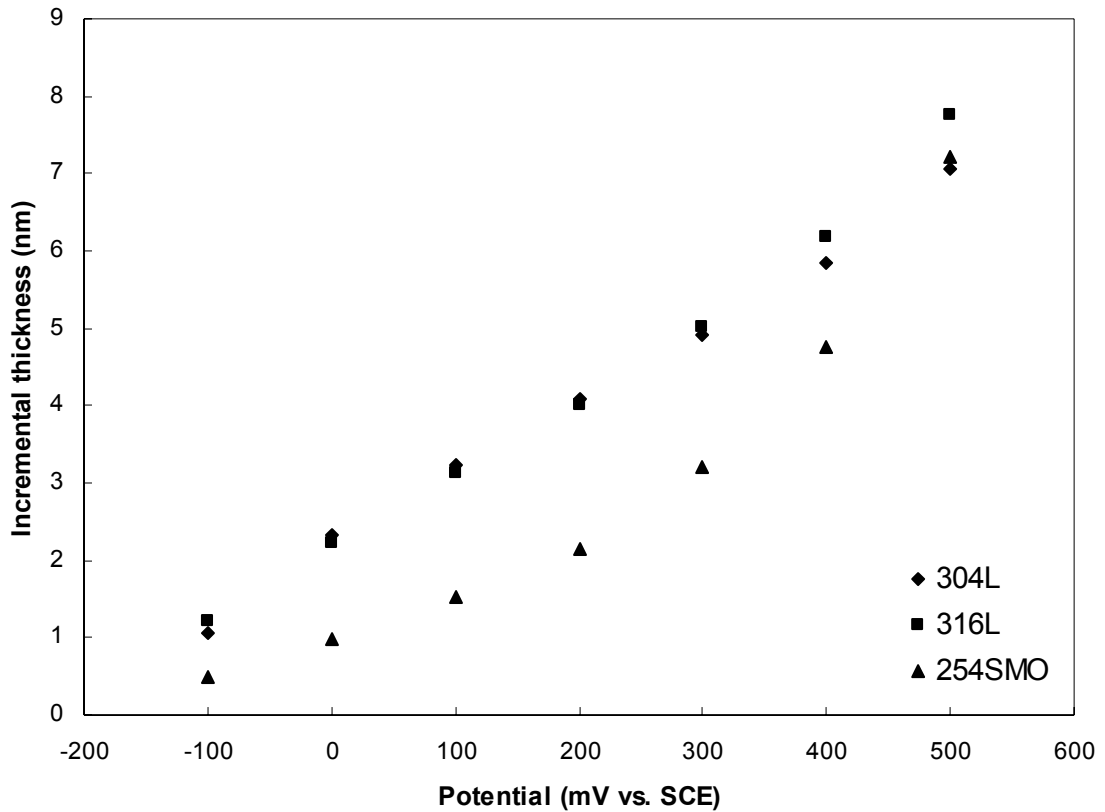


Figure 4.04. The incremental thicknesses of stainless steels passivated in the borate solution.

4.4 Pitting corrosion

4.4.1 Pitting potential and metastable pitting

The pitting corrosion resistance of the different stainless steels in chloride environments was tested. Figure 4.05 shows the polarization curve for 304L stainless steel to locate the E_{pit} , the pitting potential. At the critical potential, E_{pit} , a dramatic increase in the current can be observed. The E_{pit} was estimated by considering the lowest potential for a stable pit to occur as being that at which the current density grows above $100 \mu\text{A}/\text{cm}^2$. This was supported by macroscopical and microscopical

^{††} PREN number: 254SMO>316LVM>316L>304L

investigations. The variation for E_{pit} of different stainless steels with different chloride concentrations is shown in Figure 4.05; for 254SMO no pitting was observed with any tested NaCl concentration (10mM to 2M). No pits were observed (Figure 4.05) on 316LVM in the chloride concentrations below 400mM. The more noble is the E_{pit} , the more resistant is the alloy to pitting.

The study of metastable pitting provides unique opportunities for understanding pitting corrosion since metastable pits involve initiation, propagation and repassivation steps in short, discrete, and plentiful events. The only difference between these and stable pits is that metastable ones repassivate in a short time, thus the current increases once the pits forms and dies once it repassivates. The metastable pitting current transients of 304L stainless steel in 0.1 M NaCl solution at a potential of 100 mV is shown in Figure 4.07. Figure 4.08 shows plots of the number of metastable pits occurring per 1000 seconds per unit area (λ) against the applied potential in 0.5M NaCl for different stainless steels. Figure 4.08 clarifies the use of metastable pitting count for grading different stainless steels against pitting resistance. The metastable pitting count (λ) was calculated by counting the number of metastable pits that grew beyond 10nA; the noise level of the measuring instrument. The 254SMO did not show any significant metastable event in NaCl up to 1M concentration. Likewise 316LVM, the vacuum melted stainless steel, showed very few metastable current transient events and unlike the other alloys the metastable pitting rate count (λ) did not increase with potential.

Investigating both stable and metastable pitting results in Figures 4.06 and 4.08 respectively, it is clear that the order of pitting resistance is

254SMO>316LVM>316L>304L>304L high sulphur. This diversity is governed by main constituents; Cr%, Mo%, S% and N%. The role of Ni in the passivity process is still uncertain. The following salient features can be concluded according to the pitting characteristics in Figures 4.06 and 4.08.

- The 254SMO is the strongest against pitting probably due to high Mo% and also the presence of a small amount of N. However, it also has a higher amount of Ni although there is no reported evidence of Ni, participating in pitting resistance. At the same time the deleterious effect of sulphur seems to be combated.
- If the influence of the small amount of N in 316LVM on its pitting resistance is neglected, a comparison between the two types of 316L clearly shows the detrimental effect of sulphide inclusions on pitting resistance. This is further signified by comparing 304L with 304L high sulphur stainless steels. However, 316LVM, which has the least amount of sulphur still shows some pitting events, this implies that sulphide inclusions may not be the sole cause of pit initiation.

A deeper clarification of stable and metastable pitting events can be found in references 10 to 12.

The pitting results can be analysed based on two main considerations under consistent environmental conditions;

- the Mo content and
- the sulphur content (hence sulphide inclusions) of the different stainless steels.

4.4.2 Mo content

The effect of Mo on pitting characteristics is quite obvious (see also section 2.3.4). Furthermore, the pitting potential values and metastable pitting events reflect the

influence of Mo on the pitting resistance (Figures 4.06 and 4.08). The 254SMO, which has more than 6% Mo, did not show any pitting event under the experimental conditions. Although it is clearly evident that the Mo helps to prevent pitting there is no information on the exact mechanism of how Mo helps.

4.4.3 Sulphide inclusions

It is well known that the pitting on stainless steels starts preferentially at sulphide inclusions (see Section 2.4.2). Figures 4.06 and 4.08 are additional proof of the effect of sulphide content on stainless steel pitting characteristics. Comparing E_{pit} and λ values of 304L with 304L, a high sulphur sample and 316L with 316LVM, the significance of sulphide content on pitting resistance properties can be elucidated.

SEM images: Figure 4.09 shows an SEM image of a sulphide inclusion found in 304L high sulphur stainless steel with its EDX compositional analysis given in the figure legend. Sulphide inclusions are distributed on the surface with different sizes (100 nm to few microns), shapes (in most of the cases round to oval) and compositions (different S and Mn percentages). The 304L and 316L specimens also show similar behaviour, with the existing number of inclusions descending in the order of 304L high sulphur > 304L > 316L.

The number, the size distribution, shape and the composition (sulphur richness) of inclusions are important in determining the pitting susceptibility of a particular stainless steel.¹³⁻¹⁵

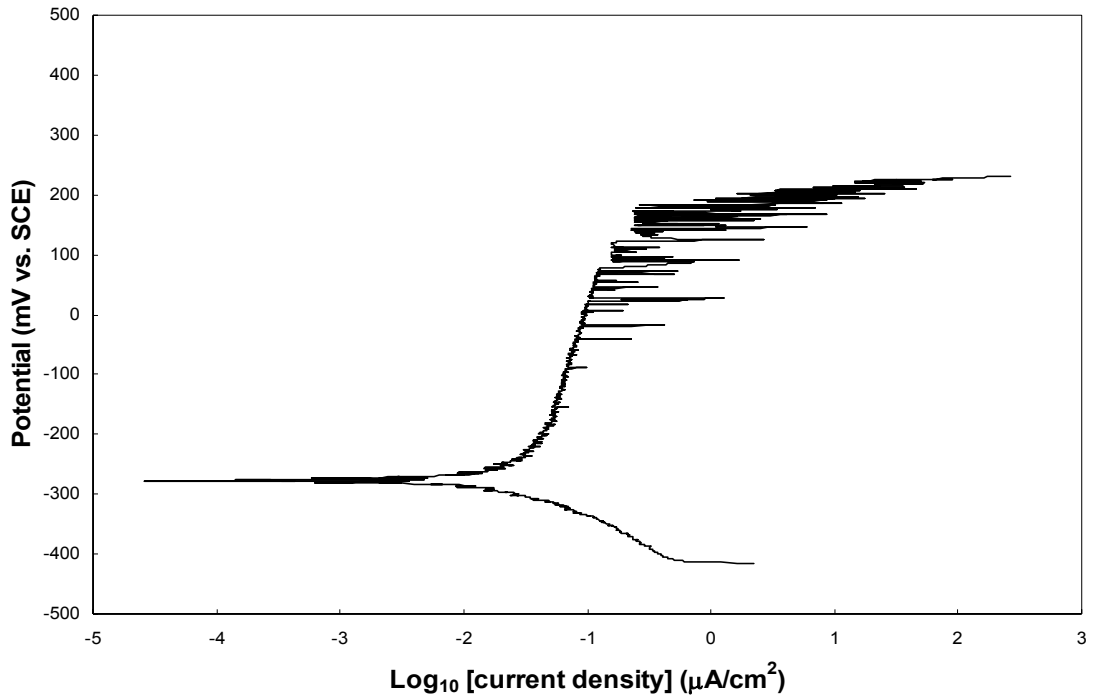


Figure 4.05. Polarization curve for 304L stainless steel at 0.1 M NaCl. Sample was scanned at a rate of 10 mV / min in the anodic direction. Stable pitting started around 230mV after a series of metastable pitting events. Current rises sharply and remains high once the stable pit forms.

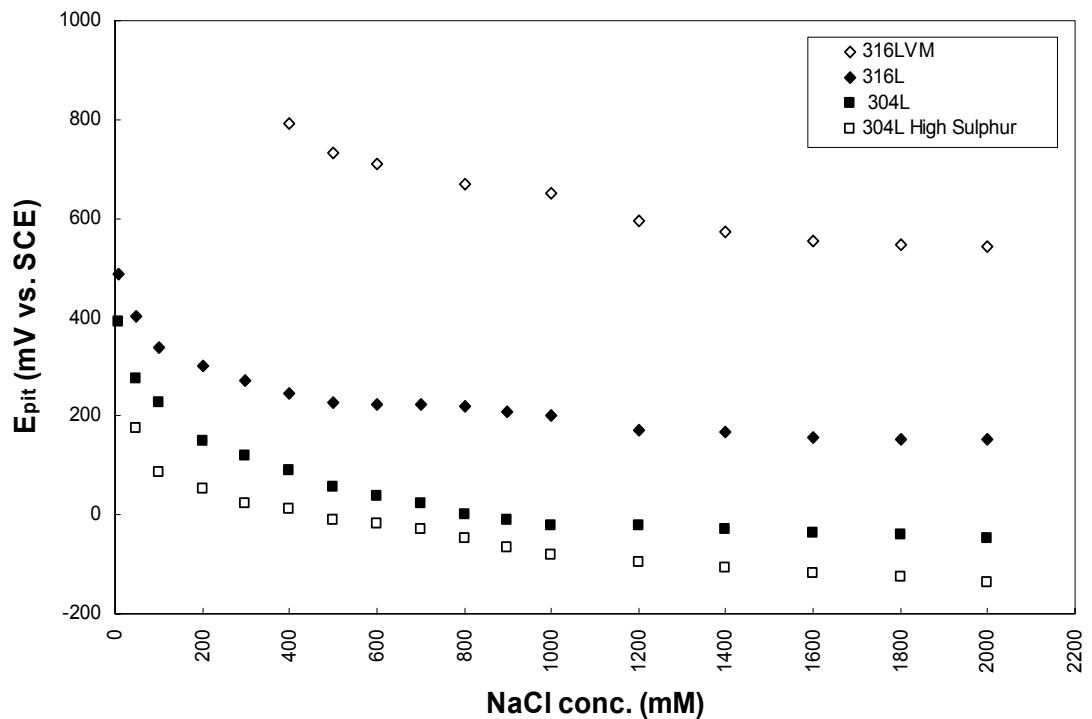


Figure 4.06. E_{pit} vs. NaCl concentration of different stainless steels. E_{pit} is estimated by considering the lowest potential for a stable pit which grows beyond a current density of 100 $\mu\text{A} / \text{cm}^2$ to occur. Note that each E_{pit} reading has an error limit of $\pm 20\text{mV}$.

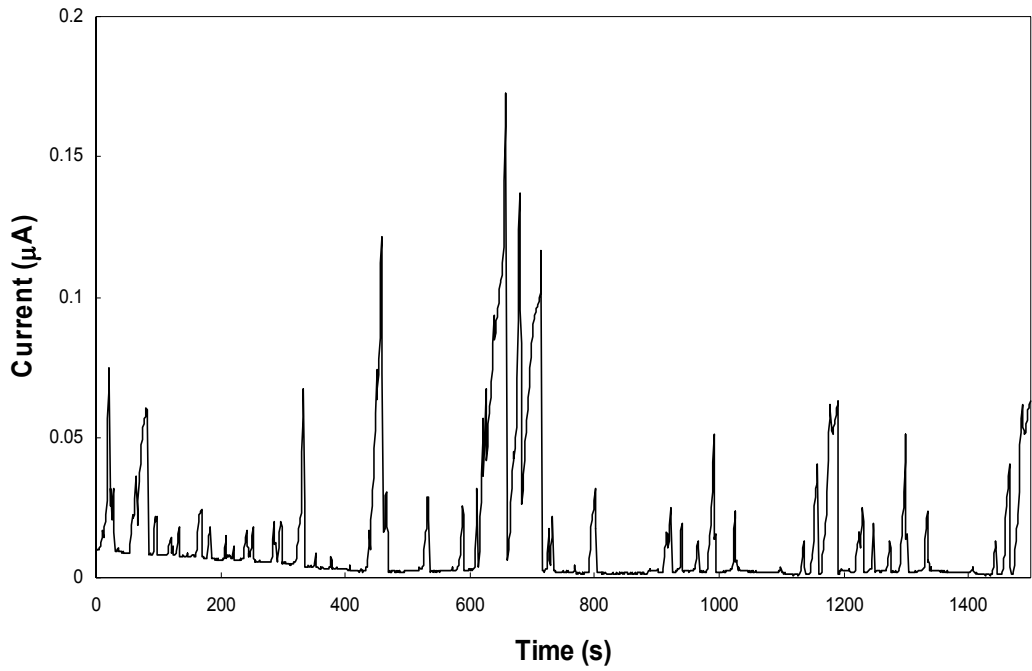


Figure 4.07. Metastable current transients of 304L stainless steel in a 0.1M NaCl solution at 100mV (SCE)

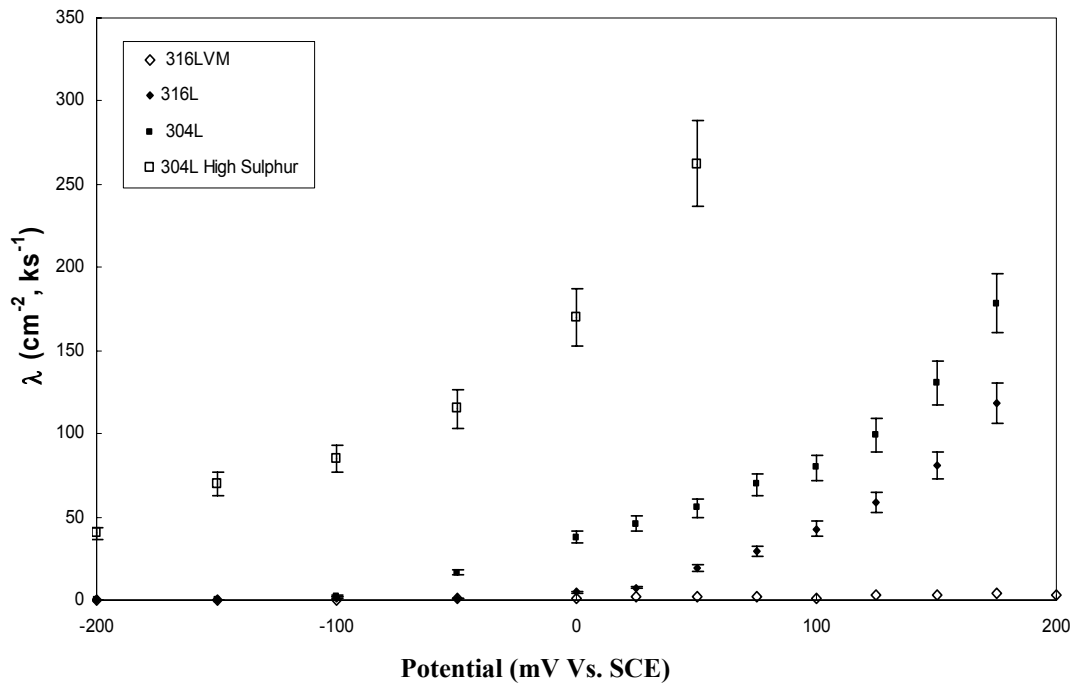


Figure 4.08. Number of metastable pits occurred per 1000 seconds per unit area (λ) against the potential at a 0.5M NaCl. In 316LVM, λ is low and independent of potential. Only metastable pits that grew beyond the noise level of the instrument have been counted.

According to SEM studies, it can be seen that in most of the cases sulphide inclusions exist as clusters. The number of inclusions in a cluster and number of clusters per unit area varied in different grades of stainless steels. Out of 316L, 304L and 304L high sulphur stainless steels, the 304L high sulphur stainless steel showed the highest number of clusters per unit area, whilst the 316L showed the lowest. The number of inclusions per cluster varied as: 304L high sulphur from 2 to 15; 304L from 2 to 10; and 316L from 2 to 6. The compositions and the size of the inclusions were sporadic over different stainless steels. Average sulphur composition (as weight percentage) of inclusions was in the range of 2% to 20% regardless of the grade, although in 304L high sulphur stainless steel, some inclusions with nearly 40% of sulphur could be found. However, this study was not extended to scrutinize the effect of inclusion characteristics (size, shape and distribution) on the pitting properties. No sulphide inclusion could be observed in 316LVM or 254SMO.

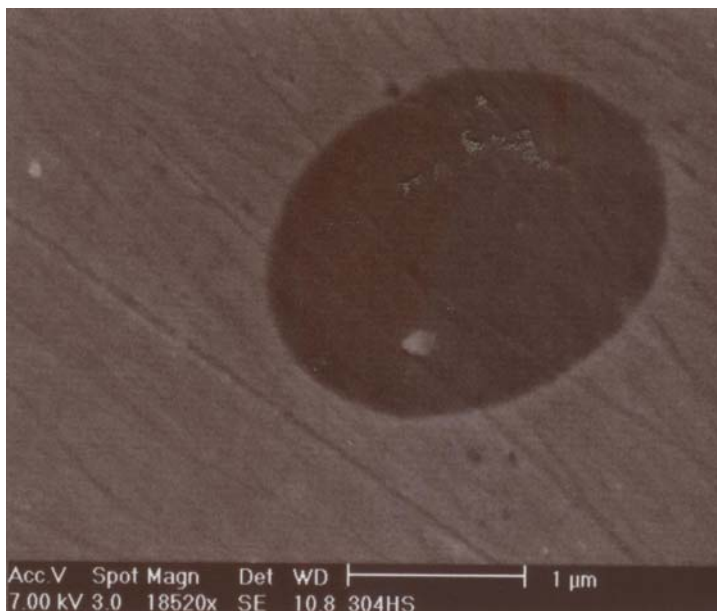
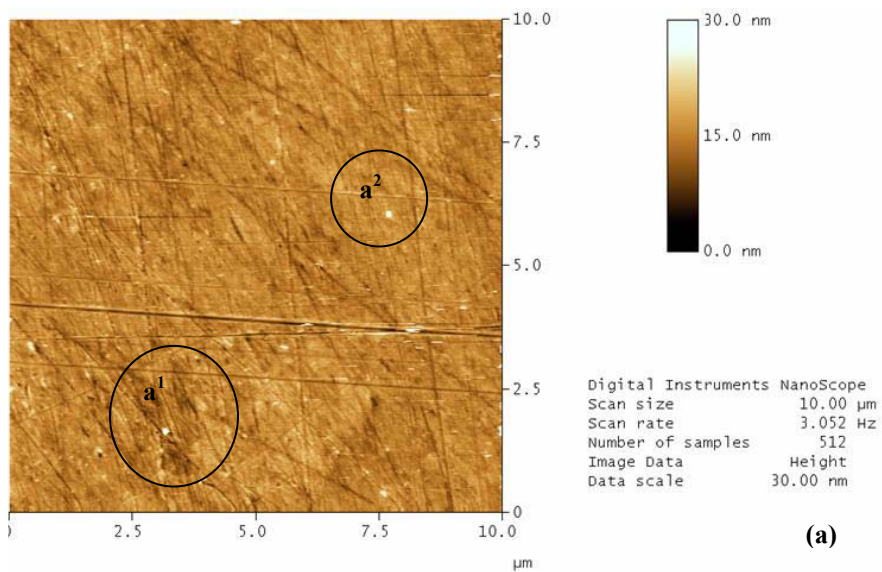
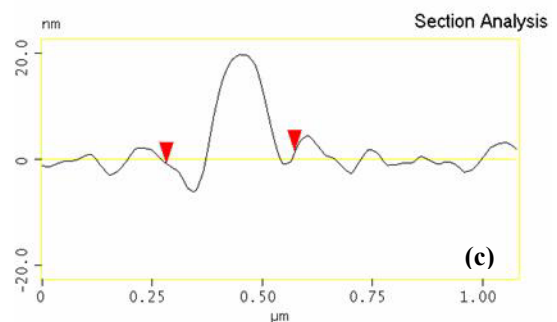
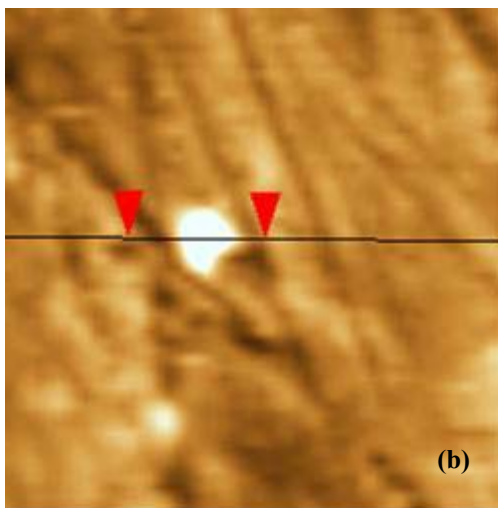


Figure 4.09. A scanning electron microscope image of a MnS inclusion in 304L high sulphur stainless steel. Energy dispersive spectrometer quantification reveals the nominal composition of the inclusion in weight percentages as follows; S-16.5, Mn-26.5, Cr-12, Ni-5.2, O-1.5 and the rest of Fe.

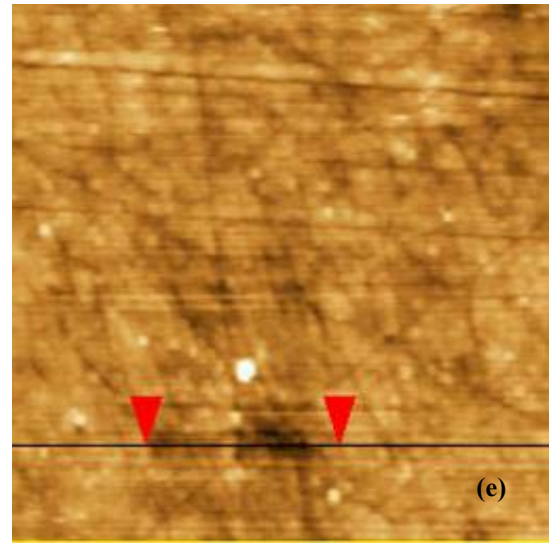
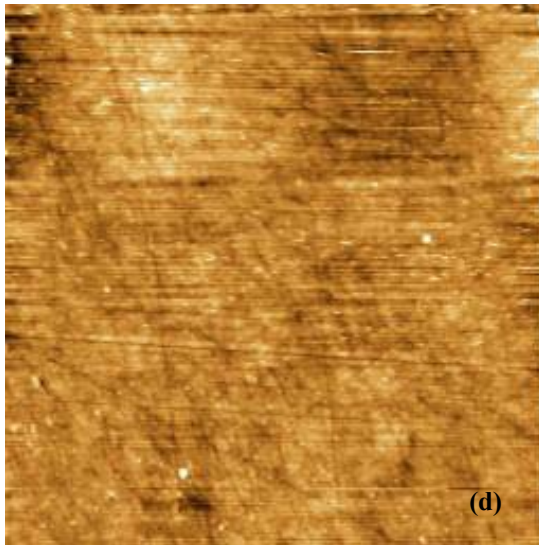
In situ AFM studies: Figures 4.10 (a) to (d) show *in situ* AFM images obtained on 304L stainless steel while polarising potentiostatically in 0.028M NaCl (see section 3.4). Some identified sulphide inclusions by SEM imaging just prior to the *in situ* AFM are shown in Figure 4.10 (a); marked by black circles. The figures illustrate the formation of a pit near the sulphide inclusion a^1 . These results are consistent with the idea that the pit initiation triggers near the sulphide inclusions, possibly due to the inclusion leading to a region of Cr depletion as claimed by Ryan *et al.*¹⁶ Alternatively it is speculated that the stress built up around the inclusion instigates the pit initiation.¹⁷ However, the results are not sufficient to comment on the other possible mechanisms of pit initiation.



(a) At $t = 0\text{s}$, white spots are sulphide inclusions which are marked by black circles and labelled a^1 and a^2 .



(b) Magnification of a^1 and
 (c) The sectional analysis of (b).



- (d) At $t = 60\text{s}$ the pit initiates;
- (e) Magnification of (d);
- (f) The section analysis of (e);
- (g) At $t = 180\text{s}$ the pit further propagates and
- (h) The sectional analysis of (g).

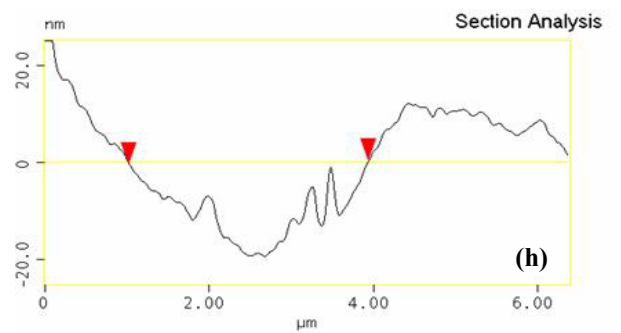
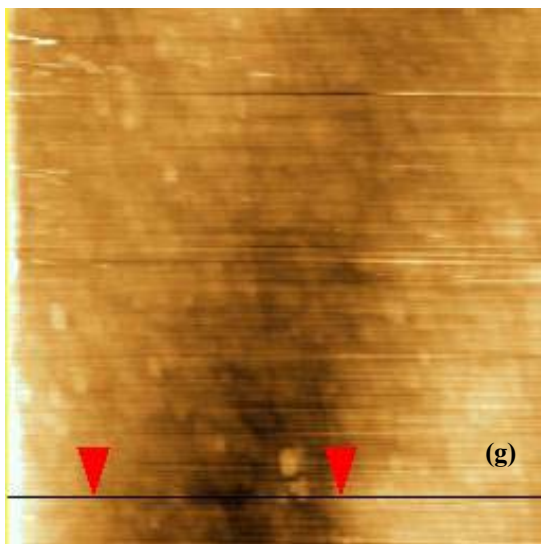
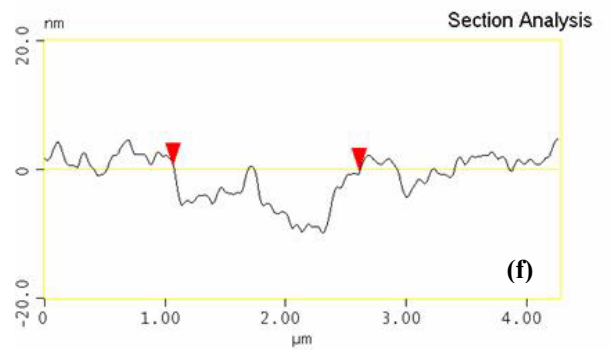


Figure 4.10. *In situ* AFM images of 304L stainless steel potentiostatically polarised in 0.028M NaCl at 200mV (SCE). Figures (a) to (h) show different stages of pit initiation and propagation at various time intervals near a sulphide inclusion, magnifications and sectional analyses (i.e., depth profiles) of certain images.

4.5 Photocurrent spectroscopy

Photocurrent spectroscopy is a powerful analytical tool to obtain information on the electronic structure and also yields indirect information regarding chemical composition of the oxide films. Passive films of 316L, 304L and 254SMO stainless steels were studied under three considerations by photocurrent spectroscopy:

- 1) photocurrent-voltage behaviour at a constant wavelength;
- 2) photocurrent spectra; photocurrent-wavelength relationship at constant potentials that provided bandgap estimations;
- 3) photocurrent transients at different potentials.

4.5.1 Photocurrent-voltage behaviour

Figures 4.11 and 4.12 show plots of the magnitude of the photocurrent versus voltage at constant wavelengths of $\lambda=340\text{nm}$ (3.65eV) and $\lambda=550\text{nm}$ (2.26eV) respectively for 316L during the reverse potential scan. No photocurrent could be observed at wavelengths above 660nm (<1.9eV).

According to Figure 4.11 at potentials positive of -400mV, a positive photocurrent was observed, consistent with an n-type semiconductor. Starting from the extreme positive potential end the magnitude of the photocurrent increases as the potential moves negative to around 450mV and then declines and shows a minimum at around $100\text{mV}\pm 50\text{mV}$. This is the voltage region where the voltammograms of 316L and 254SMO (Figures 4.01 and 4.02) show cathodic peaks, which could be attributed to a reduction phase change. It has been postulated that Cr(III) ions in the passive film act as effective recombination centres.¹⁸ Below 100mV vs. SCE, the photocurrent increases up to a maximum, then declines and vanishes at about -450mV. The absence of a net photocurrent response indicates the potential, where the rate of photoassisted

anodic charge transfer is equal to the rate of photoassisted cathodic charge transfer and defines the situation where the bands are flat such that the space charge is reduced to zero. At extreme negative potentials from -600mV down to around -950mV a negative photocurrent was observed, consistent with a p-type semiconductor. This feature cannot be observed in Figure 4.12 (with $\lambda=550\text{nm}$) indicating the phase responsible for the negative photocurrent has a bandgap larger than 2.2eV.

Note that photocurrent data alone is not sufficient to find the exact flat band potential value since in the potential region -350mV to -800mV, the photoresponse was very weak so that the photocurrent values were hard to distinguish from the background noise. In addition, when the band bending decreases close to flat band potential recombination effects are more significant, such that the photocurrent can be reduced to zero prior to reaching V_{fb} . The situation as regard to V_{fb} can be further clarified using photocurrent transients (section 4.5.3).

The photocurrent-voltage responses for both 304L and 254SMO were similar to that of 316L except for differences in the magnitudes of the photocurrent.

4.5.2 Photocurrent spectra and bandgap estimations

In order to estimate the bandgap of the oxide films photocurrent spectra were recorded at constant potentials. Figure 4.13 shows the photocurrent spectrum for 316L in borate solution at -100mV. The inset shows the subsequent $(I_{ph}\nu)^{1/n}$ and $(h\nu - E_g)$ relationship (Tauc plot) according to Equation 2.47 for bandgap estimation. It explicates a good fit of the experimental points by using $n=2$, which is the most common relationship observed for amorphous semiconductors, corresponding to a non-direct transition between valence and conduction bands.

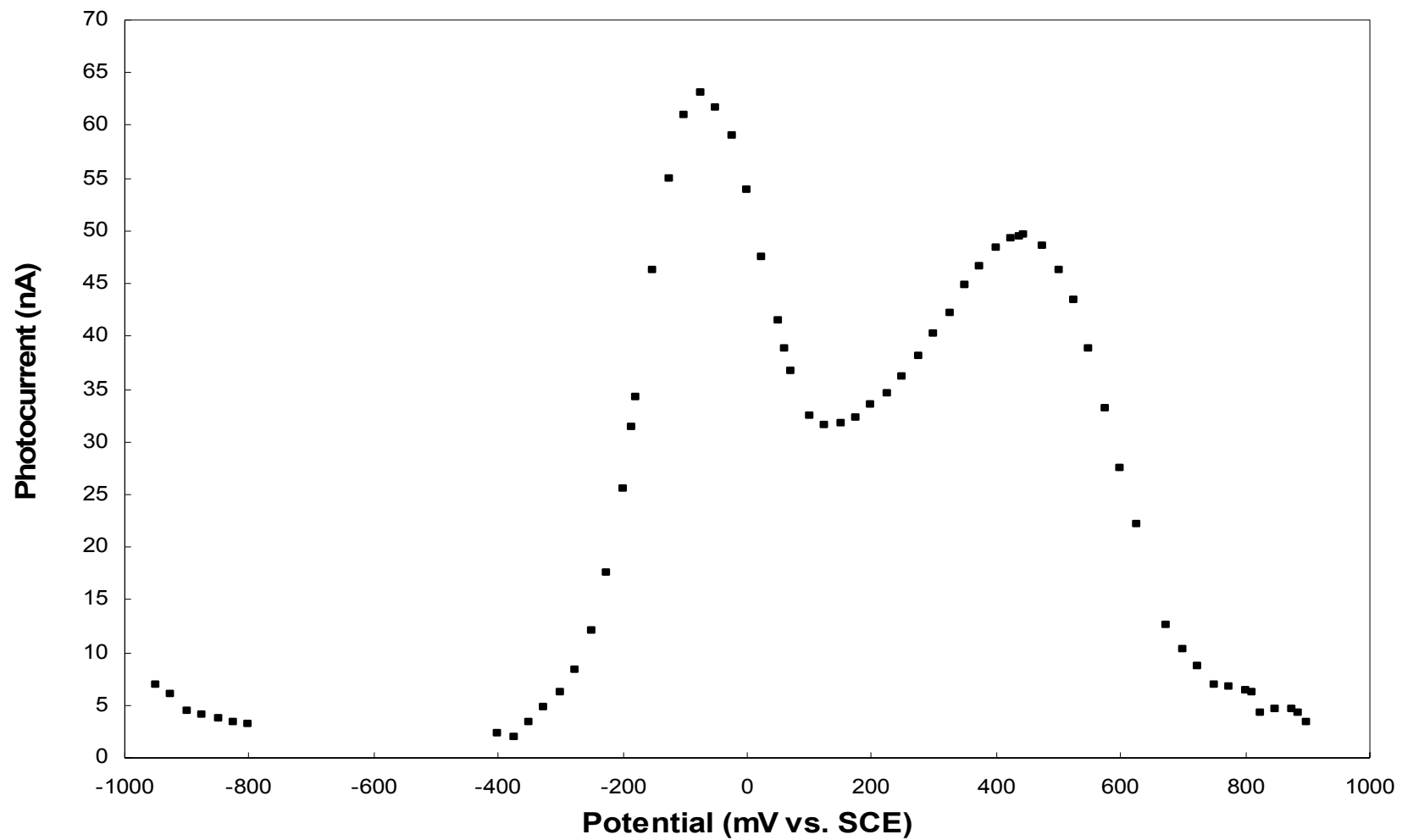


Figure 4.11. The amplitude of the photocurrent vs. electrode potential of 316L in a 0.1M borate solution recorded at a constant wave length ($\lambda=340\text{nm}$) under the reverse scan. Note that below -800mV , the photocurrent was negative.

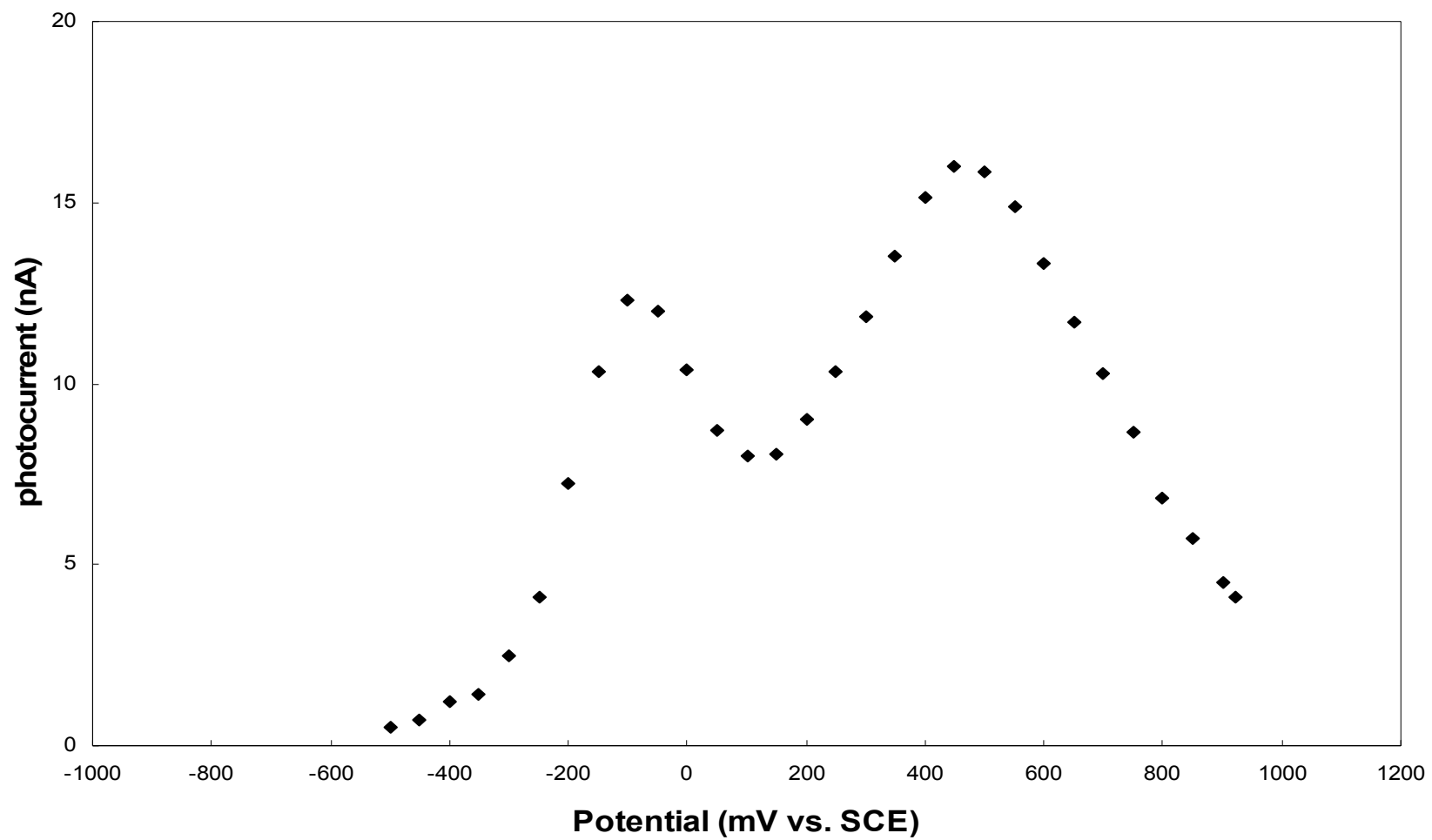


Figure 4.12. The photocurrent vs. electrode potential of 316L in a 0.1M borate solution recorded at a constant wave length ($\lambda=550\text{nm}$) under the reverse scan.

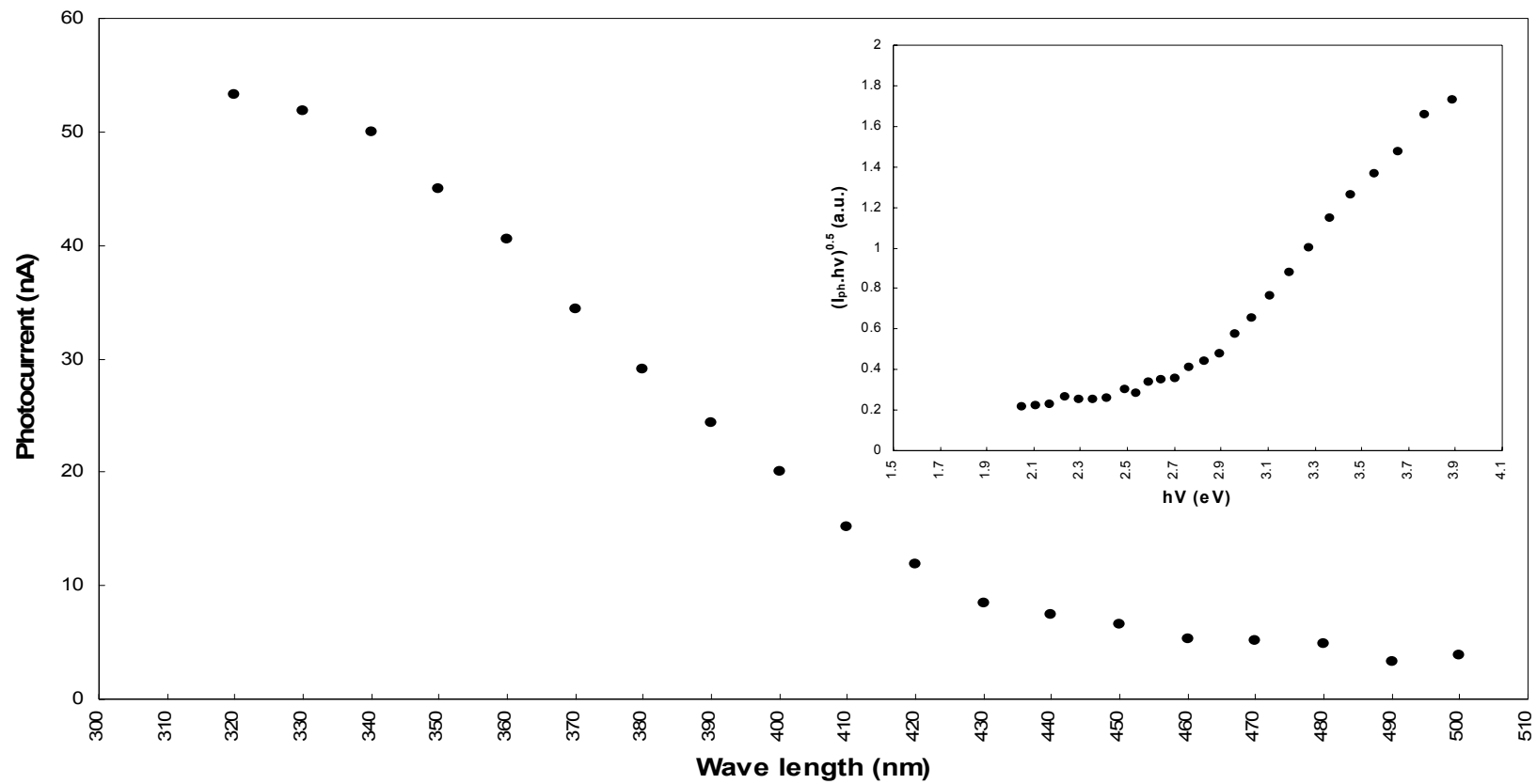


Figure 4.13. Photocurrent spectrum and the relevant $I_{ph} \cdot h\nu$ vs. $h\nu$ plot (Tauc plot) for bandgap determination (inset) for passive film grown on 316L stainless steel in a 0.1 M borate solution recorded at -100mV under the reverse polarization.

According to Equation 2.47 $[(I_{ph}h\nu)^{1/2} = const.(h\nu - E_g)]$, the bandgap can be found by extrapolating the linear portions in the plot to intersect the x axis. According to the Mott-Davis approximations the bandgap value obtain here is the mobility gap, E_g^m for the passive film on stainless steel. However, if the linear region is less than 0.3eV, the bandgap obtained by extrapolation reflects the E_g^{opt} . (see Section 2.5.6).^{19,20}

To aide interpretation the photocurrent spectra recorded from the three grades of stainless steel were categorised into three main voltage regions.

Region (a) From 800mV to 400mV (in the n-type region): all three stainless steels showed a single bandgap near 1.95 ± 0.05 eV (Figure 4.14). This experimental bandgap estimation is in agreement with the bandgap value either for Fe_2O_3 (1.9eV) or $Fe(OH)_3$ (1.96eV) or $FeOOH$ (1.96eV). (see Appendix D).

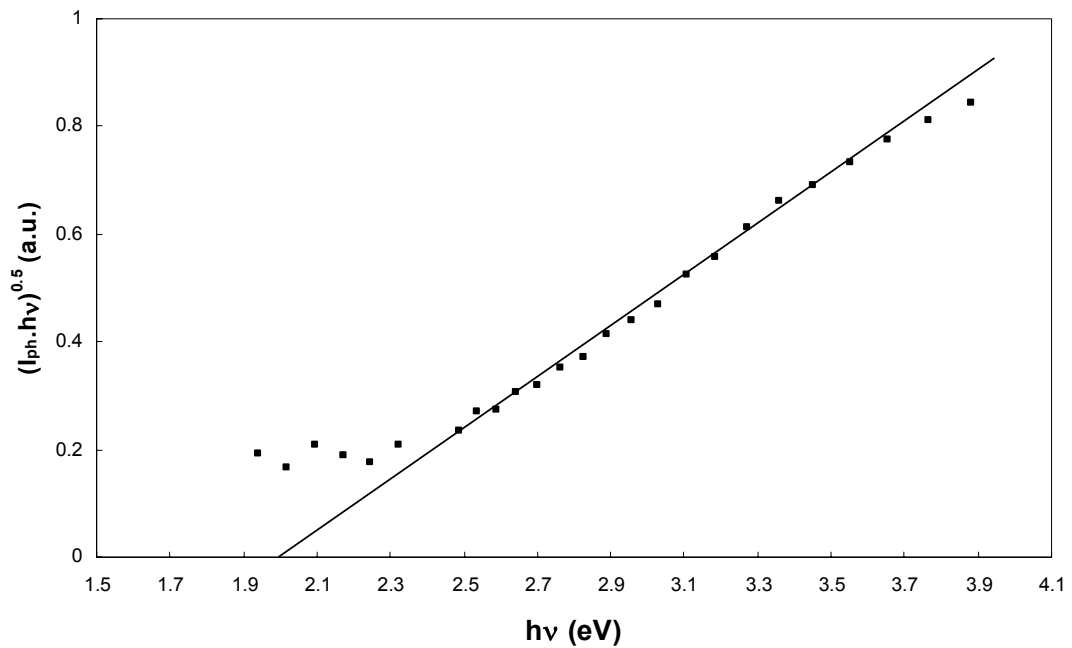


Figure 4.14. $(I_{ph} \cdot h\nu)^{0.5}$ vs. $h\nu$ plot for 316L in a borate solution at 400mV. The linear extrapolation gives a bandgap value around 1.95eV.

Region (b) Below 300-200mV (in the n-type region): all three stainless steels (316L, 304L and 254SMO) showed two linear portions and the results can be interpreted in one of two ways.

- **Interpretation I** (considering a single linear portion): Figure 4.15 is an extrapolation of a $(I_{ph} \cdot h\nu)^{0.5}$ vs. $h\nu$ plot for 316L in a borate solution, in this case at -100mV. Considering the single linear portion, which extends from 2.9eV to 3.9eV, the extrapolated bandgap value becomes around 2.5eV. However, the bandgap value obtained by this method varied both with the applied electrode potential and with the type of stainless steel being investigated. Figure 4.16 shows the variation of the bandgap of the films of different stainless steels in the n-type region (800mV to -400mV). All three stainless steels show bandgaps around 1.95 ± 0.05 eV in the potential range from 800mV to 400mV of Region (a). However, on stepping down the potential from 200mV to 100mV the bandgaps calculated for the three stainless steels started to diverge (Table 4.02). For example in the potential region from 100mV down to -200mV the bandgap variations were: 316L from 2.25 ± 0.05 eV to 2.6 ± 0.05 eV; 304L from 2.20 ± 0.05 eV to 2.55 ± 0.05 eV; and 254SMO from 2.15 ± 0.05 eV to 2.3 ± 0.05 eV. From Figure 4.16 it can also be seen that the bandgap of 304L lags slightly behind that of 316L whilst 254SMO has the smallest bandgap and showed less potential dependence.

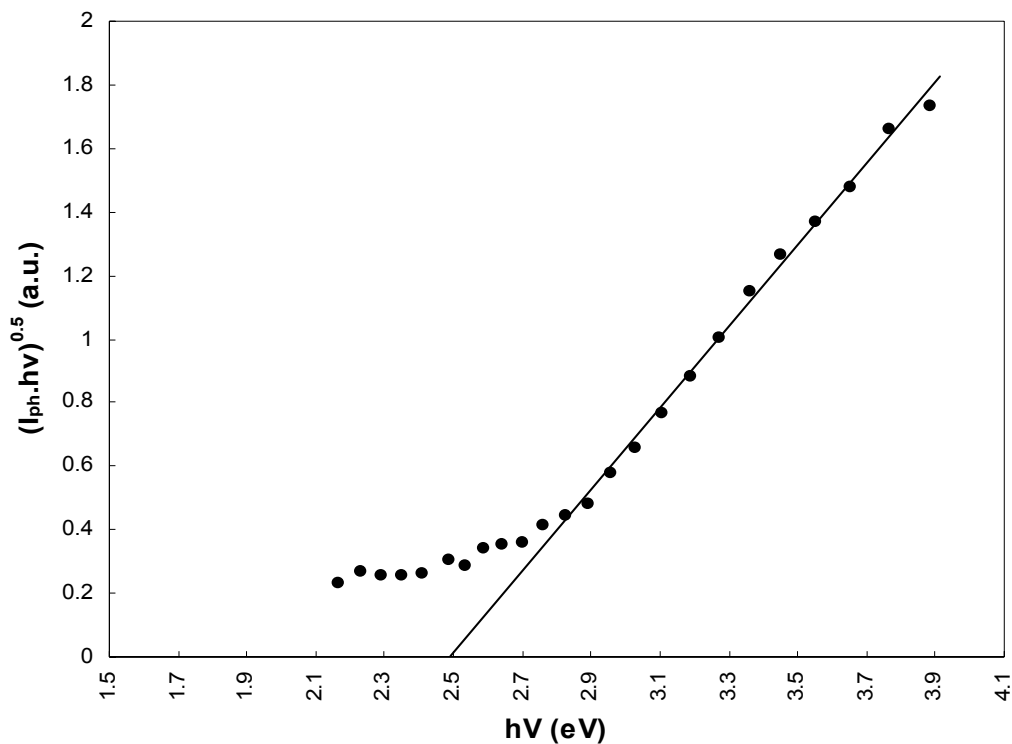


Figure 4.15. $(I_{ph} \cdot h\nu)^{0.5}$ vs. $h\nu$ plot for 316L in borate solution at -100mV. The extrapolation yields a bandgap value around 2.5eV.

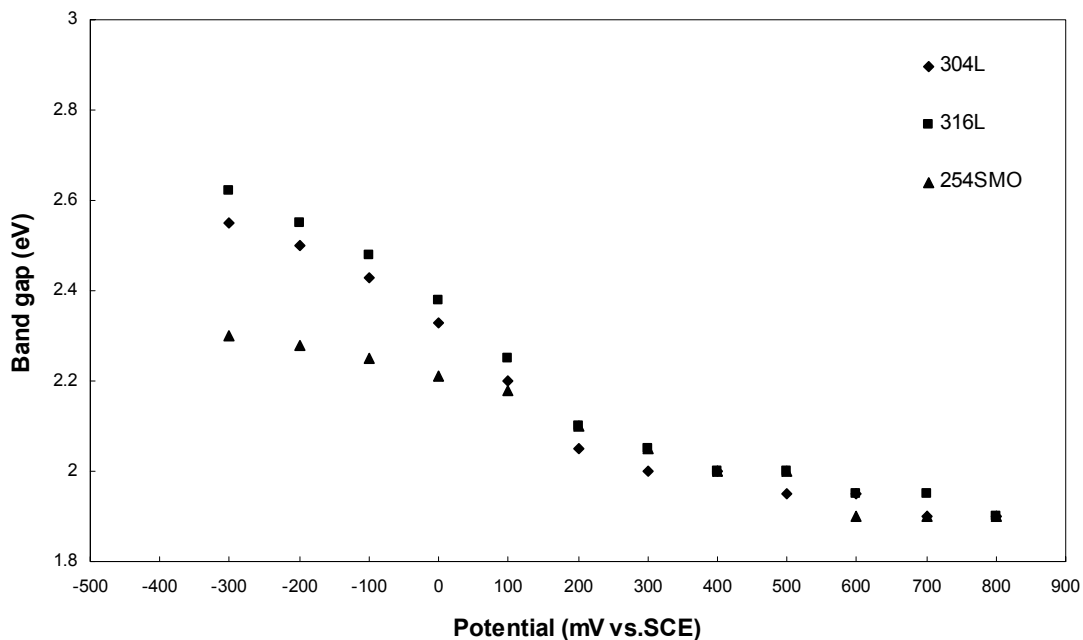


Figure 4.16. Dependence of the bandgap on the electrode potential for 316L, 304L and 254SMO between -400mV and 800mV. Note that each bandgap reading has an error limit of ± 0.05 eV.

Stainless steel	300mV	200mV	100mV	0mV	-100mV	-200mV	-300mV
316L	2.05	2.1	2.25	2.38	2.48	2.60	2.62
304L	2.05	2.1	2.2	2.34	2.43	2.5	2.55
254SMO	2.0	2.05	2.18	2.2	2.25	2.28	2.3

Table 4.02. Bandgap values in eV of three stainless steels according to Figure 4.16.

- Interpretation II** (considering two linear portions): The same $(I_{ph}\cdot h\nu)^{0.5}$ vs. $h\nu$ plot for 316L that was shown in Figure 4.15 can also be interpreted in a different manner considering two linear segments (Figure 4.17). The existence of two linear regions starts only at potentials below 200mV on the reverse scan. It is possible that these two linear regions are due to two different oxides. Table 4.03 summarises the bandgap values for three stainless steels when one uses the two oxides assumption. It can be seen in this case that the bandgaps become independent of potential. In addition, the larger bandgap has the same set of values as observed in the p-type region [see the next section Region (c)].

Type of stainless steel	E_g (eV) (200mV to -300mV)	
	L ₁	L ₂
316L	1.95±0.05	2.9±0.05
304L	1.95±0.05	2.8±0.05
254SMO	1.95±0.05	2.4±0.05

Table 4.03. Bandgap values of different stainless steels for case II.

Some of the bandgap values tabulated in Table 4.03 have similarities to experimental and theoretical findings (see Appendix D). The $E_g=1.9\text{eV}$ can be assigned to either Fe_2O_3 or $\text{Fe}(\text{OH})_3$ and $E_g=2.9\text{eV}$ is nearly equal to the theoretical bandgap value of FeCr_2O_4 . There are several possible candidate values for the $E_g=2.4\text{eV}$ observed with 254SMO including $\text{Cr}(\text{OH})_3$ (2.4eV), $\text{Ni}(\text{OH})_2$ (2.1eV), FeO (2.4eV) and NiFe_2O_4 (2.15eV).

The validity of these two interpretations (I and II above) will be explored in the discussion section.

Region (c) The bandgap values estimated for the p-type region (-800mV to -900mV) did not show a significant dependence on the electrode potential. However, due to the weak signals in this region the photocurrent can be recorded over the range -800mV and -900mV, which may be too short a window to draw firm conclusions on its potential dependence. The following are bandgap values estimated for this potential region for three different stainless steels:

- 316L = $2.9 \pm 0.05 \text{ eV}$;
- 304L = $2.8 \pm 0.05 \text{ eV}$;
- 254SMO = $2.4 \pm 0.05 \text{ eV}$.

The relative magnitude of these bandgaps is constant with that found at the negative potential end of the n-type region when interpretation (II) was used.

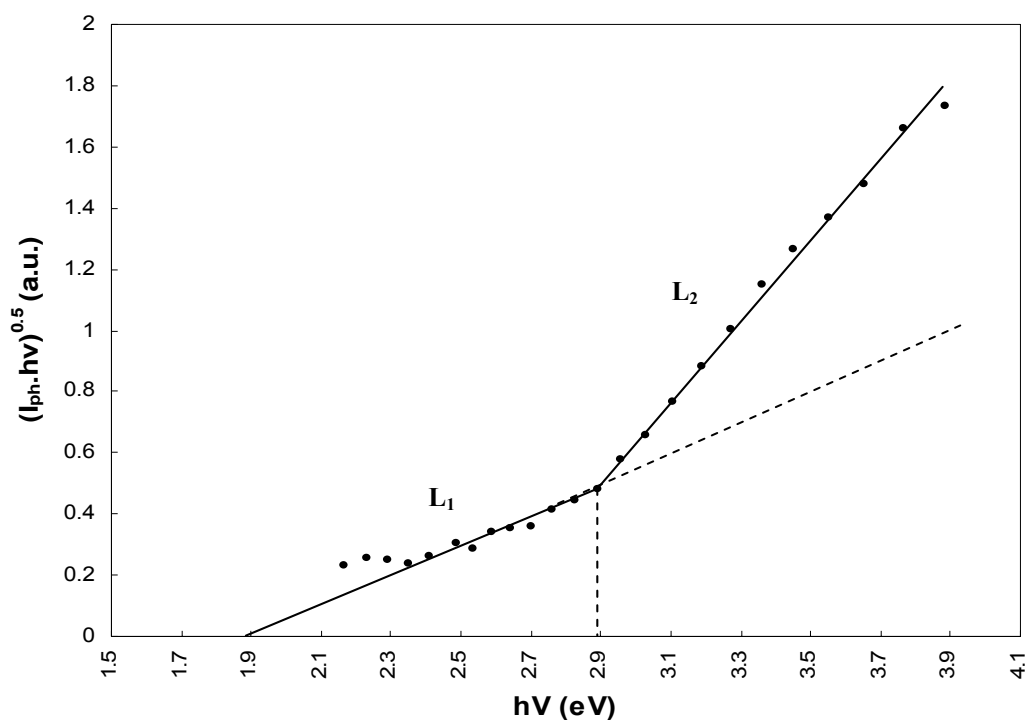


Figure 4.17. $(I_{\text{ph}} \cdot h\nu)^{0.5}$ vs. $h\nu$ plot for 316L in a borate solution at -100mV. Two linear extrapolations; L_1 and L_2 yield two different bandgap values, 1.9eV and 2.9eV, respectively.

4.5.3 Investigation of cathodic photocurrent of stainless steel

The cathodic photocurrent observed in stainless steel passive films was investigated to confirm its p-type behaviour rather than a photoemission phenomenon. External photoemission occurs due to the direct electron injection from the metal to the solution. Because the passive film is only a few nanometers thick electrons could theoretically tunnel through it. According to the theory²¹ the dependence of photoemission current I'_{ph} (in solution) on the electrode potential V_e and on the photon energy $h\nu$ is given by the “5/2 power law”:

$$I'_{ph} = A'(h\nu - h\nu_0 - eV_e)^{5/2} \quad \dots\dots\dots (2.50)$$

where $h\nu_0$ is called the photoelectric threshold that can be obtained by extrapolating the plot of $I'_{ph}{}^{0.4}$ vs. electrode potential to $I_{ph}=0$, under the irradiation with light at a fixed wavelength. Based on Equation (2.50), the cathodic threshold energy / photoemission energy (E_{th}) for direct photoemission in solution can be obtained from an extrapolation of a plot of $I'_{ph}{}^{0.4}$ vs. $h\nu$.²² Furthermore the slope of E_{th} vs. V_e plot should be nearly equal to 1 eV/V.

In the case of the stainless steel passive films investigated in this thesis, a cathodic photocurrent was observed under cathodic polarization. This photocurrent has been tested for photoemission process according to the above relationship. Figure 4.18 shows a plot of $I'_{ph}{}^{0.4}$ vs. $h\nu$ for 316L SS and the extrapolated E_{th} vs. V_e (inset). It can be seen that although a linear relationship for $I'_{ph}{}^{0.4}$ vs. $h\nu$ plots could be claimed, the fit is poor. However, more importantly the E_{th} vs. V_e plot yields a slope of about 4.5eV/V, much larger than the theoretical value. Hence, it can be verified that the cathodic photocurrent observed in stainless steel is not due to a photoemission process, making the presence of a p-type semiconductor the most likely explanation.

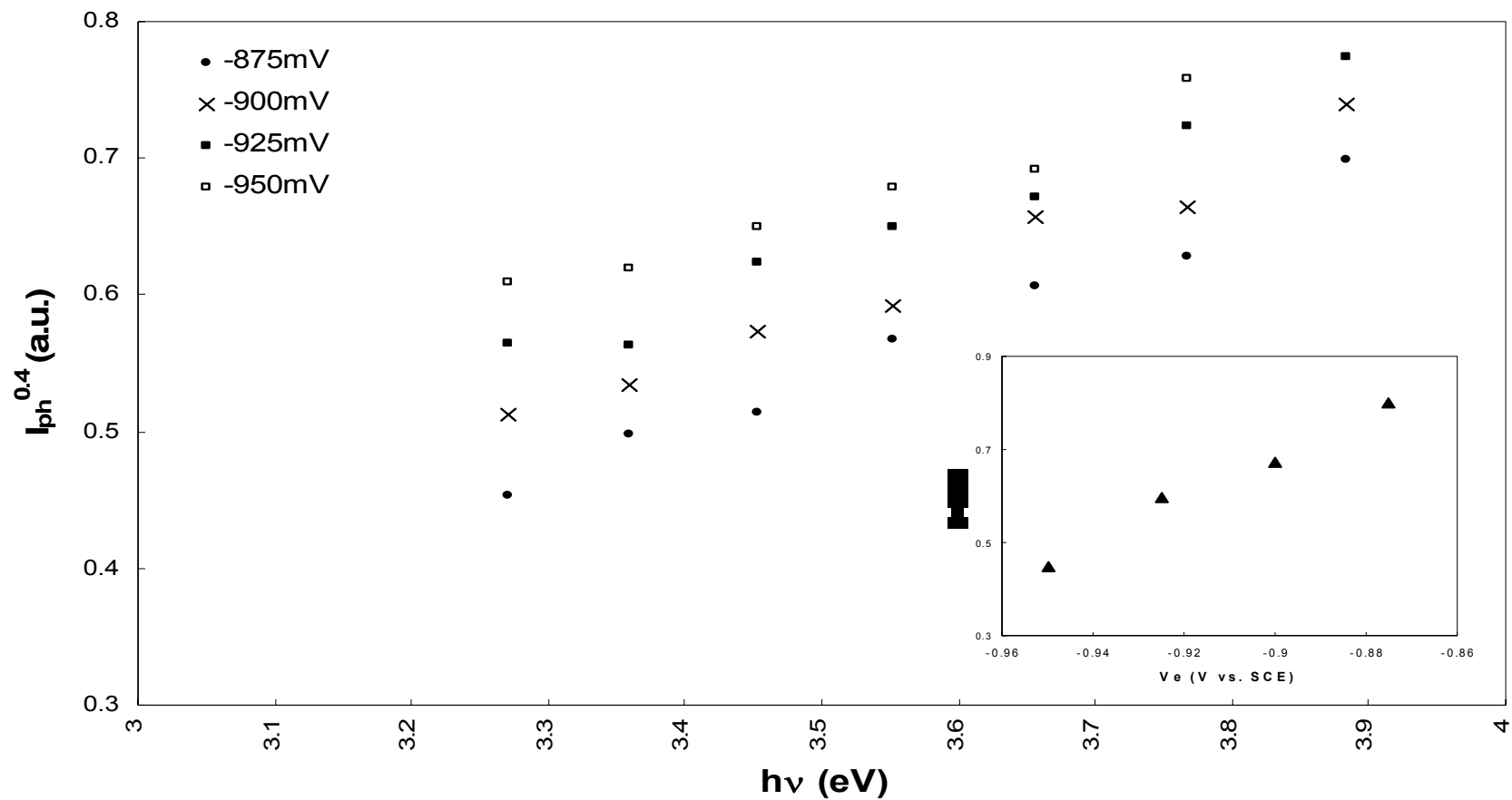


Figure 4.18. Plot of $I_{ph}^{0.4}$ vs. $h\nu$ for 316L stainless steel in a 0.1M borate solution under cathodic polarization and inset is the extrapolated E_{th} vs. V_e .

4.5.4 Photocurrent transients

Photocurrent transients from the three different stainless steels (316L, 304L and 254SMO) were recorded at 100mV intervals on the reverse scan after initially polarising the samples potentiodynamically at 10mV/min from -1.0V to 800mV (see Section 3.5). The samples were held for 10 minutes at each recording potential and then illuminated for 10 seconds. Two sets of experiments were conducted:

Set 1) polarised up to 800mV subsequently subjected to light $\lambda=325\text{nm}$ (3.82eV, with an intensity $\sim 5.77 \text{ mW} / \mu\text{m}^2$);

Set 2) polarised up to 800mV subsequently subjected to light $\lambda=514\text{nm}$ (2.42eV, with an intensity $\sim 1.36 \text{ mW} / \mu\text{m}^2$);

The results obtained from each set are summarised below.

Set 1: The shape and amplitude of photocurrent transients depend on several factors, such as electrode potential, energy of the light, light intensity, film thickness and electrolyte composition.²³⁻²⁷ Figure 4.19 shows the photocurrent transients recorded for 316L at different potentials. The transients shown in Figures 4.19 (a) to (e) in which the photocurrent rises to a plateau value were recorded at the higher potential values. The amplitude of the plateau declined dramatically as the polarising potential was reduced. These anodic steady state transients substantiate the n-type behaviour of the oxide film. The current transient at 100mV Figure 4.19 (f) shows an initial anodic peak immediately after the light was switched on, which decayed towards an anodic steady state plateau value. When the light was turned off a cathodic spike was recorded. This is typical of surface recombination processes via surface

states²³ or a back reaction of the photogenerated species.²⁸ This feature continued until -300mV, however, a gradual reduction in the amplitude of the steady state photocurrent was observed. Around -400mV [Figure 4.19 (h)], only the anodic and cathodic spikes remained, this could signify a complete recombination, which is expected to occur near the flat band potential.^{23,26} When the potential reached -600mV [Figure 4.19 (i)], the spikes switched signs, i.e. a cathodic “on” spike and an anodic “off” spike. The cathodic peak at -800mV [Figure 4.19 (j)] clearly indicates p-type semiconductor characteristics.

The main characteristic features of photocurrent transients of 254SMO and 304L were similar to those of 316L.

Set 2: In Set 2, the photocurrent transients were recorded by illuminating the sample with $\lambda=514\text{nm}$ (2.42eV, with an intensity $\sim 1.36 \text{ mW}/\mu\text{m}^2$) light after polarising the sample up to 800mV. Figure 4.20 shows the relevant photocurrent transients obtained for 316L. Anodic transients appeared at the more positive potentials, indicating the n-type semiconductivity. Again recombination spikes started to appear at around 100mV and became significant at around -100mV [Figure 4.20(c)]. However, the signal became weaker toward more negative potentials and no photocurrent transient could be observed below -400mV. This explicates either an absence of any film with semiconductive properties at potentials more negative than -400mV or a semiconductive film with a higher bandgap energy (larger than 2.42eV) such that the energy of the light was insufficient to generate a photocurrent. The photocurrent transient behaviour of 304L was analogous to 316L.

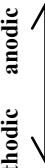
In contrast to 316L (and 304L), where no photocurrent was observed below -400mV with 254SMO (Figure 4.21) the anodic photocurrent transients were gradually changed to cathodic photocurrent transients below -500mV. This clarifies the existence of p-type semiconductive film on 254SMO at more negative potentials (more negative than -500mV) with a bandgap energy less than 2.4eV. These observations are consistent with the bandgaps determined for the passive films of 316L, 304L and 254SMO by photocurrent spectroscopy (Table 4.03).

The shapes of the various photocurrent transients formed at different potentials can be explained by extending the interpretations made by Preusser *et al.*²⁷, who investigated films on titanium and considered a narrow band of localised electronic states (mid bandgap states) to be situated within the bandgap. The following mechanism is proposed to explain the photocurrent transients results of stainless steels passive films in a borate solution (Figures 4.19-4.21) extending Preusser *et al.*'s²⁷ interpretation.

The mid bandgap states mentioned above are filled or emptied, as the Fermi level passes through them [Figure 4.22(a)]. Therefore once irradiation of the electrode commences (n-type semiconductor), there are two possible fates for the electrons that have been excited into the conduction band:

- (i). the electrons migrate to the bulk; leading to a photocurrent in the normal way [Figure 4.22(b)]. The abrupt initial increase in the photocurrent [Figures 4.19(a) to (e)] is due to this;
- (ii). the electrons drop into the empty localise mid bandgap states filling them, such that these states act as traps [Figure 4.22(c)]. Eventually the trapped electrons drop back down to the valence band, emptying the trap to receive another.

cathodic
anodic



cathodic
anodic




Figure 4.19. Set 1. Photocurrent transients of 316L stainless steel in a 0.1M borate solution measured with monochromatic illumination ($\lambda=325\text{nm}$) at different potentials: (a) 800mV; (b) 600mV; (c) 400mV; (d) 300mv; (e) 200mV; (f) 100mV; (g) -100mV; (h) -400mV; (i) -600mV; (j) -800mV.

cathodic
↑
anodic

Figure 4.20. Set 2. Photocurrent transients of 316L stainless steel in a 0.1M borate solution measured with monochromatic illumination ($\lambda=514\text{nm}$) at different potentials: (a) 800mV; (b) 400mV; (c) 0mV. No photocurrent observed below -400mV.

cathodic
↑
anodic

cathodic
↓

Figure 4.21. Set 2. Photocurrent transients of 254SMO stainless steel in a 0.1M borate solution measured with monochromatic illumination ($\lambda=514\text{nm}$) at different potentials: (a) 800mV; (b) 400mV; (c) 0mV; (d) -800mv.

electron. Initially, this effect is rapid, as all the localised states are empty, but at longer times, it reaches a steady state situation [Figures 4.19(a) to (e)]. Once the light turns off; the normal photocurrent first dies, leading to an abrupt decrease in the observed photocurrent, however a residual photocurrent persists for a while (Figure 4.19). This photocurrent relaxation behaviour can be explained by tunnelling of electrons trapped in mid bandgap states within the space-charge region and at energies above the conduction band of the bulk of the oxide [Figure 4.22(d)]. This effect is particular likely to occur when the doping density is high such that the band bending in the space-charge layer is steep. In Section 4.6.2, it will be shown that the doping levels in the oxide films of stainless steels are indeed high. This feature continues until around 100mV when anodic and cathodic spikes start to appear [Figure 4.19(f)] indicating surface recombinations.²³ It is clearly evident that this particular photocurrent transient feature starts to appear at around the same potential (100mV), where a phase change occurs (see cyclic voltammograms of 316L and 254SMO, Figures 4.01 and 4.02). However, it is not known which species acts as the surface recombination centres.

As the potential is made more negative, the amplitudes of photocurrent transients decreased as the space charge length decreases. However, beyond about -500mV, sharp negative photocurrent transients features appeared, signifying a p-type behaviour. Figure 4.19(j) suggests that the effects of mid bandgap states are not significant under both light “on” and “off” conditions when the oxide film displays p-type behaviour.

The intensity of the He-Cd laser ($\sim 5.77 \text{ mW} / \mu\text{m}^2$) was higher than the Ar-ion laser ($\sim 1.36 \text{ mW} / \mu\text{m}^2$), hence steady-state occupancy of the localised states was reached

much faster with the former illumination than with the latter (compare current transients in Figures 4.19 and 4.20).

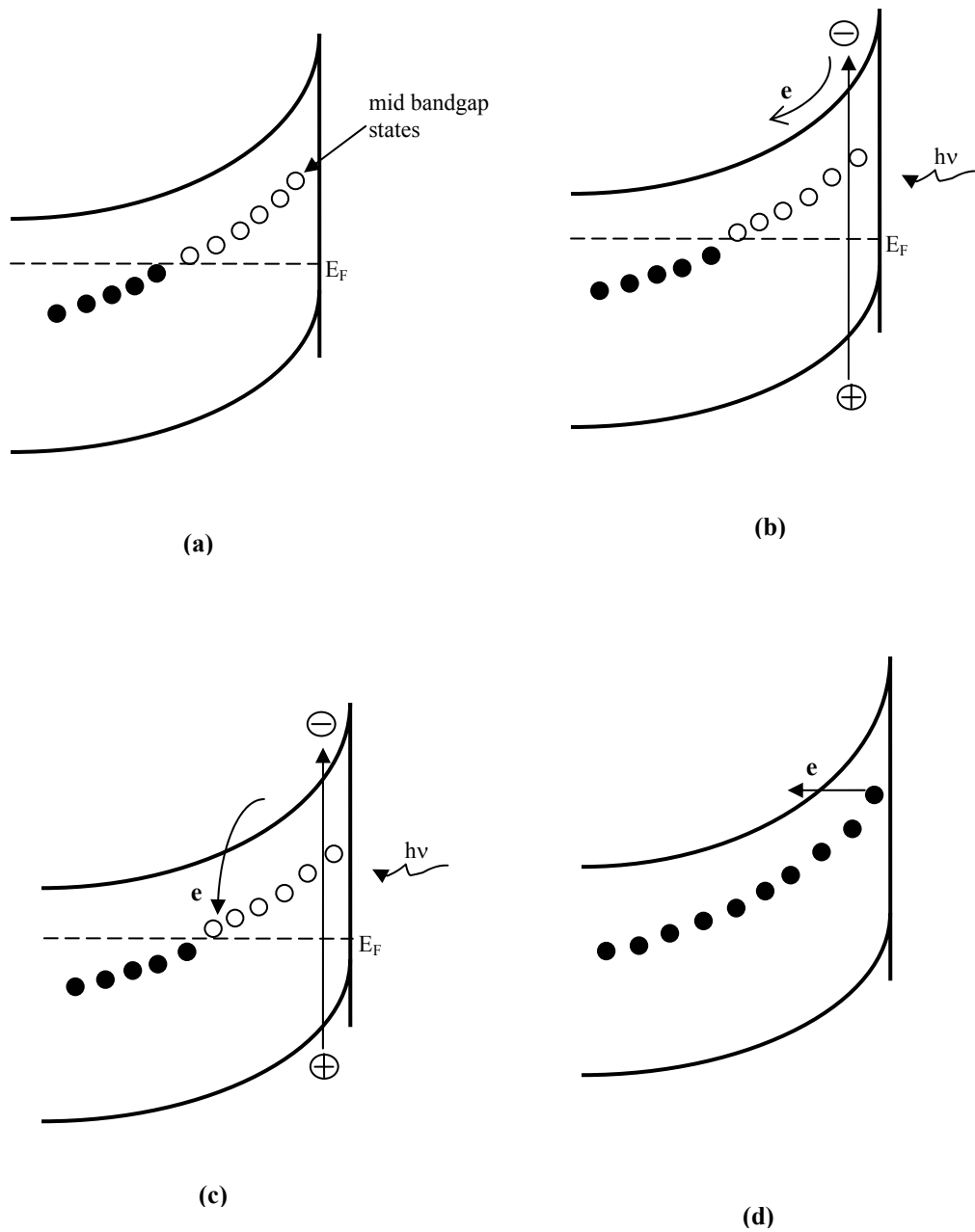


Figure 4.22. Schematic representation of the effect of mid bandgap states on the photocurrent in an n-type semiconductor: (a) band diagram with mid bandgap states (either full or empty); (b) electrons migrate to the bulk, leading to a photocurrent (when the light is on); (c) electrons drop and fill empty mid bandgap states (when the light is on); (d) electrons tunnel to the conduction band (when the light is off).

4.6 Capacitive measurements

4.6.1 Capacity-potential measurements

Capacitance measurements were recorded for three stainless steels; 316L, 304L and 254SMO in a 0.1M borate solution in order to scrutinise the capacitance-potential relationship and the capacitance-frequency relationship.

Figure 4.23 shows the capacitive-voltage relationship recorded at 500Hz on the reverse sweep after the film was grown up to 800mV. It is apparent that the behaviour of 316L and 304L is very similar over the whole potential range. From 800mV to 600mV a decrease in the capacity can be observed. This initial decrease of the capacitance values can be attributed to either the strong dependence of the Faradaic current on the potential in the transpassive region or the consequence of thickening of the oxide in this potential region. This has also been observed on iron electrodes, where it was explained in terms of an inversion layer developing in the passive film so that it becomes conductive.^{29,30} Conductivity differences due to transpassivation have also been argued to cause this capacitance increase.³¹

The capacity remained low and approached nearly a constant value in the potential region of 600mV to -200mV, except a small hump appearing around 100mV. The small hump could be associated with Faradaic currents from the reduction phase change seen in the cyclic voltammograms (Figures 4.01 and 4.02). Below -200mV, the capacitance starts increasing as a consequence of the reduction of the space charge layer thickness with the reduction in band bending. Capacitance reached a peak at a potential between -400mV and -500mV; with a value of $\sim 25 \mu\text{F cm}^{-2}$ suggesting that the Helmholtz double layer now dominated the capacitance response. At more negative potentials than -500mV, in the p-type semiconductive region (according to

the photocurrent spectroscopy results, Section 4.5), the capacitance declined as the space charge width again increased.

The 254SMO behaved in a slightly different manner than the other two stainless steels. At the most positive potentials (800mV to 600mV), the capacitance of 254SMO was greater than that of both 304L and 316L, in contrast to the potential range of the passive region where the 254SMO capacitance was the lowest. From Figure 4.23, it can be observed that the capacitance of 254SMO continued to lie below that of the other two grades towards more negative potentials. This diversity has been attributed by Hakiki *et al.*³² to a decreased number of donor species due to the high Mo content in super austenitic stainless steels; however, this explanation is at odds with the similarity between the capacitances of 316L and 304L.

Figure 4.24 shows how the frequency of the applied perturbation influences the capacitance dependence on the applied potential. It can be observed that there is a strong frequency dependence for lower frequencies (less than 10Hz), but the capacitance becomes almost independent of frequency above ~100Hz. The dependence of the capacitance on frequency is further shown in Figure 4.25. Di Paola³⁰ previously obtained similar results for the same stainless steels.

Possible reasons behind the frequency dependence of the capacitance behaviour were discussed in Section 2.5.5. This particular behaviour has been used to signify the amorphous and the nstrongly disordered semiconductor nature of stainless steel passive films.³⁰ Amorphous semiconductors are characterised by a high density of states between the valance and the conduction band, and charging of these states can lead to the strong frequency dependent capacitance behaviour (see Section 2.5.4).^{30,33}

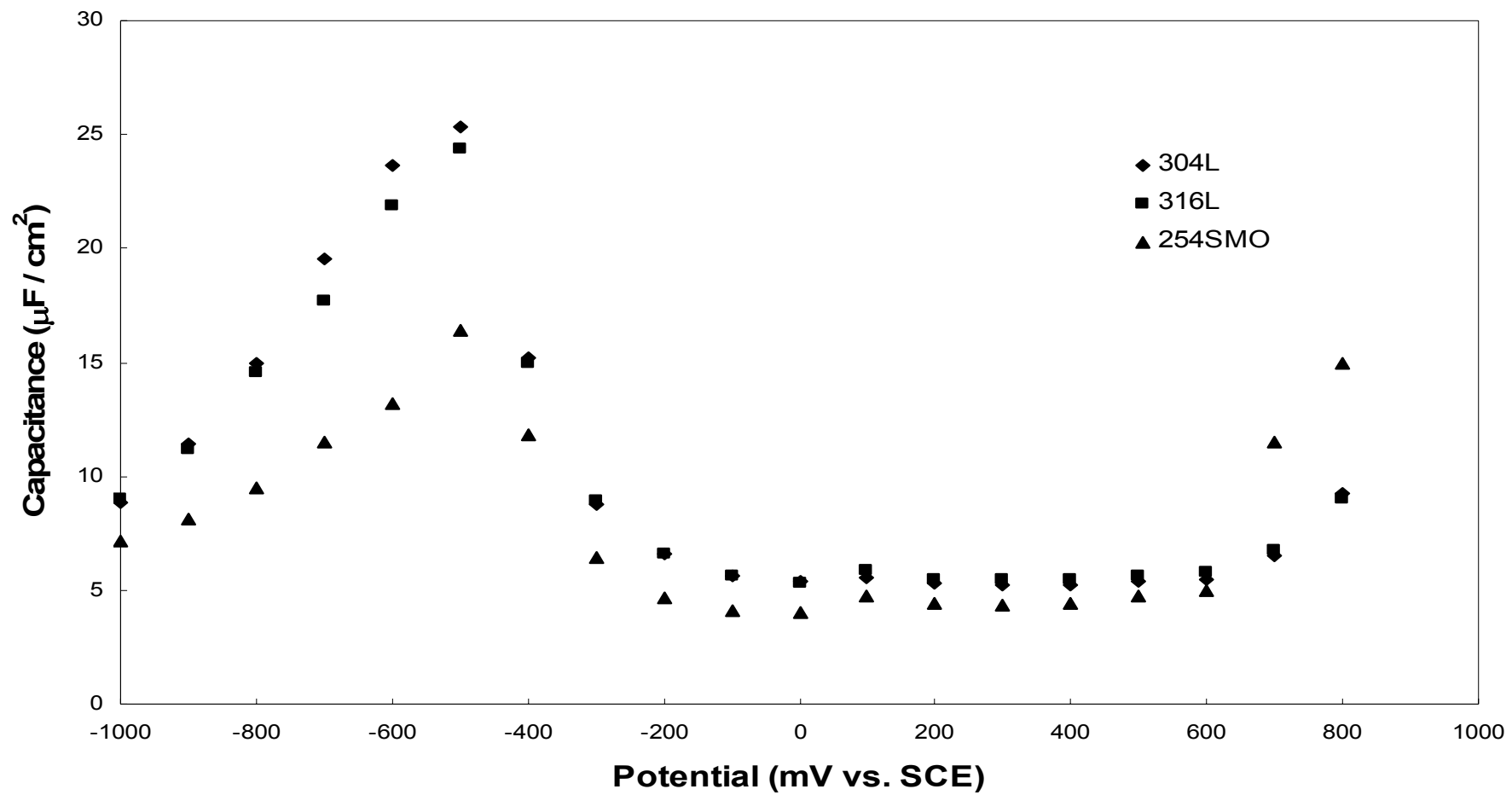


Figure 4.23. Plots of capacitance vs. potential for passive films on 304L, 316L and 254SMO in a 0.1M borate solution.

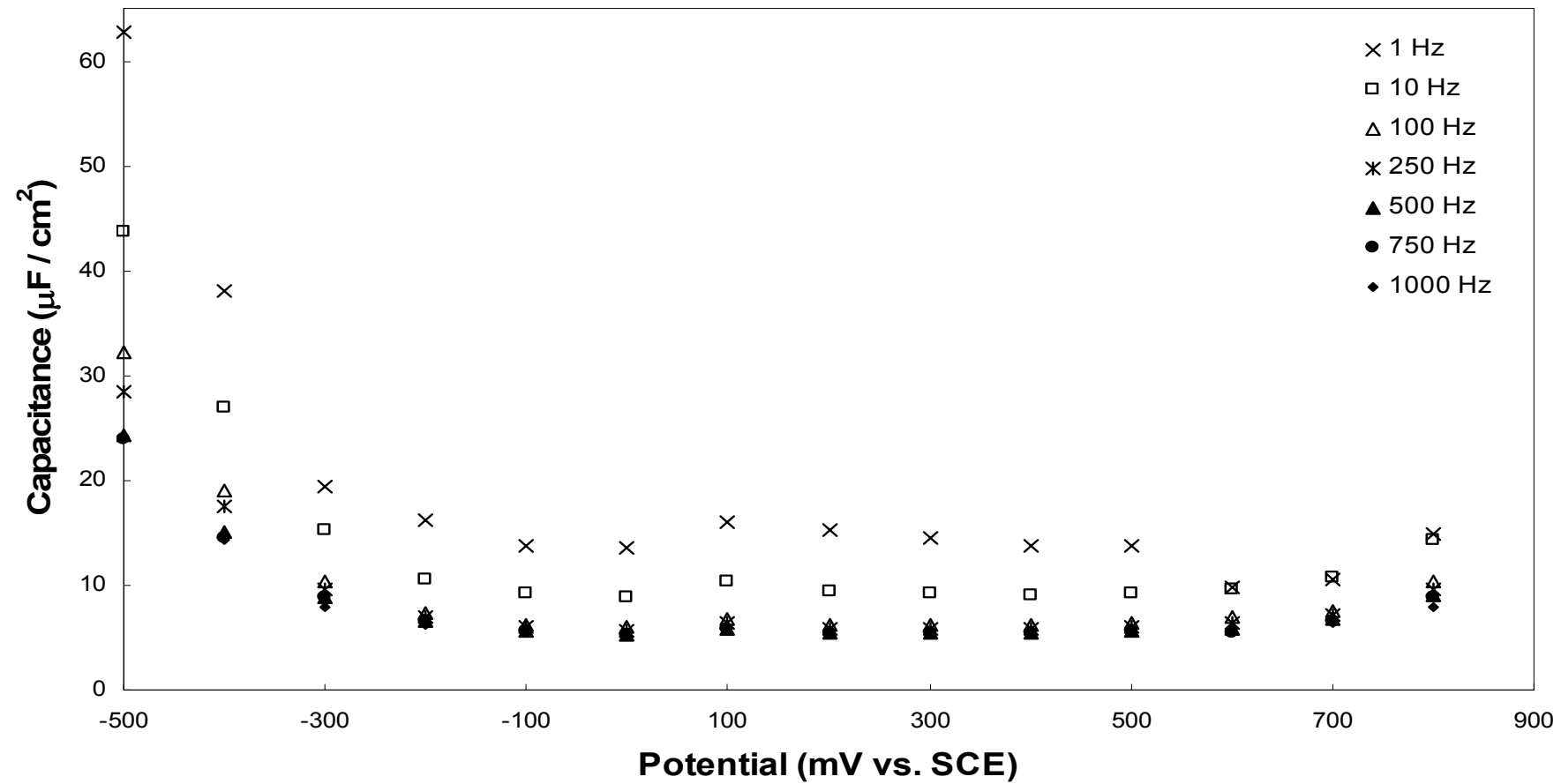


Figure 4.24. Plots of capacitance vs. potential for 316L in a 0.1M borate solution at different frequencies.

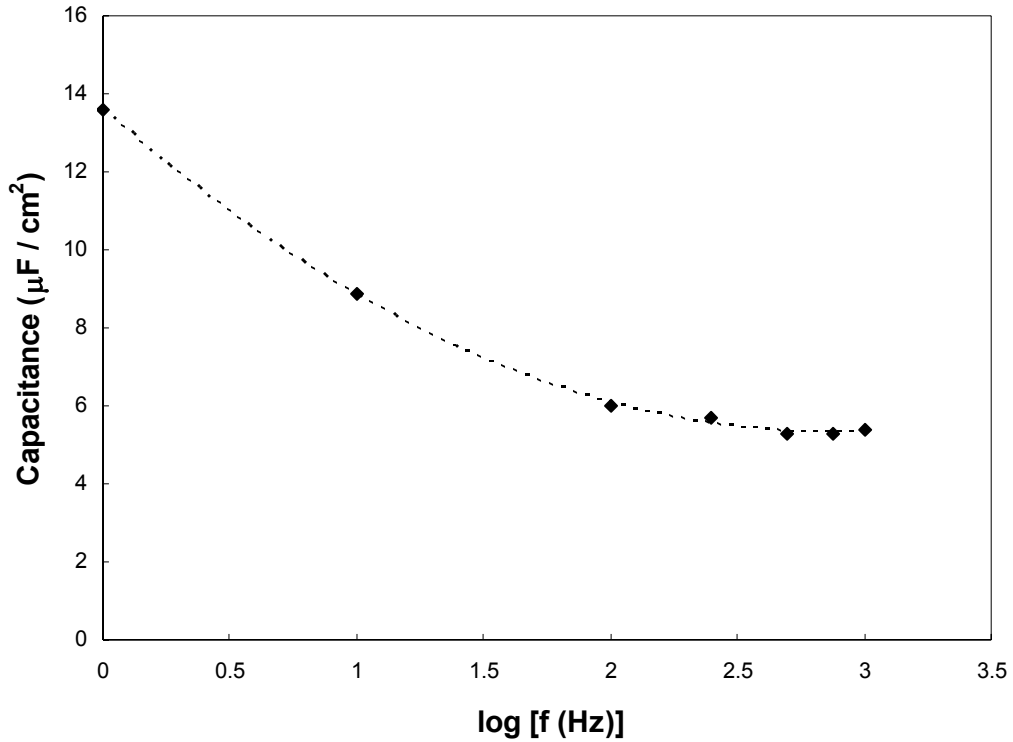


Figure 4.25. Plot of capacitance vs. log (frequency) of 316L in a 0.1M borate solution at 0mV.

4.6.2 Mott-Schottky (MS) plots

Capacitance behaviour can be studied under the Mott-Schottky approach to yield a better understanding of the electronic structure of the passive films (see Sections 2.5.3 and 2.5.5). By analysing the MS plots, it is possible to obtain:

- the type of semiconductivity (a positive slope for n-type and a negative slope for p-type);
- donor (N_d) or acceptor (N_a) concentrations;
- flat band potential (V_{fb}).

Figure 4.26 shows the MS plots using Equation(2.33) $\left[\frac{1}{C_{sc}^2} = \frac{2}{e\epsilon\epsilon_0 N_d} \left(V_e - V_{fb} - \frac{kT}{e} \right) \right]$

for three stainless steels; 304L, 316L and 254SMO in a 0.1M borate solution recorded at 500Hz on the reverse sweep after the film was grown up to 800mV. All three

grades showed some common characteristics despite different amplitudes and slopes of the plots as summarised below starting from the most positive potential.

- a) In the region of 800mV to 400mV the amplitude of the plot increased. This may be due the thickening of the passive film on reverse sweep, assuming it was dissolved due to transpassivation while sweeping forward. Another possibility is the oxide is getting less conductive in this region, this can also widen the space charge region.³¹
- b) At 300mV the amplitude started to decrease for a short potential range until 100mV and then started to increase, signifying a clear minimum at 100mV. This significant change at 100mV has been used as the basis of the an argument for the presence of two donor levels by some authors.^{32,34,35} These authors postulated a shallow donor level and a deep donor level below and above this potential region, respectively, based on the two linear portions of the MS plots. However, based on experimental results in this thesis (Sections 4.1 and 4.7), it is quite evident that a phase change occurs at 100mV, causing the change in the capacitance behaviour.
- c) A linear region in the MS plots for all three grades can be observed at potentials negative of 0mV. The positive slope confirms the n-type semiconductivity of the passive film at these potentials and can be used to obtain donor concentrations.
- d) Negative slopes were observed below -500mV, confirming a switch to p-type behaviour and can be used to obtain acceptor concentrations.

Figure 4.27 (MS plots of 316L at different frequencies) reveals a convergence of all the slopes at a common point close to -450mV regardless of frequency. This behaviour was consistent for all three grades except for different slopes (hence different donor concentrations), confirming the validity of the MS plots to locate flat band potential and to calculate acceptor and donor concentrations.

Donor and acceptor concentrations: Donor (N_d) and acceptor (N_a) concentrations calculated using the MS plots for three grades (at pH=9.2) are tabulated in Tables 4.04 and 4.05, respectively. The relative permittivity (ϵ) was assumed as 15.6 as in the literature,³⁰ although it is recognised that there is some controversy in using the same ϵ value for all frequencies. However, it has been argued that any error caused by this assumption is not significant; the dielectric constant of iron and chromium oxides tends to be in the range of 10~20.^{30,32} In addition, using $\epsilon=15.6$ allows an easy comparison with previously published results.

According to data in Tables 4.04 and 4.05, it is evident that the donor and acceptor concentrations in the passive films on 304L and 316L stainless steels are quite similar, as are the frequency dependencies of these species. However, both the donor and acceptor concentrations in the passive film of 254SMO had stronger frequency dependencies, such at lower frequencies they were more numerous than with 304L/316L, but this order reversed at high frequencies (check Equation 2.42, the time constant of the mid bandgap states to ionise). The main reason for different donor densities (or acceptor densities in p-type) of 254SMO is probably the influence of different donor species (or acceptor species).

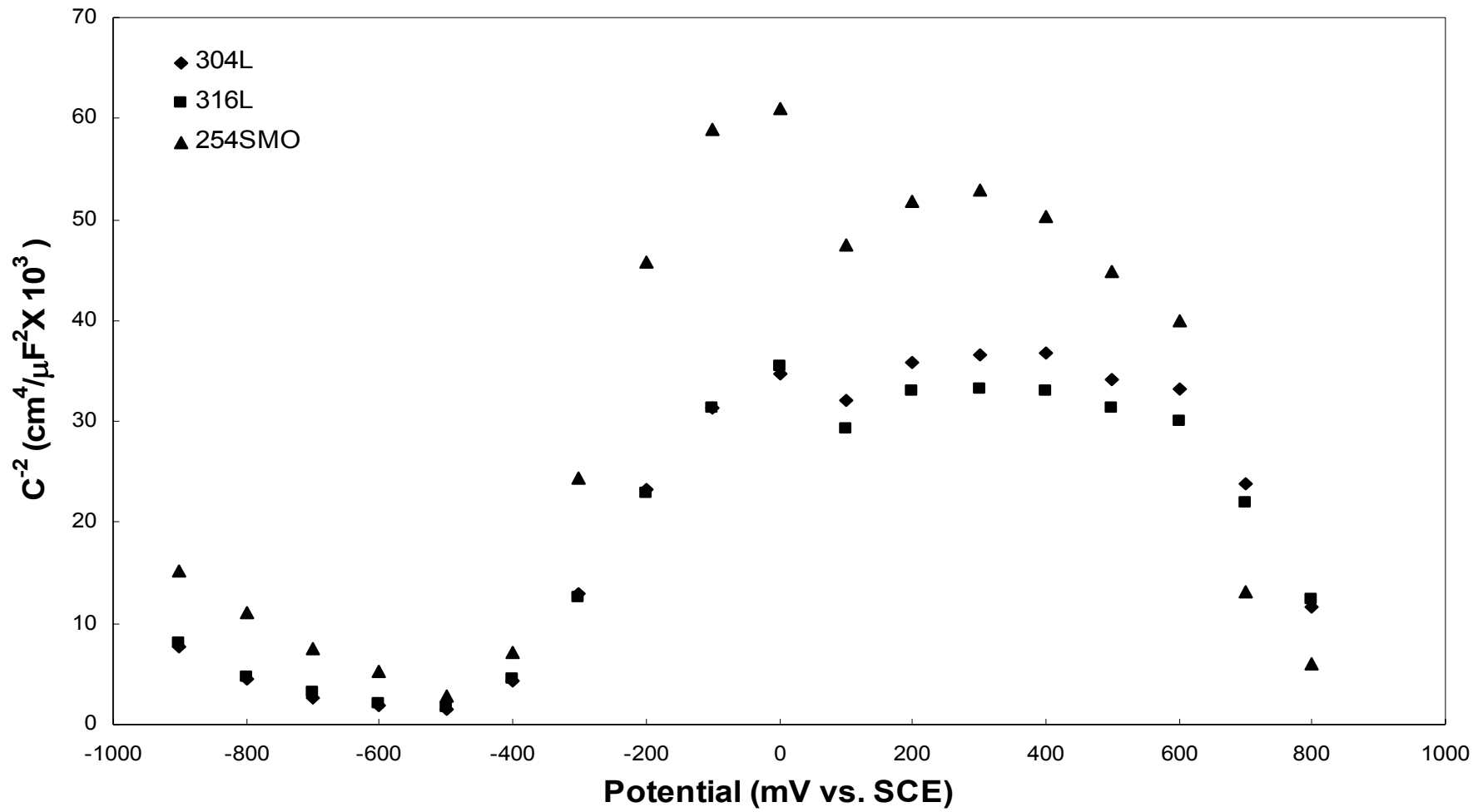


Figure 4.26. Mott-Schottky plots for 304L, 316L and 254SMO in a 0.1M borate solution (pH=9.2) at 500Hz.

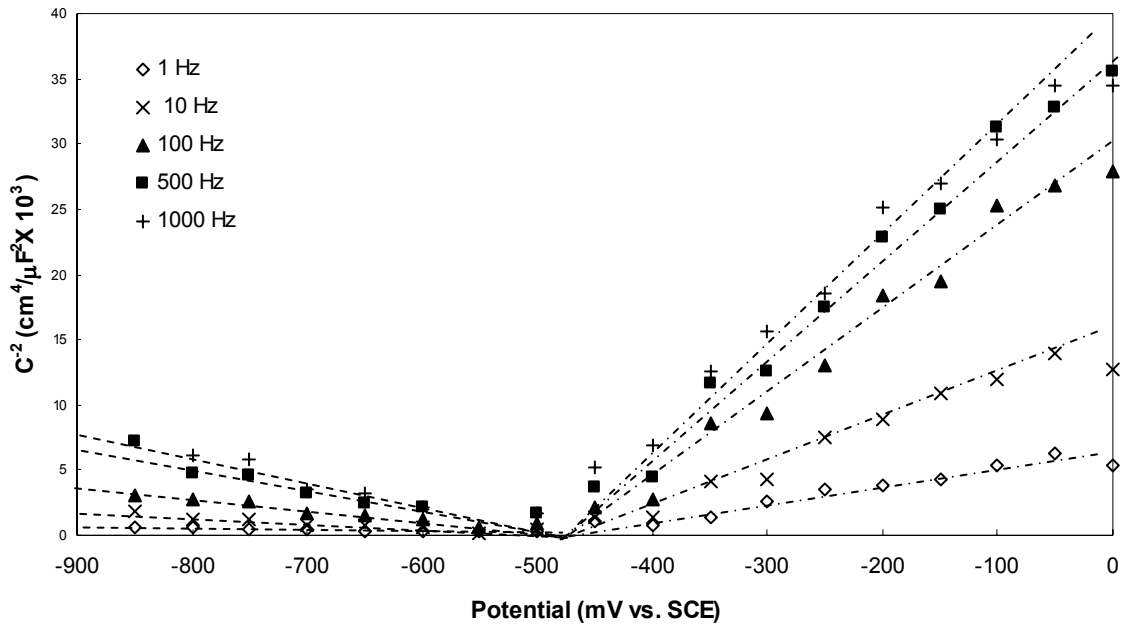


Figure 4.27. Mott-Schottky plots for 316L in a 0.1M borate solution at different frequencies. Mott-Schottky plots for grades 304L and 254SMO also converged to common intercepts.

N_d ($\times 10^{20} \text{ cm}^{-3}$) (at pH=9.2)			
f (Hz)	304L	316L	254SMO
10	2.63	2.98	5.83
100	1.39	1.44	1.92
500	1.19	1.19	0.63
1000	1.20	1.27	0.64

Table 4.04. Donor concentrations of 316L, 304L and 254SMO in a 0.1M borate solution (pH=9.2) at different frequencies.

N_a ($\times 10^{21} \text{ cm}^{-3}$) (at pH=9.2)			
f (Hz)	304L	316L	254SMO
10	2.28	1.93	3.93
100	0.89	0.87	1.71
500	0.55	0.54	0.38
1000	0.42	0.34	0.37

Table 4.05. Acceptor concentrations of 316L, 304L and 254SMO in a 0.1M borate solution (pH=9.2) at different frequencies.

Figure 4.28 shows a plot of donor concentration versus $\ln(\text{frequency})$ for the three different stainless steels and further signifies the frequency-donor density diversity. At the same time, this relationship can be used to shed light on the band structure model in amorphous semiconductors (see Section 2.5.4). The non-linear variation in density of states against $\ln(\text{frequency})$ observed in Figure 4.28 contradicts with the

simplified Di Quarto *et al.*¹⁹ model, in which a constant density of donor states is assumed to exist in the bandgap. (Figure 2.11 and Equation 2.43).

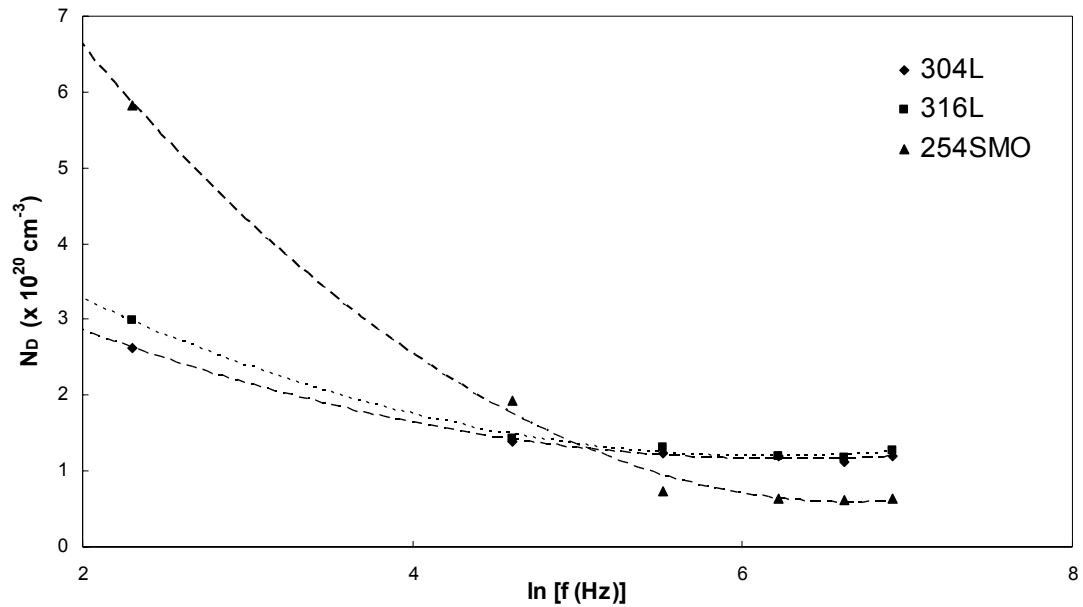


Figure 4.28. The plot of donor density versus ln(frequency) for 304L, 316L and 254SMO in a borate solution (pH=9.2).

Flat band potential: According to Equation 2.33, flat band potentials can be obtained from the Mott-Schottky plots by extrapolation to the abscissa. . The Intersection potential V_i is given by:

$$V_i = V_{fb} + \frac{kT}{e} \quad \dots\dots\dots (4.01)$$

where all symbols have the same meaning as in Equation (2.33).

Determination of the V_{fb} according to Equation (4.01) is correct when the space charge layer capacitance is small compared with Helmholtz layer capacitance, such that the potential drop caused by the applied potential falls entirely across the space charge region within the semiconductor. According to Equation (2.44) the determined V_{fb} can be further corrected for Helmholtz capacitance (C_H).

$$V_i = V_{fb} + \frac{kT}{e} - \frac{\epsilon\epsilon_0 e N_d}{2C_H^2} \dots\dots\dots (2.44)$$

By using Figures 4.23, 4.24, 4.26 and 4.27 along with the data shown in Table 4.04, it is possible to derive the following parameters for 316L in a 0.1M borate solution (pH=9.2) at a perturbation frequency of 500Hz.

- $C_H \sim 25 \mu\text{F} / \text{cm}^2$
- $N_d = 1.19 \times 10^{20} \text{ cm}^{-3}$
- $V_i = -470\text{mV}$

Considering the other parameters (T=301K and $\epsilon=15.6$) Equation (2.44) can be solved as;

$$V_{fb} = -470\text{mV} - 4.87\text{mV} = \mathbf{-475\text{mV}}.$$

Likewise, a virtually identical V_{fb} was obtained for 304L under the same conditions, whilst for 254SMO, V_{fb} was slightly lower at **-472mV**. However, within experimental error it appears that the flat band potential of passive films formed on stainless steels in a 0.1M borate solution may well be independent of the steel composition.

4.7 Raman spectroscopy

The passive films on stainless steels (316L, 304L and 254SMO) grown in a 0.1M borate solution and in a 0.028M NaCl solution were studied using *in situ* Raman spectroscopy for possible identification of various oxide phases formed at different potentials. Experimental results were compared with literature values for the identification of phases present. Tables 4.06 to 4.08 show Raman shifts obtained from the literature for Fe, Cr, Ni and Mo oxides/hydroxides.

There are both advantages and disadvantages in using Raman spectroscopy as a fingerprinting technique to identify the oxide phases. Some of these points were discussed in Section 3.3. The main drawback of Raman spectroscopic characterisation is the possible existence of Raman inactive phases. However, the usefulness of *in situ* Raman as a characterisation technique when the results are supported by other techniques, such as photocurrent spectroscopy will become evident in the Discussion chapter.

4.7.1 Background peaks

First, it was necessary to screen out the Raman peaks caused by the solution (0.1M Na₂B₄O₇) and by the cell's Quartz window to distinguish these from the constituents of the passive films. Figure 4.29 shows the Raman spectrum obtained from borate solution with the Quartz window that without any sample. It revealed bands at:

- 430-436cm⁻¹, 484-486cm⁻¹, 600-605cm⁻¹ and 1066-1070cm⁻¹ peaks for Quartz;
- 743-744cm⁻¹, 878-880cm⁻¹ and 1636-1640cm⁻¹ (water) for the borate solution.⁵⁴

Unfortunately some of the Raman shifts for quartz (e.g. 400cm⁻¹ to 500cm⁻¹, 600cm⁻¹ to 605cm⁻¹) overlap with possible locations of many of the ferrous oxide phases (Table 4.06), making the detection of such oxide phases difficult.

	Reference number						
	36	37*	38	39*	40	41*	42*
$\alpha\text{-Fe}_2\text{O}_3$	225, 247, 293, 299, 412, 489, 613, 1320	302, 405-420	350-500, 1380 (α and γ Fe_2O_3)				
Fe_3O_4	298, 320, 420, 472, 550, 676		670	546-547, 668- 669	616, 665	524-574	
$\text{Fe}(\text{OH})_2$			560				544
$\text{Fe}(\text{OH})_3$							696
$\alpha\text{-FeOOH}$	298, 397, 414, 474, 550		400, 520, 670	390-391			
$\gamma\text{-FeOOH}$	252, 380						
$\delta\text{-FeOOH}$							664

Table 4.06. Raman shifts recorded in the literature for ferrous compounds. All were recorded under *in situ* conditions. **in situ* in a borate solution. Note that all the readings are wavenumbers measured in cm^{-1} .

	Reference number						
	43	44*	41*	40	45	46	38
NiFe_2O_4	490, 570-579, 655-665, 700-705	339, 490, 579, 666, 700					
NiOOH			545	475, 545			
NiO			475, 510	525			
$\text{Ni}(\text{OH})_2$							450
molybdate					320, 848, 890	320, 840, 898	

Table 4.07. Raman shifts recorded in the literature for Ni and Mo compounds. All had been recorded under *in situ* conditions, except * recorded for single crystals. Note that all the readings are wavenumbers measured in cm^{-1} .

	Reference number									
	47 ^ψ	48 ^ψ	49 [±]	50	51	52	53 ^ψ	40	43	54 [±]
Cr₂O₃	352, 531, 557, 619 (α-Cr ₂ O ₃)	560				351, 397, 530, 551, 609 (α-Cr ₂ O ₃ single crystal)	560			
Cr(OH)₃								620		
Fe-Cr Spinel [Fe _{3-x} Cr _x O ₄ (0≤x≤2) / Fe _{1+x} Cr _{2-x} O ₄ (0≤x≤1)]	686 (FeCr ₂ O ₄)	670-700 (Fe _{3-x} Cr _x O ₄)	550, 636, 679, 1335 (Fe _{3-x} Cr _x O ₄ x=1.6) 686, 1265, 1357 (FeCr ₂ O ₄)				684 (Fe _{1+x} Cr _{2-x} O ₄)	700 (FeCr ₂ O ₄)	660-690, 700 (FeCr ₂ O ₄)	
chromate				420, 505, 910 (aqueous)	846 (aqueous)					335-409, 861- 957, 838-899 (solid)
dichromate⁻					904, 943 (aqueous)					355-384, 227- 253, 903-939 (solid)

Table 4.08. Raman shifts recorded in the literature for Cr compounds. All had been recorded under *in situ* conditions except; * for single crystals, ± for solid solutions and Ψ for samples oxidised in air. Note that all the readings are wavenumbers measured in cm⁻¹.

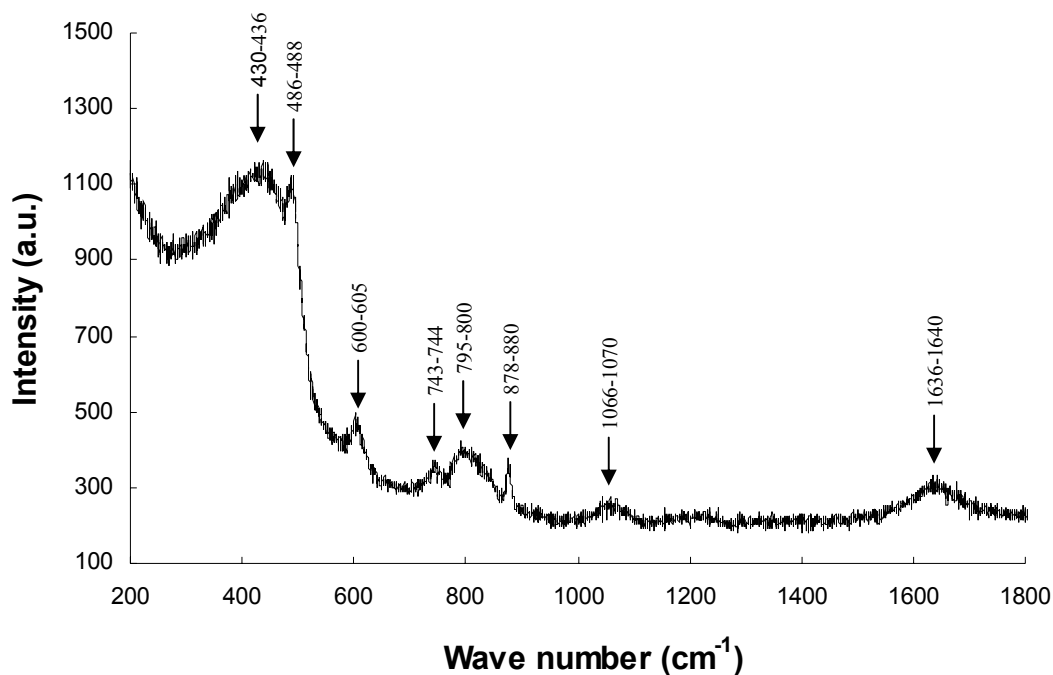


Figure 4.29. Raman spectrum of a sodium borate solution and a quartz window. Note that the spectral resolution of the Raman instrument is $\pm 2.5\text{cm}^{-1}$.

4.7.2 Raman spectra of 316L in a 0.1M borate solution

The *in situ* Raman spectra were recorded at every 100mV interval in the positive direction from -900mV to 900mV (see Section 3.3.2 for the experimental steps). The salient features of the results are discussed below:

- a) Between -900mV and -700mV, only the Raman shifts for borate and quartz were observed (Figure 4.30). Although this indicates some evidence that the passive film may have been removed by polarising at more negative potentials, this cannot be confirmed, as there is a possibility that some oxide phases which cannot be detected by Raman are still present;
- b) At -600mV, a broad Raman shift centralised at 700cm^{-1} appeared (Figure 4.31). This can be attributed to the Raman shift of the Fe-Cr spinel (Table 4.08). The

broad band width represents crystalline disorders, which can be observed in amorphous materials.⁵⁵

- c) When the potential reached -500mV, several new Raman shifts appeared (Figure 4.32). Other than the broad Raman shift centralised at 700cm^{-1} , there were many unidentified Raman shifts; 1159cm^{-1} , 1269cm^{-1} , 1452cm^{-1} , 1498cm^{-1} , 1554cm^{-1} , 1576cm^{-1} . No clear evidence from the literature was found to identify the substances or species responsible for these Raman shifts.

Whether the Raman shift appearing at 610cm^{-1} – 613cm^{-1} was formed due to an oxide/hydroxide phase is controversial as one of the Quartz Raman shifts happens to fall near the same wavenumber region (600cm^{-1} – 605cm^{-1}). According to Tables 4.06 to 4.08, there are several main oxide/hydroxide phases, $\alpha\text{-Fe}_2\text{O}_3$ (613cm^{-1}), Cr_2O_3 (619cm^{-1}), Fe_3O_4 (616cm^{-1}) and $\text{Cr}(\text{OH})_3$ (620cm^{-1}) that have Raman shifts in the 613cm^{-1} to 620cm^{-1} range. However, as this particular Raman shift (610cm^{-1} – 613cm^{-1}) appeared to gain intensity beyond -500mV, it is more likely due to an oxide/hydroxide than of Quartz.

- d) Between -400mV and 100mV, the main feature was the growth of the 700cm^{-1} Raman shift which represents the Fe-Cr spinel; in the 100mV to 200mV region, it reached its highest intense. Figures 4.33 (a) to (d) show how this particular Raman shift grew in this potential region. This implies that the oxide phase represented by this particular Raman shift is the most abundant in the 100mV to 200mV region.

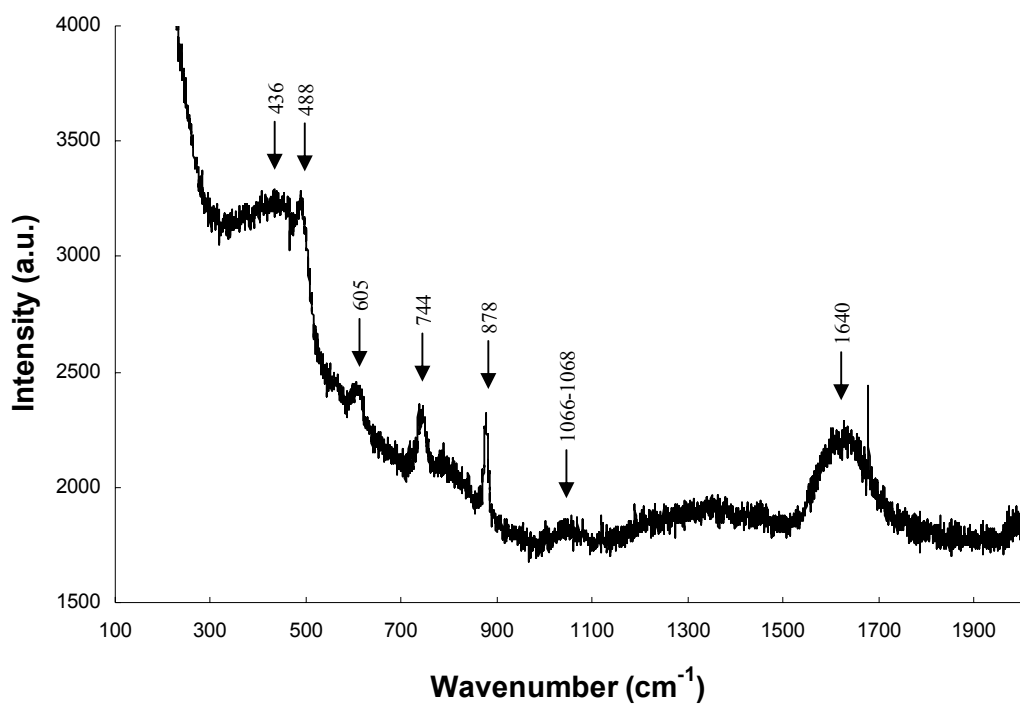


Figure 4.30. The *in situ* Raman spectrum of 316L at -900mV in a 0.1M borate solution. The peaks were similar to those of Figure 4.29 recorded from the borate solution and quartz.

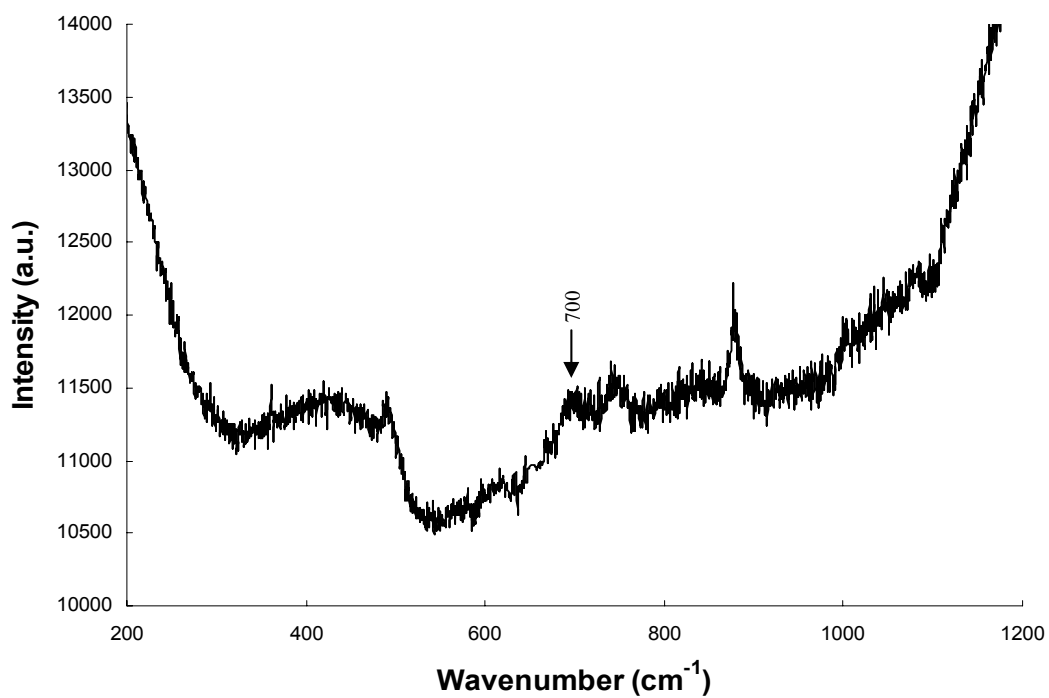


Figure 4.31. The *in situ* Raman spectrum of 316L at -600mV in a 0.1M borate solution. Unlabelled Raman peaks are the same as in Figure 4.30.

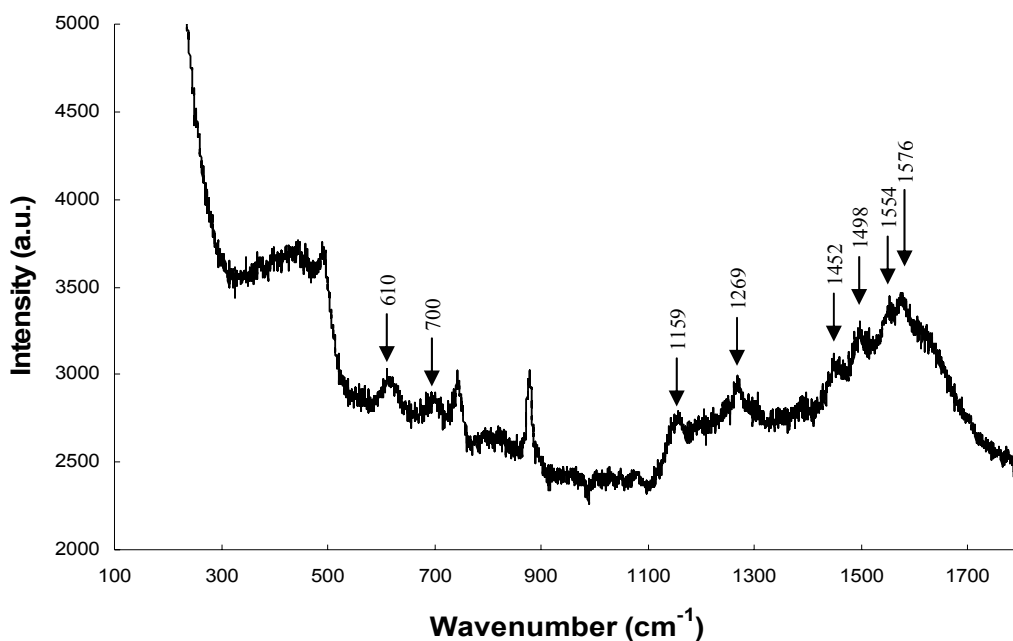
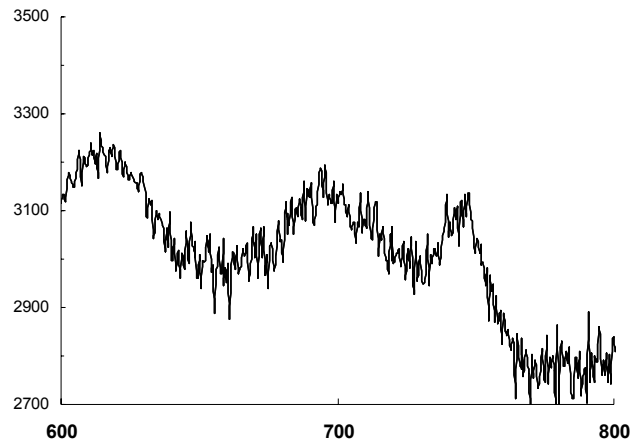


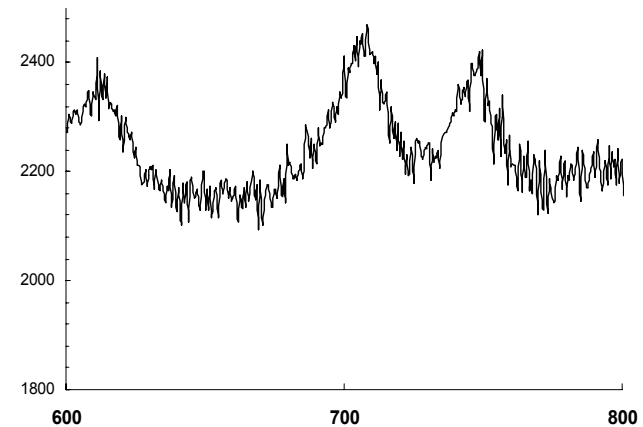
Figure 4.32. The *in situ* Raman spectrum of 316L at -500mV in a 0.1M borate solution. Unlabelled Raman peaks are the same as in Figure 4.30.

- e) The intensity of the 700cm^{-1} shift reduced from 300mV onwards and disappeared in the region of 600mV to 700mV.

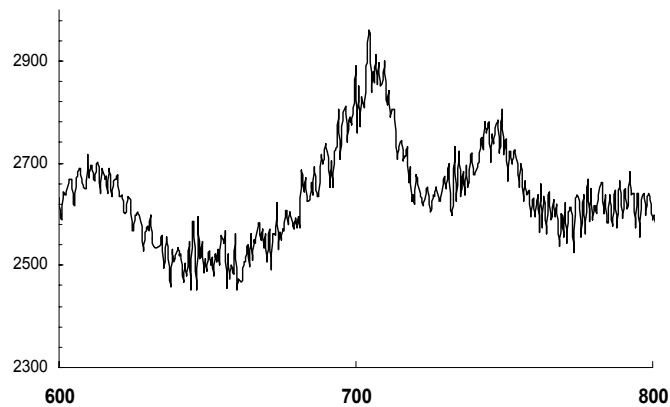
At 300mV, some other Raman shifts; 890cm^{-1} , 930cm^{-1} and 968cm^{-1} started to appear (Figure 4.34) as the band at 700cm^{-1} started to decline. According to Tables 4.07 and 4.08 molybdate, chromate and dichromate are possible oxide phases that could be responsible for Raman shifts around these wavenumbers. However, as the same Raman shifts were observed on 304L stainless steel, these shifts cannot be due to any Mo phase. Likewise forming dichromate is not feasible in neutral or weak basic solutions; unless there is a strong pH gradient through the passive films.⁶ As a result, the 890cm^{-1} and 930cm^{-1} Raman shifts were assigned to the chromate phase indicating the Cr(III) to Cr(VI) transformation in this potential range. These Raman shifts remained visible until at least 800mV with further growth of the 890cm^{-1} shift, above 800mV, bubbles from oxygen evolution prevented further Raman spectra from being collected.



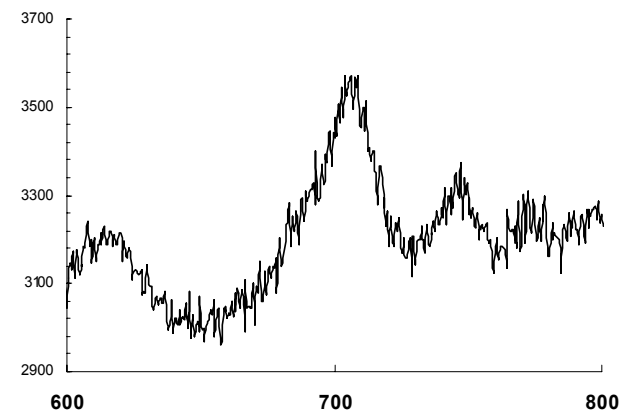
(a) -400mV



(b) -100mV



(c) 100mV



(d) 200mV

Figure 4.33. The growth of the 700cm^{-1} Raman shift in the potential region from -400mV to 200mV ; (a) -400mV , (b) -100mV , (c) 100mV and (c) 200mV . Note the x axis (wavenumbers) in cm^{-1} and y axis (intensity) in arbitrary units.

Although it was not possible to assign an exact phase for the 968cm^{-1} shift, the chromate phase does have a nearby shift at 957cm^{-1} (Table 4.08).

- f) By 400mV, another broad Raman shift appeared, centralised at 228cm^{-1} (Figure 4.35). This can be attributed to the $\alpha\text{-Fe}_2\text{O}_3$ phase (Table 4.06), suggesting that this replaces the Fe-Cr spinel phase in the passive film. The 228cm^{-1} Raman shift existed until 800mV. Beyond 800mV, Raman examination could not be performed due to the oxygen evolution.

The prominent features of Raman spectra recorded on the reverse sweep (from 800mV to -800mV) are given below.

- Several Raman shifts (838cm^{-1} , 890cm^{-1} - 900cm^{-1} , 933cm^{-1}) appeared around 800mV remained until around 300mV, which can be assigned to represent the chromate phase.
- A Raman shift centralised around 228cm^{-1} to 230cm^{-1} which can be attributed to the $\alpha\text{-Fe}_2\text{O}_3$ phase existed from 800mV to around -400mV.
- At around 100mV, a broad Raman shift centralised between 690cm^{-1} and 700cm^{-1} started to appear (Figure 4.36) which can be assign to the Fe-Cr spinel. Raman shifts became very weak below around -600mV, probably due to thinning of the oxide.

For 304L stainless steel, the salient features were similar to those of 316L, except the 700cm^{-1} Raman shift attributed to the Fe-Cr spinel was much weaker.

The Raman results obtained for 316L in a borate solution are summarised in Table 4.09.

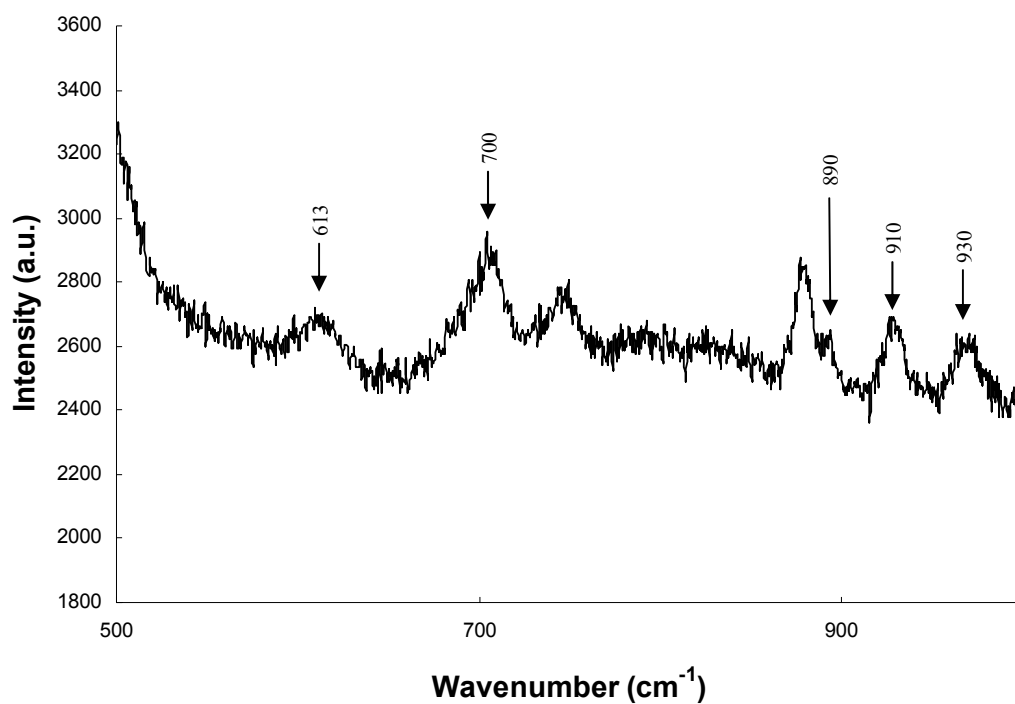


Figure 4.34. The *in situ* Raman spectrum of 316L at 300mV in a 0.1M borate solution. Unlabelled Raman peaks were the same as in Figure 4.30.

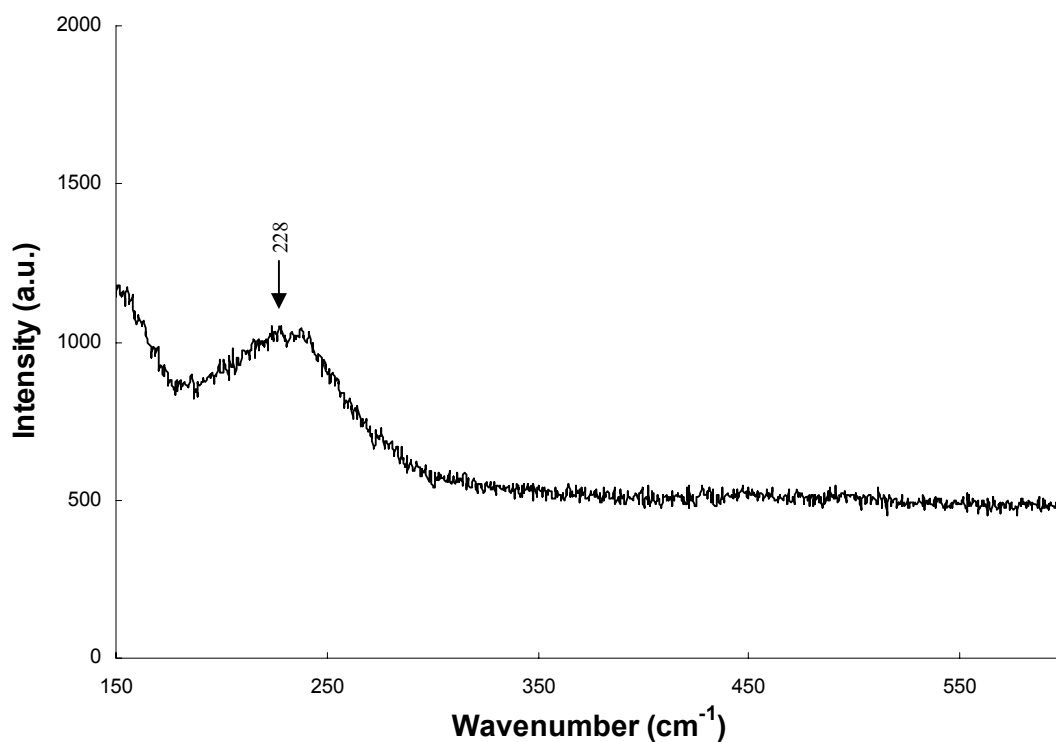


Figure 4.35. The *in situ* Raman spectrum of 316L at 400mV in a 0.1M borate solution.

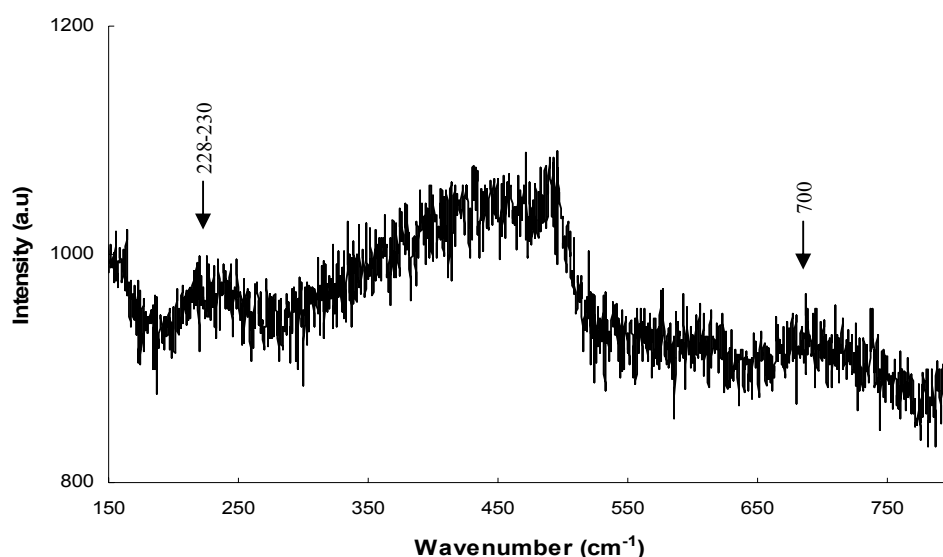


Figure 4.36. The *in situ* Raman spectrum of 316L at 100mV under the reverse potential scan in a 0.1M borate solution.

Raman shift	Existing potential range	Identified oxide phase	Remarks
<i>Forward sweep</i>			
700cm ⁻¹ (695cm ⁻¹ to 705cm ⁻¹)	From -600mV to 600mV (maximum intensity around 200mV)	Fe-Cr spinel (FeCr ₂ O ₄)	
613cm ⁻¹ (610cm ⁻¹ to 620cm ⁻¹)	-500mV to 800mV (more intense from -500mV)	<ul style="list-style-type: none"> • Quartz (600-605) • α-Fe₂O₃ • Cr₂O₃ • Fe₃O₄ • Cr(OH)₃ 	Difficult to identify due to the quartz Raman shift. Likely due to the α-Fe ₂ O ₃ as it appeared strongly beyond -500mV.
890cm ⁻¹ and 930cm ⁻¹	300mV to 800mV	chromate [probably Fe ₂ (CrO ₄) ₃]	Consistent with the transpassivation reaction; the oxidation of Cr(III) into Cr(VI).
228cm ⁻¹ (225 cm ⁻¹ to 240cm ⁻¹)	400mV to 800mV	α-Fe ₂ O ₃	May become more significant in the transpassivation region as the Fe-Cr spinel gets weaker.
968cm ⁻¹	200mV to 800mV		Could be due to Cr(VI) oxide
<i>Reverse sweep</i>			
838cm ⁻¹ , 890cm ⁻¹ -900cm ⁻¹ , 933 cm ⁻¹	800mV to 300mV	chromate [probably Fe ₂ (CrO ₄) ₃]	
228cm ⁻¹ to 230cm ⁻¹	800mV to -400mV	α-Fe ₂ O ₃	
690cm ⁻¹ to 700cm ⁻¹	100mV to -600mV	Fe-Cr spinel (FeCr ₂ O ₄)	Very weak intensities of Raman shifts below -600mV may due to thinning of the oxide.

Table 4.09. Summary of the Raman spectroscopy results obtained for 316L in a 0.1M borate solution. Gas evolution prevents collection of Raman shifts beyond 900mV.

4.7.3 Raman spectra of 316L in a 0.28M NaCl solution

The salient features of *in situ* Raman studies of 316L in a 0.028M NaCl solution are listed below.

- The Raman shift that can be attributed to the Fe-Cr spinel appeared at -700mV and disappeared before 400mV (Figure 4.37), interestingly this is just before the potential at which stable pitting started. Unlike in a borate solution, where the position of the 700cm^{-1} shift remained constant within $\pm 5\text{cm}^{-1}$ in NaCl, it was seen to shift within the range of 680cm^{-1} to 700cm^{-1} as the potential was varied (Figure 4.37). This could be as a result of stress building up in the passive film in the corrosive NaCl environment; Raman frequency (band position) is sensitive to the presence of stresses and strains. The position of the Raman shift depends on the bond length between atoms which could be changed by stresses and strains.⁵⁵ However, there was no direct relationship between the position of the Raman shift and the applied potential (Fig 4.37).
- Broad Raman bands, even broader than those observed in a borate solution. This may be a consequence of the passive film being more structurally disordered in the NaCl solution.

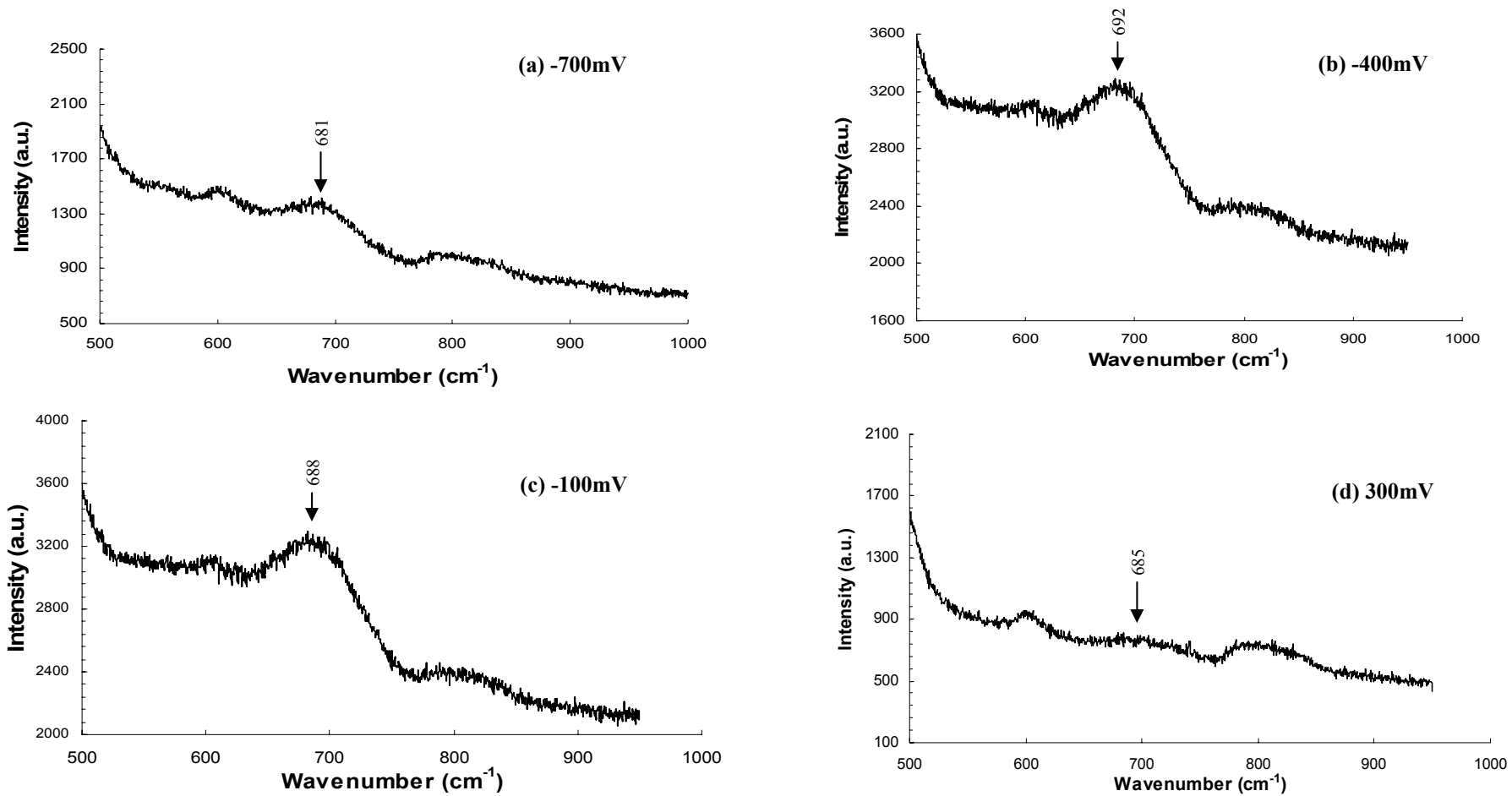


Figure 4.37. The *in situ* Raman spectra of 316L in a 0.028M NaCl solution; the growth and the displacement of the Raman shift close to 700cm^{-1} which can be attributed to the Fe-Cr spinel.

4.7.4 Raman spectra of 254SMO in a 0.1M borate solution

Raman shifts observed on 254SMO in a borate solution were broader than those seen with 316L in the same solution. Some of the significant features are listed below and compared with the literature values given in Tables 4.06 to 4.08.

- At -700mV, a Raman shift at 692cm^{-1} started to appear, which may be due to the formation of the Fe-Cr spinel structure. However, this may also be due to NiFe_2O_4 , as there was evidence for the presence of Ni in the passive film of 254SMO in the cyclic voltammograms. At -600mV, other than the 692cm^{-1} shift, a strong Raman shift appeared around 621cm^{-1} (Figure 4.38) which is difficult to identify clearly due to many possible candidate phases; $\alpha\text{-Fe}_2\text{O}_3$ (613cm^{-1}), Cr_2O_3 (619cm^{-1}), Fe_3O_4 (616cm^{-1}) and $\text{Cr}(\text{OH})_3$ (620cm^{-1}).
- At more positive potentials (-500mV to -400mV; Figure 4.39) the intensity of the 621cm^{-1} shift decreased, whilst the intensity of the 692cm^{-1} (688cm^{-1} - 694cm^{-1}) increased slightly.
- In the potential region of -300mV to -200mV, two Raman shifts can be observed between 665cm^{-1} and 705cm^{-1} . According to literature (Tables 4.06 to 4.08) both Fe-Cr spinel and NiFe_2O_4 give Raman shifts in the 655cm^{-1} to 705cm^{-1} region. The intensity of these bands increased at -100mV (Figure 4.40). These two broad shifts; 660cm^{-1} - 665cm^{-1} and 696cm^{-1} - 703cm^{-1} can be representations of either NiFe_2O_4 or FeCr_2O_4 or both spinel phases. However, Fe_3O_4 can also show Raman peaks in the same wavenumber range (Table 4.06).

- At potentials more positive than -100mV, the two broad Raman shifts at 660cm^{-1} - 665cm^{-1} and 696cm^{-1} - 705cm^{-1} combined to form a broad peak centralised around 695cm^{-1} . It is not known if this was due to the growth of a new phase or simply increased disorder causing the peaks to broaden. However, the fact that these two peaks converged suggest that they probably arise from the same phase (probably NiFe_2O_4) rather than two separate oxides. It is also worth noting that a weak broad band near 700cm^{-1} has been assigned to a spinel structure compound of $(\text{Ni,Fe})\text{Cr}_2\text{O}_4$ in the literature.⁵⁶ The broad peak at 695cm^{-1} started to diminish at 100mV and disappeared at around 300mV.
- The 229cm^{-1} - 238cm^{-1} Raman shift existed throughout the potential range of -600mV to 800mV; becoming stronger at more positive potentials; this can possibly be the Raman shift for Fe_2O_3 .
- At 200mV, the 695cm^{-1} Raman shift diminished and several other peaks appeared between 830cm^{-1} and 870cm^{-1} (Figure 4.41). These may be representations of the chromate⁻ phase resulting from transpassivation. These Raman shifts all existed until around 800mV, suggesting that the Cr(VI) oxide remains insoluble, which perhaps suggests that it initially forms at the metal oxide interface, where it cannot be dissolved by the solution.

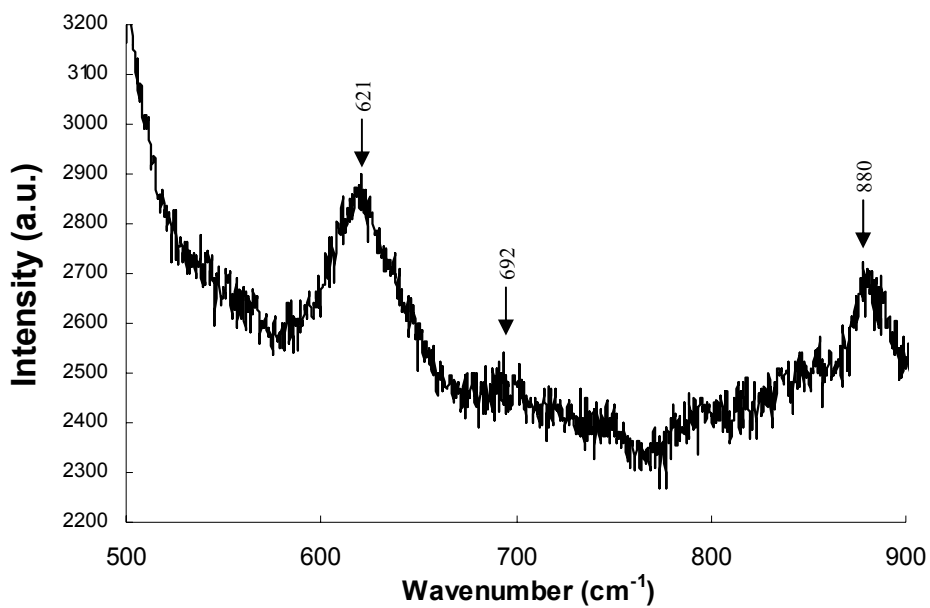


Figure 4.38. The *in situ* Raman spectrum of 254SMO at -600mV in a 0.1M borate solution.

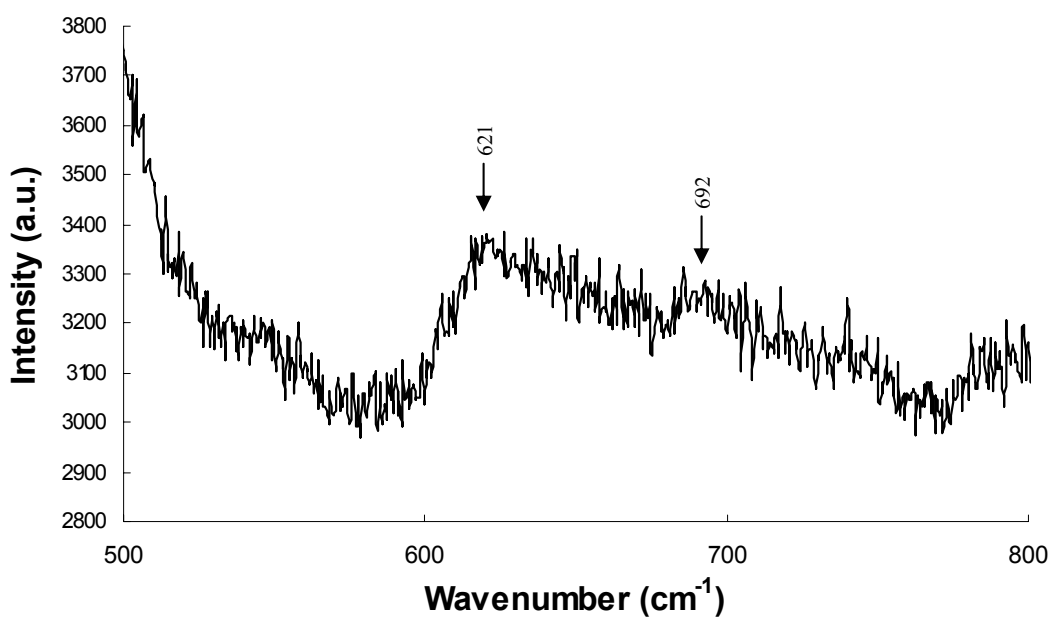


Figure 4.39. The *in situ* Raman spectrum of 254SMO at -500mV in a 0.1M borate solution.

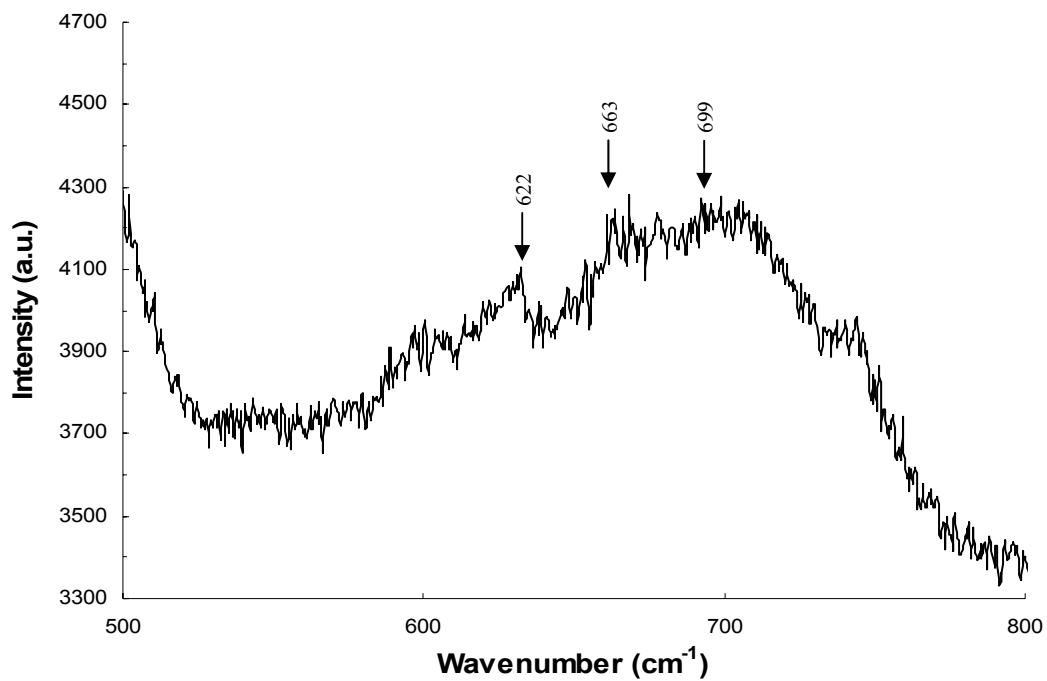


Figure 4.40. The *in situ* Raman spectrum of 254SMO at -100mV in a 0.1M borate solution.

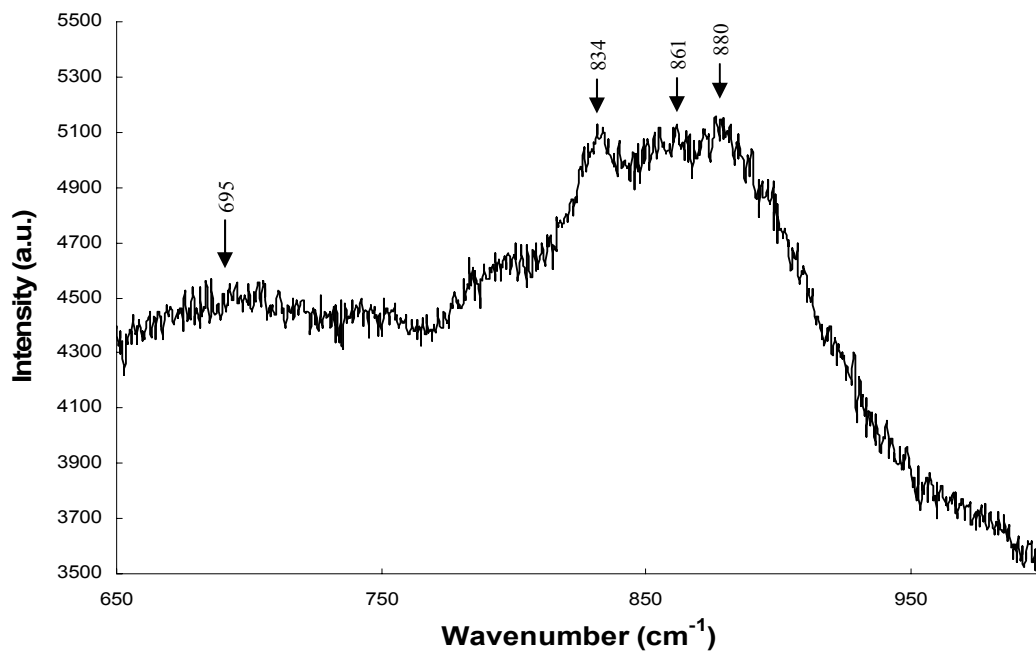


Figure 4.41. The *in situ* Raman spectrum of 254SMO at 200mV in a 0.1M borate solution. The 880cm⁻¹ is due to the borate solution.

The prominent features of the Raman spectra of 254SMO in a 0.1M borate solution recorded under the reverse sweep (from 800mV to -800mV) are given below.

- Several Raman shifts between 840cm^{-1} and 870cm^{-1} appeared around 800mV and remained until around 300mV; may represent the chromate phase.
- A Raman shift around 225cm^{-1} - 230cm^{-1} existed from 800mV down to around -400mV; most likely due to the Fe_2O_3 phase.
- Once the potential reached 600mV a weak Raman shift appeared around 700cm^{-1} . This was likely due to the formation of an Ni-Fe phase; according to the cyclic voltammogram of 254SMO (Figure 4.02), there is a possibility to form a Ni(II) phase below about 670mV. However, this shift was of low intensity until 100mV, where a broad Raman shift centralised around 695cm^{-1} started to appear. This may be due to the formation of a Cr(III) phase either as the Fe-Cr spinel or as the Fe-Cr-Ni oxide phase.⁵⁶

The Raman spectroscopy results obtained for 254SMO in a 0.1 M borate solution are summarised in Table 4.10.

Raman shift	Existing potential range	Identified oxide phase	Remarks
<i>Forward sweep</i>			
690cm ⁻¹ – 705cm ⁻¹	-700mV to -100mV	<ul style="list-style-type: none"> • FeCr₂O₄ or NiFe₂O₄ or both • Fe₃O₄ 	These two Raman shifts combined after -100mV and formed a broad shift centralised around 695cm ⁻¹ ; existed until 300mV.
660cm ⁻¹ – 665cm ⁻¹	-300mV to -100mV		
621cm ⁻¹ – 624cm ⁻¹	-600mV to 0mV	Likely to be Cr(OH)₃	
229cm ⁻¹ – 238cm ⁻¹	-600mV to 800mV	Fe₂O₃	
830cm ⁻¹ to 870cm ⁻¹	200mV to 800mV	chromate [probably Fe₂(CrO₄)₃]	
<i>Reverse sweep</i>			
840cm ⁻¹ to 870cm ⁻¹	800mV to 300mV	chromate [probably Fe₂(CrO₄)₃]	
225cm ⁻¹ - 230cm ⁻¹	800mV to -400mV	Fe₂O₃	
700cm ⁻¹	From 600mV	Likely to be NiFe₂O₄	
695cm ⁻¹	100mV to -600mV	Fe-Cr spinel or Fe-Cr-Ni phase	Very weak intensities of Raman shifts below -600mV may due to thinning of the oxide films

Table 4.10. Summary of the Raman spectroscopy results obtained for 254SMO in a borate solution. Gas evolution prevents collection of Raman shifts beyond 900mV.

References

- (1) Pallotta, C., De Cristofano, N., Salvarezza, R.C. and Arvia, A.J., *Electrochim. Acta*, **31** (1986) 1265.
- (2) Urretabizkaya, M., Pallotta, C., De Cristofano, N., Salvarezza, R.C. and Arvia, A.J., *Electrochim. Acta*, **33** (1988) 1645.
- (3) Ramasubramanian, N., Preocanin, N. and Davidson, R.D., *J. Electrochem. Soc.*, **132** (1985) 793.
- (4) Pourbaix, M., “*Atlas of Electrochemical Equilibria in Aqueous Solutions*”, NACE, Houston (1974).
- (5) Langevoort, J.C., Sutherland, I., Hanekamp, L.J. and Gellings, P.J., *Appl. Surf. Sci.*, **28** (1987) 167.
- (6) Gojić, M., Marijinn, D. and Kosec, L., *Corrosion*, **56** (2000) 839.
- (7) Bojinov, M., Fabricius, G., Laitinen, T. and T., Saario, *Electrochim. Acta*, **44** (1998) 4331.
- (8) Betova, I., Bojinov, M., Laitinen, T., Mäkela, K., Pohjanne, P. and Saario, T., *Corros. Sci.*, **44** (2002) 2675.
- (9) Southampton Electrochemistry Group, “*Instrumental Methods in Electrochemistry*”, Ellis Horwood, Chichester (1985).
- (10) Kelly, R.G., Scully, J.R., Shoesmith, D.E. and Buchheit, R.G., “*Electrochemical Techniques in Corrosion Science and Engineering*”, Marcel Dekker, New York (2003).
- (11) Jones, D.A., “*Principles and Prevention of Corrosion (2nd ed.)*”, Prentice-Hall, New Jersey (2nd ed., 1996).
- (12) Shreir, L.L., Jarman, R.A. and Burstein, G.T., “*Corrosion, Volume: Metal/Environmental Reactions*”, Butterworth-Heinemann, Oxford (1994).

- (13) Webb, E.G., Suter, T. and Alkire, R.C., *J. Electrochem. Soc.*, **148** (2001) B 186.
- (14) Ke, R. and Alkire, R., *J. Electrochem. Soc.*, **142** (1995) 4056.
- (15) Stewart, J and Williams, D.E., *Corros. Sci.*, **33** (1992) 457.
- (16) Ryan, M.P., Williams, D.E., Chater, J., Hutton, B.M. and McPhail, D.S., *Nature*, **415** (2002) 770.
- (17) Private communication: *A personal discussion with A. J Davenport at the Corrosion 2004 Conference*, New Orleans, Louisiana, March 2004.
- (18) Jang, H.J., Cho, E.A. and Kwon, H.S., *13th Asian-Pacific Corrosion Control Conference*, Japan (2003) PL-7.
- (19) Di Quarto, F., Piazza, S., Santamaria, M. and Sunseri, C., “*Handbook of Thin Film Materials, Volume 2: Characterization and Spectroscopy of Thin Films*”, (ed. Nalwa, H.S.), Academic Press, San Diego (2002) 373–414.
- (20) Mott, N.F. and Davis, E.A., “*Electronic Processes in Non-crystalline Materials (2nd ed.)*”, Clarendon Press, Oxford (1979).
- (21) Gurevich, Y.Y., Pleskov, Y.V. and Rotenberg, Z.A., “*Photoelectrochemistry*”, Consultants Bureau, New York (1980).
- (22) Piazza, S., Splendore, A., Di Paola, A., Sunseri, C. and Di Quarto, F., *J. Electrochem. Soc.*, **140** (1993) 3146.
- (23) Peter, L.M., *Chem. Rev.*, **90** (1990) 753.
- (24) Candea, R. M., *Electrochim. Acta*, **26** (1981) 1803.
- (25) Di Paola, A., Di Quarto, F. and Sunseri, C., *Corros. Sci.*, **26** (1986) 935.
- (26) Abrates, L.M. and Peter, L.M., *J. Electroanal. Chem.*, **150** (1983) 593.
- (27) Preusser, S., Stimming, U. and Tounaga, S., *J. Electrochem. Soc.*, **142** (1995) 102.

- (28) Hardee, L. E. and Bard, A. J., *J. Electrochem. Soc.*, **124** (1977) 215.
- (29) Stimming, U. and Schutlze, J.W., *Ber. Bunsenges. Phys. Chem.*, **80** (1976) 129.
- (30) Di Paola, A., *Electrochim. Acta*, **34** (1989) 203.
- (31) Tench, D.M. and Yeager, E., *J. Electrochem. Soc.*, **120** (1973) 164.
- (32) Hakiki, N.E. and Belo, M.Da.C., *J. Electrochem. Soc.*, **143** (1996) 3088.
- (33) Peterson, M.W. and Parkinson, B.A., *J. Electrochem. Soc.*, **133** (1986) 2538.
- (34) Ferreira, M.G.S., Belo, M.D.C., Hakiki, N.E., Goodlet, G., Montemor, M.F., and Simões, A.M.P., *J. Braz. Chem. Soc.*, **13** (2002) 433.
- (35) Ferreira, M.G.S., Hakiki, N.E., Goodlet, G., Faty, S., Simões, A.M.P. and Belo, M.D.C., *Electrochim. Acta*, **46** (2001) 3767.
- (36) Thanos I.C. G., *Electrochim. Acta*, **31** (1986) 811.
- (37) Thanos I. C. G., *Electrochim. Acta*, **31** (1986) 1585.
- (38) Ferreira, M.G.S., Silva T.M., Catarina, A., Pankuch, M. and Melendres, C.A., *J. Electrochem. Soc.*, **139** (1992) 3146.
- (39) Pascale, M.L.B., Jedral, W., Odziemkowski, M.S. and Gillham, W.R., *Corros. Sci.*, **42** (2000) 1921.
- (40) Boucherit, N., Goff, A.H. and Joiret, S., *Corrosion*, **48** (1992) 569.
- (41) Schroeder, V. and Devine, T.M., *J. Electrochem. Soc.*, **146** (1999) 4061.
- (42) Rubim, J.C. and Dünwald, J., *J. Electroanal. Chem.*, **258** (1989) 327.
- (43) Maslar, J.E., Hurst, W.S., Bowers, Jr.W.J. and Hendricks, J.H., *Corrosion*, **58** (2002) 739.
- (44) Graves, P.R. and Johnston, C. and Campaniello, J.J., *Mat. Res. Bull.*, **23** (1988) 1651.
- (45) Payen, E., Grimblot, J. and Kasztelan, S., *J. Phys. Chem.*, **91** (1987) 6642.

- (46) Boucherit, N. and Goff, A. H., *Faraday Discuss.*, **94** (1982) 137.
- (47) England, W.A., Bennett, M.J., Greenhalgh, D.A., Jenny, S.N. and Knights, C.F., *Corros. Sci.*, **26** (1986) 537.
- (48) Renusch, D., Veal, B., Natesan, K. and Grimsditch, M., *Oxid. Met.*, **46** (1996) 365.
- (49) McCarty, K.F. and Boehme, D.R., *J. Solid State Chem.*, **79** (1989) 19.
- (50) Boucherit, N., Goff, A. H. and Joiret, S., *Mater. Sci. Forum*, **111-112** (1992) 581.
- (51) Michel, G. and Cathay, R., *J. Raman Spectrosc.*, **17** (1986) 79.
- (52) Thierry, D., Persson, D., Leygraf, C., Delichère, D., Joiret, C. and Goff, A. H., *J. Electrochem. Soc.*, **135** (1988) 305.
- (53) Zeng, Z, Natesan, K. and Grimsditch, M., *Corros. Sci.*, **60** (2004) 632.
- (54) Nyquist, R.A. and Kagel, R.O., “*The handbook of infrared and Raman spectra of Inorganic compounds and organic salts: volume 4, Infrared spectra of inorganic compounds*” Academic press, San Diego (1997).
- (55) Jawhari, T., *IR-Raman*, **28** (2000) 15.
- (56) Farrow, R.L. and Nagelberg, A.S., *Apply. Phys. Lett.* **36** (1980) 945.

CHAPTER 5 DISCUSSION

5.1 Amorphous or crystalline

Although there was no direct measurement to verify the extend of crystallinity of the stainless steel passive films, photocurrent readings, capacitive measurements and *in situ* Raman spectra characteristics revealed indirect identifications of the film being amorphous. Extensive tailing of electronic states into the bandgap, frequency dependent capacitance, photocurrent relaxation characteristics and broad Raman shifts all indicated an amorphous structure rather than a crystalline structure.

5.2 Compositional characterisation

The data in this thesis especially the *in situ* Raman and bandgap measurements have revealed potential dependent changes in the structure and the composition of the passive films formed on 316L, 304L and 254SMO stainless steels.

The cyclic voltammogram of 316L showed that an oxidation process occurs around -800mV (Figure 4.01). This can be postulated as the formation of the Fe-Cr spinel phase, which according to *in situ* Raman data was the dominant constituent in the 316L passive film over a wide range of potentials (see Table 4.09). The Raman results obtained to fingerprint the Fe-Cr spinel were further supported by bandgap measurements. The bandgap value $2.9 \pm 0.5 \text{ eV}$ obtained for the oxide film on 316L at more negative potentials (-800mV to -900mV, See section 4.5.2) is close to the theoretical bandgap value of 3.0eV for FeCr_2O_4 (Appendix D).

A possible reason for the small discrepancy between the measured and theoretical bandgaps will be discussed later, which will deal with a comparison of the bandgaps for the films found on 304L and 316L stainless steel. For 316L, the transpassivation of Cr(III) into Cr(VI) commenced around 200mV (see point *E* of Figure 4.01). This is consistent with Raman results as the Fe-Cr spinel phase of the oxide on 316L grew until 200mV and then started to diminish. At the same time there was some Raman evidence of chromate phase appearing around 300mV, which further testifies to transpassivation. Around 600mV once the transpassivation became more vigorous, the Fe-Cr spinel disappeared. However, no clear evidence of any dissolution process involved with transpassivation can be obtained; solution analysis failing to find chromium ions. On the reverse sweep, the reformation of the Cr(III) phase occurred at around 100mV (Figure 4.01). This feature will be further analysed later when the behaviour of the passive film on 254SMO stainless steel is discussed in detail.

The cyclic voltammogram of 316L also showed another possible oxidation phase change at around -500mV (peak *C* in Figure 4.01). According to the Pourbaix diagram¹ of iron, this particular oxidation phase change near -500mV is likely to be the formation of a Fe(III) oxide phase. This was supported by Raman results that indicated the possible formation of Fe₂O₃ close to this potential. Raman results further suggested that this Fe₂O₃ phase existed right up to the oxygen evolution potential. Additional proof for the existence of a Fe(III) phase positive of -400mV comes from bandgap measurements that reveal the existence of an n-type semiconductor with a bandgap close to 1.95eV; in addition to the 2.9eV n-type material assigned above to the Fe-Cr spinel. The most likely oxide/hydroxide phases having bandgaps around

1.95±0.5eV are Fe₂O₃, FeOOH and Fe(OH)₃. Although it is difficult to confirm the precise phase, Fe₂O₃ is more probable according to the Raman data.

According to cyclic voltammograms, the oxidation and reduction phase changes of 304L grade were similar to those of 316L (Figure for 304L is not given in the thesis, see Section 4.1.1). However, the Raman data and the bandgap measurements were slightly different between the two grades. In 304L, the Raman shifts representing the Fe-Cr spinel were of low intensity and the bandgap values obtained at negative potentials (-800mV to -900mV) were around 2.8±0.5eV. Neither of the bandgap values obtained for 316L ($E_g=2.9\pm0.5\text{eV}$) and 304L ($E_g=2.8\pm0.5\text{eV}$) exactly match with the theoretical value for FeCr₂O₄ (3.0eV; Appendix D). Scrutinising the equations and relationships explained in Appendix D, this discrepancy can possibly be explained as the existence of Fe(III) in the spinel structure. This would make the bandgap lower, so the spinel structure should be represented in a more accurate formula as Fe(II)[Cr(III)_xFe(III)_(1-x)]₂O₄. Using bandgap values of 304L (2.8eV) and 316L (2.9eV), the x can be approximated to 0.73 and 0.85, respectively; this signifies Cr richness in the Fe-Cr spinel in the 316L passive film as compared with that of 304L. It can be argued that the differences in the bandgaps are due to the presence of Mo in 316L stainless steel. However, this would require the presence of either Mo(II) or Mo(III) species in the spinel structure, both of which are unstable; Mo is normally found in Mo(IV) and Mo(VI) states within oxides^{2,3} so it hard to see how Mo can be incorporated in to the spinel structure.

The cyclic voltammogram of 254SMO (Figure 4.02) showed that after an initial oxidation occurred around -800mV, a plateau existed from -700mV up to 0mV.

Raman results of 254SMO (Table 4.10) indicated the formation of spinels; FeCr_2O_4 or NiFe_2O_4 or both phases. Particular Raman shifts that can be assigned to the Fe-Cr spinel or the Ni-Fe spinel or both started to appear at two different potentials; at around -700mV and -300mV, suggesting the formation of two distinct phases. Other possible phases formed according to Raman spectroscopy were $\text{Cr}(\text{OH})_3$ at around -700mV; Fe_2O_3 around -600mV; and chromate around 200mV. In addition, since Fe_3O_4 also has peaks near Fe-Cr and Ni-Fe spinels, it is impossible to rule out the existence of the Fe_3O_4 phase. (Note: Fe_3O_4 does not give a photocurrent as it is not a semiconductor). The initial oxidation near -800mV in the cyclic voltammogram of 254SMO (peak B' in Figure 4.02) may be due to the formation of a Fe-Cr spinel or $\text{Cr}(\text{OH})_3$ or both. The formation of a Ni-Fe spinel would not be expected to occur until -600mV to -500mV, which is the potential region that the Pourbaix diagram¹ indicates Fe(III) becomes stable, further suggesting that the Raman feature appearing at -300mV belongs to NiFe_2O_4 . The plateau in the cyclic voltammogram may imply the formation of a stable oxide.

On 254SMO, transpassivation commenced around 0mV, which is more negative than with of 316L and 304L. Furthermore, Raman data revealed that in 254SM, the spinel structure disappears at about 300mV, which is again more negative than the case with the other two stainless steels. These results support the postulations made by some authors on the influence of Mo on transpassivation; the high level of Mo in 254SMO enhances the transpassivation⁴ and decreases the transpassivation potential.⁵ However, the mechanism of Mo on these effects remains unknown.

Analysing the reduction peak that occurred around 80mV to 100mV (K' in Figure 4.02) in the reverse scan of the cyclic voltammogram yields further information on the transpassive behaviour of 254SMO. This peak can be clearly defined as a representation of the reduction of Cr(VI) back to Cr(III) and it was by far more intense with 254SMO than the other two grades of stainless steels (see Figures 4.01 and 4.02). The charge involved with the transpassivation ($G'H'$ in the Figure 4.02) is slightly more than twice as much as that involved with the reduction phase change occurring at around 100mV (peak K' of Figure 4.02); this implies that the Cr(VI) formed the oxidation of both Cr(III) and Cr(0) in the transpassivation region (F' and $G'H'$ of Figure 4.02) is retained in the passive film and is reduced back the Cr(III) phase during the reverse sweep (peak K' of Figure 4.02). At the same time, Raman data also testify the retaining of the Cr(VI) phase in the oxide. This can be further supported by bi-layer oxide models postulated for stainless steel passive film by previous researches⁶⁻⁸ using XPS and AES results; an outer Fe(III) oxide/hydroxide and an inner Cr(III) oxide/hydroxide. This can cause the Cr(VI) cations to be trapped within the film, where they are not able to dissolve into the solution.

By comparison with the study of Ramasubramanian *et al.*⁹, the reduction peak near 670mV on the reverse scan of the cyclic voltammograms of 254SMO (peak J' of Figure 4.02) can be attributed to the reduction of Ni(III) into Ni(II). This was further supported as the same feature was seen on cyclic voltammograms with both pure Ni and nichrome alloy (not shown in this thesis). This implies the existence of Ni as Ni(II) in the oxide of the passive region, which is oxidised to Ni(III) in the transpassive region. With the complement of Raman data showing a spinel structure between -300mV and 300mV, the existence of the $NiFe_2O_4$ can be postulated.

Alternatively the spinel may also contain some Cr which would increase the bandgap of the Ni-Fe spinel (according to Appendix D).

The bandgap value; $2.4 \pm 0.5 \text{ eV}$ obtained for 254SMO, was quite different than that of 316L and 304L. The $2.4 \pm 0.5 \text{ eV}$ value is more consistent with the bandgap of Cr(OH)_3 (Appendix D). Similar bandgap value can be obtained theoretically for FeO however, there is no other experimental nor any literature evidence on formation of this phase in a borate solution. The Raman data collected under the forward sweep gave some indications of the formation of Cr(OH)_3 however, there was no bands were observed that could be assigned to Cr(OH)_3 . under the reverse sweep. However, the possibility of a complex oxide of Fe-Cr-Ni to make the 2.4eV bandgap as proposed by Di Paolo et al.^{10,11} cannot be ruled out Scrutinising all the evidence extracted from each experimental technique; cyclic voltammograms, Raman and bandgap measurements on the 254SMO passive film, and considering theoretical bandgap calculations (Appendix D), it can be postulated that the formation of a Ni-Fe-Cr oxide in the form of $\text{Ni}[\text{Fe(III)}_{0.7}\text{Cr(III)}_{0.3}]_2\text{O}_4$ is the phase responsible for the observed bandgap of 2.4eV. A similar idea; the formation of a stable and homogenous Cr-Fe-Ni oxide/hydroxide on 254SMO having a bandgap of 2.4eV was previously suggested by Di Paola *et al.*^{10,11} however, these authors did not offer a structure for the particular oxide/hydroxide.

5.3 Pitting characteristics

The deleterious effect of sulphide inclusions and the positive influence of Mo on the pitting corrosion resistance were well recognised by analysing stable and metastable pitting events of different stainless steel samples. With respect to the role of Mo, *In situ* Raman results obtained for 316L in NaCl revealed the existence of a Fe-Cr spinel

that disappears just prior to the onset of stable pitting. Raman results also revealed that the spinel peaks were much less intense with 304L. Thus, it is possible that Mo stabilised the spinel, helping to prevent the rupture of the passive film. Furthermore, prior to pitting, the Raman peak positions became unstable, indicating possible stress build up in the passive film. The role of sulphide inclusions was clearly seen in the *In situ* AFM results that suggested stable pit initiation occurred near sulphide inclusions and this may be due to either the preferential stress built up near the inclusion¹² or Cr depletion around the inclusion¹³.

5.4 Electronic properties of the passive films

5.4.1 Photocurrent–potential behaviour

Starting from the extreme positive potential end (Figure 4.11), the magnitude of the photocurrent increases until around 450mV and then declines and shows a minimum at around 100mV. The increase in the photocurrent from 800mV down to 450mV can be explained according to the Preusser *et al.*¹³ model the existence of mid bandgap states, which can be emptied or filled according to the position of the Fermi level [see Section 4.5.4, Figures 4.22(a) to (c)]. As the potential moves more negative, the Fermi energy level goes up, thus filling more mid bandgap state, reducing the relaxation effect so that the measured photocurrent increases.

The photocurrent minimum around 100mV was correlated with the reduction phase change that occurred around 120mV to 30mV in the reverse potential scan in all the stainless steels (more significantly in 254SMO; see Figures 4.01 and 4.02). Again from 100mV down to around -450mV, the photocurrent started to diminish, as the space charge length became shorter.

The photocurrent-potential results also allow two other characteristic features of the passive film to be postulated; the type of semiconductivity and the flat band potential. The complete absence of photocurrent from -450mV to -600mV with all three grades of stainless steels gives some indication for the possible location of the flat band potential. On the other hand, positive photocurrent observed above this potential region and the negative photocurrent observed below this potential region imply n-type and p-type semiconductivities, respectively. These findings were further confirmed using Mott-Schottky plots (Figures 4.26 and 4.27) and photocurrent transients (Figures 4.19 to 4.21). For 316L and 304L in a 0.1M borate solution, (pH=9.2) Mott-Schottky plots pointed to a flat band potential around -475mV (regardless of the perturbation frequency; Figure 4.27) and for 254SMO the value shifted very slightly to -472mV implying that flat band potential of the passive films formed on stainless steels in 0.1M borate solution is independent of its composition. However, as the passive film is probably a dual layer structure of Fe(III) oxide or Cr(III) oxide/hydroxide, it is not obvious, which of these layers dominates with respect to the determination of the measured flat band. Nevertheless, due to the existence of the same bandgap value, which was assigned to the Cr(III) phase, in each stainless steel both above and below the flat band potential, it is more likely that the Cr(III) phase is responsible for the observed flat band potential values.

5.4.2 Electronic band structures

Photocurrent transients (Figures 4.19 to 4.21) and Tauc plots (e.g. Figures 4.14, 4.15 and 4.17) confirmed the nature of semiconductivity, which varied with potential as follows:

- a) 800mV to 400mV: All stainless steels showed n-type semiconductivity with a bandgap around $1.95 \pm 0.5 \text{ eV}$, consistent with a Fe(III) phase, probably Fe_2O_3 . However, as it has been proposed in Sections 4.1 and 4.2 that the Cr(VI) oxide phase does not dissolve into the solution, it is necessary to consider why this particular phase did not contribute to the observed photocurrent. A possible explanation is that the Cr(VI) oxide is not a semiconductor, i.e. it is either metallic or more likely it is an insulator, or at least has a bandgap larger than 4.4 eV (the largest bandgap that can be detected with the present instrumentation).
- b) 200mV to -300mV: Bandgap measurements in this potential region can be interpreted in two ways (see Section 4.5.2). One method leads to a single oxide with a potential dependent bandgap, whilst the other leads to two separate oxides, both of which have bandgaps independent of potential. Scrutinising the results obtained from Raman spectroscopy (Tables 4.09 and 4.10) together with cyclic voltammograms on potential dependent phase transformations (Figures 4.01 and 4.02; specifically the phase change occurs at around 100mV in the reverse potential scan) points to the existence of two phases in the n-type region below 200mV. Accordingly, the interpretation of potential dependent bandgap variation can be ruled out. So the second interpretation, two oxide phases with potential independent bandgaps is believed to be correct. It cannot yet be determined whether the two bandgaps represent two different oxide phases within a single layer or two separate layers of oxide films. However, according to previous studies by Castle and Qui,⁶ Lorang *et al.*⁷ and Hakiki *et al.*⁸ based on XPS and AES techniques the two layer model; an inside Cr(III) oxide and an outside Fe(III) oxide is more likely. This postulation of a two layer model is

further supported by the transpassivation data in which the Cr(VI) did not dissolve into solution, possibly because it was trapped underneath the outer Fe(III) oxide layer. Consequently, it was decided to use a two oxide layer model consisting of an n-type high bandgap oxide inner layer ($2.9\pm 0.5\text{eV}$ in 316L, $2.8\pm 0.5\text{eV}$ in 304L and $2.4\pm 0.5\text{eV}$ in 254SMO) and an n-type low bandgap oxide outer layer ($1.95\pm 0.5\text{eV}$) (Table 5.01). The schematic presentation of the particular electronic band structure is given in the Figure 5.01(a). This interpretation is similar to the model proposed by Tsuchiya *et al.*¹⁴ for stainless steel passive films grown in neutral solutions.

- c) -800mV to -900mV: All the three grades showed p-type semiconductivity in this potential region, although with different bandgap values. A possible electronic band structure in this potential range is shown in Figure 5.01 (b). However, from the Raman data, which showed the absence of Fe_2O_3 below -500mV (Tables 4.09 and 4.10) coupled with cyclic voltammogram results (reduction peaks at around -600mV; L in Figure 4.01 and \acute{L} in Figure 4.02), it can be postulated that the Fe(III) oxide phase does not exist at potentials below -700mV.

For all three stainless steels, the bandgap of p-type oxide observed below -800mV was identical to that of the high bandgap n-type oxide. This obviously suggests that these are the same oxide; acting as both an n-type and a p-type semiconductor due to the influence of different donor and acceptor species, respectively.

Based on all the data presented in this thesis, it is believed the most likely oxide phases on the different stainless steels at different potentials are as shown in Table 5.01.

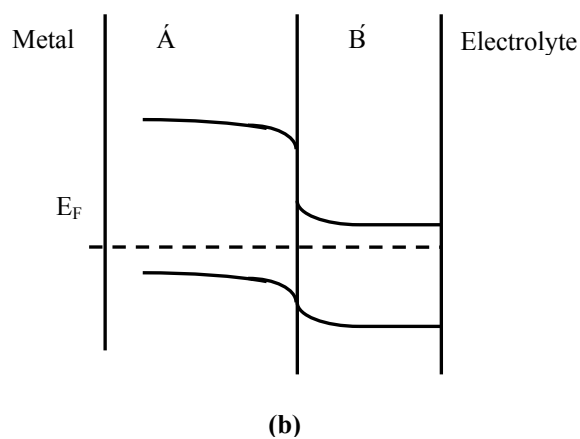
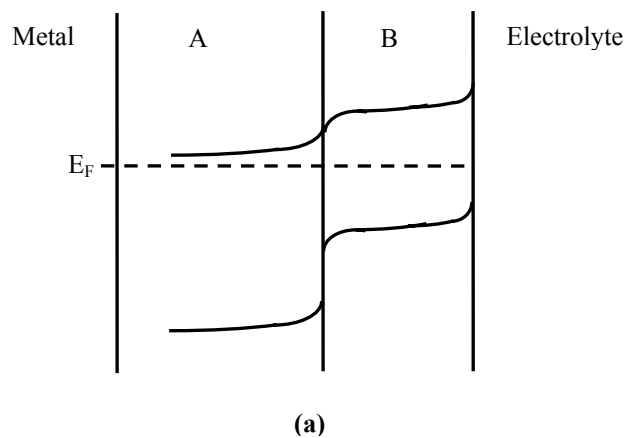


Figure 5.01. Schematic representations of electronic band structures of stainless steel passive films formed in a 0.1M borate solution: (a) for the potential region 200mV to -300mV, both n-type films, where A is n-type Fe-Cr spinel (316L and 304L) or Ni-Fe-Cr oxide (254SMO) and B is n-type Fe(III) oxide (all three stainless steels); (b) for the potential region of -800mV to -900mV, p-type and n-type films, where \acute{A} is p-type Fe-Cr spinel (316L and 304L) or Ni-Cr-Fe oxide (254SMO), \acute{B} is n-type Fe(III) oxide (all three stainless steels).

5.4.3 Frequency dependence of electronic properties

Capacitance data together with Mott-Schottky plots further reveal information on the electronic properties of the stainless steel passive films (Figures 4.23 to 4.27). The salient features are summarised below:

- a) Frequency dependence capacitance characteristics clearly demonstrate the disordered nature of the passive films. Amorphous semiconductors are characterised by a high density of states between the valence and the conductance bands; charging of these states lead to strong frequency dependence (Figure 4.25).^{††} Tailing of electronic states into the bandgap were further testified by studying the behaviour of donor concentrations of the three stainless steels at various frequencies (see Figure 4.28). The mid bandgap donors appeared to only ionised at frequencies lower than 100Hz. Furthermore, on comparing the frequency dependence of the measured donor concentrations (Figure 4.28) in the oxide films on the three stainless steels, it is apparent that at lower frequencies the density of states of 254SMO is higher than that of 304L and 316L. This implies that the DOS in the mid bandgap of 254SMO is higher than that in 304L, 316L. This might suggest that the oxide film on 254SMO is more amorphous of the three samples studied.

- b) The diverse behaviour of donor and acceptor concentrations implies the nature of the donor/acceptor species is different for films on 254SMO than for those of 304L and 316L. Possibly, the high level of mid bandgap states may be associated with the Ni that is present in the film on 254SMO.

^{††} Note that due to the apparent amorphous nature of the passive films the bandgap values obtained by photocurrent spectroscopy are the mobility gaps; $E_g^m = E_C - E_V$ (section 2.5.6).

- c) The break between 400mV and 0mV shown in Mott-Schottky plots of stainless steel passive films (Figure 4.26) has been interpreted by previous authors⁸ as being due to a deep donor level, which becomes ionised when the Fermi level moves through it lead to a reduction in the space charge length. However, based on the data presented in this thesis, it is clearly evident this particular feature is consistent with the reduction phase change that occurs around 100mV on the reverse potential scan (Figures 4.01 and 4.02), which has been interpreted as the formation of a Cr(III) oxide phase. The appearance of this phase would naturally change the electronic properties of the film, thereby causing the changes observed in the Mott-Schottky plots.

Stainless steel grade		Potential region			
		800mV to 400mV	200mV to -300mV (duplex bandgap region)		-800mV to -900mV
316L	Bandgap (eV)	1.95±0.05	1.95±0.05	2.9±0.05	2.9±0.05
	Oxide/hydroxide phase	Fe(III)oxide (probably Fe ₂ O ₃)	Fe(III)oxide (probably Fe ₂ O ₃)	Fe(II)[Cr(III) _x Fe(III) _(1-x)] ₂ O ₄ where 0<x≤1	Fe(II)[Cr(III) _x Fe(III) _(1-x)] ₂ O ₄ where 0<x≤1
	Semiconductivity	n-type	n-type	n-type	p-type
304L	Bandgap (eV)	1.95±0.05	1.95±0.05	2.8±0.05	2.8±0.05
	Oxide/hydroxide phase	Fe(III)oxide (probably Fe ₂ O ₃)	Fe(III)oxide (probably Fe ₂ O ₃)	Fe(II)[Cr(III) _x Fe(III) _(1-x)] ₂ O ₄ where 0<x≤1	Fe(II)[Cr(III) _x Fe(III) _(1-x)] ₂ O ₄ where 0<x≤1
	Semiconductivity	n-type	n-type	n-type	p-type
254SMO	Bandgap (eV)	1.95±0.05	1.95±0.05	2.4±0.05	2.4±0.05
	Oxide/hydroxide phase	Fe(III)oxide (probably Fe ₂ O ₃)	Fe(III)oxide (probably Fe ₂ O ₃)	Ni[Fe(III) _y Cr(III) _(1-y)] ₂ O ₄ where 0<y<1	Ni[Fe(III) _y Cr(III) _(1-y)] ₂ O ₄ where 0<y<1
	Semiconductivity	n-type	n-type	n-type	p-type

Table 5.01. Summary of the phases that are believed to form, their bandgap values and semiconductivities at different potentials for the passive films on 316L, 304L and 254SMO.

References

- (1) Pourbaix, M., “*Atlas of Electrochemical Equilibria in Aqueous Solutions*”, NACE, Houston (1974).
- (2) Clayton, C.R. and Lu, Y.C., *J. Electrochem. Soc.*, **133** (1986) 2465.
- (3) Olefjord, I. and Jelvestam, U., *J. Electrochem. Soc.*, **132** (1985) 2854.
- (4) Betova, I., Bojinov, M., Englund, A., Fabricius, G., Laitinen, T., Mäkela, K., Saario, T. and Sundholm, G., *Electrochim. Acta*, **46** (2001) 3627.
- (5) Kim, J.S., Peelen, W.H.A., Hemmes, K. and Makkus, R.C., *Corros. Sci.*, **44** (2002) 635.
- (6) Castle, J.E. and Qiu, J.H., *Corros. Sci.*, **29** (1989) 591.
- (7) Lorang, G., Belo, M.Da.C., Simões, A.M.P. and Ferreira, M.G.S., *J. Electrochem. Soc.*, **141** (1994) 3347.
- (8) Hakiki, N.E., Belo, M.D.C., Simões, A.M.P. and Ferreira, M.G.S., *J. Electrochem. Soc.*, **145** (1998) 3821.
- (9) Ramasubramanian, N., Preocanin, N. and Davidson, R.D., *J. Electrochem. Soc.*, **132** (1985) 793.
- (10) Di Paola, A., *Corros. Sci.*, **31** (1990) 739.
- (11) Di Paola, A., Di Quarto, F. and Sunseri, C., *Corros. Sci.*, **26** (1986) 935.
- (12) Private communication: *A personal discussion with A. J. Davenport at the Corrosion 2004 Conference*, New Orleans, Louisiana, March 2004.
- (13) Ryan, M.P., Williams, D.E., Chater, J., Hutton, B.M. and McPhail, D.S., *Nature*, **415** (2002) 770.
- (14) Preusser, S., Stimming, U. and Tounaga, S., *J. Electrochem. Soc.*, **142** (1995) 102.
- (15) Tsuchiya, H., Fujimoto, S. and Shibata, T., *J. Electrochem. Soc.*, **151** (2004) B 39.

CHAPTER 6 CONCLUSION

The nature of the passive films formed on austenitic stainless steels was studied by photocurrent spectroscopy and *in situ* Raman spectroscopy coupled with electrochemical measurements. This experimental scenario was capable of revealing an in depth understanding of the electronic properties of the passive film together with its structure and composition. The major conclusions drawn from this study are as follows:

In a borate solution (pH=9.2)

- The reduction phase change that occurred at around 100mV on the reverse potential scan, due to the formation of Cr(III) phases; had a significant influence on the characteristics of the passive films. The break in the Mott-Schottky plots between 400mV and 0mV arose due to the change in electronic properties of the passive films as a consequence of this phase change.
- The flat band potentials of passive films formed on stainless steels in a 0.1M borate solution were independent of composition and the frequency.
- The bandgaps of the oxides in the passive films are independent of potential.
- The existence of a high density of states localised between the valence and the conduction bands demonstrated the amorphous nature of the passive films on all three stainless steels; charging of these states lead to a strong frequency dependence of the measured capacitance.

The mid bandgap states influenced the photocurrent characteristics including the relaxation of the photocurrent due to filling of empty states under irradiation and tunnelling of electrons from filled mid bandgap states into the conduction band.

- Based on the charged passed it appears that within the passive region the oxide films increase linearly with potential, with anodising ratios for 304L, 316L and 254SMO being 10 nm / V, 10.5 nm / V and 5 nm / V, respectively. However, at a potential of 200mV (SCE), the anodising ratio of 254SMO suddenly increases, possibly due to the production of a Cr(VI) oxide.
- The structure, composition and type of semiconductivity of passive films of three stainless steels; 316L, 304L and 254SMO varied according to three different applied potential regions:
 - *800mV to around 300mV* - Fe(III) oxide with n-type semiconductivity and a bandgap of $1.95\pm 0.05\text{eV}$ (all three stainless steels);
 - *200mV to -300mV* - dual oxide layered structure consisting of an n-type chromium based high bandgap oxide ($2.9\pm 0.5\text{eV}$ in 316L, $2.8\pm 0.5\text{eV}$ in 304L and $2.4\pm 0.5\text{eV}$ in 254SMO) inner layer and an n-type iron based low bandgap oxide ($1.95\pm 0.5\text{eV}$) outer layer;
 - *-800mV to -900mV* - chromium based oxide with p-type semiconductivity with bandgaps of $2.9\pm 0.5\text{eV}$ in 316L, $2.8\pm 0.5\text{eV}$ in 304L and $2.4\pm 0.5\text{eV}$ in 254SMO.
- Evidence was found for the presence of Ni in the passive film on 254SMO.

- The $\text{Fe(II)[Cr(III)}_x\text{Fe(III)}_{(1-x)}\text{]}_2\text{O}_4$ structure was proposed as the high bandgap oxide phase ($2.9\pm 0.5\text{eV}$ in 316L, $2.8\pm 0.5\text{eV}$ in 304L) in 316L and 304L passive films with a higher content of Cr in the film on 316L than that on 304L. An $\text{Ni[Fe(III)}_y\text{Cr(III)}_{(1-y)}\text{]}_2\text{O}_4$ structure was proposed as the high bandgap oxide phase ($2.4\pm 0.05\text{eV}$) in the passive film on 254SMO.
- The Cr(VI) oxide formed in the transpassive region appears not to dissolve. As yet it is unclear if this is due to low solubility or protection by an outer insoluble iron oxide layer. The effect was the most dramatic on 254SMO, where an analysis of the charge passed in the cyclic voltammogram suggested that all the Cr(VI) formed in the transpassive region was reduced back to Cr(III) on the reverse sweep.

In a sodium chloride solution

- In situ Raman spectroscopy indicated that in NaCl the Fe-Cr spinel disappears just prior to the onset of pitting, this spinel also appeared to be more stable on 316L than 304L. It was thus postulated that Mo helps to stabilise the spinel, thereby preventing pitting corrosion.
- *In situ* electrochemical AFM allowed real time imaging of pitting corrosion. It was found that pits initiate close to sulphide inclusions. However, this is consistent both with a chromium depletion mechanism¹ and a stressed oxide mechanism.²

- The detrimental effect of sulphide inclusions on the pitting resistance of stainless steels was confirmed by studying pitting potentials and metastable pitting current transients of the different grades in NaCl. The sulphide inclusions on stainless steels appeared as clusters and the number of inclusions per cluster increased, in as the bulk sulphur composition increased in the stainless steel. However, as pitting was observed in the very low sulphur containing 316LVM, it was also postulated that sulphide inclusions may not be the sole cause of pit initiation.

References

- (01) Ryan, M.P., Williams, D.E., Chater, J., Hutton, B.M. and McPhail, D.S., *Nature*, **415** (2002) 770.
- (02) Sato, N., *Electrochim. Acta*, **16** (1971) 1683.

CHAPTER 7 FUTURE RESEARCH

This research inspired additional works to be proposed that would lead to a more complete understanding of the nature of passive films formed on stainless steels. However, these tasks are proposed as future work, since it was not feasible to conduct them within the limited time frame of a PhD programme and in some cases due to unavailability of instrumentation.

- a) *In situ* ellipsometric studies: *In situ* ellipsometry can provide a more reliable estimate of thickness variations with applied potential. Furthermore ellipsometry can also pin-point the potential at which any compositional or structural changes in the passive film occurs.

- b) Scrutinising the passive films formed on pure Cr, Fe and Ni: Studying the passive films formed on pure Cr, Ni and Fe, which are the main constituents of stainless steel will give a deeper insight of their individual behaviour. Although there is some work in the literature for the pure metals, it is far from complete especially in relation to Raman spectroscopy coupled with electrochemical characterisation. In particular, mixed metal oxide spinels obviously cannot be formed on pure metals, hence Raman shifts assigned to the spinels in this thesis should be absent. Whereas peaks associated with Fe_2O_3 , $\text{Cr}(\text{OH})_3$ etc. should still be present.

- c) Rotating ring disc electrode: Rotating disc electrode technique can be used to study any dissolution product of the oxide involved in the passivation process.

The technique is advantageous to investigate the transpassivation of Cr(III) into Cr(VI) to resolve the controversy of the nature of Cr(VI) product; whether it dissolves into the solution or is retained in the passive film.

- d) *In situ* atomic force microscopy (AFM): *In situ* AFM has proved its remarkable advantages for studying real time pit initiation events on stainless steels (see Section 4.4.3). However, thorough *in situ* AFM experimentation could not be accommodated within the limited time period of this thesis work. The work can be directed to rationalise the relationship between the sulphide inclusions and the pit initiation. Deeper understand of pitting events can be expected. However, some constraints have to be overcome, such as confining the surface area of the sample and locating sulphide inclusions.
- e) Vacuum melted stainless steel: The effect of sulphide inclusions on the pitting corrosion resistance can be further studied if a vacuum melting facility is available. Although 316LVM was used in the research, it cannot be totally compared to 316L based on sulphide percentage alone as there are slight differences in the weight percentages of other elements, such as Mo, Cr and Ni. However, if 304L can be vacuum melted to remove sulphur, its pitting resistance may improve to a level similar to 316L. If it does not, then the role of the Mo would have to be more than suppressing the role of inclusions, for example it may reduce stress in the oxide film.
- f) Photocurrent transients studies: To enhance the accuracy of the results obtained on films formed on stainless steels with various bandgap values,

photocurrent transients investigations should be further extended using monochromatic light sources with different wavelengths and intensities. This would shed light on the nature of the mid-bandgap studies thought to be responsible for unusual shape of the photocurrent transients on 254SMO (Figure 4.21). Using a 633nm He-Ne laser would allow the iron rich oxide with a bandgap of $\sim 1.95\text{eV}$ to be investigated without any interference from the Chromium (III) oxide phases that have larger bandgaps.

- g) XPS studies: XPS studies can be conducted to confirm the reduction phase change occur at around 100mV in stainless steels passive films as well as to get some indication about the Cr(VI) phase formed in the transpassive region

Appendix A: Surface states at solid/liquid interfaces^{A01,A02}

The electronic energy levels that are localised at the surface are called surface states. They can be donors or acceptors. Surface states at a clean surface are termed intrinsic states and those due to interaction with external sources, such as adsorbates from the solution (or gas phase in the case of solid/gas interface), are called extrinsic surface states. Nonadsorbed ions in the solution close enough to the surface for electron exchange with the bands can also be considered to provide surface states.

The intrinsic surface states on the clean surface of a covalent solid can arise due to dangling bonds and are called “Shockley surface states”. The clean surface of a more ionic compound semiconductor or insulator will get ionic surface states called “Tamm states”. The existence of bonding via directed metal *d*-states in compounds may result in dangling bonds of metal *d*-character at the surface for certain crystal plane terminations. Extrinsic surface states are mainly due to adsorbed electroactive species; species that tend to give up or accept electrons.

Surface states have a substantial influence on both the chemical and physical properties of the liquid / solid interface, these include:

- space charge and double layer induced by charge on surface states;
- recombination of minority carriers may occur at surface states;
- surface state energy levels can act directly in electrochemical reactions by acting as intermediate states in the electron transfer between the semiconductor’s bands and ions in the solution;
- shift of the flat band potential in Mott Schottky plots. (Fermi energy can be pinned by surface states and the capacitance becomes independent of voltage.)

References

- (A01) Morrison, S.R., "*Electrochemistry at Semiconductor and Oxidised Metal Electrodes*", Plenum Press, New York (1980).
- (A02) Jaegermann, W., *Mod. Aspec. Electrochem.*, **30** (1996) 35.

Appendix B: Recombination processes

Not all electron hole pairs excited by irradiating a semiconductor by light with suitable energy will result in a photocurrent, instead they may recombine. Figure B.01 shows the possible bulk and surface recombination processes schematically. Due to this the photocurrent conversion efficiency does not only depend on the generation and collection terms but also on electron hole recombination rates via energy levels in the space charge region and at the surface (surface states).^{B01}

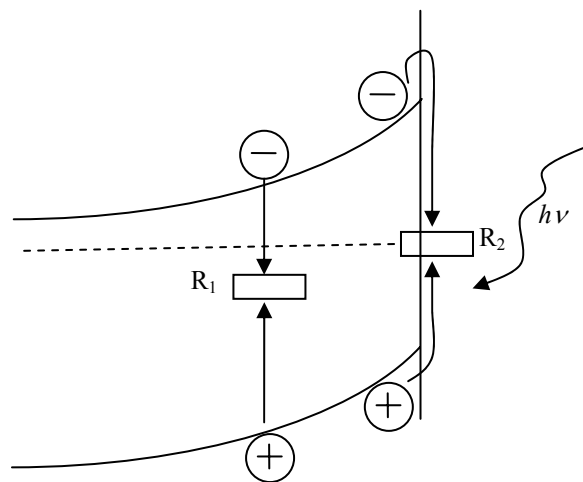


Figure B.01. Photocurrent loss mechanisms: photogenerated minority carriers can recombine either via energy levels in the bulk and space charge regions (R1) or via surface states (R2). In both cases, minority carrier capture results in a flux of majority carriers into the recombination zone. (adapted from the reference B02)

Bulk recombination can occur via:

- ◆ emission of a photon (i.e., thereverse of absorption);
- ◆ recombination centres associated with imperfections in the crystal structure;
- ◆ the excited electron being caught in a vibrationally excited interband state, before it cascades through a series of lower lying states emitting a lattice phonon with each step;

- ◆ localised defects that may provide a continuum of states right across the bandgap (the most common mechanism that occurs in amorphous passive films^{B02}).

Surface recombination occurs mainly via surface states (see Appendix A).^{B03-B05} As minority carriers accumulate on the surface states, the electron occupation factor (the quasi-Fermi level) shifts away from its equilibrium value and the majority carriers begin to flow into the surface where they annihilate the trapped minority carriers. This process is rapid close to flat band potential however, it is generally much slower under depletion conditions, since it depends on the concentration of majority carriers at the surface.

References

- (B01) Southampton Electrochemistry Group, “*Instrumental Methods in Electrochemistry*”, Ellis Horwood, Chichester (1985).
- (B02) Di Quarto, F., Piazza, S., Santamaria, M. and Sunseri, C., “*Handbook of Thin Film Materials, Volume 2: Characterization and Spectroscopy of Thin Films*”, (ed. Nalwa, H.S.), Academic Press, San Diego (2002) 373–414.
- (B03) Peter, L.M., *Chem. Rev.*, **90** (1990) 753.
- (B04) Li, J. and Peter, L.M., *J. Electroanal. Chem.*, **193** (1985) 27.
- (B05) Li, J. and Peter, L.M., *J. Electroanal. Chem.*, **199** (1986) 1.

Appendix C: Optical Transitions^{C01- C03}

Band to band transitions or in other words electronic excitation from the top of the valance band into the bottom of the conduction band in a crystalline material can be subdivided into direct and indirect. This is according to the k selection rule. When the bottom of the conduction band and the top of the valance band are located at the same k space, direct transitions are possible. Indirect transitions occur when they are located at different positions in the k space by intervention of phonons (Figure C.01)

If the optical transition can occur for all the values of k the transition is referred to as being *allowed*. On the other hand if that only occur if $k \neq 0$ the transition is termed to as being *forbidden*.

The relationship between the optical absorption coefficient and the bandgap for optical transition can be written in the form of;

$$\alpha h\nu = \text{const.} (h\nu - E_g)^n \quad \dots\dots\dots (C.01)$$

Here the value of the n depends on the nature of the optical transition where;

- $n = 1/2$ - direct allowed transition,
- $n = 3/2$ - direct forbidden transition,
- $n = 2$ - indirect allowed transition or nondirect transition in amorphous semiconductors,
- $n = 1/3$ - indirect forbidden transition.

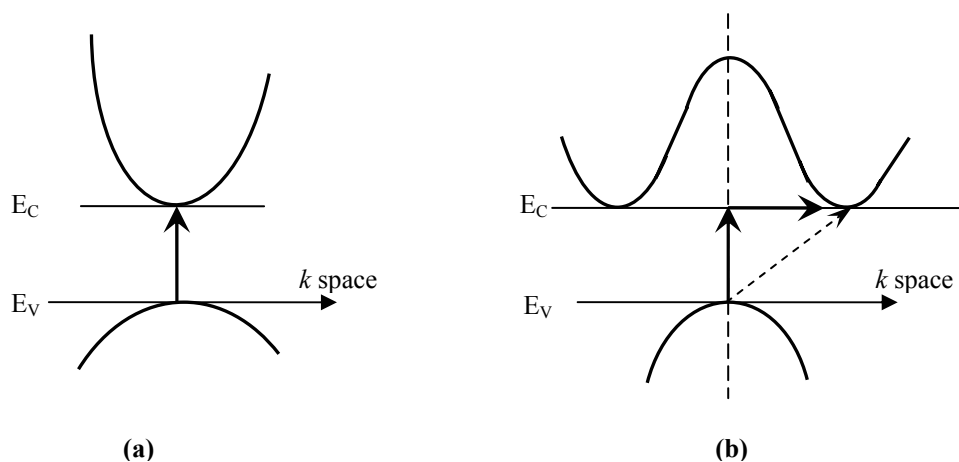


Figure C.01. The scheme for optical transition from the valance band to the conduction band; (a) direct and (b) indirect.

In amorphous semiconductors, the k selection rule is relaxed, due to the lack of periodicity. Consequently no intervention of phonons is invoked to conserve momentum and all energy required is provided by the incident photons. The photons interact with the solid as a whole in amorphous materials and the transition is termed as *nondirect* and n is found to be 2; that is the same as for an indirect allowed transition.

References

- (C01) Morigaki, K., “*Physics of Amorphous Semiconductors*”, Imperial College Press, London and World Scientific Publishers, Singapore (1999).
- (C02) Mott, N.F. and Davis, E.A., “*Electronic Processes in Non-crystalline Materials (2nd ed.)*”, Clarendon Press, Oxford (1979).
- (C03) Belo, M.D.C., “*Electrochemical and Optical Techniques for the Study and Monitoring of Metallic Corrosion*”, (ed. Ferreira, M.G.S. and Melendres, C.A.), Kluwer Academic Publishers, Boston (1991).

Appendix D: Correlation between the bandgap (E_g) and composition

Correlation between the bandgap of inorganic solids and single-bond energy was first modelled by Manca.^{D01} The model revealed a linear relationship between the band gap energy (E_g) and single-bond energy (E_s) in the form of:

$$E_g = a(E_s - b) \quad \dots\dots\dots (D.01)$$

where a and b are constants. The single-bond energy can be estimated by Pauling's equation:

$$D_{A-B} = (D_{A-A}D_{B-B})^{1/2} + (X_A - X_B)^2 \quad (\text{eV}) \quad \dots\dots\dots (D.02)$$

where D_{A-A} and D_{B-B} represent the bond energy of molecules A-A and B-B respectively in the gas phase, X_A and X_B are the electronegativity (measure of the tendency of an atom to attract shared electrons in a chemical bond) values of the elements A and B respectively in Pauling's scale. Later Vijn^{D02} attempted to rationalise Manca's results [Eq. (D.01)] using a thermochemical procedure correlating empirically the bandgaps and enthalpies of molecules.

Considering the above relationships Di Quarto *et al.*^{D03} proposed a semiempirical correlation between the optical bandgap of binary oxides and the difference between the electronegativities of oxygen and metallic elements (Pauling's extra-ionic energy). These authors further extended their model to ternary oxides and hydroxides by using the concept of average cationic or anionic group electronegativity and also considered the amorphous nature of passive films. The model has been extensively used for the *in situ* characterization of passive films.^{D04} The relevant relationships devised by Di

Quarto *et al.*^{D03} are presented below. Here X_M , X_O are electronegativities, on the Pauling's scale of metal cation and oxygen, respectively.

◆ For d – metal oxides;

$$E_g = 1.35(X_M - X_O)^2 - 1.49 \text{ eV} \quad \dots\dots\dots (D.03)$$

◆ For sp – metal oxides;

$$E_g = 2.17(X_M - X_O)^2 - 2.71 \text{ eV} \quad \dots\dots\dots (D.04)$$

◆ The average electronegativity ($\overline{X_C}$) of the cationic group for mixed oxides;

$$\overline{X_C} = \frac{aX_A + bX_B}{a + b} \quad \dots\dots\dots (D.05)$$

where a and b represent the stoichiometric coefficients of the mixed oxide $A_aB_bO_o$, and X_A and X_B are the electronegativities of the two metallic cations in the oxide.

The average electronegativity ($\overline{X_{an}}$) of the anionic group of an oxyhydroxide having a formula $MO_{(y-m)}OH_{2m}$;

$$\overline{X_{an}} = \frac{2mX_{OH} + (y-m)X_O}{y + m} \quad \dots\dots\dots (D.06)$$

◆ For sp – metal hydroxides;

$$E_g = 1.21(X_M - X_{OH})^2 + 0.90 \quad \dots\dots\dots (D.07)$$

◆ For d – metal hydroxides and oxyhydroxides;

$$E_g = 0.65(X_M - X_{OH})^2 + 1.38 \quad \dots\dots\dots (D.08)$$

For stainless steels all the major alloying elements are d -metals (*i.e.* transition metals).

The calculated bandgap values of some oxides, hydroxides and spinel oxides, and relative electronegativities of metallic cations are listed in Table D1. Most experimental values seem to support the proposed correlation except for few exceptions like NiO.^{D03} However, both positive and negative remarks had been made by various authors^{D03,D05} on this theoretical hypothesis.

Oxide	X_M or \bar{X}_C (from the reference D03 and Equation D.05)	E_g (eV) (calculated using Equations D.03, D.05, D.08 and X_M/\bar{X}_C values from the reference D03)	E_g (eV) (Experimental values recorded in literature)
MgO	1.20	8.7	8.70 ^a
Al ₂ O ₃	1.50	6.0	6.30 ^b
Cr ₂ O ₃	1.60	3.4	3.5 ^c
NiO	1.80	2.4	3.45±0.5 ^d
FeO	1.80	2.4	
Fe ₂ O ₃	1.90	1.9	1.90 ^c
Cr(OH) ₃	1.60	2.4	2.4 ^c
Fe(OH) ₃	1.90	1.96	
FeOOH	1.90	1.96	
Ni(OH) ₂	1.80	2.1	
FeCr ₂ O ₄	1.67	3.0	
NiFe ₂ O ₄	1.87	2.15	

Table D.01. Band gap values of some oxides, hydroxides and spinel oxides, and electronegativities of relevant metallic cations. (^a reference D05, ^b reference D06, ^c reference D07, ^d reference D08). Note the electronegativity value of oxygen has been used as 3.5 for calculations.

References

- (D01) Manca, P., *J. Phys. Chem. Solids*, **20** (1961) 268.
- (D02) Vijh, A.K., *J. Phys. Chem. Solids*, **30** (1969) 1999.
- (D03) Di Quarto, F., Sunseri, C., Piazza, S. and Romano, M.C., *J. Phys. Chem. B*, **101** (1997) 2519.
- (D04) Di Quarto, F., Piazza, S., Santamaria, M. and Sunseri, C., “*Handbook of Thin Film Materials – Volume 2, Characterization and Spectroscopy of Thin Films*”, (ed. Nalwa, H.S.), Academic Press, San Diego (2002) 373 – 414.

- (D05) Young-Nian, X. and Ching, W.Y., *Phys. Rev. B*, **43** (1991) 4461.
- (D06) Nelson, R.L. and Hale, *Faraday Discuss. Chem. Soc.*, **52** (1971) 77.
- (D07) Di Quarto, F., Piazza, S. and Sunseri, C., *Corros. Sc.*, **31** (1990) 721.
- (D08) Sunseri, C., Di Quarto, F. and Piazza, S., *Mater. Sci. Forum*, **185-188** (1995) 435.